CHRISTIAN-ALBRECHTS-UNIVERSITÄT ZU KIEL

TECHNISCHE FAKULTÄT

NANOSCALE SCULPTURING: ENHANCING ADHESION AND PRESERVING INTRINSIC MECHANICAL PROPERTIES OF METALLIC MATERIALS FOR MULTIFUNCTIONAL APPLICATIONS

DISSERTATION

Zur Erlangung des akademischen Grades eines

Doktor der Ingenieurswissenschaften (Dr.-Ing.)

der Christian-Albrechts-Universität

vorgelegt von

Herrn M.Sc. Chima Obobi KALU

aus

Aba-Nigeria

Kiel, June 2023

Datum der Einreichung: 30.06.2025

1. Gutachter: Prof. Dr. Rainer Adelung

2. Gutachter: Prof. Dr. Franz Faupel

Datum der mündlichen Prüfung: 29.11.2023

Abstract

The requirements for modern materials are multifaceted and often conflicting. For instance, materials should possess high-strength properties, similar to steels, while also being chemically inert, similar to low-surface energy polymers. These contradictory demands can be resolved by effectively integrating disparate materials into composites that enable the combination of different classes of materials, including ceramics, polymers, and metals. To achieve this, it is crucial to ensure adequate adhesion between the individual materials. Adhesion can be achieved through mechanical interlocking, chemical compatibility, and chemical bonding. If adhesion is based on mechanical interlocking, the chemistry and chemical compatibility of the individual materials play a negligible role in the adhesion. Still, the mechanical properties of the materials are exclusively important.

The state-of-the-art surface pre-treatment methods, such as grit-blasting, plasma treatment, and laser ablation, which aim to enhance surface adhesion, have limitations in terms of their insensitivity to changes in grain structure, crystallographic orientation, and poor mechanical interlocking structure. Recently, the formation of mechanically stable interlocking structures through nanoscale sculpturing has demonstrated improved surface adhesion properties. However, the effect of initial surface morphology on the evolution of these interlocking structures remains under-explored. Additionally, the preservation of mechanical properties, such as those of a thin metal wire, post-surface pre-treatment is crucial and requires further investigation.

This thesis investigates the structure nucleation efficiency in the mechanical hook-like interlocking structures evolution on metal surfaces [commercially available Aluminium alloy (AlMg3) and Austenitic grade 304 stainless steel (SST)] through chemical and electrochemical nanoscale sculpturing processes. Surface abrasion and the grit-blasting surface pre-treatment processes commonly used to increase surface roughness and total surface area of metal surfaces are tuned to achieve micro surface defects with different groves and grit indentation tip curvatures. The effect of the initial surface morphologies is emphasized, and it is found that the nucleation stage of the mechanically stable hook-like interlocking structure evolution depends on the initial surface morphology. This leads to a difference in mass loss and structure

nucleation times at the individual initial surface morphology, resulting in different times to complete the formation of mechanically stable hook-like interlocking structures.

Furthermore, the study characterizes the improved surface adhesion on sculptured SST strips through electrochemical nanoscale sculpturing, resulting in a super-hydrophilic micromechanical interlocking structure using a low aggressive/low toxic seawater-like and diluted HNO_3-based electrolyte. The resulting mechanical hook-like interlocking structure is found to comprise a multitude of bowl-shaped interconnected undercuts of different sizes that can also intergrow and form more extensive undercuts with wavy porous walls. In single-lap shear tests, different 2-component adhesives failed cohesively on sculptured SST while showing more than doubling the ultimate shear strength compared to the reference grit-blasted SST composites, which only showed adhesive failure.

The study also investigates the challenge of preserving the mechanical properties of SST wire during intense surface pre-treatment of such a thin wire to improve surface adhesion. Using an HCl-based electrolyte, an electrochemical nanoscale sculpturing model has been developed, preserving the mechanical property of the SST wire after an intense surface pre-treatment. This was successfully transferred from static laboratory nanoscale sculpturing to dynamic industrial large-scale nanoscale sculpturing.

Overall, this work provides new insight into the structure nucleation efficiency in mechanical hook-like interlocking structures evolution on metal surfaces and the potential for improved surface adhesion in SST strips. Additionally, it presents a model for intense surface pre-treatment of SST wire that preserves the intrinsic mechanical property of metallic materials.

Kurzfassung

Die Anforderungen an moderne Werkstoffe sind vielschichtig und oft widersprüchlich. So sollten die Werkstoffe beispielsweise hohe Festigkeitseigenschaften aufweisen, ähnlich wie Stähle, und gleichzeitig chemisch inert sein, ähnlich wie Polymere mit niedriger Oberflächenenergie. Diese widersprüchlichen Anforderungen können durch die effektive Integration unterschiedlicher Materialien in Verbundwerkstoffe gelöst werden, die die Kombination verschiedener Materialklassen, einschließlich Keramik, Polymere und Metalle, ermöglichen. Um dies zu erreichen, muss eine ausreichende Haftung zwischen den einzelnen Materialien gewährleistet sein. Adhäsion kann durch mechanische Verzahnung, chemische Kompatibilität und chemische Bindung erreicht werden. Wenn die Adhäsion auf mechanischer Verzahnung beruht, spielen die Chemie und die chemische Kompatibilität der einzelnen Materialien eine vernachlässigbare Rolle für die Adhäsion, aber die mechanischen Eigenschaften der Materialien sind ausschließlich wichtig.

Die modernen Methoden der Oberflächenvorbehandlung, wie z.B. Sandstrahlen, Plasmabehandlung und Laserablation, die darauf abzielen, die Oberflächenfunktionalität zu verbessern, haben ihre Grenzen in Bezug auf ihre Unempfindlichkeit gegenüber Veränderungen der Kornstruktur, der kristallografischen Ausrichtung und der schlechten mechanischen Verzahnungsstruktur. In jüngster Zeit hat sich gezeigt, dass die Bildung mechanisch stabiler, ineinandergreifender Strukturen durch Nanoscale Sculpturing die Adhäsionseigenschaften der Oberfläche verbessert. Die Auswirkungen der anfänglichen Oberflächenmorphologie auf die Entwicklung dieser verzahnten Strukturen sind jedoch noch nicht ausreichend erforscht. Darüber hinaus ist die Erhaltung der mechanischen Eigenschaften, wie z. B. die eines dünnen Metalldrahtes, nach der Oberflächenfunktionalisierung von entscheidender Bedeutung und bedarf weiterer Untersuchungen.

In dieser Arbeit wird die Effizienz der Strukturbildung bei der Entwicklung mechanischer hakenförmiger Verriegelungsstrukturen auf Metalloberflächen [AlMg3 und Edelstahl (SST) Band] durch chemische und elektrochemische Prozesse im Nanoscale Sculpturing untersucht. Der Oberflächenabrieb und die Oberflächenvorbehandlung durch Sandstrahlen, die üblicherweise zur Erhöhung der Oberflächenrauheit und der Gesamtoberfläche von Metalloberflächen eingesetzt werden, werden so eingestellt, dass Mikrooberflächendefekte mit unterschiedlichen Rillen und Krümmungen der Körnerspitzen

entstehen. Der Einfluss der anfänglichen Oberflächenmorphologie wird hervorgehoben, und es wird festgestellt, dass die Keimbildungsphase der mechanisch stabilen hakenartigen Verriegelungsstruktur von der anfänglichen Oberflächenmorphologie abhängt. Dies führt zu einem Unterschied im Massenverlust und in den Keimbildungszeiten der Strukturen bei den einzelnen anfänglichen Oberflächen morphologien, was zu unterschiedlichen Zeiten für die vollständige Bildung mechanisch stabiler hakenförmiger Verzahnungsstrukturen führt.

Darüber hinaus wird in dieser Dissertation die verbesserte Oberflächenfunktionalität auf skulpturierten SST-Streifen durch elektrochemisches Nanoscale Sculpturing charakterisiert, die zu einer superhydrophilen mikromechanischen Verriegelungsstruktur unter Verwendung eines wenig Aggressiven/wenig toxischen meerwasserähnlichen und verdünnten HNO_3-basierten Elektrolyten führt. Die daraus resultierende mechanische hakenartige Verriegelungsstruktur besteht aus einer Vielzahl schalenförmiger, miteinander verbundener Hinterschneidungen unterschiedlicher Größe, die auch miteinander verwachsen und umfangreichere Hinterschneidungen mit wellenförmigen porösen Wänden bilden können. In einlagigen Schertests versagten verschiedene 2-Komponenten-Klebstoffe auf skulpturiertem SST kohäsiv, wobei sich die ultimative Scherfestigkeit im Vergleich zu den gestrahlten SST-Verbundwerkstoffen, bei denen nur der Klebstoff versagte, mehr als verdoppelt hat.

Die Studie untersucht auch die Herausforderung, die mechanischen Eigenschaften von SST-Draht während der intensiven Oberflächenvorbehandlung eines so dünnen Drahtes zu erhalten, um die Oberflächenhaftung zu verbessern. Unter Verwendung eines HCl-basierten Elektrolyten wurde ein elektrochemisches Modell für die Nanoscale Sculpturing entwickelt, bei dem die mechanischen Eigenschaften des SST-Drahts nach einer intensiven Oberflächenvorbehandlung erhalten bleiben. Diese Methode wurde erfolgreich von der statischen Nanoscale Sculpturing im Labor auf die dynamisches, industrielles Nanoscale Sculpturing im großen Maßstab übertragen.

Insgesamt bietet diese Arbeit neue Einblicke in die Effizienz der Strukturkeimbildung bei der Entwicklung mechanischer hakenartiger Verriegelungsstrukturen auf Metalloberflächen und das Potenzial für eine verbesserte Oberflächenfunktionalität von SST-Bändern. Darüber hinaus wird ein Modell für eine intensive Oberflächenvorbehandlung von SST-Draht vorgestellt, dass die intrinsischen mechanischen Eigenschaften der metallischen Werkstoffe bewahrt.

Contents

Chapter 1

1.0 Introduction

Metals and their alloys have been used by humans for thousands of years, with the discovery of copper and bronze marking a significant turning point in human history [1,2]. Today, metals and alloys continue to play a vital role in modern society, with new and innovative alloys being developed to meet the demands of increasingly complex applications. These include automotive, aerospace, medical, construction, and household goods among others. Each of these applications has specific requirements regarding the mechanical, chemical as well as physical properties of the metals. For example, the chemical and physical properties of aluminium and its alloys, such as ductility, lightweight, and high strength-to-weight ratio, have given it a wide variety of applications. However, in terms of absolute loading capabilities, corrosion resistance, and biocompatibility, there is almost no alternative to stainless steel (SST), which is why SST has been the most preferred construction material [3–9].

In recent times, almost all branches of modern manufacturing industries have shown a growing demand for high-performance materials, i.e., high-strength and lightweight construction materials with ultra-high reliability to their interface and strength. However, a single material struggles to meet all these challenging and demanding advanced function requirements. In contrast, a composite system built on well-tailored materials offers a single solution to many issues [10]. Composites are categorized based on the fundamental substances used, e.g., ceramics, polymers, and metals [11]. They are made from two or more materials that retain their separate identity without chemically combining, mixing, or dissolving and are often joined by adhesive bonding to form structural components [4, 12, 13]. Here, surface adhesion is improved before combining two similar or different materials with adhesive [14–17]. However, the adhesive bond's quality determines the adhesive-bonded structure's reliability and integrity.

Several theoretical models explain adhesion theory, such as adsorption, chemical bonding, and physical or mechanical interlocking [18]. Adsorption theory explains the molecular contact, promoted by entire surface wetting between the substrate interfaces, commonly called van der Waals forces, and classified as secondary bonds [19]. In the case of

chemical bonding theory, primary bonds such as ionic, covalent, and metallic bonding are formed across the adhesive and substrate interface. It further explains the uses of adhesive promoters such as organosilanes, which form a bridge between the surface and the adhesive of a metallic surface [15]. The mechanical interlocking or keying model is one of the earliest adhesion mechanisms, and it was proposed by Mc Bain in 1925 [18]. According to this theory, the adhesion results from the adhesive penetrating the surface irregularities such as peaks, valleys, or open pores. Adhesion occurs because of the mechanical interlocking in-between such structures present on the substrate and the adhesive that fills these structures. The performance and durability of the adhesive bond depend not only on the properties of the adhesive itself but mainly on the surface properties and morphology of the substrate [18, 20 – 23]. Usually, surface modification or pre-treatment improves the adhesion properties of materials by changing the surface functionalities of the substrate. Furthermore, surface pre-treatments mainly help remove all contaminants and weak layers from the surface, increasing surface area and surface energy, and triggering all bonding mechanisms responsible for adhesion (physical, chemical, and mechanical) [24].

Conventional metal surface pre-treatments, including state-of-the-art grit-blasting, plasma treatment, laser ablation, abrasive scrubbing, and acid/alkaline etching, are employed to enhance the functionality of metal surfaces such as higher surface energy and area by changing the surface morphology (roughness), chemical activation, building of thick oxide layer, etc. [16,20,25]. These techniques show principle limitations because of their insensitivity to crystal orientations, aggregate grain structure changes, and poor mechanical hook-like interlocking structures [26–31]. However, a new chemical and electrochemical etching technique called nanoscale sculpturing, has been developed to overcome the problems of conventional surface pre-treatment techniques to provide microscale rough surfaces for reliable mechanical hook-like interlocking structures [21,23,32,33]. In contrast to the grit-blasting surface roughening process, nanoscale sculpturing precisely tunes the kinetics of oxide formation on the metal surface, controls its dissolution, and the subsequent intermediate passivation of certain crystal lattice planes (e.g., Al) [33]. This leads to the formation of mechanically stable hook-like interlock structures with undercuts. In SST, mechanically stable hook-like structures with undercuts are formed due to systematic and kinetically influenced dealloying of less noble constituents in the alloy composition and rate-dependent dissolution of less stable metal oxide [32]. Generally, nanoscale sculpturing is not sensitive to grain boundaries (like electropolishing) but sensitive to crystal orientations and chemical

compositions (like defect etching) and thus results in unique surface morphologies with mechanical hook-like interlocking structures.

The framework of this thesis outlined the structure nucleation efficiency during the evolution of mechanically stable hook-like interlocking structures on metal surfaces (AlMg3 and SST), as well as the improved surface functionalities of stainless steel. Additionally, the thesis presented a developed model for intense surface pre-treatment of stainless steel wire used as a medical guidewire while preserving its intrinsic mechanical properties through electrochemical nanoscale sculpturing.

Previous works on surface pre-treatment processes such as nanoscale sculpturing and micro-structuring of metal surfaces through chemical and electrochemical etching [21,23,33,34] focus on the improved adhesion property as a result of the presence of mechanical hook-like interlocking structures without details of the structures evolution and the effects of initial surface morphology in the structure nucleation efficiency. However, this thesis investigates the structure nucleation efficiency in the mechanical hook-like interlocking structures evolution on metal surfaces (AlMg3 and SST strip) through chemical and electrochemical nanoscale sculpturing processes, respectively, for the first time. Additionally, the effect of the initial surface morphologies is emphasized. Herein, the state-of-the-art grit-blasting surface pre-treatment process, which is generally used to increase the surface roughness, and the total surface area of the metal surface [2, 16], has been tuned to achieve micro surface defects with different curvatures of the grit indentation tip during the surface preparation of the samples. A quasi-flat surface obtained through surface abrasive scrubbing with different grades, distribution, and slope of the abrasive paper asperity [17] and as-received sample surfaces gave a variation of initial surface morphologies. It was found that the nucleation stage of the mechanical interlocking structure evolution depends on the initial surface morphology. This led to a difference in mass loss and structure nucleation times at the individual initial surface morphology, resulting in different times to complete the formation of mechanical hook-like interlocking structures.

The concept of drastic improvement in adhesion with mechanical hook-like interlocking microstructures for metals such as Al, Ti, Zn, and several of their alloys has been shown by Refs. [21,23,34], but not for SST, one of the frequently used construction materials. However, the improved surface functionality on austenitic grade 304 SST strip by electrochemical nanoscale sculpturing through the formation of super-hydrophilic micromechanical interlocking structure using a low aggressive/low toxic seawater-like and diluted HNO_3-based electrolyte is described in this work. The resulting mechanical hook-like interlocking structure

comprises a multitude of bowl-shaped interconnected undercuts of different sizes that can also intergrow and form more extensive undercuts with wavy porous walls. These mechanically stable undercut structures are grown by a highly selective/passivation etching (dealloying of less noble components) without any preferential etching, either elemental, grain boundary, or otherwise. As a result, these structures form in a self-organized manner and grow self-similar in depth. The formation of the micromechanical interlocking/hooking structures mainly depends on the control of the oxidation and passivation kinetics of the electrolyte composition, the flow rate of the electrolyte, and the chosen voltage/current regime. In single-lap shear tests, different two-component adhesives failed cohesively on sculptured SST strips while showing more than doubling the ultimate shear strength (USS) compared to the state-of-the-art grit-blasted SST composites, which only showed adhesive failure. These developed mechanical interlocks act as hooks in the polymer and establish a highly robust connection between the SST-polymer-SST composite which can easily adapt to a variety of different polymer classes.

SST wire has played an important role in the medical industry ranging from biomedical implants, stents, and medical guidewire [8, 33]. These wires are usually in the micrometer range (< 200 µm diameter), coated with a biocompatible polymer, and undergo rigorous manufacturing steps, e.g., the medical guidewire's production. Here, the adhesion of the biocompatible polymer on the wire is essential, whereas preserving the mechanical properties of such a thin SST wire during surface pre-treatment to improve surface adhesion is of great concern. Previous works on electrochemical micro-structuring of SST wire used for medical stents led to preferential grain boundary etching, low surface adhesion, and low mechanical interlocking [31]. The common state-of-the-art surface modification to increase adhesion is grit-blasting. However, the surface grit-blasting procedure imposes mechanical stresses, which is problematic when damageable parts like thin SST wire are used for a medical guidewire. In addition, conventional laser and plasma metal surface pre-treatment can alter the grain structure because of excess heating on such a thin SST wire used in the medical guidewire. This usually leads to grain structure re-orientation, affecting its mechanical properties [28].

This work describes a model developed for the intense surface pre-treatment of SST wire (~200 µm diameter) used in the medical guidewire through electrochemical nanoscale sculpturing. The intrinsic mechanical properties of the SST wire are preserved after bowl-like structures with distributed islands of an unsculptured surface, which seemingly preserves the diameter of the wire are formed. Furthermore, the influence of varying the concentration of the HCl-based aqueous electrolyte, the sculpturing time, and the current density were investigated. Different voltages were needed to drive the applied constant current (current density) in each

electrolyte, hinting at varying oxide thickness formation. This led to different sizes and distribution of the bowl-like structure formation, broader bowl-like structure with increasing sculpturing time, a preferential etching on the manufacturing process defect lines, the formation of spongy-pit structures, and a transition from anisotropic to isotropic etching [36–38]. In addition, a non-preferential grain boundary etching, a non-manufacturing process defect-line etching electrolyte, and sculpturing time to achieve evenly distributed shallow bowl-like interlocking structures with the distributed islands of unsculptured surface are found.

In the current pulsing approach described in this thesis, a cathodic regime, which serves as a passivation regime, is introduced between two anodic current pulsing spikes. This led to the passivation of the first-generation bowl-like structures, which left the island of unsculptured surface vulnerable, hence the formation of the second-generation bowl-like structures in the second anodic current pulsing spike. The formation of these two generations of bowl-like structures led to an increase in structure density, the formation of bowl-in-bowl structures, and an increase in bowl-like structure depth. The current pulsing approach offers a wide range of degrees of freedom in tuning different sizes of bowl-like structures, generational formation of bowl-like structures, formation of bowl-in-bowl structures, and an increase in structure density while preserving the mechanical properties of the SST wire. This model is so robust that the transfer from static laboratory electrochemical nanoscale sculpturing surface pre-treatment to dynamic industrial large-scale nanoscale sculpturing intense surface pre-treatment of SST wire used for medical guidewire was successful. Also, it exhibits great potential for improving the adhesion of biocompatible polymer on the nanoscale sculptured SST wire used for the medical guidewire.

This thesis follows a structured framework, where Chapter 2 provides the necessary theoretical background for the research. Chapter 3 provides detailed information on the materials, experimental set-ups, and procedures used in this work. The results of the research are presented in Chapter 4 and extensively discussed in Chapter 5. The new findings presented in this work were summarized in Chapter 6, along with recommendations for future research areas. Additionally, Appendix A and B highlight in comparison the results of the successful transfer from static to dynamic industrial large-scale nanoscale sculpturing and the improved surface adhesion.

Chapter 2

2.0 Theory

2.1 Solid-state materials

The properties of solid-state materials are understood by examining their electronic structure. The ability to conduct electricity is commonly used to classify them. According to the Electric Conductivity σ [Scm^{-1}], solid-state materials are classified into three major groups [39–41] isolators, semiconductors, and conductors. Table 2.1 shows typical conductivity values for each group.

***Table 2.1**: Materials and conductivity* [40].

Material	**Conductivity σ [Scm^{-1}]**
Isolator	$10^{-18} - 10^{-8}$
Semiconductor	$10^{-8} - 10^{4}$
Conductors	$10^{4} - 10^{6}$

Different theories describe the behaviour of materials. The free electron gas model describes some thermal properties of electrical conducting materials, i.e., heat capacity, while the band theory can classify the materials and simultaneously explain their electronic properties. Each atom has discrete atomic orbitals or energy levels likely occupied by electrons. According to Pauli's exclusion principle, each energy level hosts a maximum of two electrons with opposite spins. If more atoms are brought together and form a solid, the orbitals overlap, valence electrons interact, and a quasi-continuous energy spectrum, commonly called an energy band, forms. Electrons tend to occupy the lowest energy levels. The last occupied band is called the Valence Band (V_B), and the first unoccupied band is called the Conduction Band (C_B). The energy difference between the highest energy level of the valence band (E_V) and the lowest energy level of the conduction band (E_C) is called the Energy Band Gap E_G (i.e., $E_G = E_C - E_V$). The size of the band gap determines the conductivity and type of material. Materials are classified according to the band gap, as shown in Figure 2.1. Semiconductors typically show a band gap of 0.3 to 3 eV. The band gap of semiconductors depends on the external temperature. Ge, Si, and GaAs have a band gap of 0.66 eV, 1.12 eV, and 1.42 eV, respectively, for an

external temperature of 300 K. Insulators show band gaps larger than 3 eV. Metals have an energy band gap lower than 0.3 eV or even show an overlap of both conduction and valence bands.

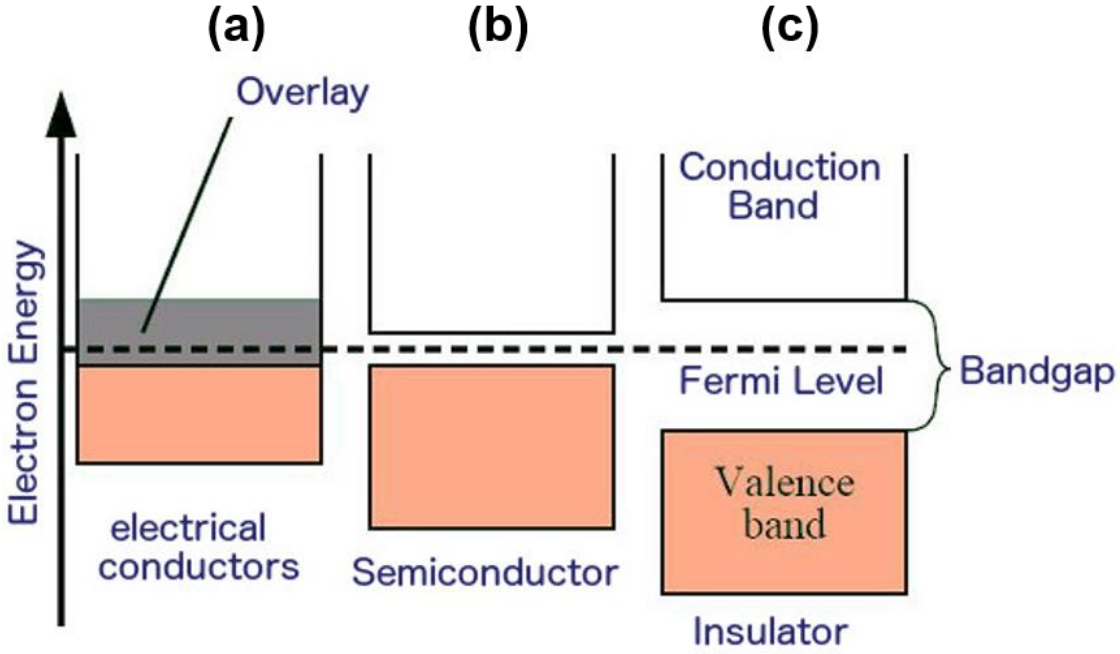

Figure 2.1: *Electron energy diagram of solid-state materials showing the fermi level and band gap of metals/electrical conductors* ***(a)****, semiconductor* ***(b)****, and insulator* ***(c).***

The movement of charge carriers through solid materials requires that electrons occupy free or partially filled orbitals. The valence band is generally filled and therefore occurs the conduction band where many unoccupied orbitals are still available. Insulators have such a large band gap that electrons cannot excite from V_B to the C_B and are hence not electrically conductive. On the contrary, the C_B and V_B overlap for conductors. Consequently, electrons from the V_B migrate to the C_B, hence metals are highly conductive. Semiconductors have small band gaps, and electrons at the V_B move into the C_B if excitation is applied. Electrons are excited thermally, electrically, or photonically. As electrons migrate from the V_B to the C_B, they leave a positively charged carrier at the V_B called Hole h^+. Therefore, the current in semiconductors has two components: electrons and holes. Both are mobile and have opposite charges [41,42]. In this thesis work, the focus is on conductors, for example, metals and their alloys.

2.3 Aluminium and its alloys

Aluminium (Al) is the third most abundant element (after oxygen and silicon), almost twice as plentiful as iron, and the fourth most abundant metal [43]. Its alloys are widely used in engineering applications due to their light weight, ease of shaping during fabrication, and

economic aspects. Aluminium is remarkable for its low density and ability to resist corrosion due to passivation (formation of a native oxide layer when in contact with air). The native oxide layer, which is transparent and inert, adheres firmly on the Al bulk and does not flake off as in the case of rust on iron or some steel [44], thus inhibiting the Al bulk from further oxidation. Structural components made from aluminium and its alloys are vital to the aerospace industry and are essential in other areas of transportation and structural materials. The most valuable compounds of aluminium, at least on a weight basis, are oxides and sulphates. As shown in Figure (2.2), Al has a face-centered cubic (fcc) structure with 12 slip systems, i.e., the combination of slip plane and slip direction. In the case of Al with its fcc crystal structure, the {111} planes are the most densely packed and provide four distinct slip planes with three <110> slip directions each. In the fcc structure, slip occurs in the {111} planes in the <110> direction. A high number of slip systems enable a tremendous amount of plastic deformation before fracture bringing forth the ductility in fcc metals [33,45].

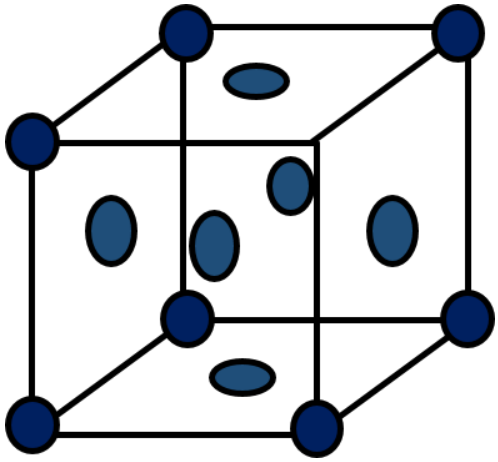

Figure 2.2*: *The fcc crystal structure of Aluminium.

2.3.1 Al Alloys

Aluminium is second only to iron as the most important metal of commerce. Pure aluminium has a relatively high strength-to-weight ratio. The density of Al alloys (99.65-99.99 %) is of the order of 2.7 g/mL, one-third that of steel. In addition to recycling and new smelting processes, aluminium has a relatively low cost, and its alloys provide a high strength ratio to weight. Salts of aluminium do not damage the environment or ecosystems and are non-toxic. Aluminium and its alloys are nonmagnetic and have high electrical conductivity, thermal conductivity, reflectivity, and non-catalytic action [44]. The typical alloying elements are copper, magnesium, manganese, silicon, tin, and zinc. There are two principal classifications, casting and wrought alloys, further subdivided into heat-treatable and non-heat-treatable. Cast

and wrought alloy nomenclatures have been developed. The Aluminium Association system is most widely recognized in the United States. Their alloy identification system employs different nomenclatures for wrought and cast alloys but divides alloys into families for simplification. A four-digit system is used for wrought alloys to produce a list of wrought composition families. Wrought alloys that constitute heat-treatable (precipitation-hardenable) aluminium alloys include the 2xxx, 6xxx, 7xxx, and some of the 8xxx alloys, as shown below [33,44,46].

•**1xxx:** Controlled unalloyed (pure) composition, used primarily in the electrical and chemical industries.

•**2xxx:** Alloys in which copper is the principal alloying element, although other elements, notably magnesium, may be specified. 2xxx-series alloys are widely used in aircraft where their high strength (yield strengths as high as 455 MPa, or 66 ksi) is valued.

•**3xxx:** Alloys in which manganese is the principal alloying element, used as general-purpose alloys for architectural applications and various products.

•**4xxx:** Alloys in which silicon is the principal alloying element, used in welding rods and brazing sheets.

•**5xxx:** Alloys in which magnesium is the principal alloying element, used in boat hulls, gangplanks, and other products exposed to marine environments.

•**6xxx:** Alloys in which magnesium and silicon are the principal alloying elements, commonly used for architectural extrusions and automotive components.

•**7xxx:** Alloys in which zinc is the principal alloying element (although other elements, such as copper, magnesium, chromium, and zirconium, may be specified) used in aircraft structural components and other high-strength applications. The 7xxx series is the strongest aluminium alloy, with yield strengths ≥500 MPa (≥73 ksi) possible.

•**8xxx:** Alloys characterizing miscellaneous compositions. The 8xxx series alloys may contain appreciable amounts of tin, lithium, or iron.

For the cast alloy series, the casting compositions are described by a three-digit system followed by a decimal value. The decimal .0 in all cases pertains to casting alloy limits. Decimals .1 and .2 concern ingot compositions, which after melting and processing, should result in chemistries conforming to casting specification requirements [43,45]. The 3xx.x cast series represents the sole exception in the nomenclature of Al alloys. This series is composed of Al-Si alloys with additional Si or Mg, while the corresponding 3xxx wrought Al alloy incorporates Mn as its primary alloying element. In all other cast and wrought Al alloys, the nomenclature of the first digit remains consistent.

In this thesis work, commercially available AW5754 aluminium alloy is used, which is an alloy in the wrought aluminium-magnesium family (5xxx series). It is a work hardenable alloy and exhibits moderate to high strength and toughness properties. It demonstrates favourable corrosion resistance, particularly in marine environments.

2.4 Allotropy of Iron (Fe)

Allotropy, in its general definition, is the ability of an element to exist in more than one physical state. It could also be defined as the existence of a chemical element in two or more forms, which may differ in the arrangement of atoms in crystalline solids or in the occurrence of molecules that contain different atoms. Allotropes may be monotropic, in which case one of the forms is the most stable under all conditions, or enantiotropic, in which case different forms are stable under different conditions and undergo reversible transitions from one to another at characteristic temperatures and pressures [47]. Iron (Fe), being one of the few chemical elements (tin, phosphorous, etc.) that exhibit such characteristics, could be in the form of Alpha (α), Gamma (γ), Delta (δ), and Epsilon (ε) allotropes of iron. Alpha, gamma, and delta iron are all found at atmospheric pressure, while epsilon is only found at high pressures [47]. Therefore, the emphasis will be on the first three allotropes.

2.4.1 Alloys of Fe

Alpha (α) is a body-centered cubic (bcc) (Figure 2.3) allotrope that forms when molten iron is cooled to 912°C and is the most stable form of iron found at room temperature. Alpha iron contains the highest volume and is the least dense of the three atmospheric allotropes [47] (Figure 2.3 a). Below 912 °C (1,674 °F), iron adopts the bcc structure characteristic of α-iron, also called ferrite. As it cools to 770 °C (1,418 °F), the Curie point [T_C (A_2)], the iron is a relatively soft metal and becomes ferromagnetic. Above the curie point, the substance assumes a paramagnetic property [48]. As iron passes below the Curie temperature, no structural change occurs but the magnetic properties as the magnetic domains become aligned. Carbon dissolves poorly in α-iron: no more than 0.021 % by mass at 723 °C. This form of iron is stable at room temperature. α-Fe can be subjected to pressures up to 15 GPa before transforming into a high-pressure form termed ε-iron, which crystallizes in a hexagonal close-packed (hcp) structure [47,49,50].

Gamma iron or Austenite (γ-Fe) is a face-centered cubic (fcc) allotrope of iron that is formed through the cooling of molten iron to a temperature of 1394 °C. This particular allotrope

exhibits the lowest volume and highest density. In the γ-iron phase, the iron matrix is capable of dissolving a significant amount of carbon, with a maximum solubility of approximately 2.04% by mass at a temperature of 1146 °C [47,51,52]. This γ form of carbon saturation is exhibited in stainless steel. Several grades of stainless steel (SST) depend primarily on its strength and corrosion resistance. The corrosion resistance of SST is a result of varying alloying elements such as chromium, nickel, and molybdenum.[52]. Table 2.2 summarizes the various types of SST.

Table 2.2: *Different grades and types of SST with their compositions and corrosion susceptibility.*

Grades of Stainless Steel	Alloying Elements compositions	Corrosion Susceptibility
Austenitic Alloys		
Grade 304 Stainless steel	*C (0.08 % max), Mn (2 % max), Ni (8 - 10.50 %), Cr (18 - 20 %), S (0.08 % max), Si (1 % max), and P (0.045 % max)*	*Good overall resistance to corrosion*
Grade 316 Stainless steel	*C (0.08 % max), Mn (2 % max), Ni (10-14 %), Cr (16-18%), S (0.08 % max), Si (1 % max), P (0.045 % max), and Mo (2 – 3 %)*	*Excellent chloride resistance*
Ferritic Alloys		
Grade 430 Stainless steel	*C (0.12 % max), Mn (1 % max), Cr (16-18 %), S (0.03 % max), Si (1 % max), and P (0.04% max).*	*Good nitric acid resistance*
Grade 434 Stainless steel	*C (0.08 % max), Mn (2 % max), Cr (16 - 18 %), S (0.08 % max), Si (1 % max), P (0.045% max), and Mo (0.75-1.25 %)*	*Superior pitting resistance*
Martensitic Alloy		
Grade 420 stainless steel	*C (0.15 - 0.40 % max), Mn (1 % max), Cr (12 - 14 %), Ni (0.50 %), S (0.03 % max), Si (1 % max), P (0.04 % max), and Mo (0.75 - 1.25 %)*	*Resistant to mild acids, alkalis, and water when hardened*

At 1,475 °C, δ-iron can dissolve as much as 0.08 % of carbon by mass. As molten iron cools down, it solidifies at 1,538 °C into its δ allotrope (δ-Delta), which has a bcc crystal structure. [47,49,50].

In this work, austenitic stainless steel of grade 304 in the form of strips and wire was utilized. This particular grade of stainless steel has demonstrated extensive utility in various industries, including automotive, construction, and medical, due to its exceptional strength, superior corrosion resistance, and biocompatibility after coating [53].

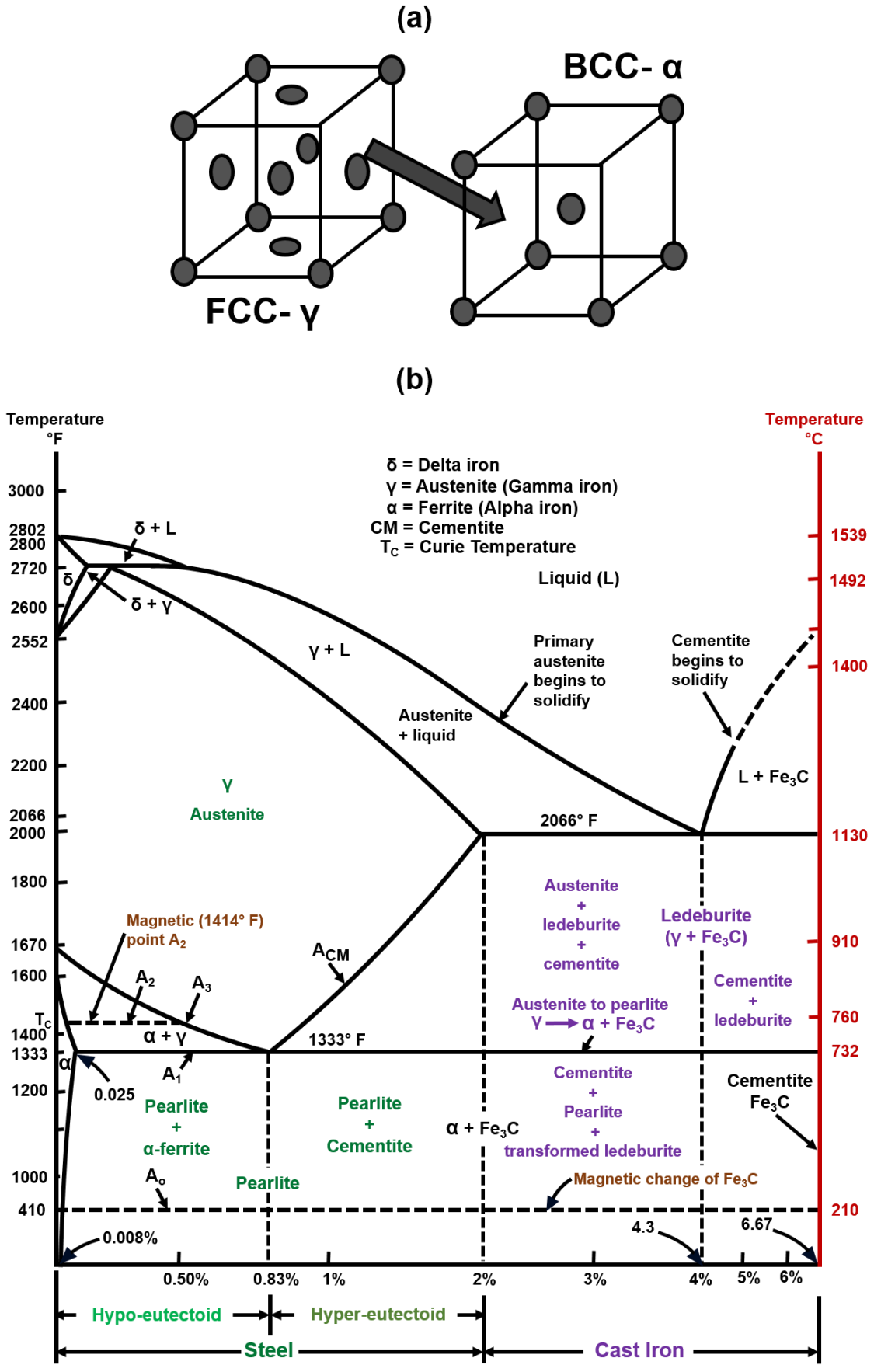

Figure 2.3**:** *Schematics of iron crystal structures* ***(a)*** *and a portion of the iron-carbon phase diagram* ***(b)*** [51].

2.5 Metal – Electrolyte interface

Generally, when a metal electrode is immersed in an electrolyte, the interfacial region is highly inhomogeneous in terms of both the electronic structure and the distributions of solvent molecules as well as ionic species. This complication is chiefly caused by a dense network of water dipoles in the electrolyte and by the competitive adsorption of different species on the metal surface. Particularly complex conditions exist in the case of corrosive and inhomogeneous materials prone to localized attack, which leads to etching and significant changes in the composition of the metal-adhering layer of the electrolyte. However, the exchange of electrons between the metal electrode and the ions in the electrolyte leads to the formation of an electrolyte double layer (i.e., stern layer and diffuse layer) [54,55].

As depicted in Figure 2.4 schematic showing fully solvated and partially solvated ions, the positively charged metal surface has the negatively charged ions adsorbed through the terminal of no hydration shell (partial solvated ions). These are called adsorbed ions because they are chemically bonded to the metal surface. Here, the Inner-Helmholtz-Plane (IHP) is formed, which originates from the center of the adsorbed partially solvated ions. Following the IHP is a layer of fully solvated ions close to the positively charged metal surface. The center of the fully solvated ion forms the Outer-Helmholtz-plane (OHP). Beyond the OHP is the Gouy-Chapman layer, also called the diffuse layer. This contains free-moving and randomly distributed fully solvated ions (cations and anions). However, the concentration of such fully solvated ions decreases as they move further away from the metal surface due to a decrease in the electrostatic force of attraction [54–56]. Furthermore, the electric potential (φ) tends to be stronger at the IHP as a result of the strong chemical bonding at the interface. This drops linearly at the OHP, where the ion is sparsely distributed, and exponentially at the Gouy-Chapman layer, where the ions are rather randomly distributed.

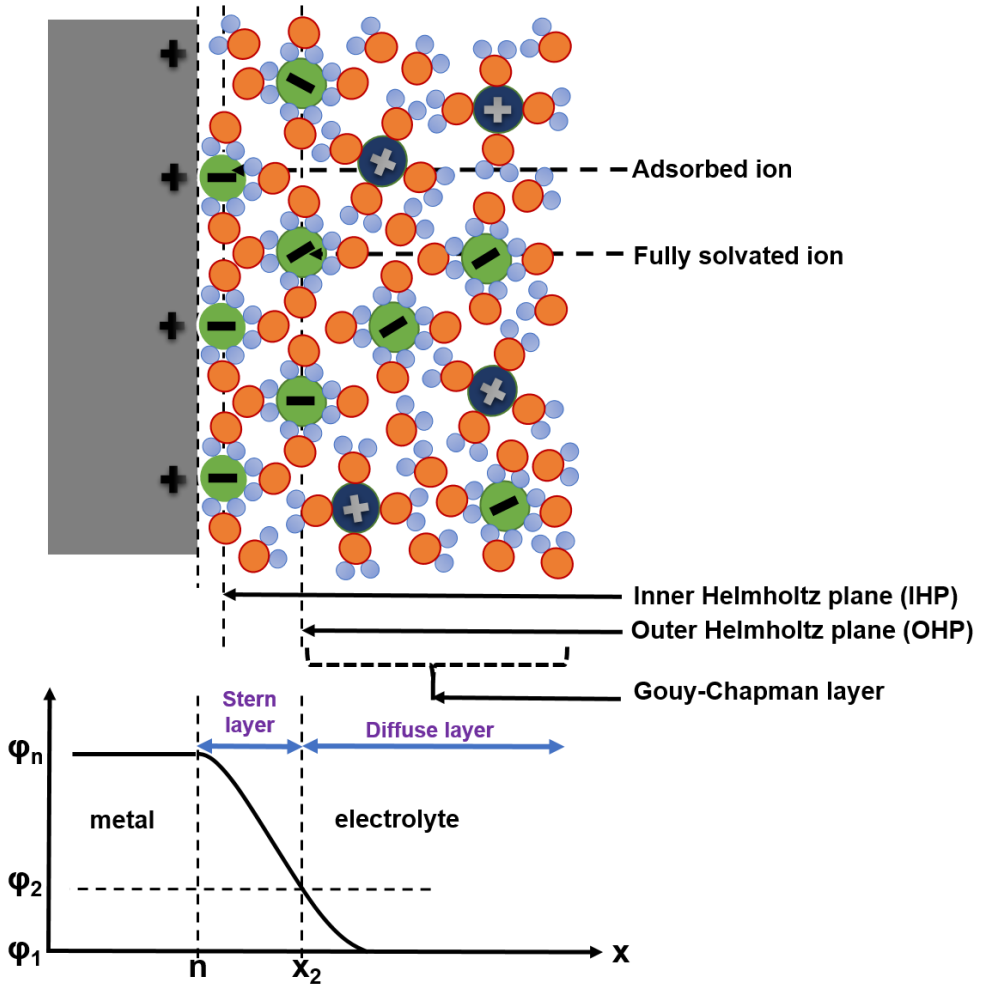

Figure 2.4: *Schematic of the metal-electrolyte interface showing the inner and outer Helmholtz plane, Gouy-Chapman layer, Stern layer, Diffuse layer, and the potential drop across the interface.*

2.5.1 Electric field strength

Electric field strength is a quantitative expression of the intensity of an electric field at a particular location. The standard unit is the volt per meter *(v m $^{-1}$).* An electric field always exerts a force on other charged particles, either repelling like charges or attracting opposite charges. This strength depends on three variables: the electric charge's magnitude, the surface's curvature, and the distance from its source [57]. Usually, an electric field is defined as a vector field. A vector field is where each point in space can be assigned a vector (a quantity with both a magnitude and direction). In an electric field, the magnitude assigned is the strength of the push or pull on a theoretical particle, and the direction defines whether that particle would be attracted or repelled. This is quite different from a scalar field, in which each point in space is assigned a magnitude (i.e., the temperature around a heat source).

Any electrically charged object produces an electric field. This field affects other charged objects in the vicinity. The field strength at a certain distance from an object is directly proportional to the electric charge, in coulombs, on that object. Conversely, the field strength is inversely proportional to the distance from a charged object. The field-strength-vs-distance curve is a direct inverse function and not an inverse-square function because electric field strength is specified in terms of a linear displacement (per meter) rather than a surface area (per meter squared) [57].

Electric field and surface curvature

One of the characteristics of conducting objects (metal) at electrostatic equilibrium is that the electric fields are strongest at locations along the surface where the object is most curved [58]. The curvature of a surface can range from absolute flatness on one extreme to being curved to a sharp tip on the other extreme (Figure 2.5).

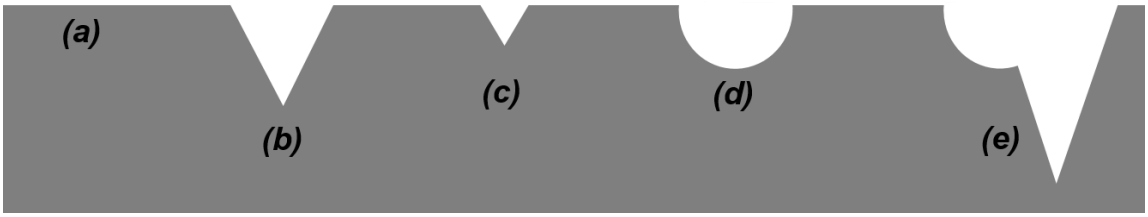

Figure 2.5: *Schematic of different surface curvatures: quasi-flat surface* ***(a)****, deep grove* ***(b)****, shallow grove* ***(c)****, indentation/round tip curvature* ***(d)****, and mixed tip curvatures* ***(e)****.*

The electric field strength on a flat surface is characterized by being relatively weak, while that of a sphere with the same radius of curvature is uniform throughout the surface. However, a surface with a high degree of tip curvature, such as a sharp tip, is characterized by relatively strong electric fields [58,59]. This phenomenon can be explained by the behavior of negatively charged objects with a sharp tip curvature [Figure 2.6 (a)]. Here, the electrostatic force causes excess electrons to disperse in a manner that reduces the effect of their repulsive forces by increasing their distance from each other. Therefore, the excess electrons would accumulate in greater density along the sharp tip curvature.

In comparison, as shown in Figure 2.6 (a), electrons located on a flat surface section, such as A and B, repel each other along a connecting line that is parallel to the surface. On the other hand, electrons C and D along a surface section with a sharp tip curvature experience a repulsive force that is directed at the tip angle, causing the parallel components of the forces to be considerably less. This causes the excess electrons to move along the surface because most of the repulsive force between electrons C and D is directed perpendicular to the surface. The

electrons move and distribute themselves until electrostatic equilibrium is reached, resulting in a relatively large accumulation of charge on the sharp tip curvature [Figure 2.6 (b)]. This accumulation of charge, combined with the fact that the repulsive forces are primarily directed perpendicular to the surface, leads to a stronger electric field at surfaces with sharp tip curvature [Figure 2.6 (c)] [59].

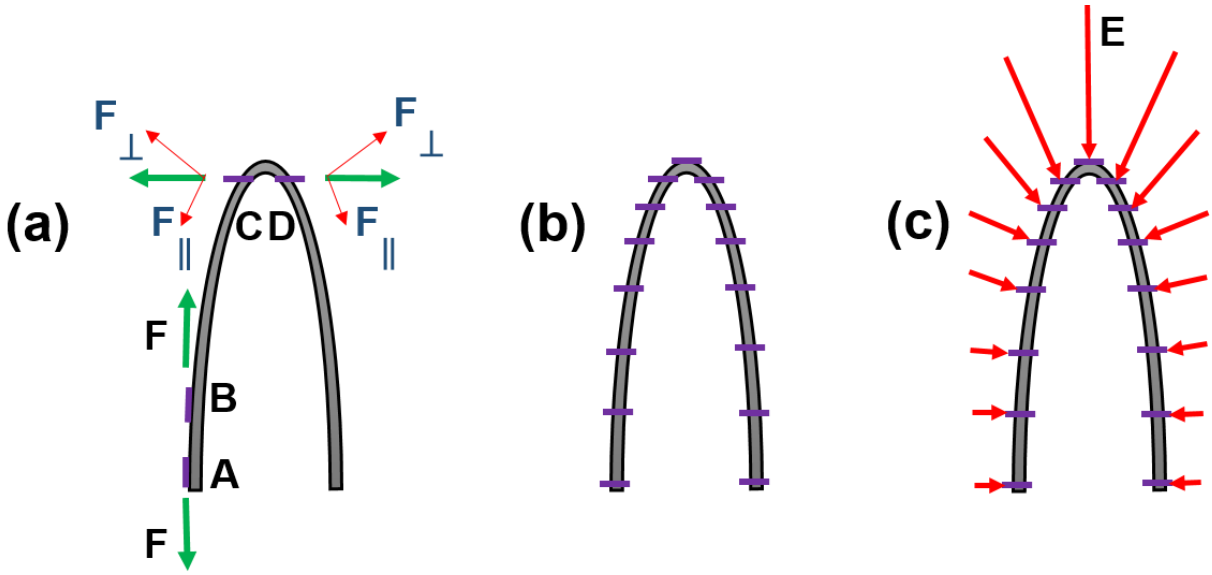

Figure 2.6: *Schematic of charge distribution in a sharp tip curvature: accumulation of charges on a flat and sharp tip curvature* ***(a)****, distribution of accumulated charges on a metal surface* ***(b),*** *and the magnitudes of electric field strength in a metal surface with sharp tip curvature* ***(c)****.*

The enhancement of the electric field at the tip curvature leads to phenomena such as local electric breakthrough, current tunneling effect, avalanche breakdown, thermionic emission, etc., as well as crack formation as a result of volume expansion of the substrate passive oxide layer during the etching process; hence the formation of porous structure and etch pits [41,60–62].

In this work, surface pre-treatment procedures, such as grit-blasting and surface abrasion with different grades of abrasive paper, predominantly used to improve surface roughness [14,63], were tuned to achieve surface roughness of different degrees and sizes with varying tip curvatures.

2.6 Nanoscale sculpturing

Nanoscale sculpturing is a surface pre-treatment process in which the metal surfaces are roughened by forming a stable mechanical hook-like structure with undercuts [21]. This aims to modify surface functionalities such as wettability, optical reflectance, adhesive properties, and corrosion resistance through chemical or electrochemical etching processes [21,33].

In this work, chemical and electrochemical nanoscale sculpturing is used in the surface sculpturing of the AlMg3 strip (chemical etching process), SST strips, and SST wire (electrochemical etching process).

2.6.1 Chemical etching of AlMg3

Chemical etching is a non-traditional machining process in which material removal is carried out using a robust chemical solution called “etchant.” This is simply the “accelerated and controlled corrosion” process. It has a long history, back to BC 2500, used to produce jewelry from copper by citric acid in Ancient Egypt and has been applied to reduce the weight of the workpiece materials [64]. However, the first chemical etchings of aluminium were mainly carried out for decorative purposes. Chemical etching of aluminium was industrially completed by M.C. Sanz from North Aviation Inc. in 1956 and named the process “chemical milling” or, in short, “chem-mill” [65,66].

Aluminium has a density of 2.7 g/cm^3 and therefore belongs to the light metals. Its crystal structure is fcc. With a standard potential of -1.66 V, aluminium does not belong to noble metals. However, the formation of thin (few nanometres) Al_2O_3 films, which is amphoteric, makes it very inert in many substances [67–70]. Nanoscale sculpturing of aluminium yields cubic crystallographic structures with stable mechanical hook-like interlocking structures. This can be explained by the crystal structure of aluminium being fcc and the different surface energies of each crystal plane. The process of structure formation consists of several steps: oxide formation, oxide dissolution, and specific crystalline plane passivation [21,33].

An oxide layer is formed by immersing the aluminium in an aqueous hydrochloric acid (HCl) electrolyte. Due to volume expansion during the formation of the oxide layer, there is oxide layer perforation as a result of chlorine ions (Cl^-) adsorption [71]. The adsorption process is chiefly influenced by the open circuit potential, the electrolyte's temperature and pH value, and the initial surface morphology, which is typical for aluminum [61,62,71–74]. Furthermore, the aluminium fcc crystal structure exhibits a certain degree of preferential etching arising from the crystallographic symmetry, surface energy, degree of passivation, and packing density at individual planes [73,75]. For example, the {100} plane, which has the second highest packing density when compared to the {111} plane (the highest packing density), serves as a stopping plane arising from its quick passivation inclined with the symmetry leading to the formation of the cubic crystallographic structures [Figure 2.7 (a) – (d)], hence the mechanical interlocking structures [73]. This is the opposite of what is already known in porous silicon etching [41].

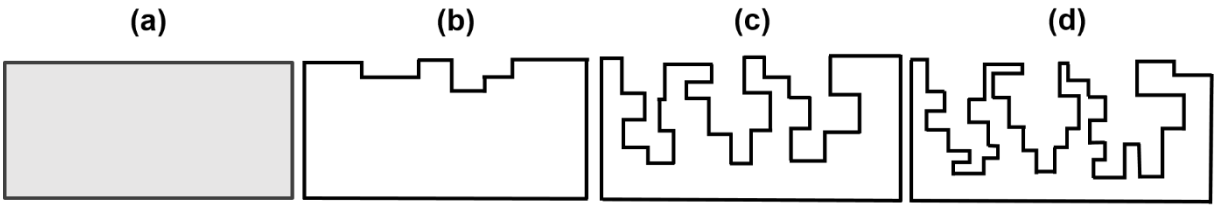

Figure 2.7: *Schematic of AlMg3 structuring steps and stages: bulk AlMg3* ***(a)****, structure nucleation* ***(b)****, stable mechanical hook-like interlocking structure* ***(c),*** *and self-amplifying and continuous in-depth formation of hook-like interlocking structure* ***(d).***

The corrosion reaction of HCl with aluminium yields, most likely an aluminium salt (aluminium chloride - $AlCl_3$), and hydrogen gas as another reaction product (see equation 2.1).

$$2Al + 6HCl \rightarrow 2AlCl_3 + 3H_2 \uparrow \tag{2.1}$$

In general, aluminium forms an oxide layer when immersed in water. The structure of this oxide layer is temperature-dependent. It is amorphous for temperatures below 400 °C, but because of the formation rate, it is a mixture of amorphous and crystalline for temperatures above 500 °C. Since oxide layer formation temperatures are far below 400 °C in nanoscale sculpturing, the layer is most likely amorphous. During the reaction, the oxide layer is dissolved. Redox products and reaction rate depend on the pH; below a pH of 10, the reaction rate is constant since it mainly depends on the hydrolysis of the Al-O bonds. Hydrolysis depends on the diffusion of protons into the oxide layer [76]. Therefore, the reaction occurring during nanoscale sculpturing is rate-dependent selective oxide layer dissolution (see equation 2.2).

$$Al_2O_3 + 6HCl \rightarrow 2AlCl_3 + 3H_2O \tag{2.2}$$

Here, the non-equilibrium chemical reactions are classified into exothermic or endothermic reactions. If a reaction is endo- or exothermic depends mainly on standard Gibb's Energy of Formation $\Delta_f G^0$ (see equation 2.3) [77].

$$\Delta_f G^0 = X\Delta_{f_{products}} G^0 - X\Delta_{f_{educts}} G^0 \tag{2.3}$$

This only applies to spontaneous reactions which are not in equilibrium. If $\Delta_f G^0$ is smaller than zero, the reaction occurs without external energy and is exothermic. In case of $\Delta_f G^0$ being greater than zero, the process needs external energy to occur and is endothermic. External energy in chemical reactions is often provided by heat. $\Delta_f G^0$ is calculated by:

$$\Delta G = \Delta H - T\Delta S \tag{2.4}$$

To predict the chance for possible reaction products to form, one can use the standard enthalpy of formation $\Delta_f H$, which is defined as the change in enthalpy occurring during the formation of the compound from the elements under standard conditions [78,79]. For a spontaneous exothermic reaction at constant temperature *(T)* and pressure (no rise in entropy ΔS), $\Delta_f H$ must be negative to fulfill equation 2.4. Therefore, a rule of thumb for predicting reaction products is: The smaller the $\Delta_f H$ of a product, the more likely it is formed during the reaction. For example, the chemical etching of AlMg3 is exothermic; therefore, heat is produced during the structuring process.

2.6.2 Electrochemical etching of stainless steel

Electrochemistry is the study of reactions in which charged particles (ions or electrons) cross the interface between two phases of matter, typically a metallic phase (the electrode) and a conductive solution or electrolyte, i.e., electricity-related applications of oxidation-reduction reactions. Such a process can always be represented as a chemical reaction and is generally known as an electrode process [79]. Electrode processes take place within the double layer (Figure 2.4) and produce a slight unbalance in the electric charges of the electrode and the electrolyte [42,54–56,78]. The importance of electrochemistry lies in how these potential differences can be related to the thermodynamics and kinetics of electrode reactions. In particular, manipulating the interface potential difference affords an important way of exerting external control on an electrode reaction [78,79].

The Nernst equation relates the activities of the species involved with the electrode potential, *E*, of the half-reaction and its standard electrode potential, E^O, which is the value of the potential relative to the standard hydrogen electrode when the activities of all species are unity. For the generic half-reaction

$$\sum p_i O_i + ne^- \rightarrow \sum p_i R_i \tag{2.5}$$

Where *n* is the stoichiometric number of electrons transferred for each species, the Nernst equation is

$$E = E^\theta - \frac{RT}{nF} \sum p_i In\, a_i \tag{2.6}$$

In which *R* is the universal gas constant, *T* is temperature, and *F* is the Faraday constant. When p_i has positive values for products [reduced species (*R*)] and negative values for reagents [oxidized species (*O*)]. This can be written as

$$E = E^{\theta} + \frac{RT}{nF} In \frac{\prod a_{O_i}^{p_i}}{\prod a_{R_i}^{p_i}} \quad (2.7)$$

The cell potential indicates the maximum energy that can be obtained from an electrochemical cell, which is equivalent to the Gibbs free energy change *(ΔG)* of the cell reaction. This quantity represents the maximum amount of work that the cell can provide. This value is

$$\Delta G = -nFE_{cell} \quad (2.8)$$

The removal of energy in the form of current or chemical conversion leads to a reduction in the quantity of unconverted substances, which is indicative of changes in the concentrations of species present in the liquid phase. In contrast, in the solid phase, however, no activity alteration is usually accepted as unity [78].

Surface passivation

The transition from the active to the passive state of some metal surfaces under certain environmental conditions, usually over a few hundred millivolts, is defined as surface passivation. The corrosion resistance of high alloyed steels is due to their ability to protect themselves by forming so-called passive films on their surfaces. The stability of the passive state is variable. If aggressive anions, such as halogens or oxidizing agents, are present in the environment, the passive film is broken down, and the steel is attacked locally [80,81].

Anodization of stainless steel

An electrochemical process converts the SST surface into a corrosion-resistant, anodic oxide film by applying a high electric field. When a sufficient DC voltage is applied between an anode and cathode, oxidation and reduction reactions repeatedly, occur at the electrode surfaces [82,83]. The oxidation reaction at the anodic regime (see anodic regime reaction equations below) leads to the formation of an oxide layer. However, in a very acidic electrolyte, the passive oxide layer is broken down, and the SST is attacked locally through anions (Cl^-) adsorption across the passive oxide layer [82–85].

Anodic regime (Anodic reaction in the bowl-like structure)

$$3\,Fe\ + 4\,H_2O\ \rightarrow\ Fe_3\,O_4\ + 8H^+ + 8e^- \tag{2.9}$$

$$Fe\ \rightarrow\ Fe^{2+} + 2e^- \tag{2.10}$$

$$Fe^{2+}\ +\ H_2O\ \rightarrow Fe(OH)^+ +\ H^+ \tag{2.11}$$

$$2Fe(OH)^+ +\ H_2O \rightarrow\ Fe_2O_3\ + 4H^+ + 2e^- \tag{2.12}$$

The hydrolysis of the cations (Fe^{2+}) is accelerated in the presence of the anions (Cl^-)

$$Fe^{2+} +\ Cl^{2-} \rightarrow FeCl_2 \tag{2.13}$$

$$FeCl_2\ +\ H_2O \rightarrow Fe(OH)^+ + H^+ +\ 2Cl^- \tag{2.14}$$

$$Fe^{2+} +\ H_2O\ \rightarrow Fe(OH)^+ +\ H^+ \tag{2.15}$$

Cathodic regime (surface passivation)

$$^1/_2\,O_2 +\ H_2O + 2e^- \leftrightarrow\ 2(OH^-) \tag{2.16}$$

$$H^+ + e^- \rightarrow\ H \tag{2.17}$$

$$2H^+ + 2e^- \rightarrow\ H_2\uparrow \tag{2.18}$$

As depicted in Figure 2.8, the electrochemical diffusion of chloride ions within the bowl-like structure activates the redox reactions. This increases the entropy of the ions and electrolytic reactions in the bowl-like structure, including hydrogen evolution reactions in the cathodic region (see Equations 2.17 and 2.18), thereby accelerating the etching process on the SST surface. The etching process is based on the induced ionization of metal atoms in the shell structure, which as cations, attract the negatively charged anions (Cl ion adsorption). The size difference between the anodic and cathodic sites catalyzes the etch rate and the after-effects of the process, i.e., the formation of $FeCl_2$, $Fe(OH)_3$, etc., inside and on the outer portions of the bowl-like structure. The breakdown of the passive layer can be seen as partially dependent on the circumstances associated with the etching process, such as the substrate's initial surface morphology [82]. At a particular potential, the passive layer perforates due to anion adsorption [82,84,85]. Once a structure nucleates, metal dissolution self-propagates, causing the passive oxide layer to lose its capacity to re-passivate [82–85].

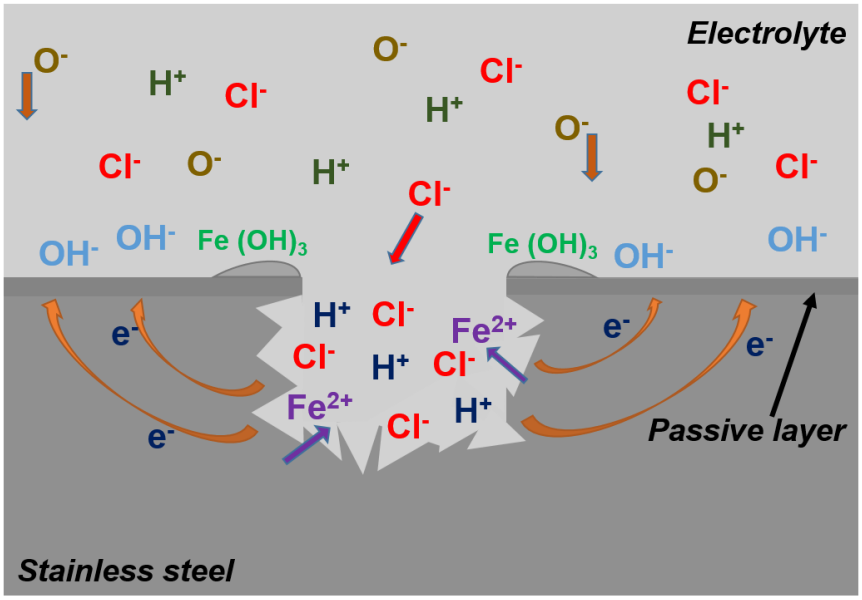

Figure 2.8: *Electrochemistry of an actively growing bowl-structure schematic in an HCl-based electrolyte.*

2.7 Adhesives

This umbrella term refers to any substances that can be used to hold, fasten, or bond when applied between the surfaces of two substrates. They are widely employed throughout the industry for permanent, semi-permanent, and temporary attachment purposes in a variety of residential, commercial, industrial, and structural applications [86]. Some characteristics that can be classified and categorized include load-carrying capacity (structural), chemical composition, and reactivity or inertness [87]. The focus in this section is on adhesives based on their chemical position. This work used polymers such as epoxy resin, acrylic, and polythiourethane (PTU) as an adhesive to form a metal-polymer-metal sandwich structure.

2.7.1 Epoxy resin

Epoxies are structural adhesives and generally consist of resin and hardening agents. They are highly temperature and solvent-resistant and can be structurally bonded to most materials, such as metals, ceramics, wood, and plastics [86,87]. They exhibit high shear and peel strength and have excellent mechanical and electrical properties as well as chemical stability, which makes them suitable for gap-filling and bonding dissimilar substrates [88,89]. The epoxy resin comprises a reactive functional group (the epoxy or oxirane group) [90] which is cross-linkable (see Figure 2.9).

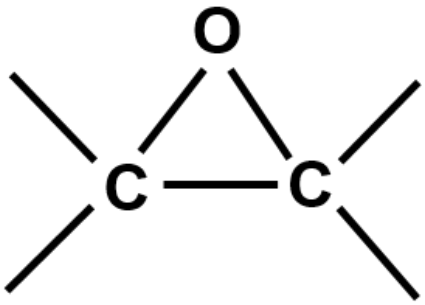

***Figure 2.9*: *Molecular structure of epoxy resin showing its functional group*.**

The epoxy group is characterized by its reactivity towards both nucleophilic and electrophilic species, and it is thus receptive to a wide range of reagents or curing agents. Such curing agents are of two types: they may be either catalysts or hardeners. Catalysts are usually drawn from tertiary amines or Lewis acids, and they function by initiating the ionic polymerization of the epoxy compound to produce polyether structures. Typically, catalysts are used in low concentrations [90]. They are often used in association with hardeners in resin formulations. Aliphatic and aromatic amines and carboxylic anhydrides provide typical examples of hardeners. These compounds react directly with the epoxy and other resin groups, influencing the cured resin's structure.

2.7.2 Acrylic adhesives

Acrylic adhesives are another functional class of structural adhesives and are often used in applications that demand faster curing speeds than epoxies. In addition, they can bond to lower surface energy surfaces such as plastics because of lower solubility parameters and surface tensions. This leads to inherently tolerant oil contamination on adherence [87]. Usually, acrylic adhesives polymerize by a free-radical addition process: the basic monomer is methyl methacrylate, as shown in Figure 2.10. However, other components, such as methacrylic acid, may be added to improve bonding. A typical initiator is cumene hydroperoxide [91].

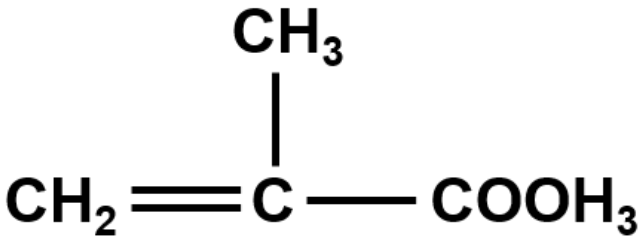

***Figure 2.10*: *Molecular structure of methyl-methacrylate*.**

The two major classes of acrylic adhesives are anaerobic and cyanoacrylate. Anaerobic adhesives are one-part acrylics that remain monomeric in the presence of air but polymerize in their absence. In contrast, the cyanoacrylates are the usual everyday 'superglue,' which are one-component adhesives in thin, colorless liquids. The bonding process (polymerization) is catalyzed by the water adsorbed on the surface of adherents [87,91]. Generally, acrylic adhesives are cured at room temperature and exhibit good strength on metal surfaces without the need for pressure, which is a peculiar attribute compared to other structural adhesives.

2.7.3 Polythiourethane (PTU)

In recent times, polythiourethane, a polyurethane class, has attracted much attention because of its unique optical properties and biocompatibility derived from the fundamental physical properties of polyurethane, such as inertness, good stability, thermal and mechanical properties [92–95]. Typically, polyurethanes (PU) are formed by the polyaddition of a polyol (-OH) and a diisocyanate (-N=C=O). The resulting structural unit (-NH-CO-O-) is therefore responsible for the name urethane group. However, many applications require the inclusion of additives such as catalysts or chain extenders [93], which enhances the possibility of a variety of properties.

Therefore, polythiourethane is fundamentally synthesized through the addition reaction between a sulfur-containing polyol (thiols) with an isocyanate [95]. On the other hand, adding amines to five-membered cyclic dithiocarbonates prepared from epoxides and carbon disulfide can easily synthesize the corresponding thiourethanes [92,94]. As a result, PTU has found usefulness in many industrial applications, such as optical lenses, coatings, and sealing materials. However, besides its excellent optical properties and biocompatibility, the flexibility and the crystallinity may be enhanced by making thiol-terminated oligomers with sulfide linkages in the oligomeric chain, followed by subsequent reaction with a combination of a diisocyanate and small molecule dithiol chain extender as reported by [94,95].

In this thesis work, the used PTU is made from a solvent-free two-component system of linear 1,6 diisocyanatohexan (HDI) and tetrafunctional Pentaerythritoltetrakis (PETMP) as shown in Figure 2.11. This was achieved after mixing and curing these two components through the polyaddition reactions process.

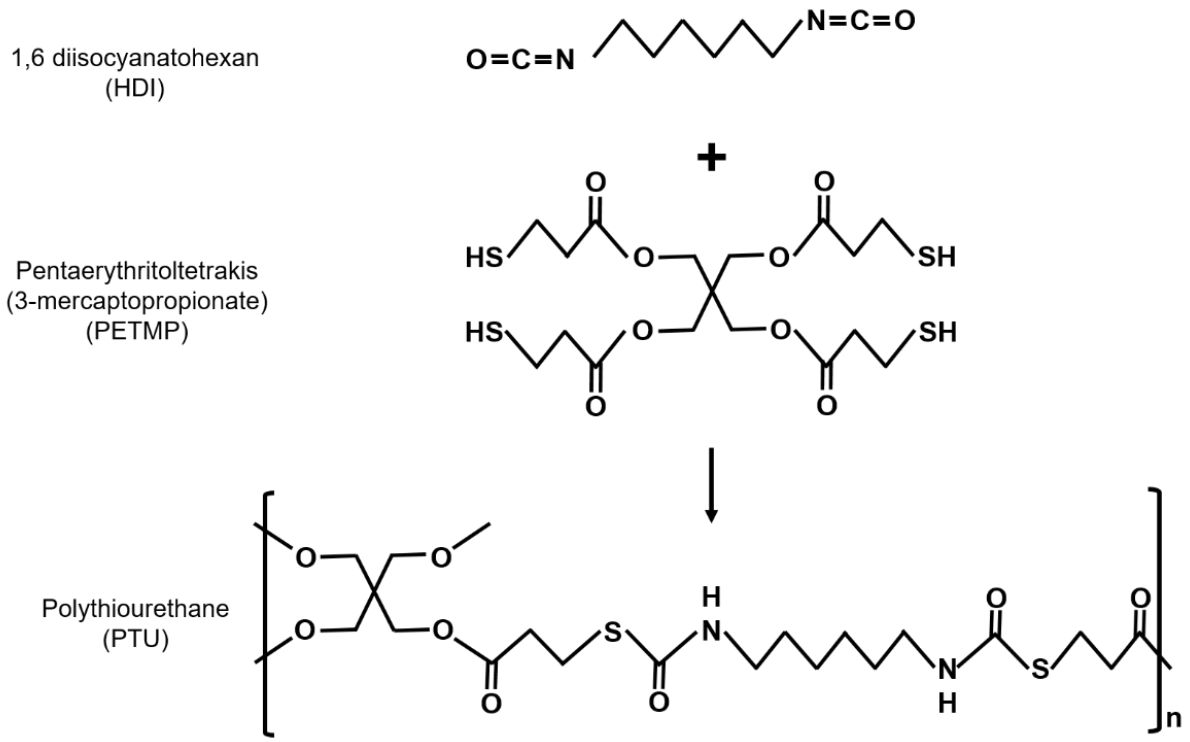

Figure 2.11: *Molecular structures of two components polyaddition process of polythiourethane.*

2.8 Adhesion mechanisms

Adhesion refers to the interaction between two surfaces at the atomic and molecular scale. It is a fundamental process for material bonding and typically involves the use of an adhesive. Because of the flexibility in adhesive bonding, it provides lots of advantages over other joining techniques such as welding, riveting, or bolting when joining different materials such as metals and polymers, etc., and also permits weight saving, provides improved stress distribution, design flexibility as well as aesthetics and most importantly it is a cost effective technique [96–100]. The adhesive joining process has many industrial applications in aviation, automobile, building, and electronics. It also found usage in composite, multilayer structures, coatings, paints, and polymer blends [101]. An adhesive must do two things when applied to surfaces that are to be bonded. It must first wet the surfaces, as manifested by spreading and making a contact angle approaching zero. It must then harden to a cohesively strong solid [87,91].

Many methods help in adhesion improvement. Technical literature usually contains a discussion of the roles of interlocking (mechanical interlocking), diffusion, adsorption, surface reaction (chemical bonding), wetting, and electrostatic forces in fostering adhesion in various material pairs [97,99,101]. There are essential mechanisms to be considered to form the

complete picture of combinations of principles for the overall adhesion processes, including crystalline properties, surface free energy, wetting, etc.

In this thesis work, the adsorption, chemical bonding, and mechanical interlocking theories are important and will be explained in more detail.

2.8.1 Adsorption theory

This mechanism is predominant when the adhesive has sufficiently low surface energy to wet the mating surface effectively. When the free energy of the surface to be bonded is sufficiently high, a fluid with a lower surface tension can spread out, making intimate contact with the surface. The free energy of a metallic surface can be increased by proper surface preparation, including removing weak adhered oxide layers and chemical contaminants. Here, adhesive forces are achieved through secondary molecular forces, such as van der Waals forces, which act over a short distance away from the interface [91,97,98]. This theory suggests that adhesion is due to van der Waals forces between molecules across the interface of two different materials. Van der Waals forces are weak and short-ranged intermolecular forces. According to the physical adsorption theory, the thermodynamic work of adhesion, W_A, between two materials, B and C, is the energy required to separate the interface into two distinct surfaces [87,91]. This work is given by:

$$W_A = \gamma_B + \gamma_C - \gamma_{BC} \tag{2.19}$$

Where,

γ_B = free energy (surface tension) of surface B,

γ_C = free energy of surface C and

γ_{BC} = interfacial free energy between the two adhered surfaces.

If this energy is positive, the bonded surface is stable. If this energy is negative, the bonded surface is unstable, which could lead to debonding [87,91,102,103]. If the de-bonding occurs in the presence of a liquid, the values γ_B and γ_C should be replaced by corresponding values for the submerged surfaces, $\gamma_{BL,}$ and $\gamma_{CL,}$ respectively.

The thermodynamics adsorption model of adhesion is based on the most apparent principle that all materials are subject to attraction forces between their atoms and molecules. The surface tension is a direct measure of intermolecular forces. The general principle of good adhesion requires that interfacial tension be minimized between the solid and liquid [87,91].

Surface tension property is known from 1855 when Young developed an equation describing the surface free energy of liquid on a solid surface [102,103]. In Figure. 2.12 a sessile liquid drop resting on a flat and planar surface is depicted together with the respective surface tensions (γ) of solid-vapour (γ_{SV}), liquid-vapour (γ_{LV}), and solid-liquid (γ_{SL}) at equilibrium. The relation between the surface tensions at the three-phase contact points and the droplet's contact angle ($\cos\theta_Y$) is related to the Young equation 2.20. The Young equation is given as:

$$\cos\theta_Y = \frac{\gamma_{SV} - \gamma_{SL}}{\gamma_{LV}} \tag{2.20}$$

Here, the water droplet's contact angle determines the wetting degree. At a contact angle of 0°, a complete wetting is achieved, and the droplets spread entirely on the surface [104]. A contact angle of above 90° signifies a hydrophobic surface, resulting in a bead-like droplet on the surface. A contact angle below 90° indicates a hydrophilic surface, in which surface wetting is favoured. The surface is termed super-hydrophobic at a contact angle beyond 150° and is not wetted at all [105]. Typically, the adhesives are applied in liquid form, and good surface wetting is a prerequisite to achieving strong adhesion. This is the crucial part in which the surface energies of the substrate and the adhesive come into play. In other to achieve complete wetting on the substrate surface, the adhesive should have a lower surface energy than the substrate [87,91,99,106].

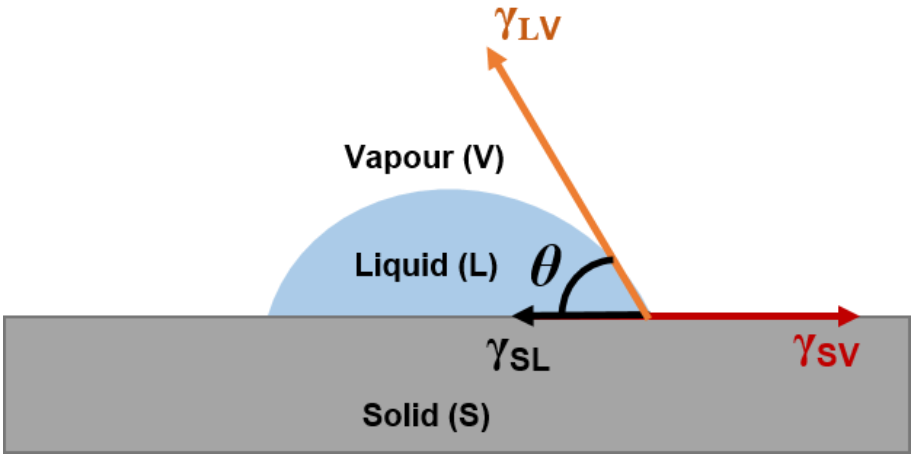

Figure 2.12**:** *A sessile droplet of water on a flat, solid surface at equilibrium.*

Considering a rough surface, two different cases need to be distinguished. First, according to Wenzel [107], as shown in Figure 2.13 (a), the water droplet wets the surface, but an additional roughness factor *R* describes the deviation from an ideally smooth surface (the ratio of the true surface area and its nominal area) has to be considered (equation 2.21) [102,103,108].

$$\cos\theta_W = \cos\theta_Y R = \frac{\gamma_{SV} - \gamma_{SL}}{\gamma_{LV}} R \quad (2.21)$$

The above equation correlates the homogeneous wetting regime as well as the Wenzel apparent contact angle *(θ_W)* with respect to the Young contact angle *(θ_Y)* and the roughness ratio *R*. It shows that when the surface is hydrophobic *($\theta_Y > 90$ °)*, the roughness increases the contact angle of the droplet. On the other hand, when the surface is hydrophilic *($\theta_Y < 90$ °)*, roughness decreases the contact angle of the droplet [102,103]. This is because wetting results from the surface chemical property, whereas the surface roughness amplifies the contact angle in the direction of the dominants.

As shown in Figure 2.13 (b), a different model introduced by Cassie and Baxter [108,109], which considered the roughness protrusion with air entrapment, assumes that the surface cannot be completely wetted. According to this model, the Cassie-Baxter contact angle *(θ_{CB})* is given as:

$$\cos\theta_{CB} = Rf\frac{\gamma_{SV} - \gamma_{SL}}{\gamma_{LV}} + f - 1 \quad (2.22)$$

Where *f* = fraction of the estimated area wetted by the water droplet on the surface

Rf = roughness ratio of the wet area.

However, these models suffer incompleteness and therefore are used for predicting the apparent contact angle. As both models are inadequate in determining the precise wetting equilibrium on rough surfaces, a third model, the mixed mode, should also be considered for a complete surface description.

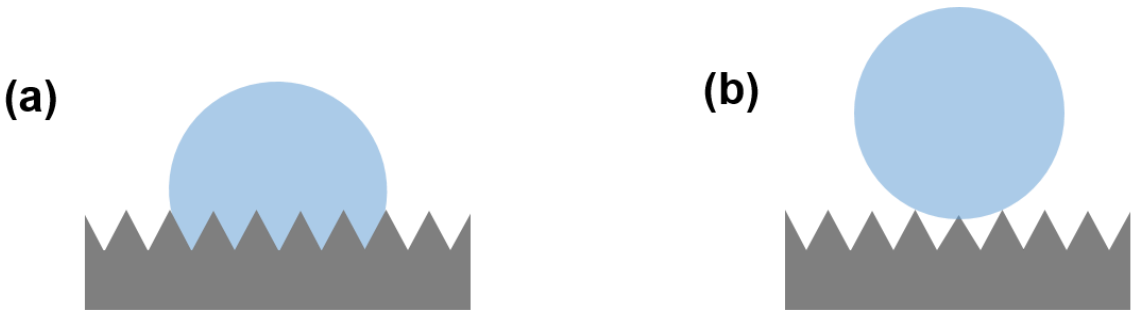

Figure 2.13**:** *Schematic of wetting on rough surfaces:* ***(a)*** *Wenzel and* ***(b)*** *Cassie-Baxter model.*

2.8.2 Chemical bonding theory

The mechanism of adhesion by participating in chemical bonding is the oldest and the most frequently proposed because chemical bonding forms reliable, easy-to-explain connections between substrates and adherents. Primary bonds, such as ionic, covalent, or

metallic bonds, and secondary bonds, such as van der Waals or hydrogen bonds, are formed across the adhesive-substrate interface [110]. The strength of the chemical bond is based on the number and type of bonds formed at the interface. The relative strength respectively the bond energy of the primary bonds is significantly higher (e.g., C-C – 347, C-O - 358, C-N – 305, C-S – 259, N-O – 201 and O-O – 146 kJ/mol) compared to the ones of secondary bonds, requiring higher energies to break down.

Substrates surface pre-treatment or applying adhesive promoters (coupling agents) changes its chemical composition, enhancing adhesion compatibility and contributing to a higher adhesion between the adhesive and the substrates. Adhesion promoters, or coupling agents, act at the interface between an organic polymer and an inorganic substrate to enhance adhesion between the two materials. Organic and inorganic materials are different in many ways, e.g., compatibility, chemical reactivity, surface properties, and coefficient of thermal expansion, such that forming a strong adhesive bond between the two materials is complex. An adhesion promoter acts at the organic-inorganic interface to chemically and physically wed these dissimilar materials into a strong, cohesive bond structure. Adhesion promoters will alter physical and chemical forces at the interface and provide a "glue" to give a much greater level of adhesion.

Adhesion promoters can impart resistance to environmental and other destructive forces, such as heat and moisture, which often act on the bonded site to destroy adhesive strength. Organosilane coupling agents are the primary chemical type of adhesion promoter [15,111]. Silanes are compounds of silicon and hydrogen of the formula Si_nH_{2n+2}. When one end of a molecule functional group forms -Si–OH, –Si-$(O–CH_3)_3$, or –Si–$(O–CH_2CH_3)_3$, that group reacts with the inorganic species such as pigments and the substrate. When the functionality at the other end is organic (vinyl-, amino-, epoxy-, methacryl-, mercapto-, etc.), that group can react with the resins in the coating, creating a coupling between the two constituents. As a result of possessing these two types of reactive groups, silane coupling agents can provide chemical bonding between an organic and inorganic material (see Figure 2.14) [112].

Adhesion promoter chemistries, other than silanes, have been extensively promoted for many years. Organotitanates and organozirconates have shown promise as adhesion promoters but have not achieved the overall success of silane coupling agents. In metals, the highly metallic nature of zircoaluminates makes them uniquely reactive with metal surfaces. Similarly, organotitanates can function as adhesion promoters via their nature as excellent wetting agents and the ability to design molecules with dual, organic, and inorganic functionality [112–114].

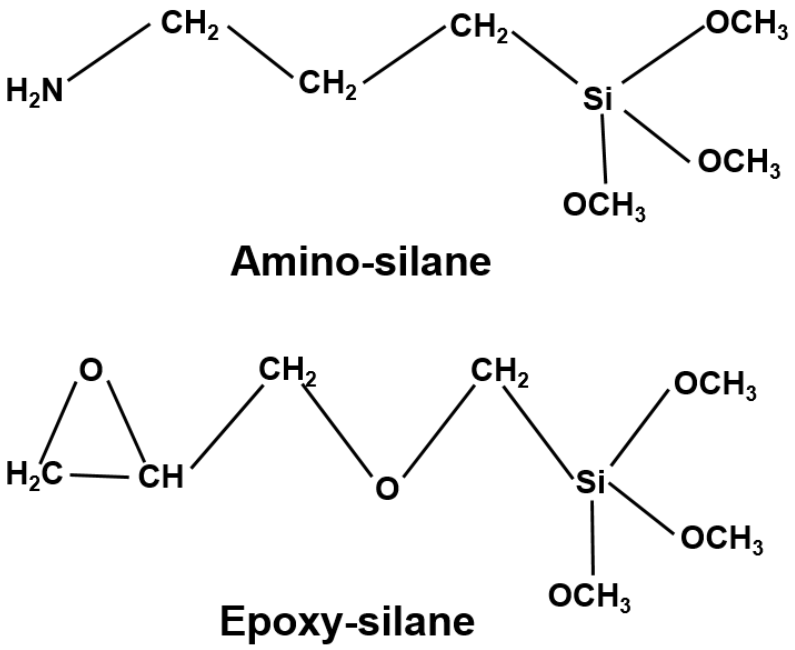

Figure 2.14: *Molecular structure of amino and epoxy silane showing their functional groups.*

2.8.3 Mechanical interlocking

In 1925, McBain [79] proposed an alternative bonding/adhesion mechanism known as the keying model or mechanical interlocking. According to this theory, mechanical interlocking represents a form-fitting connection that takes effect on a macroscopic level. The low-viscosity adhesive fills the structures, pores, cracks, and indentations in the surface of a material, which results in mechanical interlocking between the two components once the adhesive has hardened. Adhesion occurs through the mechanical interlocking between such structures on the substrate and the adhesive that fills these structures [100,115]. Exemplary, Van der Leeden *et al*. [116] distinguished three types of irregularities, of which only the type with mechanically stable hook-like interlocking structures (see Figure 2.15) may lead to mechanical interlocking.

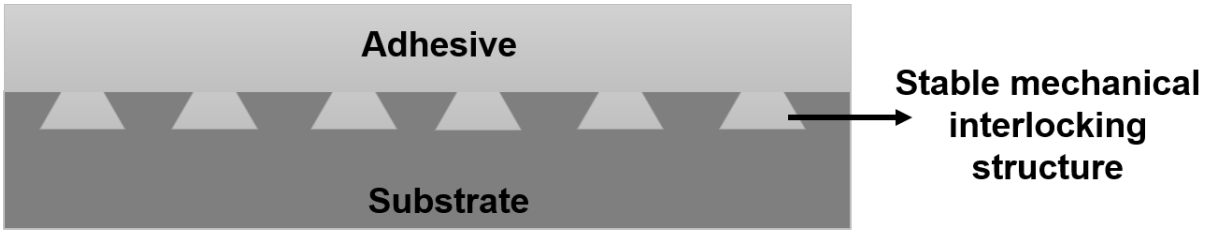

Figure 2.15**:** *Schematic of a stable mechanical interlocking structure with complete wetting and filling of an adhesive.*

The penetration of the adhesive into the surface structures and the composite strength strongly depend on the structure's geometry (meaning their depth, perforation angle, and

diameter) [115]. Purely mechanical interlocking occurs only in structures with a type of undercut in the direction of the force, thus preventing deformation. In contrast, the penetration depth depends on the adhesive's wetting properties, the surface tension, the viscosity, and the counter pressure of the gas enclosed in the structure [19,115]. More so, surface irregularities and roughness existing on the surface contribute to an extent an excellent mechanical interlocking. This is because the enhancement of the surface roughness increases the total surface area and surface energy, which also promotes adhesion at the bond interface [100,117].

2.9 Joints and failure mechanism

Joint design and failure mechanism have been a major point of discussion as structure failure mechanisms have shown dependency on the choice of joint design [118,119]. Therefore, the choice of a composite joint design and the properties of the to-be-used adhesive should be paramount in adhesive-bonded joints. Therefore, the analysis of the failure interface for a better understanding of the failure root course and mechanism to failure be encouraged for future prevention.

2.9.1 Joint design and stresses to failure

Joint design in adhesive bonding is a critical determinant of the bond's strength, reliability, and durability. The most effective joint design for a particular application depends on the stresses the part will encounter and the mechanical properties of the adhesive and adherents. The joint design aims to obtain maximum strength for a given bond area. In designing joints specifically for adhesive bonding, the essential characteristics of adhesives must dictate the design of joints [120].

The design selection is concerned with eliminating stress concentrations, which reduce the strength and useful life of the joint. Localized stresses are not always apparent and may occur due to differential thermal expansion of the adhesive and adherents or shrinkage of the adhesive during cure when volatiles are given off. Internal stresses decrease as adhesive thickness decreases, reducing the tendency to trap volatiles. The ideal adhesive-bonded joint is one in which, under all practical loading conditions, the adhesive is stressed in the direction in which it most resists failure.

Joints are subjected to several types of stresses throughout the lifetime of the part. Cleavage stress [Figure 2.17 (a)] occurs when a joint is opened at one end, while in shear stress [Figure 2.16 (b)], forces are parallel to the joint plane, and joint surfaces tend to slide over one another. Peel stress [Figure 2.16 (c)] develops when a flexible substrate is peeled or lifted off

the other substrate. In tensile stress [Figure 2.16 (d)], the forces exerted on the part are perpendicular to the plane of the joint. Tensile stresses tend to either pull a joint apart or elongate the part. Compressive stress [Figure 2.16 (e)] also acts perpendicular to the joint plane but tends to squeeze the parts together [120,121].

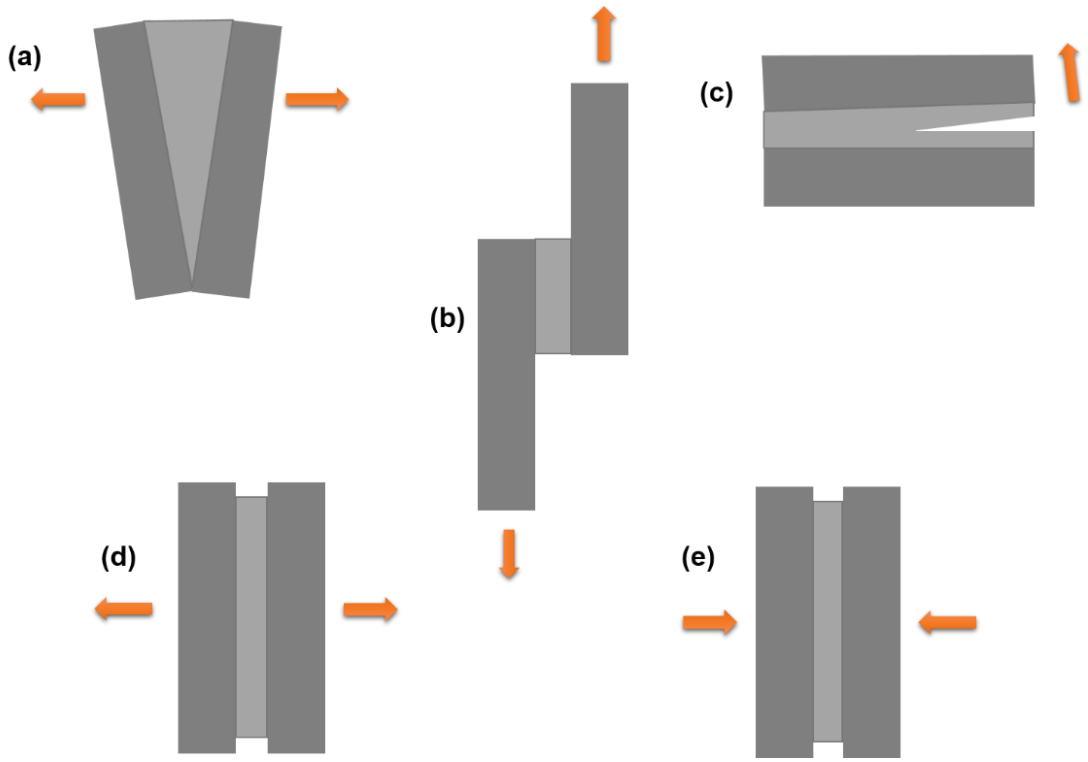

Figure 2.16: *Schematic of different types of stresses in adhesive joints: cleavage stress* ***(a)****, shear stress* ***(b)****, peel stress* ***(c)****, tensile stress* ***(d),*** *and compressive stress* ***(e).***

2.9.2 Failure mechanisms in adhesive joints

In adhesively bonded joints, there are three basic modes of failure. Substrate failure outside the joint, inside the adhesive layer (cohesive failure), and between the adhesive layer interfaces (adhesive failure). Failure of the substrate outside the joint is achievable [122–124] for well-designed and fabricated adhesive bonds in moderately thin substrate materials [Figure 2.17 (a)]. This condition is highly desirable as it enables the full structural performance of the substrates to be utilized.

Cohesive failures result in fracture of the adhesive and are characterized by the clear presence of adhesive material on the matching faces of both substrates [Figure 2.17 (b)]. Failure is usually by shear, but peel stresses or a combination of shear and peel may also cause cohesive failure. This type of failure typically occurs in lap shear tests or peel tests. It is usually the ideal type of failure because the maximum strength of the materials that constitute the joint is

achieved [125]. Here, the adhesive surface typically appears rough and may have a lighter colour than the bulk adhesive material.

Adhesive failures are characterized by the absence of adhesion on one of the bonding surfaces [Figure 2.17 (c)]. Failure occurs along the interface between the adhesive layer and the substrate due to the hydration of the chemical bonds, which form the link between the adhesive and the surface, hence the total delamination of the adhesive from the substrate interface [124–128].

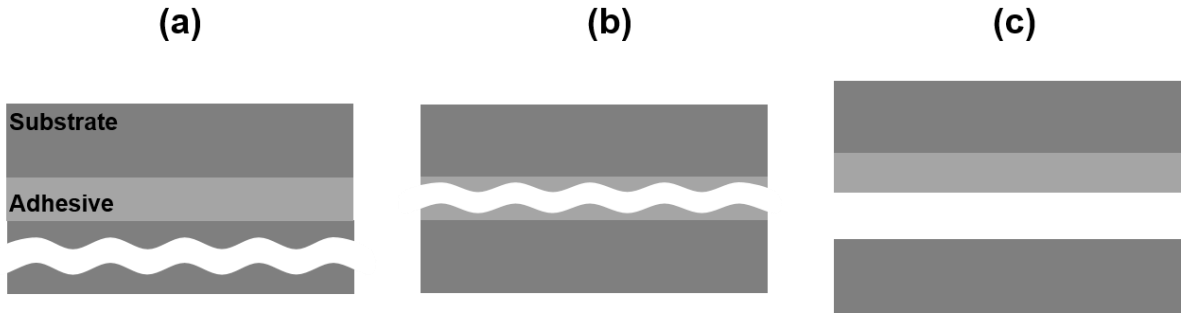

Figure 2.17: *Schematic of different types of failure mechanisms in adhesive joints: substrate failure* ***(a)****, cohesive failure* ***(b)****, and adhesive failure* ***(c)****.*

2.10 Characterization methods

This section discusses the necessary characterization approach used in this work for a proper scientific understanding of the structured surfaces' physical, chemical, and mechanical properties. This could be a destructive or non-destructive characterization technique. The change in physical properties, such as surface morphology of the sculptured AlMg3 and SST substrates, were analyzed using the light microscope, scanning electron microscope, and confocal microscope. In the same vain, the chemical properties such as surface crystallographic arrangement, elemental analysis, and wettability of the sculptured AlMg3 and SST substrates were analyzed using the X-ray diffraction spectroscopy, Energy dispersive x-ray analysis (EDX), and Contact angle measurement. The characterization techniques, as mentioned earlier, are non-destructive. However, the mechanical properties of the structured SST strip (sandwich structure e.g., SST-PTU-SST structure) and SST wire were analyzed using the tensile lap shear test and tensile test, respectively, which are destructive characterization techniques.

2.10.1 Light microscope

The light microscope is an imaging technique developed in the 17th century, mainly in biological and bio-medical related materials applications. It commonly uses visible light to

detect small objects, and through the arrangement of lenses, it focuses the light on the object, magnifies it, and thus generates an image [129,130]. There are different types of light microscopes, such as brightfield, confocal, fluorescence, phase contrast, polarized light, stereomicroscope, etc., which aim to modify some basic functionality of the microscope for better image contrast and resolution [131].

Working principle

As shown in Figure 2.18 is the basic working principle of a brightfield microscope. Here, the light source illuminates the object, while the condenser lens focuses the light on the object. The first image of the specimen is formed by the objective lens, which is a real, inverted, and magnified image. The image formed by the objective lens functions as the object for the eyepiece (ocular lens), which produces the final, virtual, and magnified image to the eye. In this way, the final image produced is inverted with respect to the object.

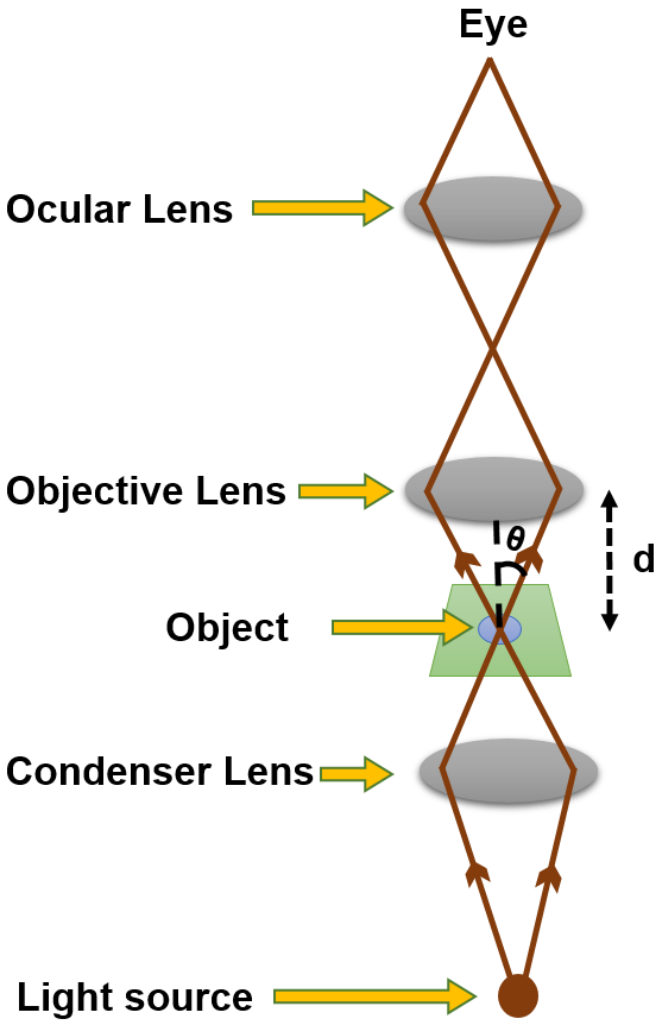

***Figure 2.18*: *Schematic of a brightfield light microscope*.**

The magnification of a light microscope (equation 2.23), i.e., the ratio of the difference between image distance and the focal length, which is its capability to enlarge an object, is usually limited by the microscope´s resolving power (equation 2.24). This is because the white light [wavelength (**λ**) of 400-700 nm] used in a light microscope has a relatively long wavelength and cannot resolve structures smaller than 0.2 µm.

$$M = \frac{v - f}{f} \tag{2.23}$$

Where: ***M*** is the magnification, ***v*** is the image distance, and ***f*** is the focal length of the microscope.

$$R = \frac{d}{2} = \frac{0.61\lambda}{n \sin \theta} \tag{2.24}$$

R is the resolution, **λ** is the wavelength, ***n*** is the refractive index, and ***n sin θ*** is the numerical aperture ***(NA)***.

At smaller **d**, the resolution increases, and the details of the object become identifiably finer. To make **d** smaller, the value of **λ** should be smaller with a greater value of ***NA***. Thus, the greatest resolution is obtained at the shortest wavelength of light, with an objective of maximum ***NA*** [129,130]. However, as imaging technology has recently improved, the resolution is no longer a limitation of the microscope but by the wavelength of light itself. Hence a different source of illumination is needed. Electron microscopes use a beam of electrons in place of light and are therefore able to produce much higher-resolution images [129].

2.10.2 Scanning electron microscope (SEM)

This is a class of electron microscopes used to investigate the surface of conductive specimens by scanning the high-energy electron beam across the surface of a substrate where electrons from different depths are emitted and collected. SEM provides the advantage of high spatial resolution (down to 2 nm), topographical imaging, and reduced chromatic aberration when compared with light and transmission electron microscopes [132,133]. However, since this technique works with an electron beam, substrates must be conductive to prevent charge accumulation on the surface. Therefore, naturally non-conductive substrates should be coated (sputtered) with a thin metallic layer such as gold to ensure conduction [134].

Working principle

The electron beam from an electron source (e.g., thermionic emission tungsten filaments or field emission gun) is accelerated toward the sample surface through an ultra-high vacuum to lower the chance of scattering electrons on gas particles within the device. The created electron beam is directed, condensed, and accelerated by magnetic and electric fields and then scanned across the surface of the substrate. The radiation can be used for signaling, and each interaction can be used to get different information on the substrate [135]. The radiations that occur upon electron scattering (i.e., elastic or inelastic scattering) include secondary electrons (SE), backscattered electrons (BE), Auger electrons, and X-rays [136]. The scattering events are schematically shown in Figure 2.19.

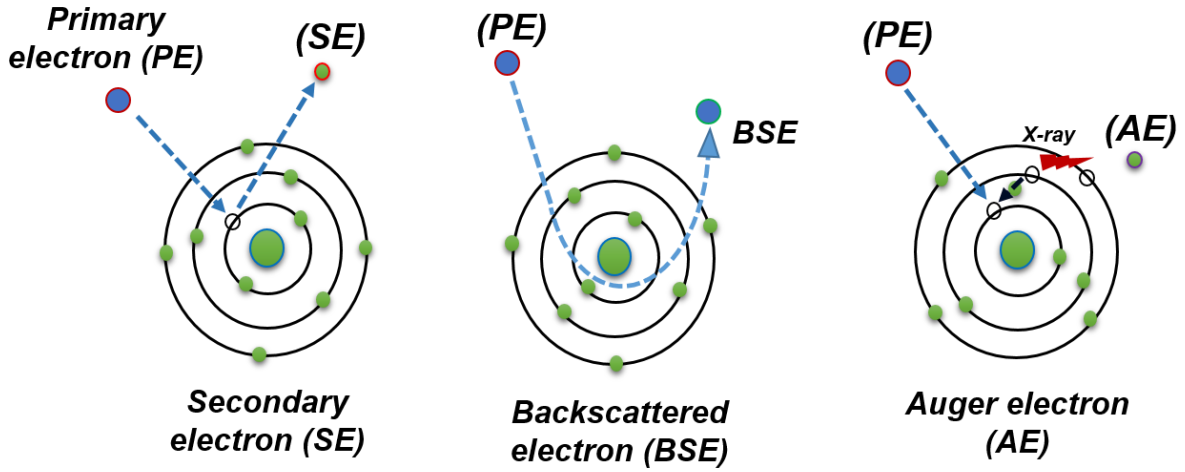

Figure 2.19: *An overview of electron beam scattering effect during surface imaging.*

The secondary electrons are inelastically scattered, while the backscattered electrons are elastically scattered, and Auger and X-rays are generated by releasing inner electrons, which are compensated by an electron from an outer shell. As depicted in Figure 2.20 is the interaction volume which is the region of the sample surface affected by the incident electron beam.

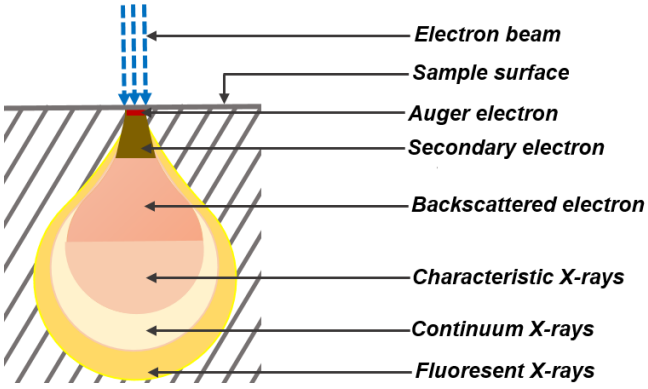

Figure 2.20: *Schematic of an interaction volume.*

The scattering of secondary electrons, an inelastic scattering, provides topographical information, as the energy level of the electrons leaving the sample atom is not high enough to travel through the sample. Therefore, only surface-level information is collected by the detector. In elastic scattering (BSE), as shown in Figure 2.19, the electron beam interacts only with the nucleus and therefore has no loss in energy and speed but a change in direction. The detection of these electrons provides compositional information, and their varying contrast upon interaction with atoms of different atomic weights in their pathway allows us to distinguish differences in the sample constituent's composition.

As depicted in Figure 2.19, the interaction of the sample with a high-energy electron beam during SEM imaging also leads to the release of the core-shell electron. A higher energy outer shell electron then proceeds to fill its place, releasing the difference in energy as an X-ray with a characteristic spectrum based on its atom of origin. This allows for the compositional analysis of a given sample volume that has been excited by the energy source. The position of the peaks in the spectrum identifies the element, whereas the signal's intensity corresponds to the element's concentration. This analytical method is known as Energy-Dispersive X-ray spectroscopy (EDX), where an energy-dispersive detector records the generated X-rays. However, atoms of elements such as hydrogen, helium, and lithium cannot be detected since the emitted energies are below the detection limit [133,135].

2.10.3 Tensile test

The tensile test is a destructive characterization technique universally used to determine the mechanical property of a material. The test is a fundamental way through a standard approach where material properties such as Young´s modulus, yield strength, Poisson´s ratio, and ultimate tensile strength (UTS) can be determined. This technique measures the force required to break a composite or a wire (plastic or stainless steel) sample and the extent to which the sample stretches or elongates to its breaking point [137]. This provides the ultimate tensile strength of the material at yield and break. After that, the force and elongation data are converted to engineering (nominal) stress and strain. In equation 2.25, engineering stress ***(σ)*** is defined as,

$$\sigma = \frac{F}{A_o} \tag{2.25}$$

Where ***F*** is the force and $\boldsymbol{A_0}$ is the cross-sectional area of the sample. While equation 2.26 defined engineering strain ***(ε)*** as,

$$\varepsilon = \frac{\Delta l}{l_o} \tag{2.26}$$

Where l_0 is the initial length of the sample and Δl is the change in length of the sample, i.e., the difference between the final length and initial length $(l - l_0)$.

Generally, the stress is usually denoted in MPa, whereas the strain is given in **%**. Furthermore, the engineering stress and strain data can also be used to plot a stress-strain curve. However, the curve's shape depends on the type of material and its mechanical properties, as shown in Figure 2.21 (a) and (b).

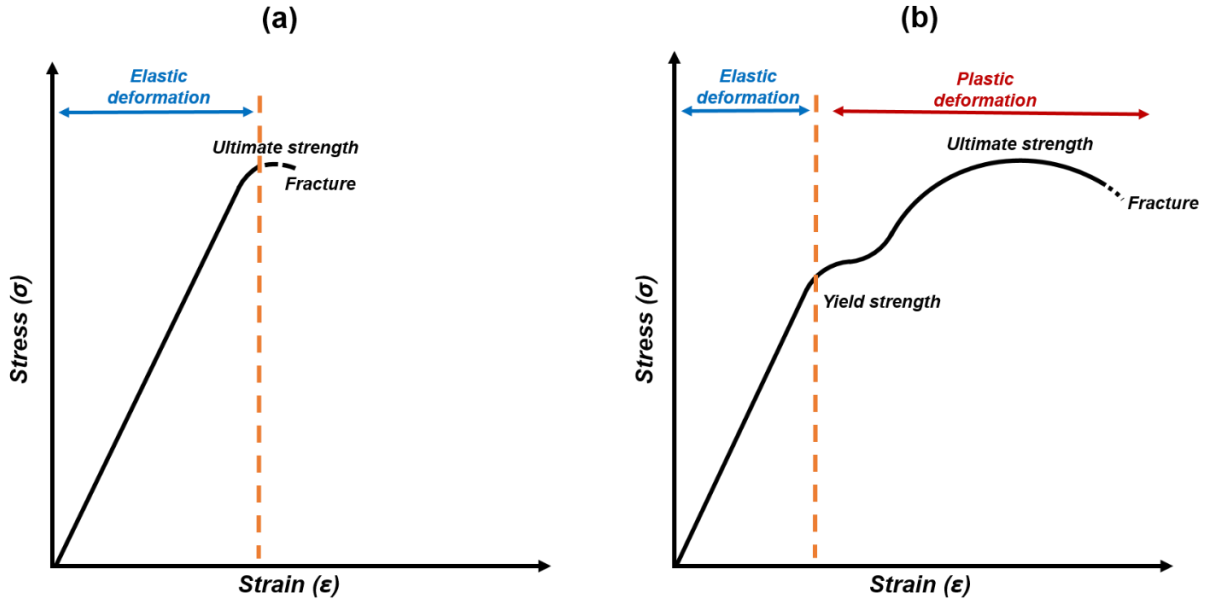

Figure 2.21: *Schematic of engineering stress-strain curves for brittle material* ***(a)*** *and ductile material* ***(b).***

From the above curves, brittle materials do not yield but rather fracture after exceeding their elastic limit. On the contrary, ductile materials yield after exceeding their elastic limit and fracture plastically. In this work, the ultimate tensile strength of a brittle SST wire after surface pre-treatment was measured using a standard tensile testing machine.

2.10.4 Single lap-shear test

Lap shear tests, including single lap, double lap, lap-strap, and thick adherent shear tests, are commonly used during characterization. This destructive characterization technique is employed to evaluate the ultimate shear strength of a bonded interface with an adhesive after a surface pre-treatment approach, such as nanoscale sculpturing.

In this thesis work, a single lap shear is used. The formed sandwich structure is standardized using the norm DIN EN 1465 [138], and the test is performed using a standard tensile testing machine.

The norm prescribed standard dimensions (e.g., sample thickness, glued area, sample length, gap distance, etc.) such that any form of substrates bending and peel stress will be eliminated so that the applied parallel tensile force to the adhesive plane will only lead to shear stress in the system. Additionally, the chosen pulling force must be such that will lead to failure within 1 min. The Ultimate shear stress (USS) is the force per area, which is calculated by dividing the maximum force measured by the total surface area covered with adhesive (see equation 2.27) [138,139].

$$USS = \frac{F_{max}}{A_{total}} \tag{2.27}$$

Generally, lap shear strength testing measures the ability of a material interface to withstand stresses set in a plane, where the exerted shear force is moving the two substrates in opposite directions. In structural application, it is one of the most common stresses that a bonded joint can face during service. An adhesive's lap shear strength is one indicator of its long-term sustenance in an application [139].

2.10.5 Contact angle measurement

This is a non-destructive characterization technique usually employed to analyze the surface wettability of a material. Typically, a material's surface properties differ from its bulk because the periodic atom arrangement of the outermost layers differs from the neighboring bulk arrangement. This leads to a difference in surface energy which is the energy required to create a new surface, i.e., the excess energy at the surface compared to the bulk, which is a key parameter to characterize a surface. Furthermore, surface properties such as native oxide layer, surface contaminant, surface roughness, etc., alter a substrate's surface energy.

Generally, contact angle measurement using sessile-drop goniometry has been used for decades to determine a substrate's surface energy (see equation 2.20 and Figure 2.12). This measurement approach could be static or dynamic contact angle measurement [140,141]. The static sessile drop method, the most commonly used method to measure contact angle, is used in this work. In this technique, a syringe pump produces a drop of liquid (usually water of about 3 µl) placed on the substrate surface. After that, the droplet baseline angle and tangent boundary

are measured using optics. Then, the droplet on the surface is backlit, and an image of the droplet is taken using a camera opposite the illumination source. After that, several images of the droplet are made, and the average contact angle is recorded. On the other hand, the dynamic contact angles can be measured using two approaches; changing the droplet's volume or tilting the surface [141].

Chapter 3

3.0 Experimental

3.1 Materials

In this work, a specific aluminium alloy strip (AlMg3-W19, AW5754) with a brushed surface (mill-finish), stainless steel (SST) strip (chromium-nickel, V2A, austenitic grade 304), which consists of an alloying element concentration of a minimum of 18 % Cr, 8 % Ni, and a maximum of 0.08 % C, and an austenitic SST wire (304 V grade) with a diameter range of 200 µm are used.

3.2 Samples surface preparation

3.2.1 AlMg3 strip

A specific commercially available aluminium alloy (AlMg3-W19, AW5754) with a brushed surface (mill-finish) purchased from Laserhub GmbH, Stuttgart, Germany, is used.
The surface morphologies of the used AlMg3 sample are in four different types (pristine surface (PS), pristine-abraded surface (PAS), pristine-grit-blasted surface (PGBS), and pristine-abraded-grit-blasted surface PA-GBS) and have a dimension of 20 × 25 × 3 mm (18 pieces for each of the four different initial surface morphologies).

- ✓ The PS sample is the commercially available AlMg3 (AW5754), which has an as-delivered brushed surface finish (mill-finish).
- ✓ The abraded surface samples, i.e., PAS and PA-GBS (before grit-blasting), are obtained using a Struers Rotopol-V grinding/polishing machine with abrasive paper grade 1200, grade 2500 and grade 4000, respectively, until a mirror-like surface is obtained.
- ✓ The grit-blasted surface samples (i.e., PGBS and PA-GBS) were achieved by a standard grit-blasting process, which uses ceramic beads (Zirblast B60, i.e., size distribution of 125 – 250 µm) with 5 – 6 bars nozzle pressure at 5 – 10 cm

distance and a normal to the surface single-run blasting. After the surface preparation (PAS, PGBS, and PA-GBS), residual dust (silicon carbide) and grit particles were removed by compressed air, and the samples were cleaned with acetone and air-dried before the chemical etching process.

3.2.2 Stainless steel strips

The utilized SST strips (chromium-nickel, austenitic grade 304) are an alloy of steel with an alloying element concentration of a minimum of 18 % Cr, 8 % Ni, and a maximum of 0.08 % C.

Stainless steel strip 1

Here, the SST sample has a dimension of 25 mm × 20 mm × 1.50 mm with four different initial surface morphologies, which are as follows: pristine surface (PS), pristine-abraded surface (PABS), pristine-grit-blasted surface (PGBS), and pristine-abraded-grit-blasted surface (PAB-GBS), which are 10 pieces each.

- ✓ The PS sample is the commercially available V2A austenitic grade 304 SST which has an as-delivered polished and mirror-like surface.
- ✓ The PABS and PAB-GBS (before grit-blasting) surfaces were obtained through a manual mechanical abrading process with an abrasive paper of grade 60. The abrading process was carried out in one direction, parallel to each other, until a groove-like surface morphology was uniformly distributed.
- ✓ The PGBS and PAB-GBS (after the abrading process) were obtained through a grit-blasting process, which uses ceramic beads (Zirblast B60, i.e., size distribution of 125 – 250 µm) with 5 – 6 bars nozzle pressure at a 5 – 10 cm distance and a normal to the surface single-run blasting. After that, the surface of the samples was cleaned with compressed air to remove the leftover grit particles.
- ✓ Before the electrochemical etching, the SST sample surfaces were degreased with acetone and air-dried.

Stainless steel strip 2

The as-received SST samples are the commercially available austenitic grade 304 SST (as mentioned above), which has an as-delivered polished and mirror-like surface with the following dimensions of 100 mm × 20 mm × 1.50 mm with a 15 mm bent edge.

- ✓ The samples were 180° bent on a length of 15 mm from the edge. This is to concentrate the parallel tensile stress evenly during the tensile test of the sandwich component, mostly on the etched area.
- ✓ The reference sample is a grit-blasted surface obtained through a grit-blasting process that uses ceramic beads (Zirblast B60, i.e., size distribution of 125 – 250 µm) with a 3 – 6 bars nozzle pressure at 5 – 10 cm distance and a normal to the surface fort and back-run blasting. After that, the surface of the samples was cleaned with compressed air to remove the leftover grit particles.
- ✓ Before the electrochemical etching, the SST sample surfaces were degreased with acetone and air-dried.

3.2.3 Stainless steel wire

The used austenitic SST wire has a nominal diameter in the range of 200 µm with the standard elemental composition of 18/8 (that is, 18 % Chromium, 8 % Nickel, and Iron as rest), which exhibits magnetic properties after cold working. The cold working process on this material leads to the embedment of die particles on the surface of the wire with a range of surface micro defects. The as-received SST wire was electrochemically nanoscale sculptured without any prior sample preparation.

3.3 Methods

3.3.1 Chemical structuring of AlMg3 strip

The prepared sample's initial weight was measured and then placed in a PTFE (Teflon) -based mesh-like sample holder, partitioned for quick sample withdrawal as the experiment was carried out in batches in a Teflon-based electrolyte tank. Before etching, the 720 ml aqueous HCl electrolyte (7.25 wt. %) was prepared using warmed de-ionized water. This pre-warming of the electrolytes is to obtain the experiment starting temperature window of 40 °C ± 2 °C. Reaction products (Al particles) within the range of 2 g, were injected into the newly prepared electrolyte by etching some pieces of Al PS samples for 10 min. The Al particle (Al^{3+}) increases the nucleation rate by enhancing the rate of chlorine ion adsorption into the substrate's top layer, thereby increasing the rate of reaction [72,73]. This seeding of the electrolyte is to achieve in-situ formed dissolution reaction products that increase the reaction rate, typically applied in the semiconductor industry for the chemical etching of Si [33,142]. After that, the samples were introduced into the electrolyte and etched from 1 min to 30 min in steps of 3 min (1 min, 3 min,

6 min, 9 min, 12 min, 15 min, 18 min, 21 min, 24 min, 27 min, and 30 min) and the electrolyte temperature was measured with a Greisinger GTH 1170 digital thermometer (produced by GHM Group - Greisinger, Regenstauf, Germany) which stayed between 42 °C to 47 °C until the end of each batch of the experiment. This temperature regime was used to obtain comparable results in the four different initial surface morphologies, as the reaction is exothermic. At each of these times, samples were withdrawn from the etching bath, rinsed several times in de-ionized water, dried with pressured N_2 gas, and subsequently oven-dried for 3 min to remove the remaining water after drying with pressured N_2 gas. Thereafter, the final weight of the individual sample was measured using a digital weighing balance of 0.001 g measuring range accuracy (Sartorius AC 210S) produced by KERN & SOHN GmbH, Balingen-Germany.

For further analysis, the influence of the initial surface morphology was investigated on the structure nucleation stage of the structure formation with the corresponding mass loss of individual samples. Generally, the sculptured sample surfaces were investigated using a Zeiss Ultra Plus scanning electron microscope (SEM). Furthermore, specific samples (before and after structuring) were additionally XRD investigated using a 9-kW rotating anode with an X-ray source ($\lambda \sim 1.54$ Å) in a grazing incidence XRD (GIXRD). The source angle omega (ω) was fixed at 5 ° at a scanning rate of 20 °/min using a high-quality semiconductor detector that supports 1D x-ray diffraction measurement (Rigaku SmartLab).

3.3.2 Electrochemical etching of stainless steel samples

The electrochemical etching of the prepared SST stripes is conducted in a four-electrode etching cell, as illustrated in Figure 3.1. This is a Teflon-based single cell setup. The SST strips (both the 25 mm × 20 mm × 1.50 mm and 100 mm × 20 mm × 1.50 mm with a bent edge) are fixed on the top of the etching cell where the opening is placed. From this opening, the SST samples come in contact with the electrolyte.

An O-ring is attached to the interface directly under the SST sample and closed with a PTFE lid to prevent electrolyte leakage at the opening. The electrolyte flow rate is 240 rpm which was controlled using a peristaltic pump (ISMATEC IP 65 MCP). The electrochemical etching cell has three electrolyte inlets with an inner tube diameter of 4.8 mm and one bigger outlet with an inner tube diameter of 6.8 mm. The setup is inverted (i.e., 180 ° turn) for quick renewal of electrolyte at the SST-electrolyte interface and easy removal of gas bubbles. All used tubes and O-rings are TYGON LFL tubes which are resistant to the chemicals in the electrolyte.

The four-electrode configuration of the electrochemical etching setup consists of the working electrode (WE), the sense electrode (SE), the reference electrode (RE), and the counter electrode (CE). The SST sample to be etched was connected to the WE. The Al foil under the sample served as the SE. The RE was a platinum (Pt) wire, which was immersed in the electrolyte and positioned near the surface of the to-be-etched SST sample without touching it. The CE was a Pt wire mesh with a fixed distance to the SST sample surface. This configuration compensates for the voltage loss due to electrolyte resistance, cable, and contact resistances, etc.

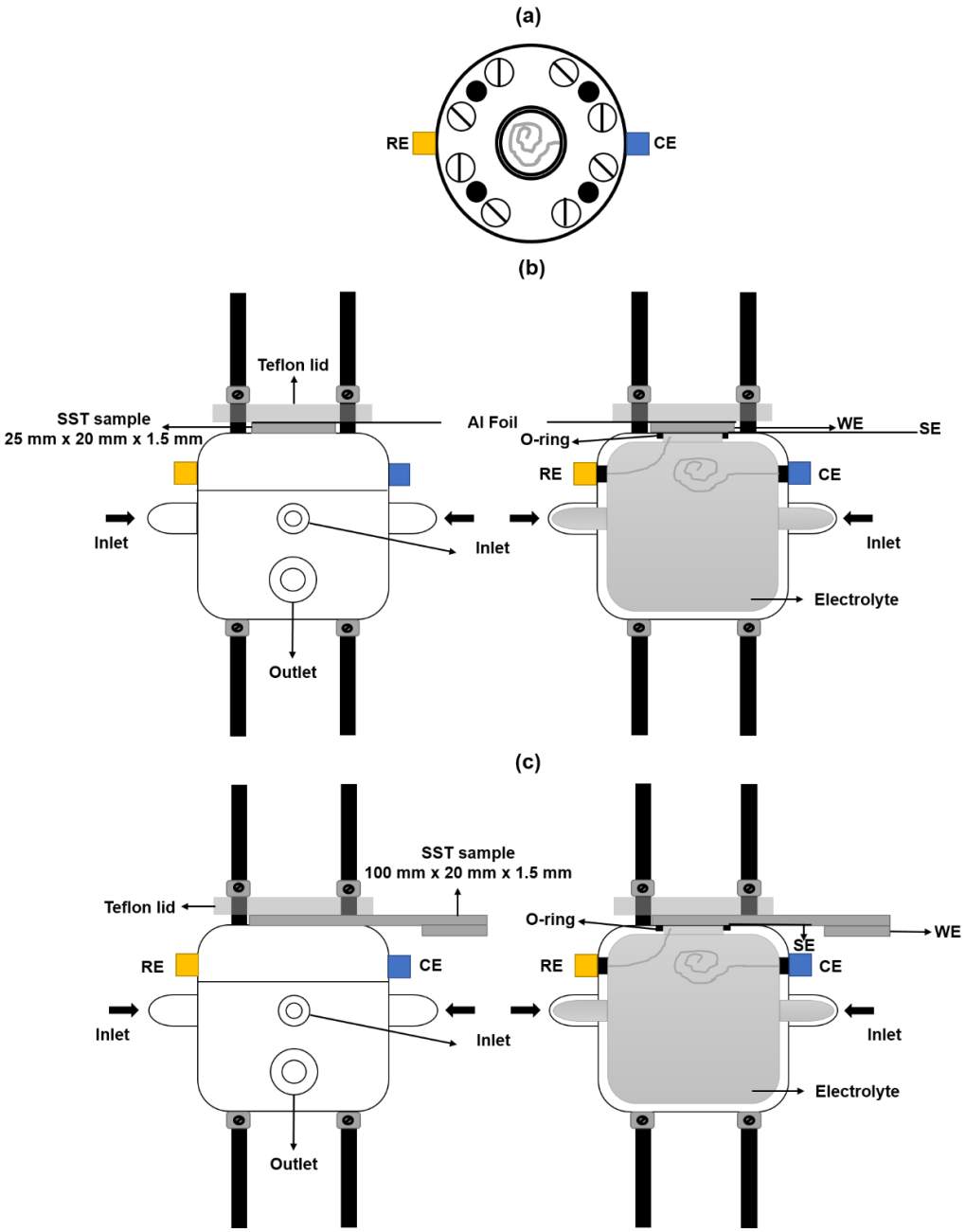

Figure 3.1**: Electrochemical etching setup schematic: Top view **(a)**, cross-sectional view of the SST sample 25 mm × 20 mm × 1.5 mm **(b)**, and cross-section view of the SST sample 100 mm × 20 mm × 1.5 mm with a bent edge **(c).

The etching electrolyte is a mixture of 0.3 l of a low aggressive/low toxic seawater-like composition (i.e., an aqueous solution of 0.75 mol/l HCl and 0.16 mol/l NaCl) and 0.63 mol HNO_3 (see Table 3.1). The samples are structured under a galvanostatic condition at a current density of 2 A/cm².

Table 3.1: *Electrochemically sculptured SST strip process parameters with a unique mechanical interlocking feature.*

Parameters	**Quantities/Units**
Etching time	1 min
Current density	2 A/cm^2
Etching temperature	25 – 26 °C (Room temperature)
Peristaltic pump speed	240 rpm
Electrolyte composition concentration	0.63 mol HNO_3/0.3l seawater-like aqueous electrolyte

For the sample with dimensions 25 mm × 20 mm × 1.5 mm, the etching time was in 3 s intervals (3 s, 6 s, 9 s, 12 s, 15 s, 18 s, 21 s, 24 s, 27 s, and 30 s), whereas the initial (before sculpturing) and final (after sculpturing) weight of the individual sample was measured using a digital weighing balance of 0.001 g measuring range accuracy (Sartorius AC 210S) produced by KERN & SOHN GmbH, Balingen-Germany. However, the predominantly used etching time for the samples with a dimension of 100 mm × 20 mm × 1.5 mm with a bent edge is 1 min.

3.3.3 Contact angle measurements of stainless steel strip

The sessile-drop technique was used to measure the SST strip 2 sculptured surface wettability through contact angle measurements. As a reference, an SST strip 2 grit-blasted surface is used. The contact angle measurements were performed on a custom build machine controlled by lab-view software. A 3 µl drop of distilled water was placed on the sample using an Eppendorf pipette (produced by Eppendorf AG, Hamburg, Germany) in between a camera and an LED lighting source system with a diffuser to provide a homogeneous illumination needed to make a drop profile to appear black on the image. For each sample measurement (5 contact angle measurements were taken), a baseline and a corresponding drop area were set manually while the software determined the corresponding contact angles on both the left and right ends of the drop.

3.3.4 Adhesion test of stainless steel strip

The mechanical properties of the structured SST strip 2 surfaces were investigated through SST-polymer-SST sandwich composite joints with different polymers by using a single-lap shear test by the European norm DIN EN 1465 [143] with little process-related deviations (such as ± 0.002 mm gap difference and little drift in overlapping of the structured surfaces). The applied parallel tensile force to the adhesive plane, and other process parameters (e.g., sample thickness, glued area, sample length, etc.) of this standard process is to eliminate any form of substrate bending as this will introduce another type of stress to the system. For this testing, an SST-polymer-SST sandwich composite structure, as depicted in Figure 3.2, was formed (6 samples for each polymer class). The reference sample surface for the sandwich structure was a conventional grit-blasted SST sample (100 mm × 20 mm × 1.50 mm dimension with 15 mm 180° bent edge, which is to eliminate further the possibility of substrates bending), degreased with acetone and subsequently air-dried to remove any residues that might interfere with the adhesion.

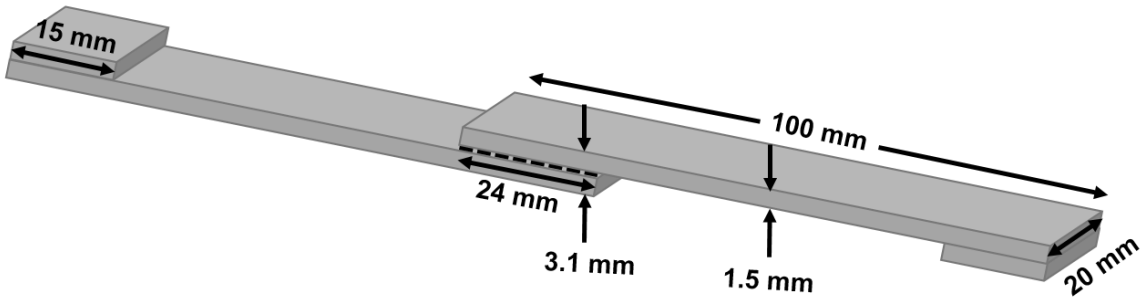

***Figure 3.2*: *Schematic of the overlapping samples for a standard lap-shear test*.**

After that, two sculptured SST strip 2 samples with circular structured surface areas of 201 mm^2 were placed opposite each other in a custom-made (by 3D printing) adjustable holder (see Figure 3.3) with an overlap of 24 × 20 mm^2 surface dimension (same gluing dimension on the grit-blasted surface) and a gap in-between. The gap was filled with adhesive and adjusted to 0.1 mm. This custom-made holder ensured a precise contact area of the substrates, especially on the circular nanoscale sculptured surface area, to avoid torsion of the samples and to ensure perfect penetration of the adhesive into the structured surface [144] irrespective of the wetting capability or wetting angle of the adhesive used.

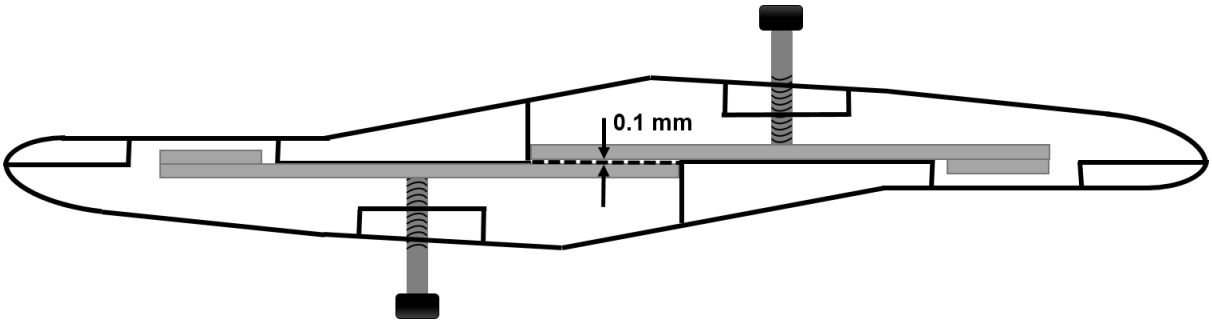

Figure 3.3: *3D printed sample holder schematic.*

Four different kinds of commercially available adhesives were used, which include a high-performance 2-component (PTU) (produced by Fluid & Prozesstechnik GmbH, Waltershausen, Germany), a 2-component acrylate adhesive (3M Scotch-Weld-DP8407NS produced by 3M Deutschland GmbH, Neuss, Germany), a 2-component epoxy-resin (UHU Plus EndFest 300 produced by UHU GmbH & Co. KG, Bühl, Germany), and another 2-component epoxy-resin (Epoxydharz L + Härter GL 1 produced by R&G Faserverbundwerkstoffe GmbH, Waldenbuch, Germany). After the adhesive application, the fixed sandwich composite structures were oven cured in accordance with the respective processing instructions, i.e., at 80 °C for 1 h for the PTU-based ones, 3 h for the acrylic-based ones, and 2 h for the epoxy-resin based adhesive. After curing, the sandwich composite structure was lap shear tested, as shown in Figure 3.4, in a Zwick Quick Test 100 kN machine at a displacement rate of 1 mm/min until failure. Subsequent photographs of the failure surface after the lap shear test of the sandwich structures were taken and examined by light microscope and SEM.

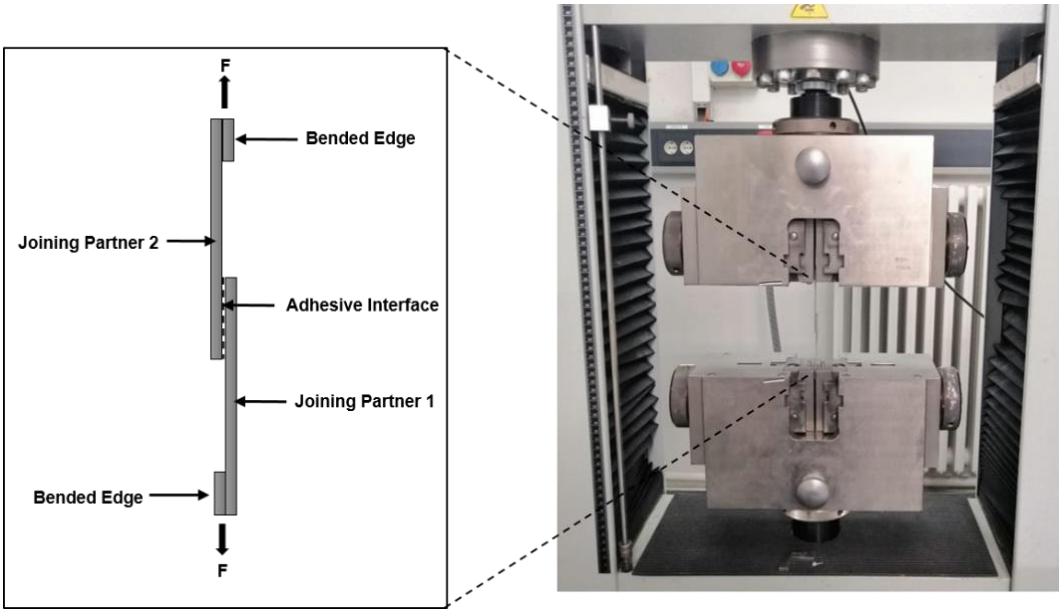

Figure 3.4: *Stainless steel sandwich composite on a tensile test machine for a shear test.*

In further investigation, the cross-section of both the SST electrochemically structured and grit-blasted samples surfaces were analyzed after a cross-section of both samples was embedded in a polymer matrix, polished with an abrasive paper of 1200 grade, 2000 grade, and 4000 grades in that order until a mirror-like surface was obtained. To enhance surface conductivity and avoid surface charging of the polymer, a thin layer film of gold (3 – 5 nm thick) was sputtered on both the cross-sectional surfaces of the samples. Subsequent images of both sample cross-sections were taken with a Leitz Ergolux 200 light optical microscope and a Zeiss Ultra Plus scanning electron microscope (SEM). In addition, an Energy dispersive X-ray spectroscopy (EDX) map of the nanoscale sculptured sample cross-section was made at an acceleration voltage of 15 kV with an Oxford X-act detector.

3.3.5 Electrochemical etching setup of stainless steel wire

The electrochemical etching of the SST wire was performed with an etching cell connected to a potentiostat used as a DC voltage source and a diaphragm pressure pump for pumping the electrolyte (Figure 3.5).

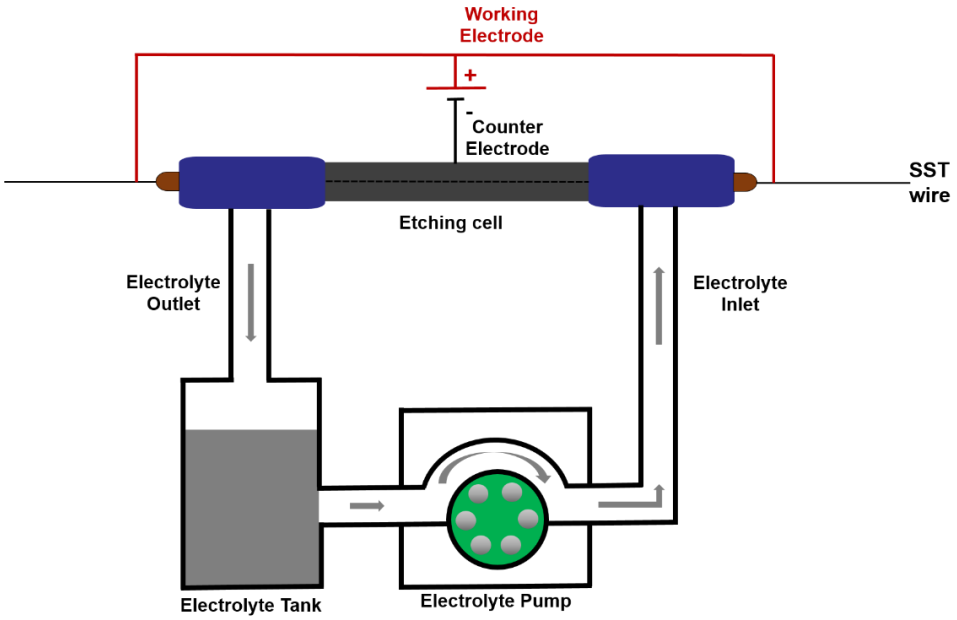

Figure 3.5: *Static stainless steel wire electrochemical etching cell.*

The SST wire, placed inside the 1 cm diameter stainless steel pipe, is connected to the positive terminal of the DC voltage source as the working electrode, while the 1 cm diameter stainless steel pipe is the counter electrode and connected to the negative terminal of the DC voltage source. The cell has an inlet and outlet point, allowing the electrolyte to flow at 11 l/min. The etching is driven via galvanostatic mode; that is, the current (current density) is controlled as a function of time and starts at the application of DC voltage between the two electrodes.

3.3.6 Electrochemical etching of stainless steel wire

Constant current application

An HCl-base electrolyte with a varying concentration in the range of 0.03 M, 0.25 M, 1 M, and 1.6 M, respectively, was used. A constant current of 2 A, which translate to 4 A/cm^2 current density (as calculated from the SST wire total surface area), is applied only on the 10 cm length of the SST wire during the etching, that is, within the 10 cm length of the counter electrode at varying sculpturing time of 0.5 s, 1 s, 2 s, and 3 s respectively using individual electrolytes as shown in Figure 3.6 for 1 s etching time.

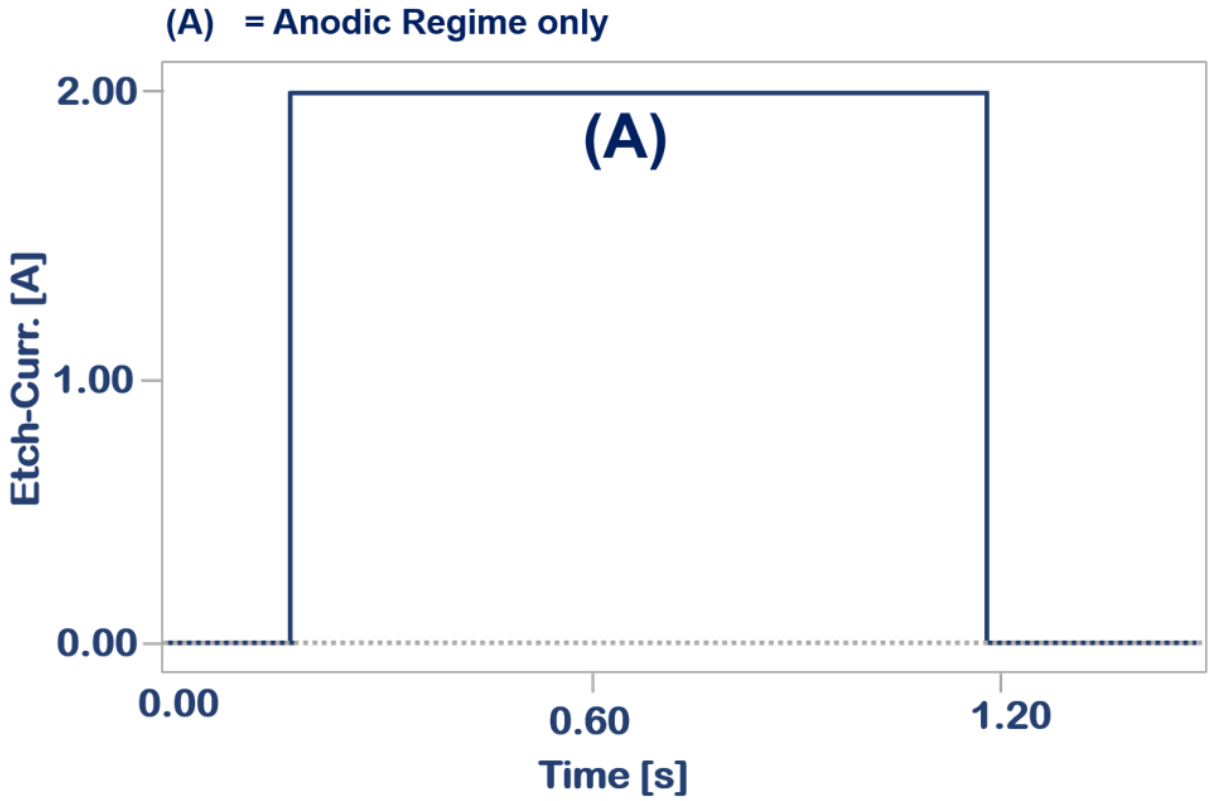

Figure 3.6: *Electrochemical etching profile of constant current application (1 s).*

The applied DC voltage at 2 A across the individual electrolytes with a constant flow rate of 11 l/min was summarized in Table 3.2.

Table 3.2: *Applied DC voltages at different electrolyte concentrations during electrochemical etching of SST wire at constant 2 A (4 A/cm^2) applied current.*

Electrolyte concentration (M)	0.03	0.25	1	1.6
Applied DC voltage (V)	15.58	6.65	4.45	3.86

Current pulsing application

Here, the 0.25 M electrolyte was used at an 11 l/min flow rate. The potentiostat, which drives both positive and negative polarities as a current source, is used to apply a current density of 4 A/cm^2 (2 A applied current) for 0.5 s at each of the anodic regimes (positive polarity) and 1 s at the cathodic regime (negative polarity) as shown in Figure 3.7.

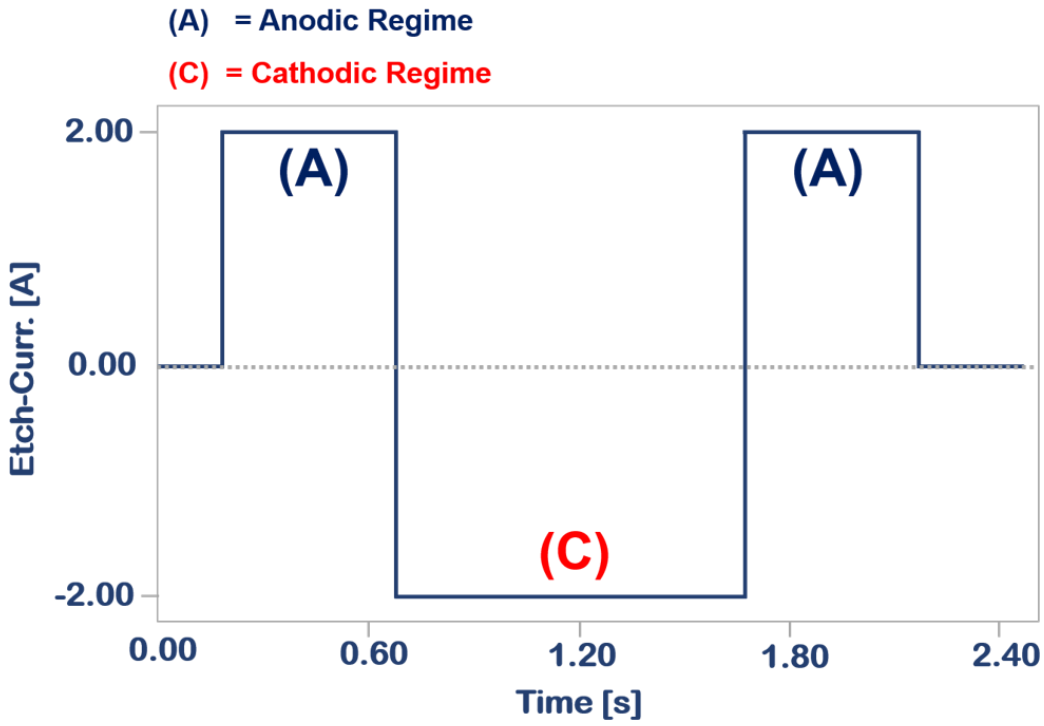

***Figure 3.7*:** *Electrochemical etching profile of current pulsing application [0.5 s (A) – 1 s (C) – 0.5s (A)].*

In addition, the current pulsing of 0.25 s (A) – 1 s (C) – 0.25 s (A) – 1 s (C) 0.5 s (A), 0.5 s (A) – 1 s (C) – 0.25 s (A) – 1 s (C) – 0.25 s (A) and 0.25 s (A) – 1 s (C) – 0.25 s (A) – 1 s (C) – 0.25 s (A) – 1 s (C) – 0.25 s (A) respectively were also carried out.

3.3.7 Characteristics features of sculptured stainless steel wires

The diameter of the sculptured SST wire and the features of the obtained bowl-like structure including the density, aspect ratio, diameter, and depth were investigated. The results obtained using 0.25 M electrolyte concentration at 2 A (4 A/cm^2) for the constant current approach at sculpturing times of 0.5 s, 1 s, 2 s, and 3 s and their SEM images taken at the same magnification were used for the analysis. The diameter of the sculptured SST wire at the individual sculpturing times was measured at 10 different points, 1 cm interval along the 10 cm pre-treated SST wire using a digital micrometer (Mitutoyo IP54 Digital micrometer) with

0 – 30 mm range, 0.001 mm resolution, ± 2 µm accuracy, and 20 mm^2 circular contact points surface area. For statistical evaluation, the mean, standard deviations, and one-way analysis of variance (one-way ANOVA) followed by a Tukey test (significance level of $p < 0.05$) were performed using OriginLab. (OriginLab Corporation, Northampton, MA, USA). In the bowl-like structure features analysis, which includes the density, aspect ratio, and diameter, Fiji ImageJ [145] image analysis was used. Here, the polygon area selection tool was used to randomly map out 10 non-overlapping complete bowl-shaped bowl-like structures at different positions using SEM images taken at the same magnification. Thereafter the area, mean, and standard deviation measurement data were analyzed using Microsoft Excel and OriginLab. In the bowl-like structure depth analysis, the pre-treated SST wire was first embedded in a polymer matrix, sliced in 4 different positions along the 10 cm sculptured surface after the curing of the polymer, polished with an abrasive paper of 1200 grade, 2000 grade, and 4000 grades in that order until a mirror-like surface was obtained. Thereafter, a 10 nm thick layer of gold was sputtered on the mirror-like surface using a Vac coat desktop sputter & carbon coater (manufactured by VacCoat Ltd, London, United Kingdom) at 10 mA for 60 s. Then, using a Zeiss Ultra Plus scanning electron microscope (SEM), the individual bowl-like structure depth was measured from the image. The mean and standard deviation measurement data were analyzed using Microsoft Excel and OriginLab.

3.3.8 Ultimate tensile test of stainless steel wires

The mechanical properties of the pristine and sculptured SST wire using both the constant current and current pulsing approaches were investigated. In characterizing the mechanical properties, tensile test experiments were performed with the universal testing device Zwick RetroLine (ZwickRoell GmbH & Co., KG, Ulm, Germany) at a speed of 1.000 %/min with a clamping length of 3 cm. The aim was to stay within the sculptured regime of the 10 cm sculptured SST wire. For the ultimate tensile test (see Figure 3.8), 3 samples per individual sculpturing times on both approaches were tested. The mean values and corresponding standard deviations were calculated. For statistical evaluation, a one-way analysis of variance (one-way ANOVA) followed by a Tukey test (significance level of $p < 0.05$) was performed by OriginLab. (OriginLab Corporation, Northampton, MA, USA).

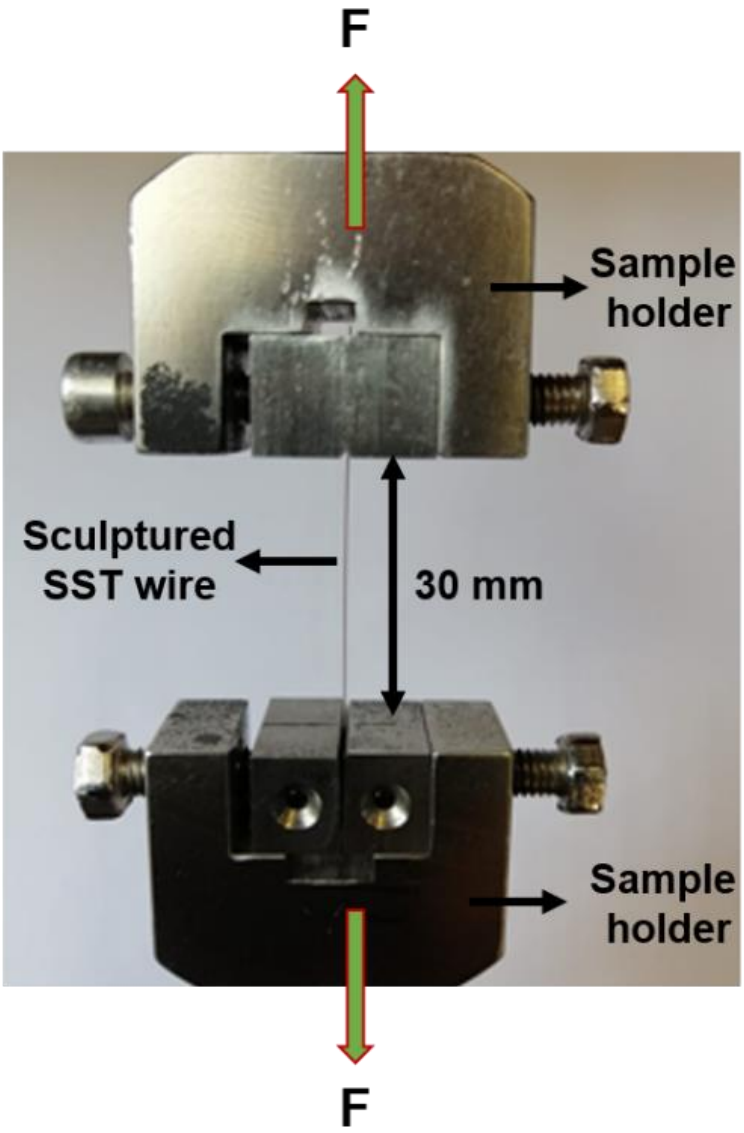

Figure 3.8: *Sculptured SST wire on a tensile test machine for ultimate tensile strength test.*

Chapter 4

4.0 Results

In this chapter, the results of the influence of initial surface morphology during structure evolution through chemical nanoscale sculpturing of aluminum alloy (AlMg3) strip and electrochemical nanoscale sculpturing of stainless steel (SST) strip 1 are presented. Also, the surface structuring of SST strip 2 and the surface pre-treatment of SST wire through electrochemical nanoscale sculpturing is presented. Furthermore, the chemical and mechanical properties of the sculptured/pre-treated metal surface through nanoscale sculpturing are demonstrated in this chapter.

4.1 Structure nucleation efficiency and its evolution as influenced by the initial surface morphology of AlMg3 strip surface through chemical nanoscale sculpturing

4.1.1 Initial surface morphology after sample preparation (AlMg3 strip)

The surface morphology of the pristine sample (PS) AlMg3 strip and its characteristics were investigated, and the results are presented in Figure 4.1. The figure illustrates the impact of the surface preparation process on the commercially available PS-brushed AlMg3 strip surface. The SEM image in Figure 4.1 (a) reveals the parallel stripes of the roller on the PS surface and some defects introduced during multiple rolling processes. The 3D confocal microscope image in Figure 4.1 (e) clearly displays the parallel rolling indentation and roughness spikes introduced by the surface brushing process, as indicated by the arrows. Consequently, the PS surface exhibits curvatures at the tips of the shallow brushing grooves, as seen in Figure 4.1 (e) and (i)

On the contrary, the pristine-abraded surface (PAS) exhibited a uniform and quasi-flat surface, devoid of rolling indentation and surface brushing effects as depicted in Figure 4.1 (b) and (f) SEM and confocal microscope images. Additionally, the roughness profile of the PAS, as shown in Figure 4.1 (j), revealed a quasi-flat surface with no identifiable roughness profile (curvatures).

The pristine-grit-blasted-surface (PGBS), as shown in Figure 4.1 (c), depicts different degrees of roughness with a deep grit impact indentation in the range of 5 µm [see the circled points in the SEM image, the arrows in the confocal microscope and the roughness profile in Figure 4.1 (c), (g) and (k) respectively]. Additionally, the PGBS exhibits a mixed surface morphology, including the pristine brush groves and the defect-oriented grit-blasting process with different grit indentation curvatures [see Figure 4.1 (c), (g), and (k)].

As depicted in Figures 4.1 (d), (h), and (l), the pristine-abraded-grit-blasted-surface (PA-GBS) exhibits a mixture of surface morphologies. This includes the quasi-flat surface resulting from abrasive scrubbing and a shallow (in the range of 2 µm) defect-oriented grit-blasting process (compared to the PGBS) grit indentation with varying tip curvatures (see in the SEM image circled points, the confocal microscope images arrows, and the roughness profile).

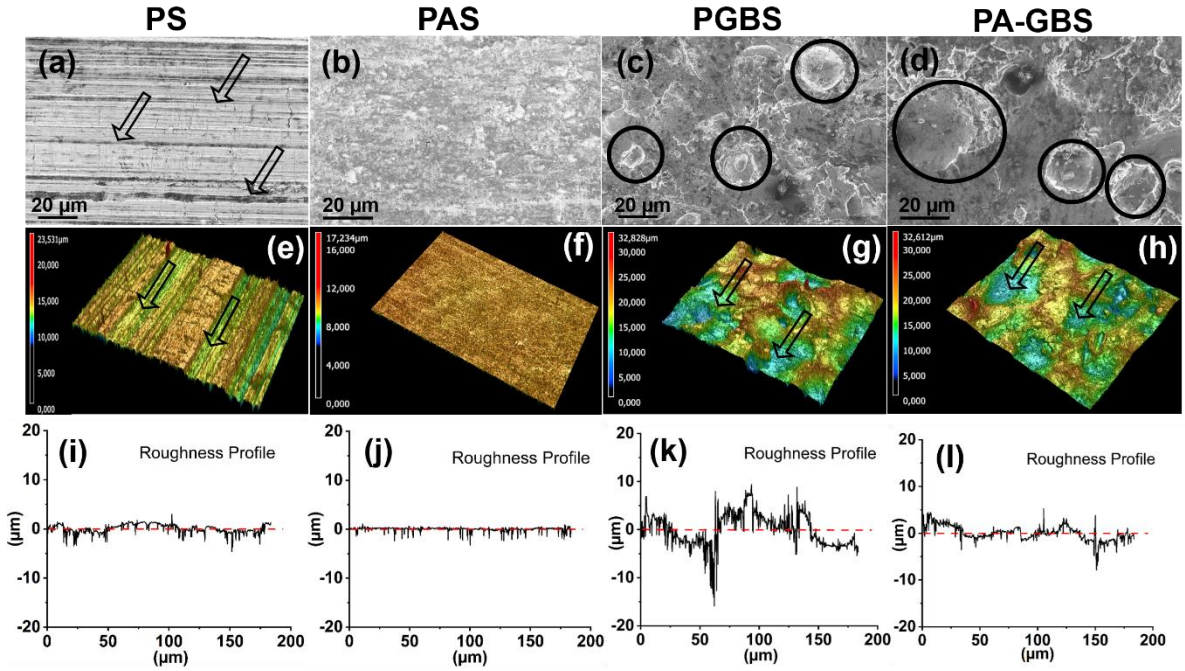

Figure 4.1: *Surface analysis of the samples' initial surface morphology using SEM and confocal microscope. This shows the surface morphology, topography, and roughness profile as follows: The PS shows the parallel lines of rolling process defects and surface brushing with groves curvatures* ***(a, e,*** *and* ***i)****. The PAS shows a quasi-flat surface due to abrasive scrubbing with different asperities* ***(b, f,*** *and* ***j)****. The PGBS shows mixed surface morphologies of surface brushing and defect-oriented grit blasting with different curvatures of grit impact indentation* ***(c, g,*** *and* ***k)****. The PA-GBS shows mixed surface morphologies of a quasi-flat surface and defect-oriented grit blasting with different curvatures of grit impact indentations* ***(d, h,*** *and* ***l)****.*

4.1.2 Structure nucleation and total sculptured surface area (AlMg3 strip)

The influence of the initial surface morphology on various parameters related to sculpturing, including structure nucleation sites density, the total sculptured surface area, and

individual sample mass loss was investigated. For these, experiments using a simple HCl-based electrolyte (7.25 wt. %) at an initial electrolyte temperature of 42 ± 2 °C, and an initial injection of Al^{3+} particles into the freshly prepared electrolyte were conducted. The chemical sculpturing process was performed at 3 min intervals for a total of 30 min sculpturing time (i.e., 1 min, 3 min, 6 min, 9 min, 12 min, 15 min, 18 min, 21 min, 24 min, 27 min, and 30 min respectively). The nucleation site density and the total sculptured surface area (> 20 μm^2) were calculated using the Fiji ImageJ image analysis polygon area selection tool by mapping out the nucleation sites from SEM images taken at the same magnification.

As depicted and mapped out with a rectangle in Figure 4.2 (a), the results showed that structure nucleation was dominant in the first three sculpturing intervals (i.e., 1 min, 3 min, and 6 min), with the highest density of nucleation sites (47 nucleation sites / μm^2) observed in the PGBS sample after 1 m of sculpturing. The PA-GBS sample showed a lower density of nucleation sites (16 nucleation sites / μm^2) at the same time while the PS and PAS did not show any nucleation sites. The total sculptured surface area of the PGBS and PA-GBS samples was found to be in the same range of 8×10^4 μm^2 after 1 min sculpturing time as shown in Figure 4.2 (b).

In Figure 4.2 (a), the results showed that after 3 min of sculpturing, the PS sample had the highest density of nucleation sites (159 nucleation sites / μm^2), followed by the PGBS sample (144 nucleation sites / μm^2) and the PA-GBS (113 nucleation sites / μm^2). No identifiable structure nucleation site was observed on the PAS sample. In Figure 4.2 (b), the PGBS sample exhibited the highest total sculptured surface area of 10×10^4 μm^2, despite having a lower density of nucleation sites compared to the PS sample with the highest nucleation sites. The PA-GBS showed 6×10^4 μm^2 total sculptured surface area, and lastly, the PS sample with a sculptured area of only 0.3×10^4 μm^2. These results suggest that the PS sample has a high density of distributed tiny nucleation sites arising from the shallow groves, a result of the surface brushing effect.

In the 6 min sculpturing time, as shown in Figure 4.2 (a), the results indicate a general drop in the number of nucleation sites on the PS, PGBS, and PA-GBS samples, which suggests interconnection and collapse of nucleation sites into one another, therefore, increasing the total sculptured surface area. At this sculpturing time, the PS surface showed 20 nucleation sites / μm^2 with a total sculptured surface area of 14×10^4 μm^2. Meanwhile, the PA-GBS showed the highest number of nucleation sites at this sculpturing time with 52 nucleation sites / μm^2 and a total sculptured surface area of 12×10^4 μm^2. PGBS showed a significant drop in the number of nucleation sites with a total sculptured surface area of

21×10^4 µm^2. On the other hand, the PAS sample in its initial structure nucleation showed 37 nucleation sites / µm^2 with a total sculptured surface area of 0.2×10^4 µm^2 [Figure 4.2 (b)].

As the sculpturing time increased to 9 min, 12 min, and 15 min as depicted in Figure 4.2 (a), the PS, PGBS, and PA-GBS showed a unitary nucleation site, meaning a quasi-fully sculptured surface with few islands of unsculptured surface. The total sculptured surface area remained constant at 21×10^4 µm^2 for all the three samples [Figure 4.2 (b)]. On the other hand, the PAS showed a linear decrease in the number of nucleation sites until reaching a unitary nucleation site at 15 min sculpturing time [Figure 4.2 (a)], while the total sculptured surface area showed a linear increase until reaching 21×10^4 µm^2 total sculptured surface area at 15 min sculpturing time, indicating a fully sculptured surface [Figure 4.2 (b)].

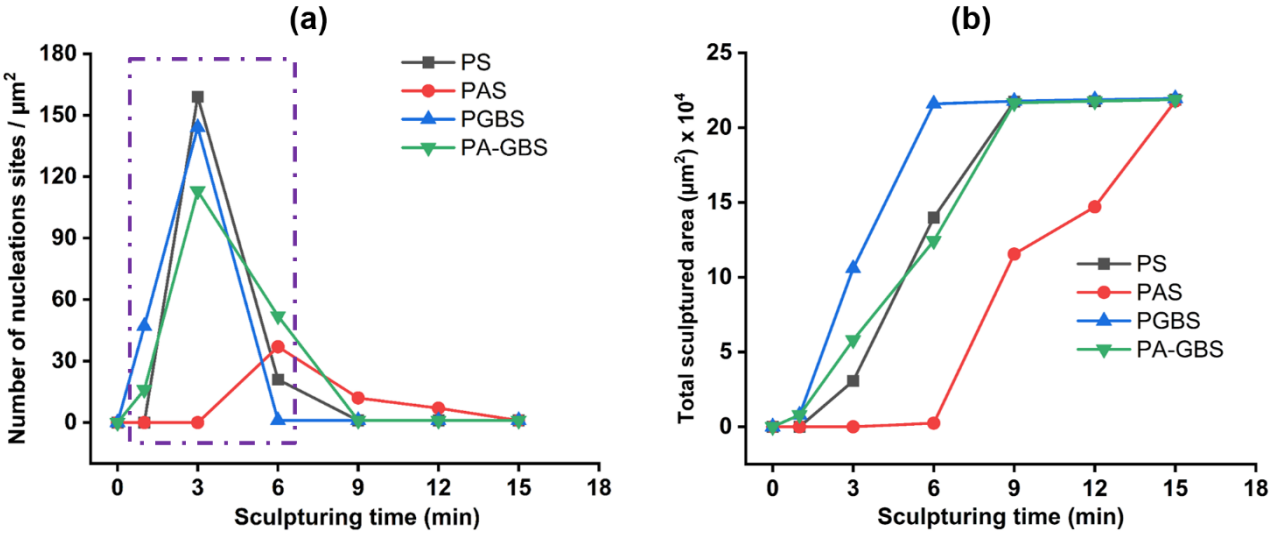

Figure 4.2: *The plots of the nucleation site density indicated with the spots rectangular block in* ***(a)*** *and total etched surface area* ***(b)*** *of an AlMg3 strip sample. This is influenced by the initial surface morphology of the sample before structuring. The individual nucleation sites and etched surface are measured from sites above 20 µm^2.*

4.1.3 Mass loss plot (AlMg3 strip)

The Figure 4.3 plot demonstrates the relationship between the sculpturing time and mass loss of individual samples with varying initial surface morphologies. The plot reveals two regimes, A and B, which exhibit different slopes in terms of mass loss. In the B regime, further differentiation can be made based on the slope steepness, which distinguishes between the grit-blasted samples (PGBS and PA-GBS), the brushed surface sample (PS), and the abraded surface sample (PAS).

At the sculpturing time of 1 min, no significant mass loss is observed in any of the samples, regardless of their initial surface morphologies. However, an increase in mass loss can be seen in the plots at the 3 min sculpturing time. The mass loss values are 0.005 g (for the PS

sample), 0.003 g (for the PAS sample), 0.011 g (for the PGBS sample), and 0.008 g (for the PA-GBS sample), respectively. In the 6 min of sculpturing, the grit-blasted surfaces (PGBS and PA-GBS) showed the highest mass loss, with values of 0.041 g and 0.040 g, respectively. The brushed surface (PS) showed a mass loss of 0.032 g, while the abraded surface (PAS) showed the lowest mass loss of 0.016 g. The differences in mass loss can be attributed to the density of structure nucleation sites, the rate of structure formation, and the total sculptured surface area at individual samples.

At further sculpturing times, all the samples, irrespective of their initial surface morphology, show a linear regime of increase in mass loss as sculpturing time increases. Here, the grit-blasted surfaces (PGBS and PA-GBS) show a steeper slope than the PS and PAS (see Figure 4.3 B). This difference in slope steepness can be attributed to a direct consequence of structure nucleation efficiency. That is, the PGBS and PA-GBS which shows a high density of nucleation sites with a corresponding large total sculptured surface area [see Figure 4.2 (a) and (b)], is a result of the surface preparation method, which results in deep and sharp tip curvatures. This high density of nucleation sites led to a higher etching rate, which results in an electrolyte temperature difference of 1 °C – 2 °C compared to the PS and PAS in the first 6 min sculpturing time.

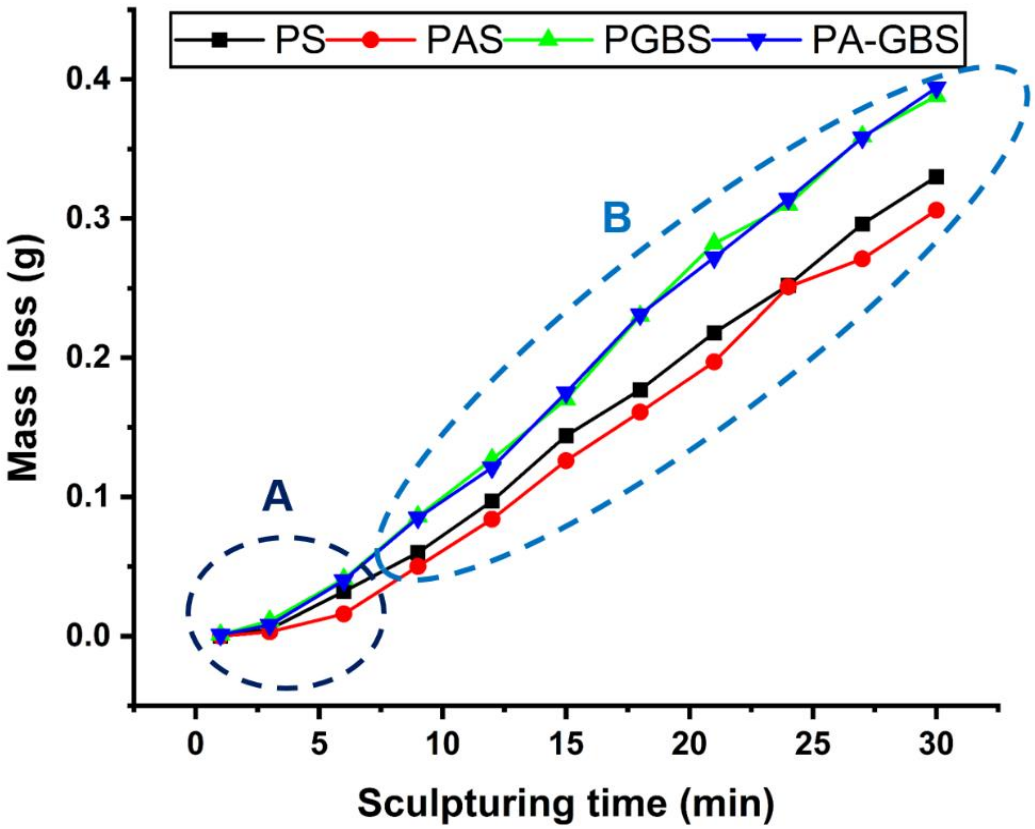

***Figure 4.3*: *Plot of individual AlMg3 sample's mass loss at different sculpturing*.**

4.1.4 Temperature-time diagram (AlMg3 strip)

The nanoscale sculpturing temperature-time diagram within the temperature window of 42 °C – 47 °C is shown in Figure 4.4. This elaborates the various stages of the nanoscale sculpturing process in relation to the electrolyte temperature and sculpturing times.

Stage I, as depicted in Figure 4.4 (i.e., between 1 min – 6 min), shows an initial temperature drop of approximately 1 °C within the first 1 min after the AlMg3 samples are introduced into the electrolyte. This temperature drop is due to the heat exchange between the samples and the warm electrolyte, which have different specific heat capacities. Following this, there is an increase in the temperature profile, which indicates the onset of nucleation of cubic crystallographic interlocking structures (as seen in the structures formation schematic and the SEM image in the insets of Figure 4.4 Stage I).

Stage II (i.e., between 6 min – 16 min), is a non-steady state regime of structure formation that shows a linear increase of electrolyte temperature with time (as shown in Figure 4.4 Stage II regime). This increase is due to the increase in reaction enthalpy, resulting from the etching of manufacturing rolling process defects, micro defect, non-perpendicular {100} planes oriented bulk materials, slow surface passivation lattice planes, and the exothermic nature of the reaction between the $AlMg_3$ samples and the aqueous HCl electrolyte. This led to the formation of a 3-dimensional surface structure, resulting in the complete formation of mechanically stable hook-like interlocking structures with undercuts (as seen in Figure 4.4 structures formation schematic and the SEM image insets in Stage II).

Stage III, as depicted in Figure 4.4, shows a reduction in slope compared to stage II, with a seemingly constant temperature between 16 min to 20 min and a linear drop in temperature thereafter. This constant temperature between 16 min to 20 min can be attributed to the gradual formation of a high ratio of {100} planes cubic crystallographic facets (i.e., passivation stopping plane formation). This indicates the onset of the self-sustaining/amplifying feature, where a completely nanoscale sculptured surface undergoes a thinning/complete etching of its top cubic crystallographic facets layer with a corresponding new formation of cubic crystallographic facets in depth (as seen in Figure 4.4 structures formation schematic insets in Stage III). The gradual temperature drop is due to the reduction in the number of samples in the etching bath, as samples are withdrawn from the electrolyte at 3 min intervals and heat loss to the environment. In a system where samples are not withdrawn at intervals, a continuous linear increase in temperature with time will be observed due to the self-sustaining/amplifying feature and the exothermic nature of the sculpturing process.

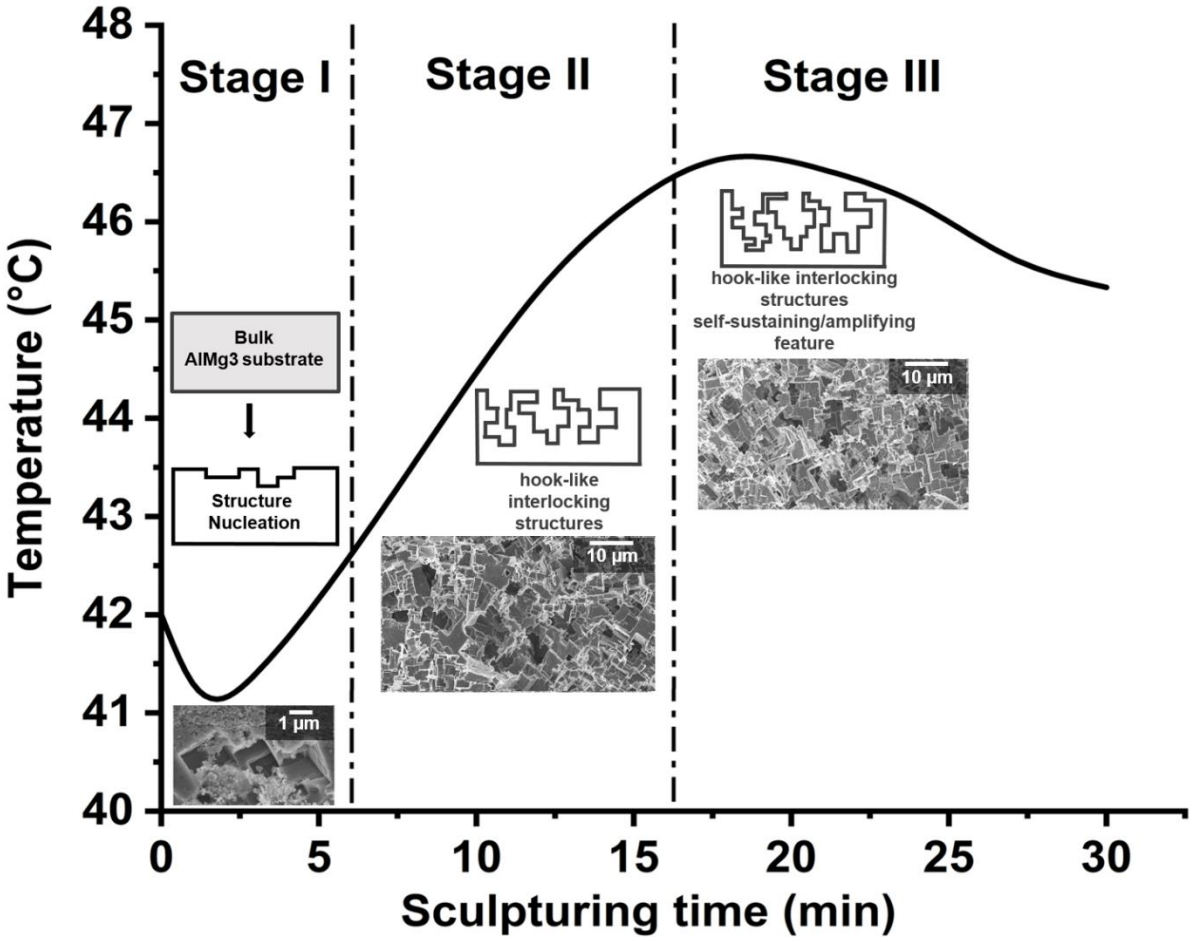

***Figure 4.4*: *Temperature-time diagram of nanoscale sculpturing of AlMg3 strip showing the evolution of the hook-like interlocking structures*.**

4.1.5 Structures evolution as influenced by the initial surface morphology of AlMg3 strip through chemical nanoscale sculpturing

The effects of the initial surface morphology of the samples on the formation of stable mechanical hook-like interlocking structures were investigated through a time-controlled nanoscale sculpturing process. The structure evolution is demonstrated in Stage I (structures nucleation stage), Stage II (formation of mechanically stable hook-like interlocking structure), and Stage III (self-sustaining/amplifying feature), respectively.

Stage I: Structure nucleation

In the 1 min sculpturing time of the PS sample with rolling defect and brushed surface, as depicted in Figure 4.5 (a), a mash-like amorphous AlMg3 surface structure with an undefined structure as shown in Figure 4.5 (a) inset can be observed. On the other hand, the PAS, which has a few nanometres of its top layer removed through the abrasive scrubbing process, shows a quasi-flat surface as depicted in Figure 4.5 (b) [see Figure 4.5 (b) inset] without any observable

mash-like surface after 1 min sculpturing time. Meanwhile, in the 1 min sculpturing time, structure nucleation has already started in the grit-blasted surfaces [i.e., PGBS and PA-GBS as shown in Fig. 4.5 (c) and (d) insets] mostly on the positions with deep and sharp tip curvatures.

Subsequently, as depicted in Figure 4.5 (e), the SEM images of the 3 min sculpturing time of the PS surface show the nucleation site primarily along the rolling impression. Therefore, one can see that the thin amorphous mash-like layer gradually degrades, thereby exposing the AlMg3 multi-crystalline layer, which enhances the sculpturing process. This led to the formation of cubic crystallographic stopping/passivating {100} plane of the AlMg3 multi-crystalline samples surface as shown in the magnified inset SEM image of Figure 4.4 (e) with a top amorphous layer of about 10 µm thick [see arrow in Fig. 4.5 (e) inset]. Similarly, the PGBS and PA-GBS in Figure 4.5 (g) and (h) show more randomly distributed nucleation sites, mostly on areas with a high degree of micro defects and close to the grit indented positions, with the PGBS surface showing a high density of nucleation sites with cubic crystallographic {100} passivating plane [see Fig. 4.5 (g) inset]. However, the PAS [Figure 4.5 (f)] shows some random white patches of nucleation sites without any sign of cubic crystallographic facet structures after the 3 min sculpturing time [see Figure 4.5 (f) inset].

The 6 min sculpturing time, as depicted in Figure 4.5 (i, k, and l), shows a mixture of a large degree of nanoscale crystallographic sculpturing between the PS, PA-GBS, and PGBS. In contrast, the PAS shows some randomly distributed nucleation sites with cubic crystallographic stopping/passivating {100} plane of the AlMg3 multi-crystalline substrates [see Figure 4.5 (j) inset].

Observations indicate that nucleation of structures occurs within the initial 6 min of the sculpturing process. Notably, early nucleation of structures is observed on the indents (deep and sharp tip curvatures) and defect areas of grit-blasted surfaces (PA-GBS and PGBS) and in the brush grooves of brushed surfaces (PS), as illustrated by SEM insets in Figure 4.4(c), (e), and (h). Conclusively, the nucleation process in nanoscale sculpturing of AlMg3 samples is a sporadic and random etching of weak grains that have non-perpendicular oriented {100} planes to the surface of the substrates that have a strong dependency on the initial surface morphology of the AlMg3 substrates with respect to the roughness tip curvature.

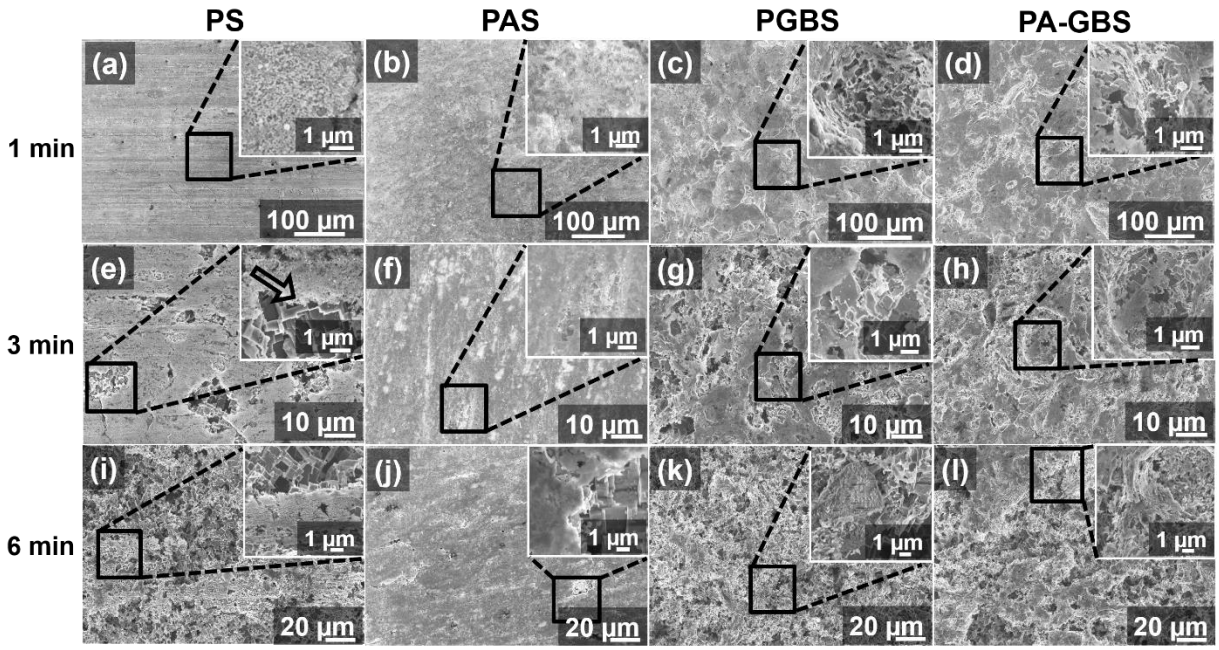

Figure 4.5: *SEM images of structures evolution-Stage I showing the structures nucleation efficiency as influenced by initial surface morphologies of the AlMg3 strip.*

Stage II: Formation of mechanically stable hook-like interlocking structures

As depicted in Figure 4.6 (a) – (d) SEM images of the 9 min sculpturing time, one can see some sketchy and randomly distributed islands of unsculptured surfaces [see Fig. 4.6 (a) and (d) insets] of the top amorphous layer with corresponding nucleation of cubic crystallographic hook-like interlocking structures. On the other hand, the PAS shows some large islands of unsculptured surface [see dark areas in Figure. 4.6 (b)] with a corresponding area of the sculptured surface showing the cubic crystallographic stopping/passivating {100} plane as depicted in Figure 4 (b) inset. Interestingly in the 9 min sculpturing time, as shown in Figure 4.6 (c), the PGBS has its amorphous layer completely etched with a corresponding complete sculptured surface which shows the cubic crystallographic stopping/passivating {100} plane [see Figure 4.6 (c) inset].

Correspondingly, the PS and PA-GBS at 12 min sculpturing time have their amorphous layer completely etched with a corresponding complete sculptured surface which shows the cubic crystallographic stopping/passivating {100} plane [see Figure 4.6 (e) and (h) inset] respectively. However, the PAS, as depicted in Figure 4.6 (f) in the same 12 min sculpturing time, shows randomly distributed islands of unsculptured amorphous layer [see dark patches in Figure 4.6 (f)] and a corresponding white patches area of a sculptured surface (see Figure 4.6 (f) inset). Finally, at 15 min sculpturing time, the dark patches of an unsculptured amorphous

layer of the PAS are completely etched with a completely sculptured surface which shows the cubic crystallographic stopping/passivating {100} plane [see Figure 4.6 (j) inset].

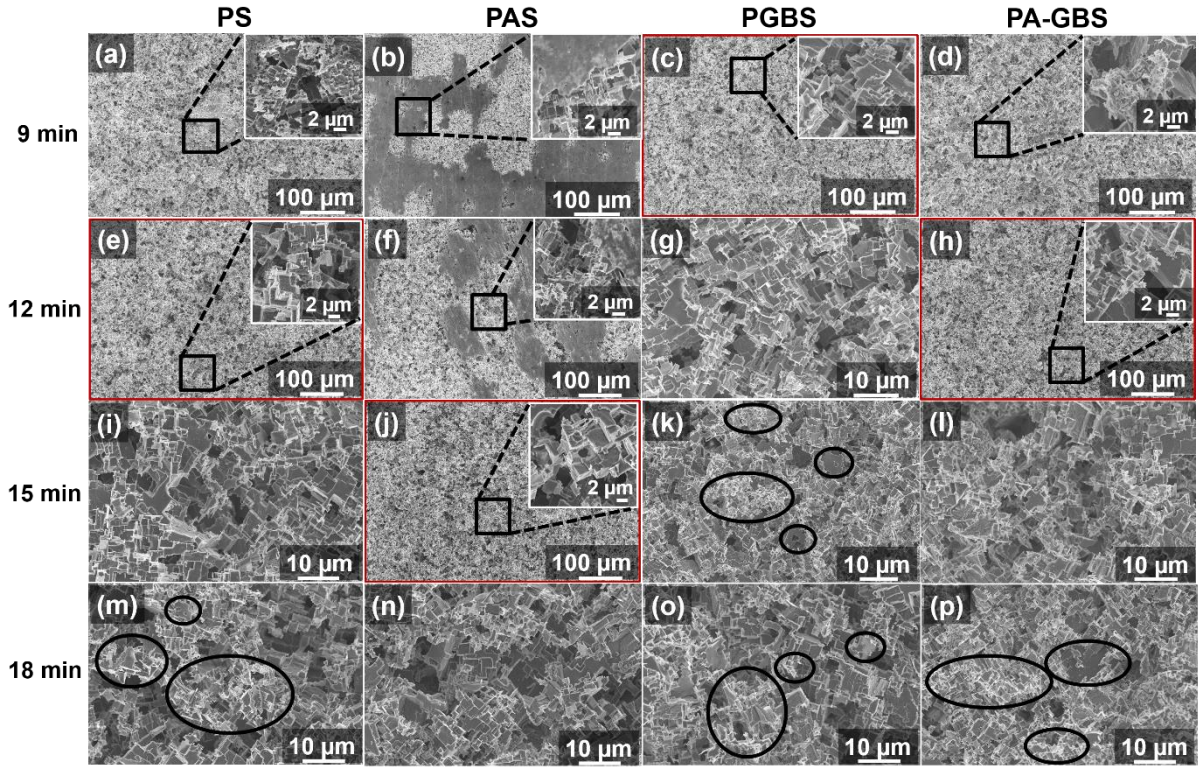

Figure 4.6**:** *SEM images of structure evolution Stage II showing the complete formation of mechanically stable hook-like interlocking structure as influenced by the initial surface morphology.*

In the subsequent sculpturing time, all the samples irrespectively of their initial surface morphology show similar cubic crystallographic stopping/passivating {100} plane hooking structure in the next sculpturing time step after the complete removal of the top amorphous layer and complete formation of mechanically stable hook-like interlocking structures [see Figure 4.6 (g), (i), (l) and (n)]. Then, as depicted in Figure 4.6 (k), (m), (o), and (p), the completely sculptured surfaces, regardless of their initial surface morphology, show a regeneration process (Stage III), which involves the thinning/complete etching of the top layer [see wide circled bright top layer in Figure 4.6 (k), (m), (o) and (p)]. This follows with a corresponding new crystallographic facet formation in depth (self-sustaining/amplifying feature).

In summary, stage II comprises the non-steady-state condition. Here, the top amorphous layer, the mechanically induced micro surface defects, and non-perpendicular {100} planes oriented bulk material are continuously etched until the complete formation of the cubic crystallographic {100} planes with mechanically stable hook-like interlocking structures [i.e.,

PS at 12 min, PAS at 15 min, PGBS at 9 min and PA-GBS at 12 min with red frames in Figure 4.6 (e), (j), (c), and (h)] are formed without any island of an amorphous layer or bulk material.

Stage III: Self-sustaining/amplifying feature

The Stage III of nanoscale sculpturing, as depicted in Figure 4.7 (a) – (h) (i.e., from 21 min and 30 min sculpturing time and as mentioned earlier in Stage II), is the continuous regeneration of the cubic crystallographic {100} planes with hook-like interlocking features. The SEM images show a similar bright top crystallographic layer of sculptured surface irrespective of the sculpturing time [see circled points in Fig. 4.7 (a) – (h)]. In addition, there is a corresponding nucleation and formation of new cubic crystallographic facets in depth which leads to an increase in surface area to volume ratio hence the self-sustaining/amplifying feature of the nanoscale sculpturing process.

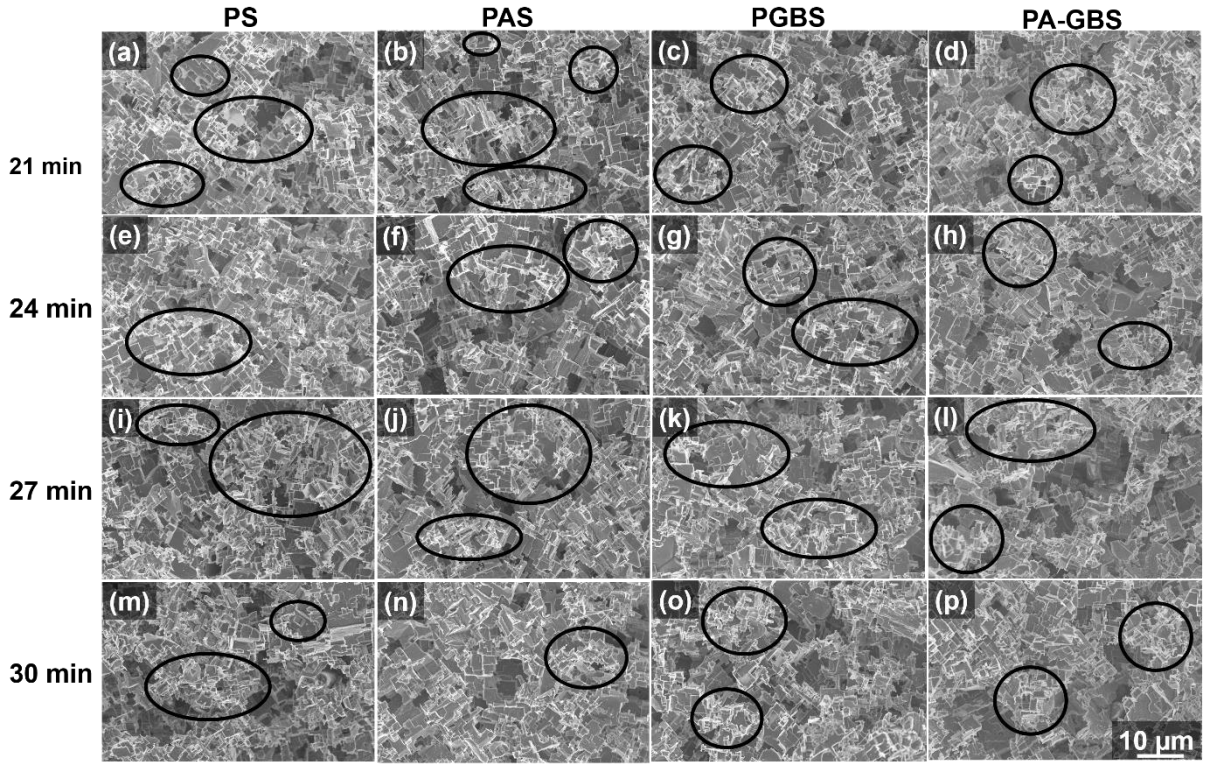

Figure 4.7**:** *SEM images of structure evolution-Stage III showing steady-state conditions self-sustaining/amplifying features irrespective of the sample's initial surface morphology.*

This is an explicit confirmation that the delay in the nanoscale sculpturing time (i.e., reaching the on-set of the steady-state condition with a completely nanoscale sculptured surface) may have arisen due to the substrate's initial surface morphology. That is, the extra pre-treatment processes partially altered the aggregate property of the pristine roll-brushed amorphous top layer and the AlMg3 samples' multi-crystalline top layer. In essence, this is a

hint that irrespective of the initial surface morphology of the AlMg3 sample, once the steady-state condition and the self-sustaining/amplifying feature commences, the nanoscale sculpturing of commercially available AlMg3 shows similar mechanically stable hook-like interlocking structures. This could also be a reason for the linear regime (Figure 4.3 regime B) in the mass loss plot against sculpturing time.

4.1.6 Structural and chemical properties of sculptured AlMg3

X-ray diffraction analysis of AlMg3 strip

As depicted in Figure 4.8, the XRD diffractograms of the different initial surface morphology of the AlMg3 strip before sculpturing [see Figure 4.8 (a)] and after the complete formation of the cubic crystallographic facet structures (i.e., PS at 12 min, PAS at 15 min, PGBS at 9 min and PA-GBS at 12 min) shows the different intensities of the dominant crystallographic planes before and after nanoscale sculpturing on these surfaces. One can see that the XRD diffractogram of the unsculptured and sculptured sample surfaces exhibits five distinct peaks.

These peaks can be allocated to α-Al {200}, α-Al {220}, α-Al {222}, α-Al {111}, and α-Al {311} peaks which are only the peaks expected for crystalline fcc α-Al. In addition, they coincide with the bulk Al reference pattern-4313217 for both samples.

The α-Al {111} and α-Al {200} are the most pronounced peaks in both XRD diffractograms, while the intensity of the α-Al {111} peak is dominant on the unsculptured samples [see Figure 4.8 (a)] been that the {111} plane has the highest packing density in the bulk fcc α-Al crystal structure. In addition, when compared with the unsculptured samples, the α-Al {222} peaks are seemingly not visible in all the sculptured samples. This could be related to the high etching rate of the highest packing density {111} plane with regard to its crystallographic orientation and surface energy. However, the sculptured samples show a dominancy of the α-Al {200} [see Figure 4.8 (b)] because it serves as a stopping plane.

Typically, the Miller indices of a crystal plane describe its orientation in reciprocal space and are related to the interplanar spacing of the plane in real space. For example, the (200) Miller indices correspond to the inverse reciprocal of the {200} lattice plane in fcc aluminium, with a crystallographic orientation of x = ½, y = ∞, and z = ∞ (i.e., the *hkl* coordinates gives *h = 2, k = 0, l = 0*). Despite having different Miller indices, both the {200} and {100} lattice plane in fcc aluminium have a specific parallel orientation with interplanar spacings of d = a/2 and d = a/√2, respectively, where a is the fcc lattice constant. As a result, the X-ray diffraction

(XRD) peak intensity produced by the {100} plane is nearly zero, whereas the {200} plane produces a large intensity peak. This is because the reflection from the {100} plane destructively interferes, while the reflection from the {200} plane is in phase, resulting in a large peak intensity [146,147].

In summary, the Miller indices and interplanar spacing of crystal planes in fcc aluminium are related, and the orientation and spacing of the {200} and {100} lattice planes are specific to the fcc crystal structure. The difference in XRD peak intensity between the {200} and {100} planes is due to the destructive interference of the {100} reflection and the in-phase reflection of the {200} plane.

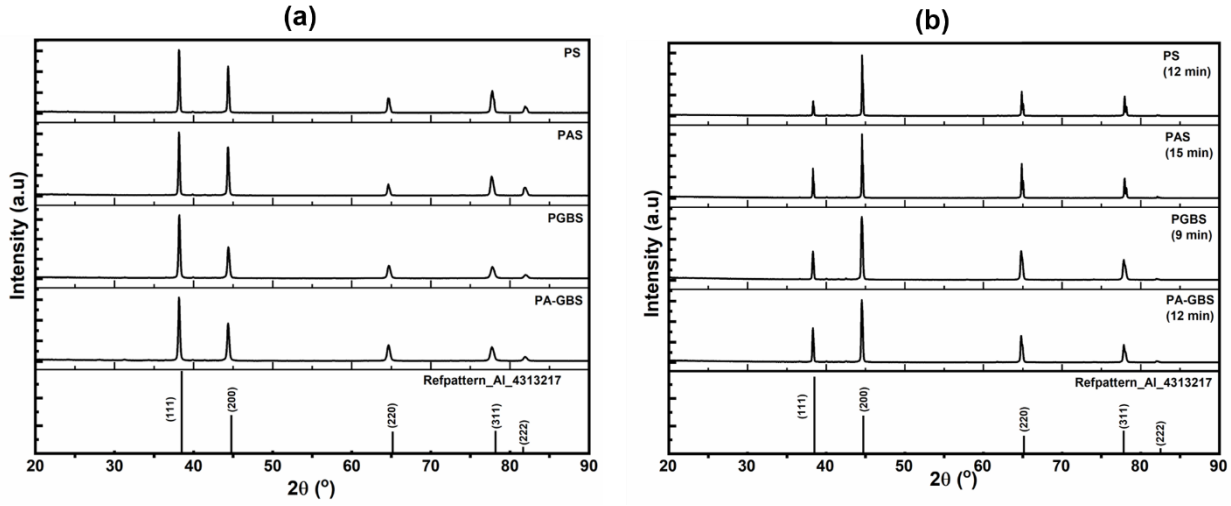

Figure 4.8: *XRD diffractogram of bulk Al reference-pattern-4313217;* ***(a)*** *Unsculptured Al strip at different initial surface morphology showing the dominancy of α-Al {111} plane, and* ***(b)*** *Completely sculptured sample surfaces showing the dominancy of the α-Al {200} plane.*

4.2 Structure nucleation efficiency and its evolution as influenced by the initial surface morphology of stainless steel (strip 1) surface through electrochemical nanoscale sculpturing

4.2.1 Initial surface morphology after sample preparation (stainless steel strip 1)

The initial surface morphology of the pristine (PS) SST strip 1 and its characteristics, as depicted in Figure 4.9, illustrate the differences and the influence of the sample preparation process. In Figure 4.9 (a) SEM image, one can see the individual grains and the grain boundaries of the polished PS SST sample, as pointed out with the arrows. However, the 3D confocal microscope image [Figure 4.9 (e)] shows a rather smooth surface with a corresponding quasi-flat roughness profile, as shown in Figure 4.9 (i).

On the contrary, the pristine-grit-blasted-surface (PGBS) sample, as shown in Figure 4.9 (b) SEM image depicts a rough morphology with deep indentations [see circled points in Figure 4.9 (b)] without clear visibility of the individual grains and the grain boundaries. Furthermore, the 3D confocal microscope image [Figure 4.9 (f)] elaborates the depth profiles of the process-induced surface indentations and micro defects with a corresponding roughness profile, as shown with the black arrows. Finally, the roughness profile of the PGBS sample [Figure 4.9 (j)] depicts the varying degree of the indentation with different tip curvatures and indentation average depths of 6 µm.

In the pristine-abraded-surface (PABS) sample, as shown in Figure 4.9 (c) SEM images, one can see the defect line introduced through the abrasive scrubbing process as pointed with the arrows and without identifiable individual grains and grain boundaries. Additionally, the 3D confocal microscope image shows the parallel groves [see Figure 4.9 (g) arrows] and surface profile, which differs in-depth and grove width [Figure 4.9 (k) roughness profile]. The roughness profile of the PABS sample, as shown in Figure 4.9 (k), depicts a grove depth in the range of 4 µm, parallel to each other and closely distributed throughout the surface.

The pristine-abraded-grit-blasted-surface (PAB-GBS) sample, which is a combination of the abrasive scrubbing and the grit-blasting sample surface preparations, depicts a mixture of surface morphologies [see Figure 4.9 (d) circled point and red arrows]. Deep indentation and micro-defects as shown in the SEM image and the 3D confocal microscopic image [Figure 4.9(h)] can be observed. The roughness profile, which depicts the varying depth of the deep indentation in the range of 4 – 6 µm with different tip curvatures, shows a similar roughness profile to that of PGBS. However, the 3D confocal microscope image [see Figure 4.9 (h)] depicts a high density of deep indentation similar to those observed in the PGBS sample.

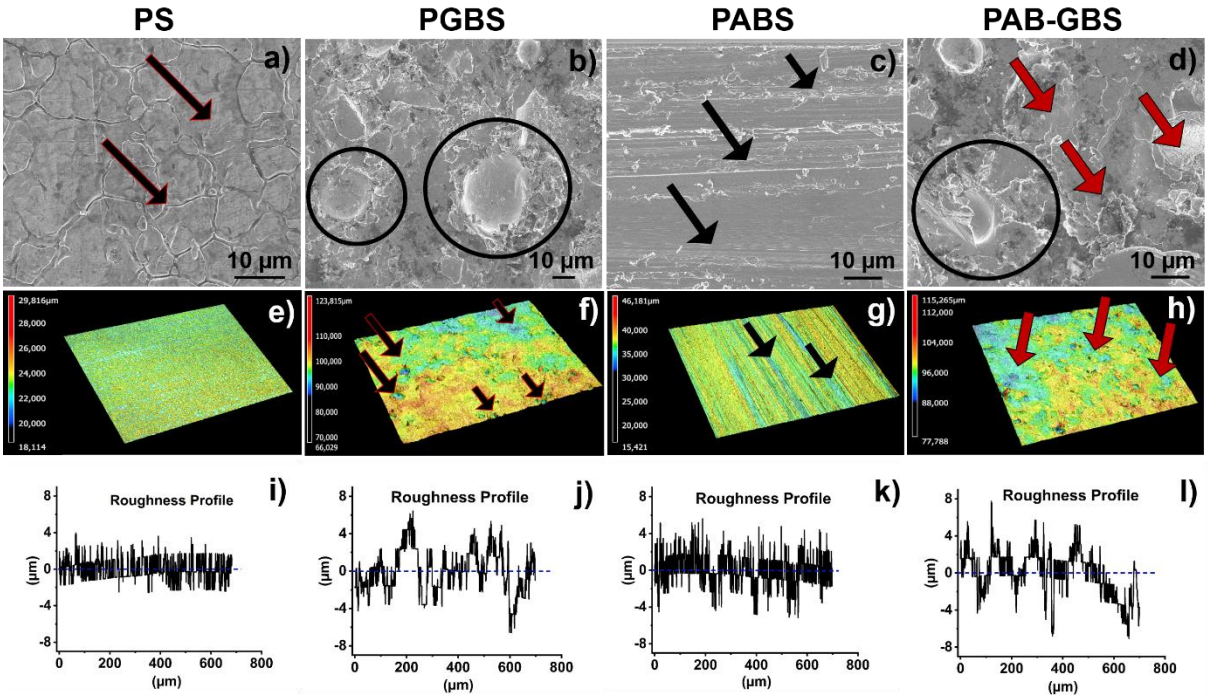

Figure 4.9: *Surface analysis of the samples' initial surface morphology using SEM and confocal microscope. This shows the surface morphology, topography, and roughness profile as follows: the PS shows a quasi-flat surface of individual grains and multiple grain boundaries [see* ***(a)*** *red arrows,* ***(e)*** *and* ***(i)****]. The PGBS shows rough surface morphology arising from the grit-blasting process [see circled points in* ***(b)****, arrows in* ***(f)****, and the roughness profile in (j)]. The PABS shows groves arising from the abrasive scrubbing process [see the black arrows in* ***(c)****, arrows in* ***(g)****, and the roughness profile in* ***(k)****]. The PAB-GBS shows mixed surface morphologies of surface groves and defect-oriented grit-blasting with different curvatures of grit impact indentations [see circled points and red arrows in* ***(d)****, arrows in* ***(h),*** *and the roughness profile in* ***(l)****].*

4.2.2 Structure nucleation and the total sculptured surface area (stainless steel strip 1)

The effect of initial surface morphology on structure nucleation in terms of density of nucleation sites, total sculptured surface area, and mass loss of the individual samples was investigated using a simple HCl-based electrolyte at room temperature with a peristaltic pump speed of 240 rpm. The electrochemical sculpturing process was performed in intervals of 3 s for a total of 30 s. Using Fiji ImageJ image analysis, the polygon area selection tool was used to map out the nucleation sites on a scanning electron microscopy (SEM) image taken at the same magnification, and the total sculptured surface area were calculated (> 2 µm^2).

The results showed that structure nucleation was dominant within 3 s to 6 s of sculpturing as seen in the rectangular mapped-out region in Figure 4.10 (a). The as-received surfaces as well as the sample surface after preparation, which signify the 0 s sculpturing time,

indicate the samples surfaces without any sculpturing activities; hence all the samples show similar starting points. In the 3 s sculpturing time, a variation in the number of nucleation sites on individual samples can be observed. The PS sample showed the highest nucleation site (81 nucleation sites / μm^2), while the PABS, PGBS, and PAB-GBS showed 47, 30, and 5 nucleation sites / μm^2 respectively. On the contrary, the PAB-GBS sample with the lowest nucleation sites had the highest total sculptured surface area of 20×10^2 μm^2 compared to PS, PABS, and PGBS, which showed the same total sculptured surface area of 10×10^2 μm^2 as depicted in Figure 4.10 (b). This can be attributed to the surface preparation processes, which result in the formation of deep groves, round, and sharp tip curvatures. These sharp tip curvatures promote rapid structure nucleation, thereby leading to a high etching rate and ultimately resulting in a large total sculptured surface area in such a short time.

When the sculpturing time is 6 s, the nucleation site density of the individual samples is rather smaller when compared with the 3 s sculpturing time, which rather showed an increase in the total sculptured surface area. For example, the PS sample showed 53 nucleation sites / μm^2, while the PABS, PGBS, and PAB-GBS samples showed 11, 10, and 2 nucleation sites / μm^2 respectively [see Figure 4.10 (a)]. Furthermore, the PAB-GBS sample showed the largest total sculptured surface area of 21×10^2 μm^2 while the PABS, PGBS, and PS samples showed a total sculptured surface area of 18×10^2 μm^2, 18×10^2 μm^2 and 15×10^2 μm^2 respectively.

As shown in Figure 4.10 (a), in 9 s sculpturing time, the nucleation sites interconnect and collapse into one another, resulting in the formation of a unitary structured surface for the PGBS, PABS, and PAB-GBS samples, while the PS sample showed 21 nucleation site / μm^2. However, the PGBS and PA-GBS samples showed a similar total sculptured surface area of 21×10^2 μm^2 at 15 s. while the PABS and PS samples showed a total sculptured surface area of 18×10^2 μm^2 and 16×10^2 μm^2 respectively.

In the subsequent sculpturing times of 12 to 21 s with the interval of 3 s apart, the number of nucleation sites for the PGBS, PABS, and PAB-GBS samples remained at unitary with near-zero slope. However, the PS sample showed a linear decrease from 18 nucleation sites / μm^2 at 12 s to 12 nucleation sites / μm^2 at 15 s respectively, and became unitary at 18 s. The PAB-GBS and PGBS samples showed a unitary total sculptured surface area of 22×10^2 μm^2, while the PABS increased from 18×10^2 μm^2 at 12 s to unitary at 15 s and remained constant thereafter. The PS increased from 17×10^2 μm^2 at 12 s and 15 s, to unitary at 18 s and remained constant thereafter.

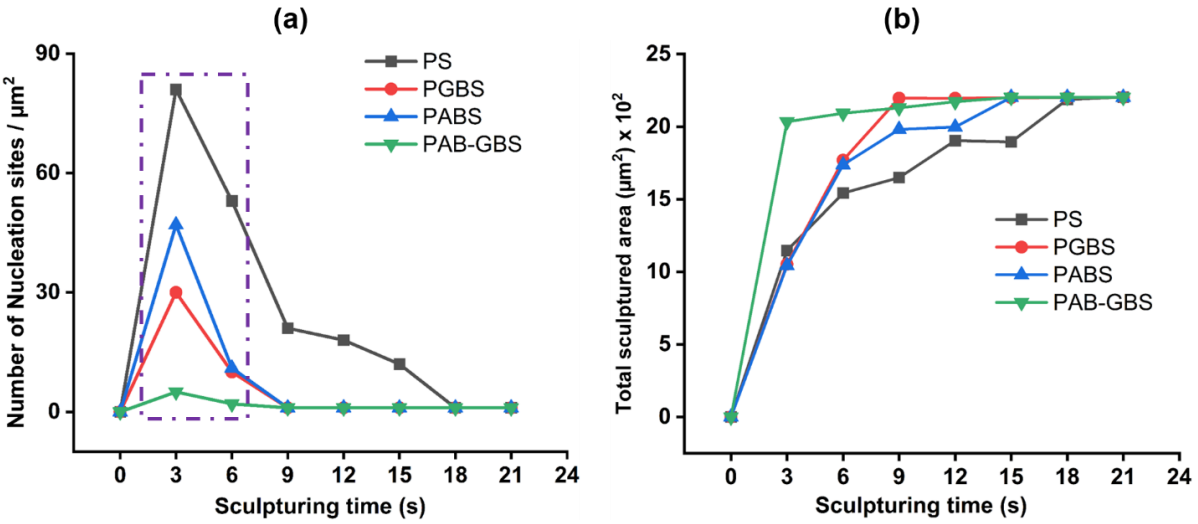

Figure 4.10: *The plots of the density of the nucleation site within the first 6 s sculpturing time as indicated with the dashed rectangular block in* ***(a)*** *and total etched surface area* ***(b)*** *of an SST strip sample.*

4.2.3 Mass loss plot (stainless steel strip 1)

The Figure 4.11 plot illustrates the mass loss of individual samples with different initial surface morphology at different sculpturing times. The circled point within the first 6 s of the sculpturing process signifies the structure nucleation regime. The individual sample surfaces showed a wide range of starting points, which translates to variations in mass loss and can be attributed to different rates of structure nucleation as influenced by the depth and tip curvatures of their initial surface morphologies.

At 3s sculpturing time, the PAB-GBS surface showed the highest mass loss of 0.006 g, while the PABS and the PGBS samples showed a similar mass loss in the range of 0.004 g, with the PS sample showing the lowest mass loss of 0.001 g. This confirms the largest total sculptured surface area of the PAB-GBS, as depicted in Figure 4.10 (b), and also suggests that the highest number of nucleation sites of the PS surface, as depicted in Figure 4.10 (a), is rather composed of a high density of tiny ($\leq 2\ \mu m^2$) nucleation sites.

When the sculpturing time is 6 s, the mass loss of individual sample surfaces showed a linear increase. The PAB-GBS sample has a mass loss of 0.008 g, while the PABS, PGBS, and PS surfaces showed a mass loss of 0.005 g, 0.006 g, and 0.004 g, respectively. This corresponds to the linear increase in total sculptured surface area as depicted in Figure 4.10 (b) at 6 s sculpturing time.

In the subsequent sculpturing times after the nucleation regime i.e., 9 s to 21 s, the mass loss of individual sample surfaces increased linearly at a similar rate. This is a hint of self-sustaining and similar growth of the structures after nucleation, irrespective of their initial

surface morphology. Furthermore, it also confirms the unitary nucleation site, the near-zero slopes in Figure 4.10 (a) and (b) after the nucleation regime.

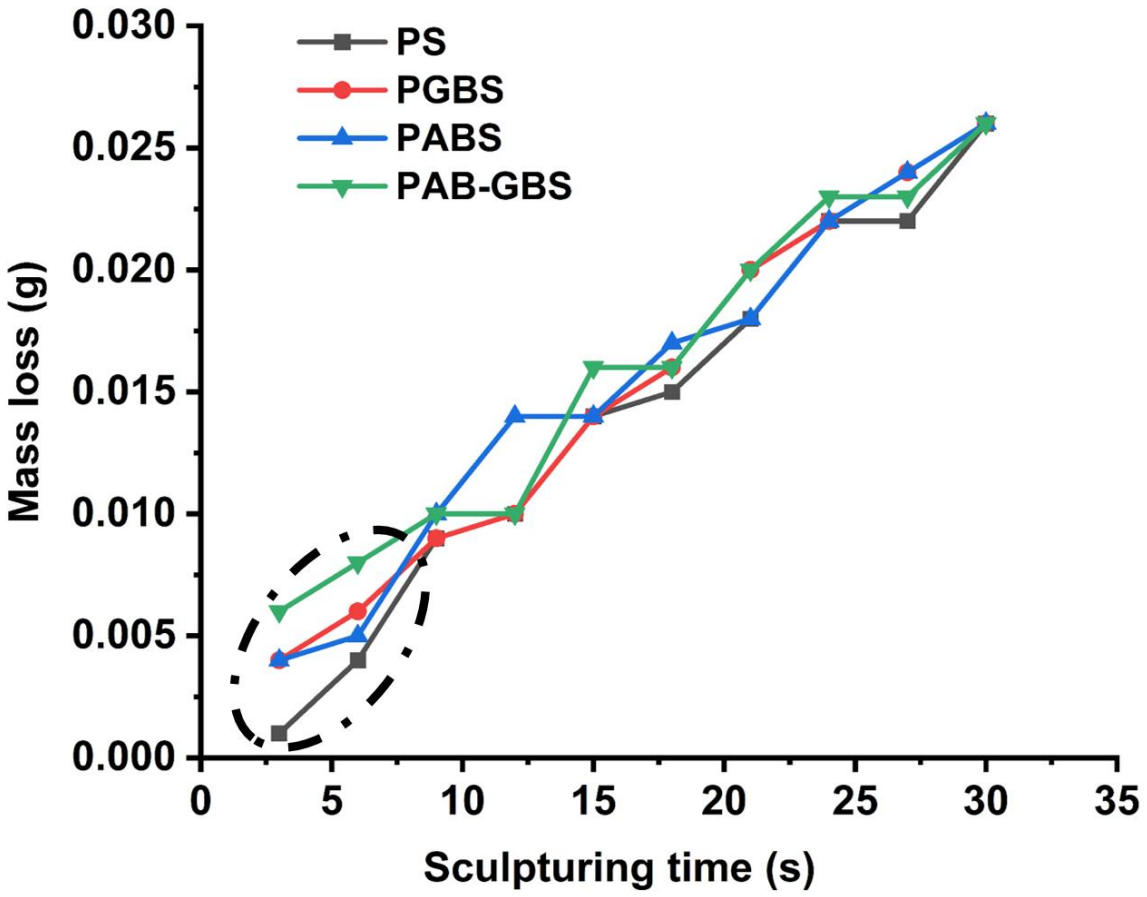

Figure 4.11: *Plot showing a mass loss of individual samples at different sculpturing times with two distinctive slopes showing the delay in nucleation time with respect to initial surface morphology and continuous mass loss after nucleation when their initial mass (after surface pre-treatments) before and after structuring are compared.*

4.2.4 Structures evolution as influenced by initial surface morphology on stainless steel strip 1 through electrochemical nanoscale sculpturing

Structures evolution on SST samples, as influenced by the initial surface morphology, was investigated through a time-controlled electrochemical nanoscale sculpturing. Sculpturing times of 3 s intervals ranging from 3 s to 30 s were used. In addition, the individual sample surfaces after sculpturing were investigated using a scanning electron microscope (SEM).

As depicted in Figure 4.12, SEM images illustrate the influence of the individual initial surface morphologies on the structure nucleation regime and the consequences thereafter. In the 3 s sculpturing time, the PS sample showed a high density of tiny structure nucleation sites [see Figure 4.12 (a)], whereas the PGBS, PABS, and PAB-GBS showed a relatively low density of rather wide nucleation sites. One can see that the structure nucleation is mostly on the deep

grit indentation with shape tip curvatures for the grit-blasted samples (PGBS and PAB-GBS surfaces) and the parallel abrasive groves with shape tip curvatures on the PAB sample [see arrows in Figure 4.12 (b), (d) and (c)] hence the broad nucleation sites. On the PS sample, the nucleation sites are randomly distributed on individual grains, which are quasi-flat; hence, tiny nucleation sites compared to surfaces with deep indentation and groves.

In the 6 s sculpturing time, as shown in Figure 4.12 (e) – (h), the nucleation site of all the surfaces grew broader. In addition, the PS sample nucleation sites grew broader within the individual grains, as shown with the arrows in Figure 4.12 (e), whereas the other sample surfaces (PGBS, PABS, and PAB-GBS) show randomly distributed sculptured surfaces and islands of unsculptured surface.

In further sculpturing times of 9 s and 12 s, the PS sample shows more broadening of the nucleation sites [see arrows in Figure 4.12 (i) and (m)], which is a result of the collapsing of the individual tiny nucleation sites into one large sculptured surface within a grain. This confirms the linear decrease of the nucleation sites with a corresponding increase in the total sculptured surface area as depicted in Figure 4.10 (a) and (b) plots. In addition, it can be observed that the grain boundaries are rather preserved but not preferentially etched. On the other hand, the other surfaces show a decrease in the surface area of the randomly distributed islands of the unsculptured surfaces, thereby interconnecting all the individual nucleation sites. This led to the unitary nucleation site of the surfaces as depicted in Figure 4.10 (a) in the 9 s and above sculpturing times. This led to a corresponding increase in the total sculptured surface area until a zero slope where the total sculptured surface area is similar irrespective of the initial surface morphology [see Figure 4.10 (b)].

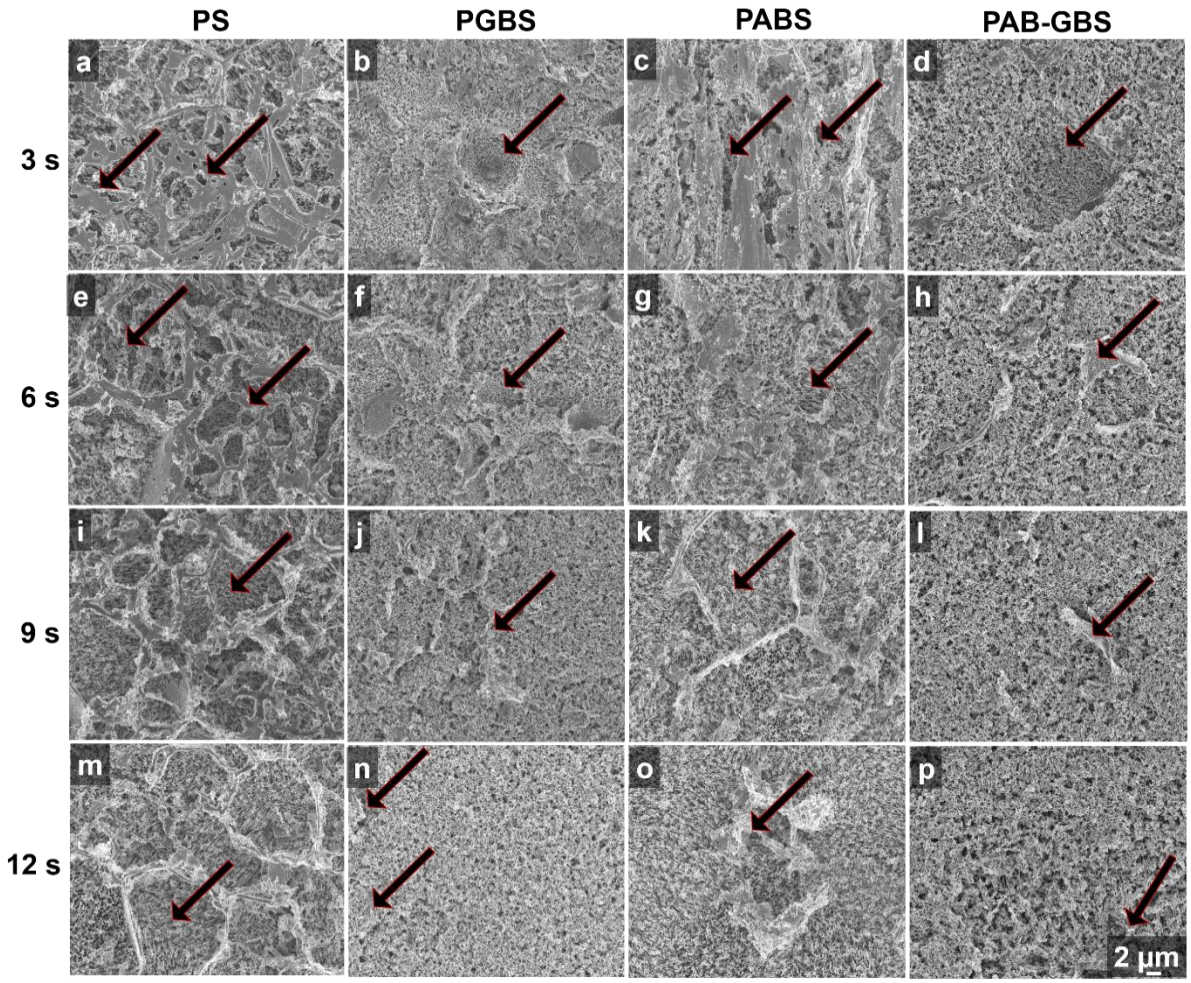

Figure 4.12**:** *SEM images of structures evolution through electrochemical nanoscale sculpturing of SST surface as influenced by the initial surface morphology. The initial surface morphology was obtained through surface pre-treatment processes such as grit blasting (PGBS), surface abrasion using abrasive paper (PABS), and surface abrasion in combination with grit blasting (PAB-GBS) on the PS.*

At 15 s sculpturing time, as depicted in Figure 4.13, the PS shows some randomly distributed islands of the unsculptured surface with some grain boundaries already interconnected, as indicated with the arrow in Figure 4.13 (a). However, the PGBS sample at this sculpturing time shows some islands of unsculptured surface, which are sporadically distributed, as depicted with arrows in Figure 4.13 (b). The PABS sample, as shown in Figure 4.13 (c) with red square dash lines, depicts a complete nanoscale sculptured surface with a wavy wall porous structure and mechanically stable interlocking features [see Figure 4.13 (c) inset]. Correspondingly, the PAB-GBS, as depicted in Figure 4.13 (d), shows a complete nanoscale sculptured surface with porous structures and mechanically stable interlocking features, which is rather spongy [see Figure 4.13 (d) inset] compared with the free-standing wavy wall porous structure of the PABS.

The PS surface at 18 s sculpturing time, as depicted in Figure 4.13 (e), shows some islands of unsculptured surface [see arrow in Figure 4.13 (e)], which is sporadically distributed with a unitary nucleation site and similar total sculptured surface area with other samples with different initial surface morphology as depicted in Figure 4.10 (a) and (b). However, the PGBS sample at this sculpturing time, as depicted in Figure 4.13 (f), shows a complete nanoscale sculptured surface with a spongy, porous structure with mechanically stable interlocking features similar to the PAB-GBS. The PABS and the PAB-GBS samples at this sculpturing time, as depicted in Figure 4.13 (g) and (h), show no identifiable difference in the completed nanoscale sculptured structures [see Figure 4.13 (g) and (h) insets] but rather an increase in mass loss as depicted in Figure 4.11 mass loss plot. This confirms the earlier hinted feature of self-sustaining and similar growth features of the structures.

At 21 s sculpturing time, the PS surface shows a complete nanoscale sculptured surface with a wavy wall porous structure with mechanically stable interlocking features as depicted in Figure 4.13 (i), which is similar to the PABS structure [see Figure 4.13 (i) inset]. In addition, the PGBS, PABS, and PAB-GBS at the 21 s sculpturing time shows an increase in mass loss as depicted in Figure 4.11 mass loss plot without any difference in the structures formed after further sculpturing time.

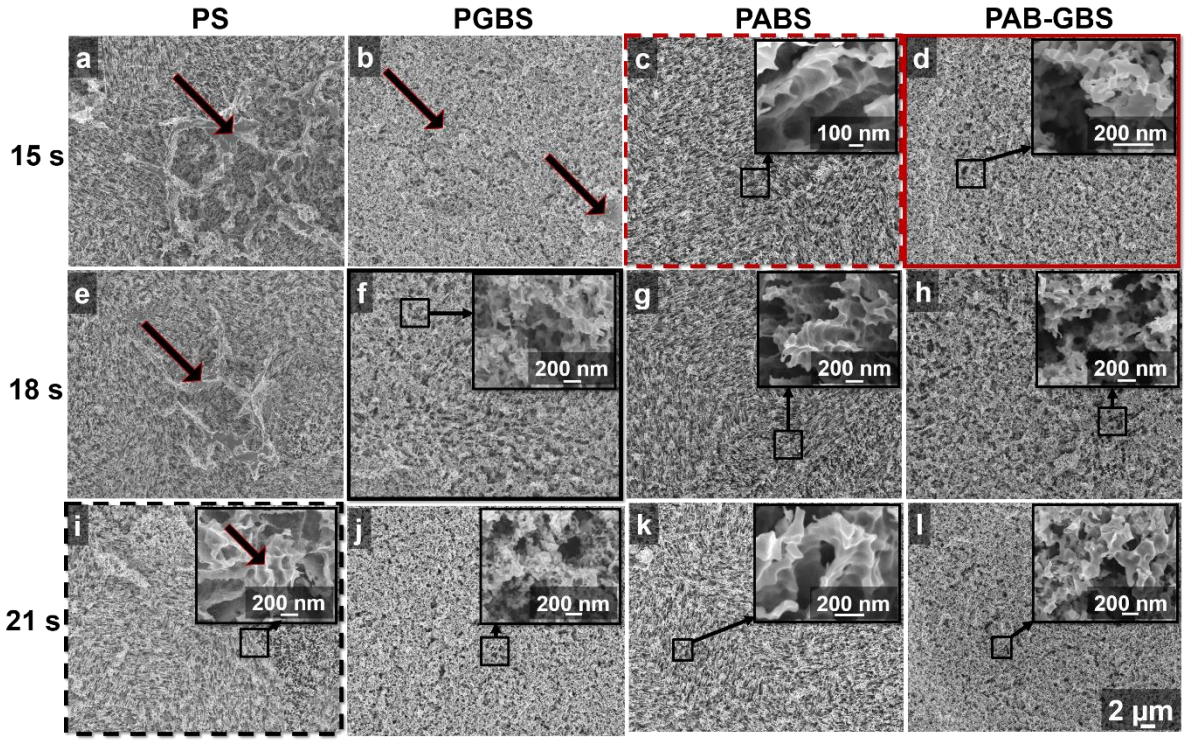

Figure 4.13: *SEM images of the structure evolution through electrochemical nanoscale sculpturing showing different sculpturing times to complete the formation of the surface structures as influenced by the initial surface morphology. The PABS and PAB-GBS at 15 s,* ***(c and d)****, PGBS at 18 s* ***(f)****, and PS at 21 s* ***(i)*** *sculpturing times respectively.*

Subsequently, at 24 s, 27 s, and 30 s sculpturing times, the completed surface structures show no identifiable differences in the formed structures irrespective of the prolonged sculpturing time after the initial sculpturing times the complete structures were formed (i.e., the PABS and PAB-GBS at 15 s, PGBS at 18 s, and PS at 21 s). However, as depicted in Figure 4.14, the individual features of the structures, as influenced by the initial surface morphology, can be seen. The PS and PABS samples show similar quasi-free standing wavy wall porous structures with mechanically stable interlocking features [see Figure 4.14 (a) and (c) insets, and the arrows in (i) and (k)] and the preserved grain boundaries as shown with the arrows in Figure 4.14 (e) and (g). In contrast, the PGBS and PAB-GBS sample structures show spongy structures with mechanically stable interlocking features. Furthermore, the spongy structures porosity of the PAB-GBS sample is rather broader when compared with the PGBS sample, as indicated with arrows in Figure 4.14 (j) and (l). This is a result of the introduced groves through the abrasive scrubbing process before the grit-blasting during sample surface preparation.

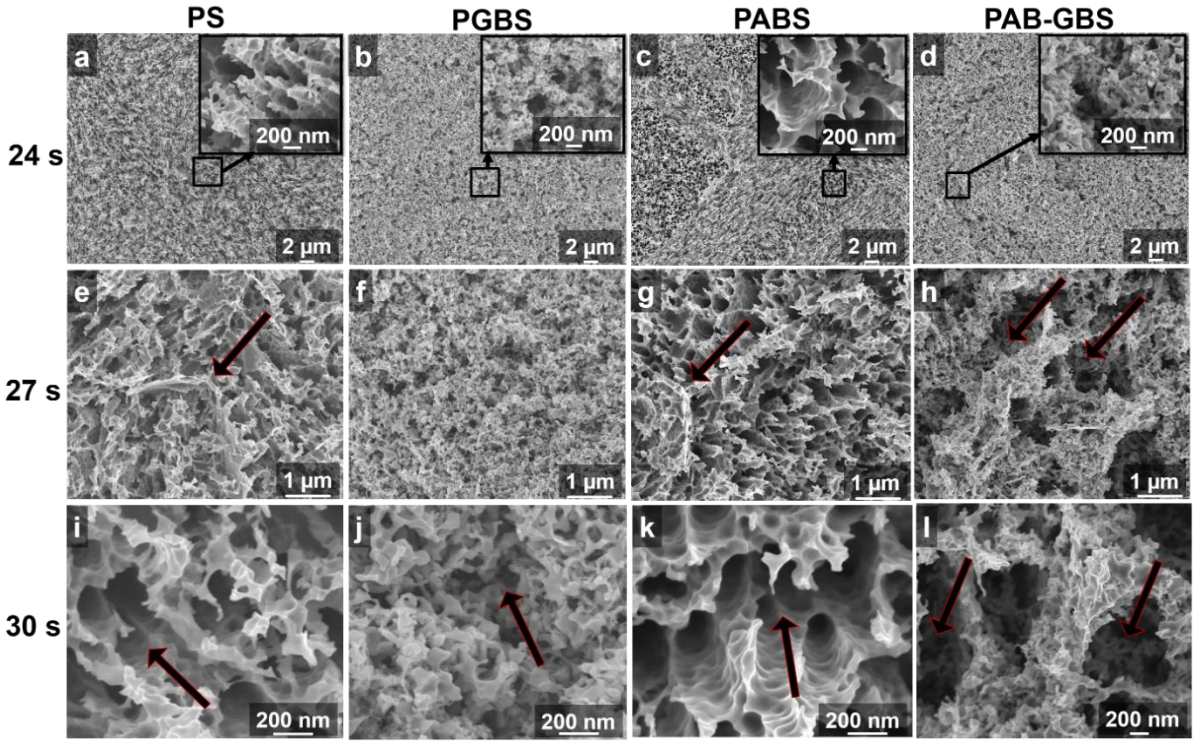

Figure 4.14: *SEM images of completely structured SST-strip at different magnifications showing different mechanical hook-like interlocking structures and spongy-like structures as influenced by initial surface morphology. The PS surface (a, e, and i) and the PABS (c, g, and k) show a preserved grain boundary porous wavy-way with mechanically stable interlocking structure [see (a) and (c) insets, and the red arrows in (e), (g), (I), and (k)]. The PGBS (b, f, and j) and the PAB-GBS (d, h, and l) show spongy-like structures [see (b) and (d) insets, and the red arrows in (h), (j), and (l)].*

4.3 Features of sculptured surface and influence of sculpturing parameter variation on stainless steel strip 2

The initial surfaces and structural features of the pristine sample, grit-blasted reference sample, and sculptured SST strip 2 were investigated. In addition, the influence of process parameter variation on the sculpturing process of the SST strip 2 surfaces through electrochemical nanoscale sculpturing is presented. This includes a systematic increase in sculpturing time and HNO_3 concentration in the 0.3 l HCl-based electrolyte, whereas other parameters are kept constant.

4.3.1 Characteristics of the pristine, reference, and sculptured surfaces of stainless steel strip 2

As depicted in Figure 4.15 (a) – (d) SEM images, the surface morphologies of the pristine SST strip 2 sample surface and the grit-blasted SST strip 2 sample surface used as reference samples were as shown. The pristine surface of the SST sample with its polished quasi-smooth surface, individual grains, and the groves at the grain boundaries are visible [see Figure 4.15 (a) and (b)]. On the other hand, the grit-blasted surfaces [Figure 4.15 (c) and (d)] show a much rougher surface; grains and grain boundaries are not visible but different sizes of randomly distributed indentations and some metal flakes, which came from the impact speed of the grit-blasting particles. The roughness profile measurements showed nearly the same average roughness (Ra) value of 0.26 µm for the pristine sample surface as well as for the nanoscale sculptured surface, whereas a significantly increased Ra value of 0.5 µm is found for the grit-blasted sample.

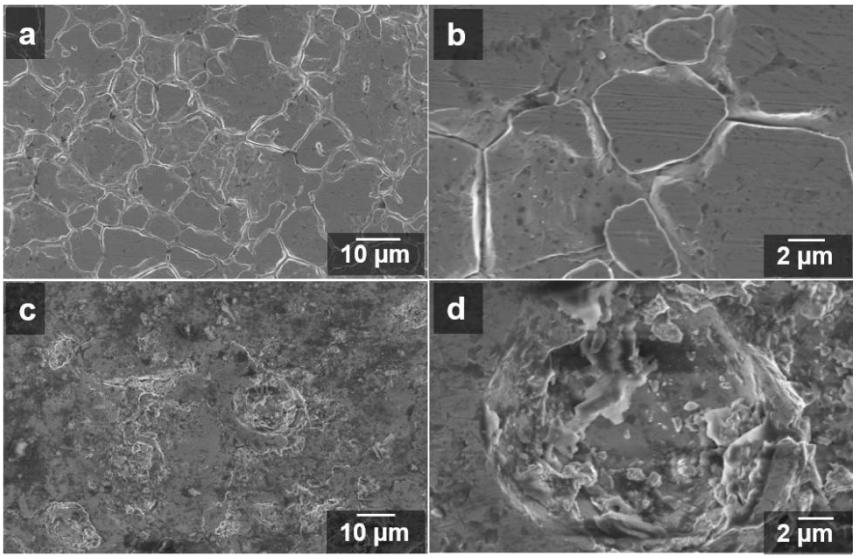

Figure 4.15: *SEM images showing the initial surface morphologies of the reference as obtained on a pristine SST sample* ***(a - b)*** *and grit blasted SST sample* ***(c - d).***

The typical structures formed on the surface of the electrochemically nanoscale sculptured SST strip 2 are depicted in Figure 4.16. In the SEM image in Figure 4.16 (a), it can be seen that the surface is homogeneously sculptured. There are no areas or islands of the original polished surface visible. At higher image magnification, as shown in Figure 4.16 (b), reveals the structure with uniform roughness, different grain orientations, and grain boundaries as indicated with the arrows [see also Figure 4.16 (c)]. The grain boundaries of the nanoscale sculptured SST sample surface were preserved and not preferentially attacked [see also Figure 4.14 (e) and (g)]. Within a grain, the structures grow parallel to each other under the same angle with respect to the surface normal. Figure 4.16 (c) depicts these structures' growth angles, which could vary from parallel to the surface normal to nearly perpendicular. Besides this, the surface structures depicted in high magnification in Figure 4.16 (d) also showed an orientation dependence with respect to the underlying grain orientation. Their openings are typically circular, with diameters ranging from 0.3 to 0.5 µm. However, they can intergrow into each other, forming non-circular openings. This intergrowth was not limited to the opening but could also occur in depth, forming an interconnected porous hook-like structure [see also Figure 4.14 (i) and (k)]. As a side effect, the remaining SST walls were rather wavy and showed many undercut features, which are significant to stable mechanical interlocking.

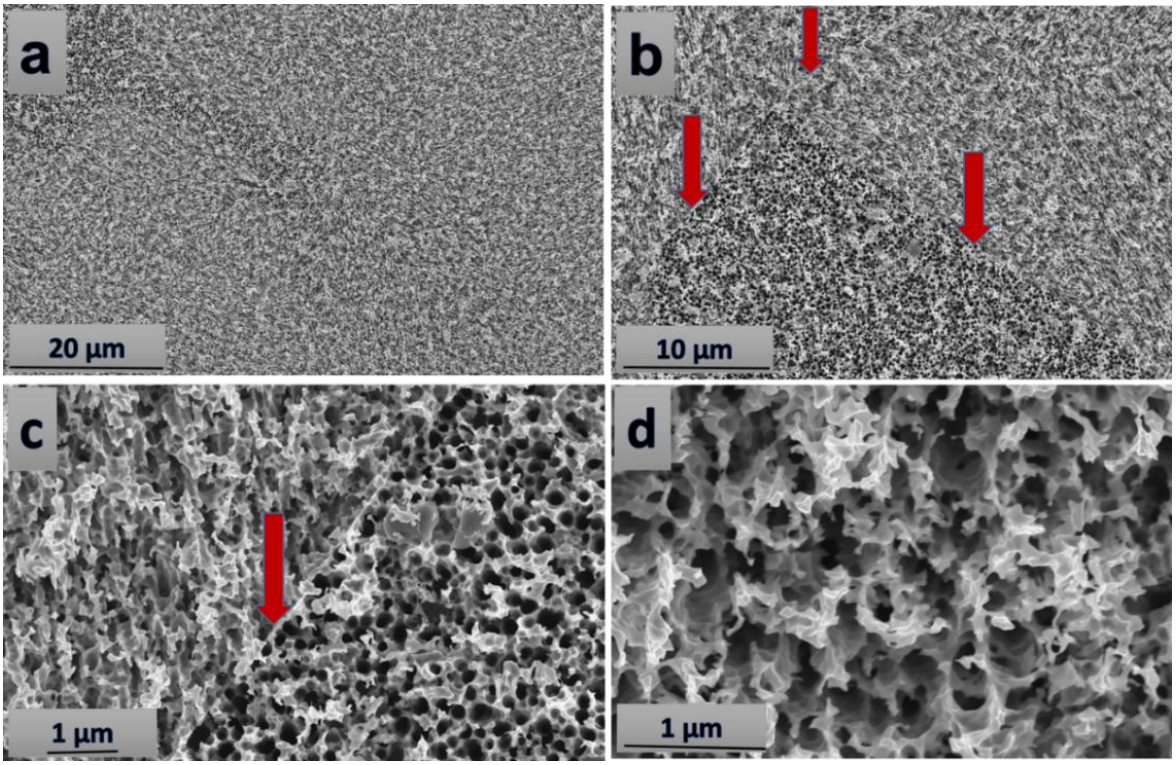

Figure 4.16: *SEM images of nanoscale sculptured SST strip 2 surfaces at increasing magnification* ***(a) – (d)****, showing the homogeneity of the sculptured surface, non-preferential grain boundaries etching, and wavy porous wall with interconnecting undercuts for stable mechanical interlocking.*

4.3.2 Influence of sculpturing time

The SEM images of the nanoscale sculptured SST strip 2 samples, as shown in Figure 4.17, depicts different electrochemical sculpturing times of 1 min, 2 min, 4 min, 8 min, 16 min, and 32 min, respectively. The SEM images show no visible variation in the nanoscale sculptured wavy porous walls and hook-like structures but a difference in thickness loss with sculpturing time, as tabulated in Table 4.1. Thickness loss is the difference between the initial thickness of the SST strip 2 sample and the final thickness of the SST strip 2 samples after a given sculpturing time. From these values in Table 4.1, the thickness loss increases arithmetically with a corresponding increase in sculpturing time, which can be said to suggest similar structural depth per time.

Table 4.1**:** *SST sample thickness loss with respect to sculpturing time.*

Etching time (min)	1	2	4	8	16	32
Thickness loss (mm)	0.06	0.07	0.13	0.22	0.39	0.81

Correspondingly, the SEM images in Figure 4.17 show that the nanoscale sculptured surface structures are self-sustaining and grow self-similar into depth on the SST surface without an increase in the structure depth. In addition, it also indicates that the initial already structured surface condition of the SST has no effect on the obtained structures by the nanoscale sculpturing process. Conclusively, these results convincingly show that a further increase in sculpturing time leads to no visible changes in the nanoscale sculptured structures (cf. Figure 4.17) but an increase in thickness loss, which is a hint that the maximum structural depth has been reached.

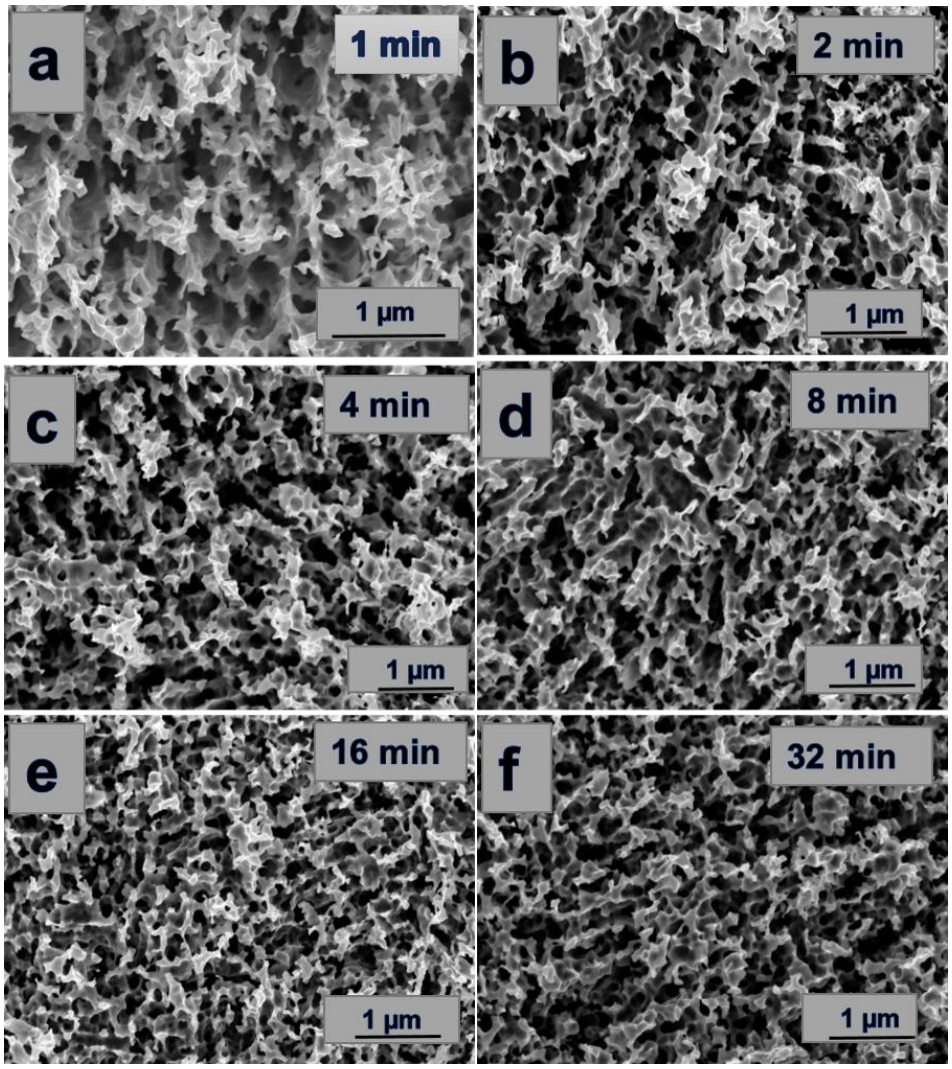

***Figure 4. 17*: *SEM images of a nanoscale sculptured SST strip 2 sample surface with respect to different sculpturing times and thickness loss*.**

4.3.3 Influence of HNO_3 concentration

In the concept of nanoscale sculpturing, the changes in the electrolyte composition have a direct effect on the resulting surface structures. Figure 4.18 shows the SEM images of the structured SST strip 2 sample surfaces after structuring with increasing content of HNO_3 while keeping the other parameters constant as shown in Figure 4.18 (a) – (f). The resulting structures of the nanoscale sculptured SST strip 2 sample surfaces showed sensitivity to variations of the HNO_3 concentration in the constant 0.3 l HCl-based structuring aqueous electrolyte.

From the results obtained, one can observe several trends. At low HNO_3 concentration in the electrolyte, the resulting surface structure shows a typical structure dimension in the nanometer range, as depicted in Figure 4.18 (a). With increasing concentration of HNO_3 in the electrolyte, the structure size increases, and the circular porous structure with undercuts become more visible. At 0.63 mol HNO_3 concentration, as shown in Figure 4.18 (d), a typical

electrochemically nanoscale sculptured structure on the SST surface is formed with its characteristics [see Figure 4.18 (d) inset].

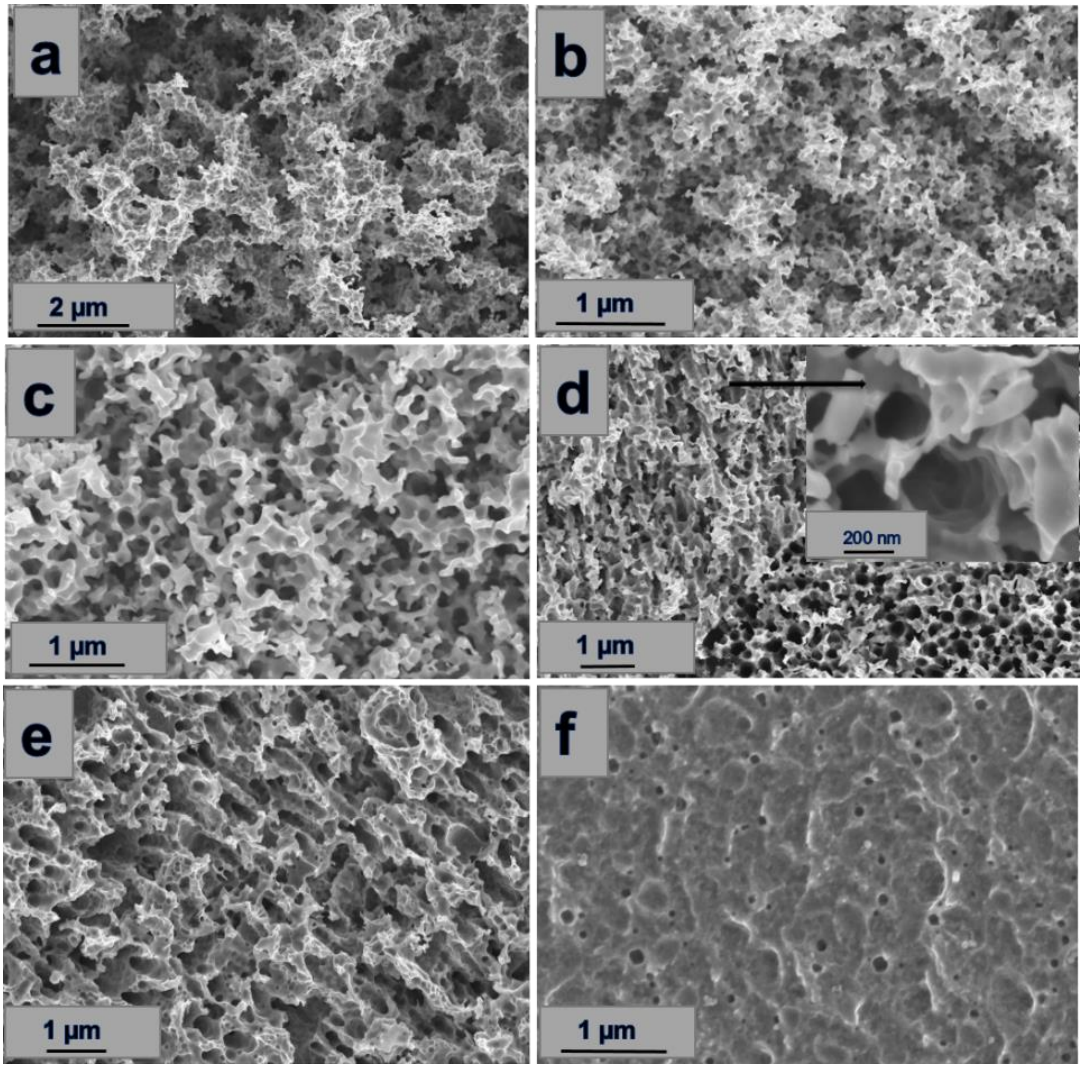

Figure 4.18: *Changes in SST strip 2 surface morphology result from increasing HNO_3 concentration in 0.3 l HCl-based aqueous electrolyte at constant current density, electrolyte flow rate, temperature, and sculpturing time.* ***(a)*** *0.16 mol HNO_3,* ***(b)*** *0.40 mol HNO_3,* ***(c)*** *0.50 mol HNO_3,* ***(d)*** *0.63 mol HNO_3,* ***(e)*** *0.80 mol HNO_3, and* ***(f)*** *0.95 mol HNO_3.*

However, as soon as the HNO_3 concentration exceeds a critical value, i.e., 0.63 mol HNO_3 / 0.3 l of HCl-based electrolyte, a gradual isotropic etching (electropolishing) of the hook-like arms / top structures can be seen as shown in Figure 4.17 (e). When the HNO_3 concentration in the electrolyte was increased to 0.95 mol HNO_3 / 0.3 l seawater-like electrolyte, Figure 4.17 (f) shows a clearer view of the isotropic etching as the quasi-free-standing hook-like arms are no longer visible rather some randomly distributed tiny pits.

4.3.4 Chemical and mechanical properties of sculptured stainless steel strip 2

Surface wettability

The influence of surface sculpturing on the surface wetting behavior of the SST strip 2 samples is investigated by contact angle measurements using the sessile-drop technique. Figure 4.19 (a) – (c) depicts the characteristic water droplet images on the investigated surfaces for the SST strip 2 PS sample, grit-blasted surface, and nanoscale sculptured surface, respectively. The as-received SST PS sample surface with a polished surface [see Figure 4.15 (a) and (b)] showed a contact angle of 95° ± 2.72° while the reference grit-blasted SST sample surface [see Figure 4.19 (b)] showed a contact angle of 70° ± 1.91°. In addition, the freshly nanoscale sculptured SST sample surface, as shown in a photographic image [see Figure 4.19 (c)], exhibits a super-hydrophilic behavior, in which the droplet completely spreads over the sculptured surface.

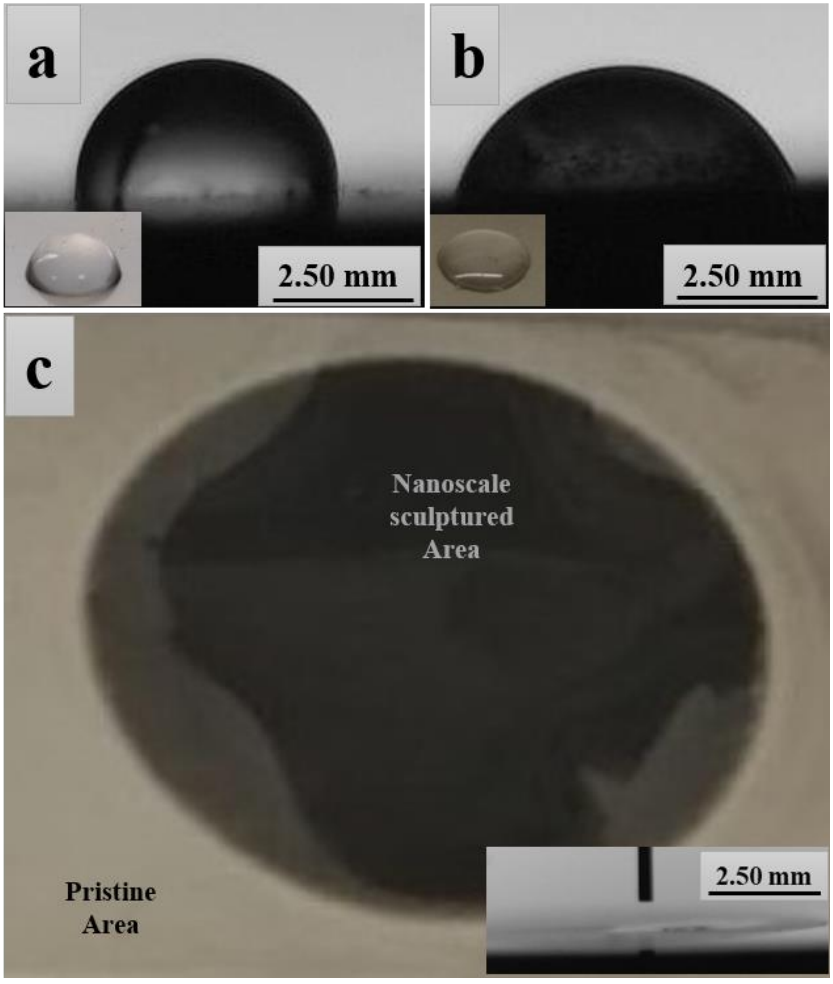

Figure 4.19: *Images of water droplets formed on SST strip 2:* ***(a)*** *PS sample surface,* ***(b)*** *grit blasted reference surface, and* ***(c)*** *freshly sculptured sample surface.*

Elemental analysis of stainless steel strip

The elemental surface composition of the sculptured SST strip 2 has been investigated by EDX analysis. The SEM images of the investigated surface area and the corresponding Fe, Cr, Ni, and O elemental maps are illustrated in Figure 4.20 both for the unsculptured (PS) and sculptured surfaces.

On the unsculptured surface, the signal intensity in the maps seems very homogeneously distributed and exhibits no morphology dependence over the investigated area, as shown in the Fe, Cr, and Ni signal maps. However, the O signal reproduced the topography of the individual grains and grain boundaries. On the contrary, the sculptured surface exhibited morphology dependency mainly on the signals of the alloying elements (Cr and Ni). Here, the signal intensity of the Fe seems homogeneously distributed over the investigated area, whereas the signal intensity of Cr and Ni (mostly) instead shows some dependency on the sculptured structured surface. Furthermore, one can see that the depleted intensity regions coincide with the porous structures on the sculptured surface, while the signal intensity increases at the walls of the porous structure. This indicates a selective de-alloying process, particularly with respect to Ni.

Generally, the intensity of the O signal on the surfaces of the SST samples is significantly influenced by the morphology of the sculptured structures. Specifically, the intensity of the O signal is observed to increase at the walls of the structures and decrease within the pores. The source of this O signal can be attributed to the passive oxide layer formed during the sculpturing process and the native oxide layer that forms on the surface upon exposure to air following the sculpturing process. Notably, the oxide layer (Cr_2O_3) cannot be detected by EDX.

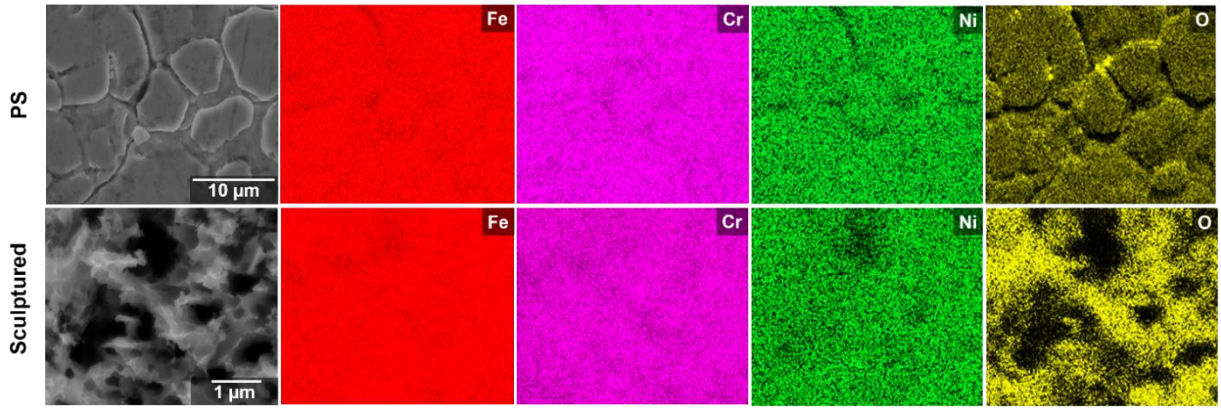

Figure 4.20: *EDX elemental surface composition analysis of stainless steel strip.*

Tensile testing of stainless steel-polymer-stainless steel sandwich structure

Figure 4.21 depicts the results of the single-lap shear tests of the SST-polymer-SST sandwich composites for three different polymer classes: polythiourethane (PTU), acrylates, and 2-epoxy resins.

It was found that the ultimate shear strengths of the nanoscale sculptured SST-polymer-SST sandwich composites are generally higher than the ones of the grit-blasted reference SST-polymer-SST sandwich composites. Looking at the SST-acrylate-SST sandwich composites, the grit-blasted reference failed adhesively at a mean ultimate shear strength (USS) of about 18.4 ± 3.0 MPa, while the nanoscale sculptured ones failed cohesively at about 33.2 ± 1.2 MPa. This increased by almost a factor of two compared to the grit-blasted reference. The SST-epoxy resin-SST sandwich composites showed the same behavior as found for the acrylate-based ones. The grit-blasted reference composites also exhibit an adhesive failure at a USS of about 13.8 ± 0.7 MPa for epoxy resin 1, resp. 19.2 ± 1.2 MPa for epoxy resin 2. The nanoscale sculptured ones failed cohesively at 32.7 ± 4.3 MPa for epoxy resin 1 and 39.7 ± 2.3 MPa for epoxy resin 2. This means that nanoscale sculpturing could double the USS for SST-polymer composites. This effect was even more pronounced for the PTU sandwich composites. The grit-blasted SST-PTU-SST sandwich composites failed adhesively at about 5.1 ± 1.5 MPa, while the nanoscale sculptured ones failed cohesively at about 35.5 ± 1.2 MPa.

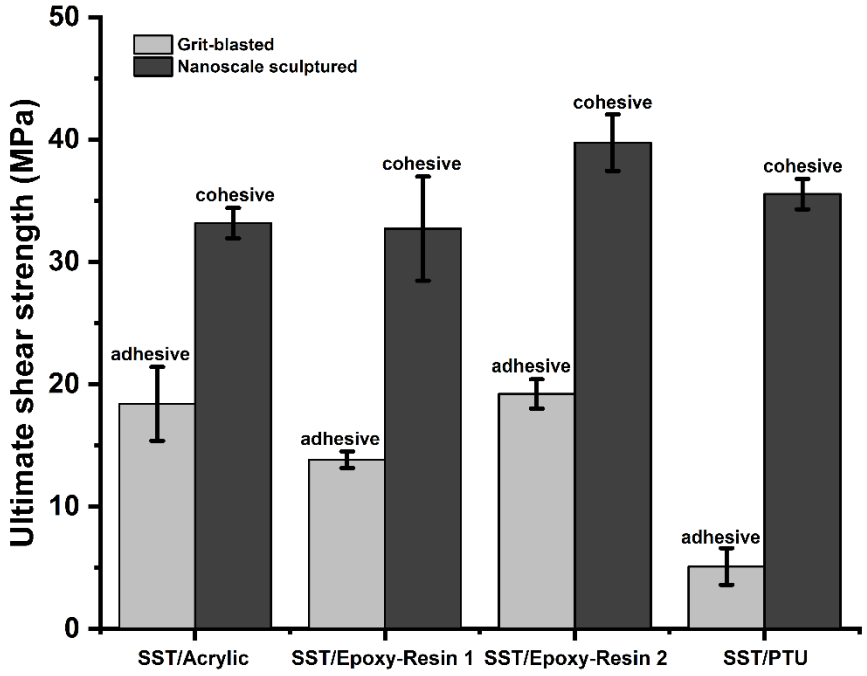

Figure 4.21: *Bar chart of ultimate shear strength for the investigated SST-polymer-SST sandwich composites showing varying adhesive and cohesive ultimate shear strength at failure after using 2-component polymer classes such as acrylate, epoxy resins, and PTU in the sandwich composite.*

Fracture surfaces of the stainless steel-PTU-stainless steel composites

In Figure 4.22, the fracture surfaces of a grit-blasted SST-PTU-SST [Figure 4.32(a)] and a nanoscale sculptured SST-PTU-SST [Figure 4.22(b)] sample are depicted. One can see the adhesive failure, which leads to almost complete delamination of the PTU from the grit-blasted SST sample surface, as shown in Figure 4.22 (a). The high magnification image of the failure surface [see Figure 4.22 (c) squared area] shows that only minor PTU residues can be identified on the surface. These are around the sharp edges of the grit-blasted surface and some sharp-edged ones where the blasting particles were most probably implanted during the grit-blasting process.

The fracture surface of the nanoscale sculptured SST-PTU-SST sandwich composite image, as depicted in Figure 4.22 (b), reveals a complete coverage with PTU on the entire nanoscale sculptured surface (see circular dark area) on both surfaces. This is an apparent characteristic of a cohesive failure. The polished outer pristine parts of the nanoscale sculptured circular area exhibited adhesive failure by complete delamination, as seen in both parts of the images in Figure 4.22 (b). Additionally, the high white contrast in this image is due to a charging-up effect of the PTU fracture under the electron beam and does not correspond to the nanoscale sculptured SST surface structure depicted in Figure 4.16.

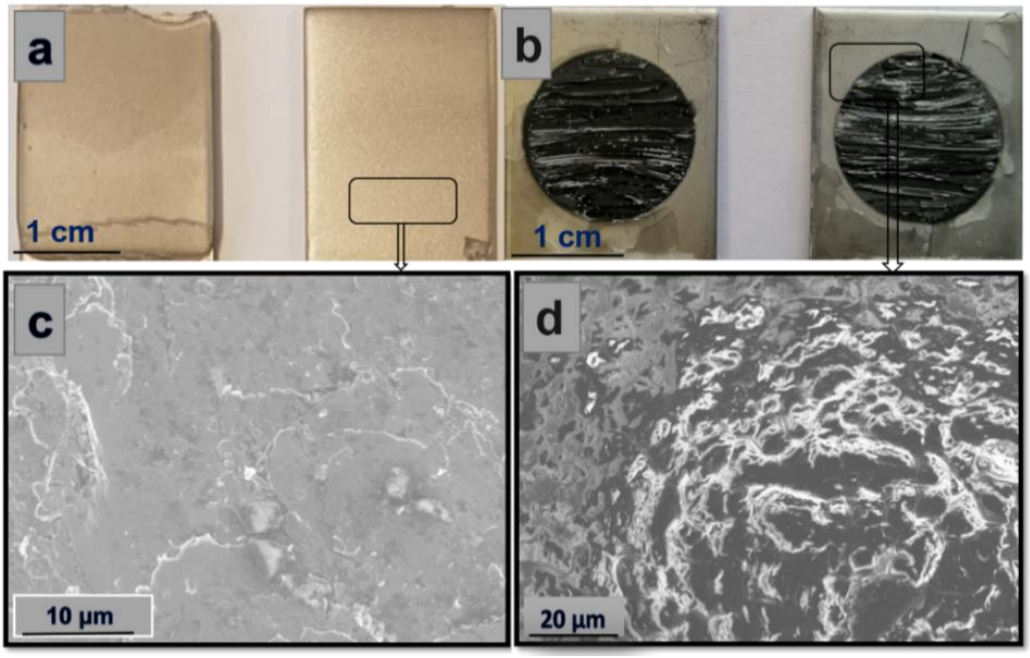

Figure 4.22: *Failure surfaces of the SST-PTU-SST sandwich composite:* ***(a)*** *photograph of both grit-blasted SST-PTU-SST sandwich structure components after failure,* ***(b)*** *photograph of both nanoscale-sculptured SST-PTU-SST sandwich structure components after failure,* ***(c)*** *SEM top view (square area) of the grit blasted SST failure surface (right side with complete delamination), and* ***(d)*** *SEM top view (square area) of the nanoscale sculptured SST failure surface (right-side with cohesive failure surface).*

4.6.3 Cross-sectional view of sculptured stainless steel-polymer interface (stainless steel strip 2)

The cross-sectional light microscope and SEM images of the grit-blasted, nanoscale sculptured surfaces and EDX images of a nanoscale sculptured surface are depicted in Figure 4.23. In the light microscope image of Figure 4.23 (a) and (b), the SST-adhesion-polymer interface profile of both the grit-blasted and nanoscale sculptured surfaces is shown. One can see the grit-blasting impact indentation with an estimated average structure depth of 10 µm, and the nanoscale sculptured interconnected undercut structures filled with a polymer with an estimated average structure depth of 15 µm.

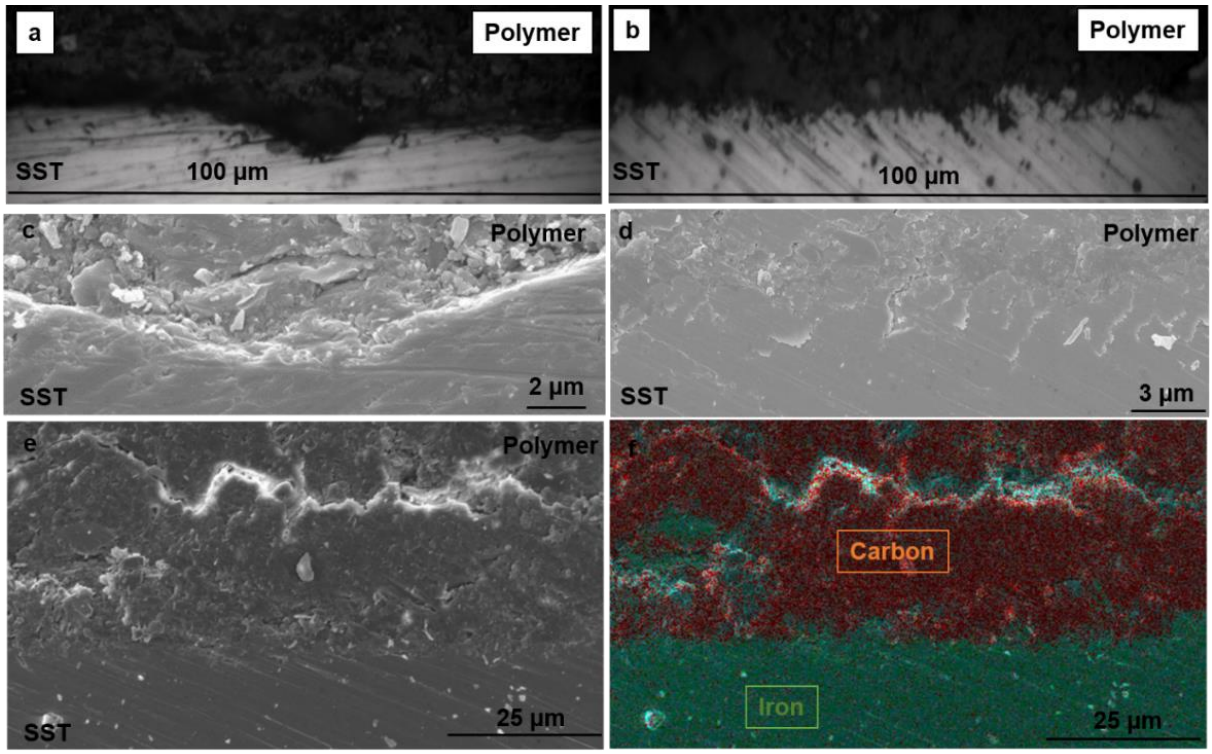

Figure 4.23: *The cross-sectional view images of a light microscope, SEM, and EDX showing the SST-adhesion-polymer interfaces of nanoscale sculptured SST sample and grit-blasted SST sample surfaces.*

Figure 4.23 (c) and (d) further illustrate the complete filling of polymers in both structures and the filling profile of polymer in the grit-blasted surface [see Figure 4.21 (b)] when compared to the view normal to the surface in Figure 4.23 (b) and (d). The EDX image of the nanoscale sculptured surface [see Figure 4.23 (f)] once again confirmed the in-depth penetration of the polymers (apparent from the presence of carbon in the EDX map, i.e., the dark areas) in the interconnected undercuts by different SST (iron in the EDX map, i.e., the light grey areas) islands as clearly shown by the coloured mapping. The light charging area is a hint of metal oxide, which relatively will have mechanical instability, but the SST Island

enveloped with polymer (the randomly distributed light grey areas in the dark carbon matrix area) confirmed the mechanical interlocking. This enveloped SST island is the reason for the high USS and cohesive failure [see Figure 4.22 (b) and (d)] of the nanoscale sculptured surfaces when compared with the grit-blasted surfaces, which have a weak chemical bond SST-adhesion-polymer interface as a result of the absence of interconnected undercuts and mechanical interlocking structures. Hence the adhesive failure and delamination of the polymer [see Figure 4.22 (a) and (c)].

4.4 Surface pre-treatment of stainless steel wire through electrochemical nanoscale sculpturing

This section presents the surface pre-treatment of SST wire through electrochemical nanoscale sculpturing. The pre-treatment was carried out using a constant and pulsing current approach and an HCl-based electrolyte. In addition, the influence of electrolyte concentration, sculpturing time, current density, and pulsing times was investigated.

The SEM images of the pristine (PS) SST wire are depicted in Figure 4.24. It can be seen that the surface is not smooth but instead contains some defect lines (see arrows in Figure 4.24) and embedded particles, as shown in the magnified SEM image of Figure 4.24. These defect lines and embedded particles may result from the manufacturing process as the wires are produced by cold drawing.

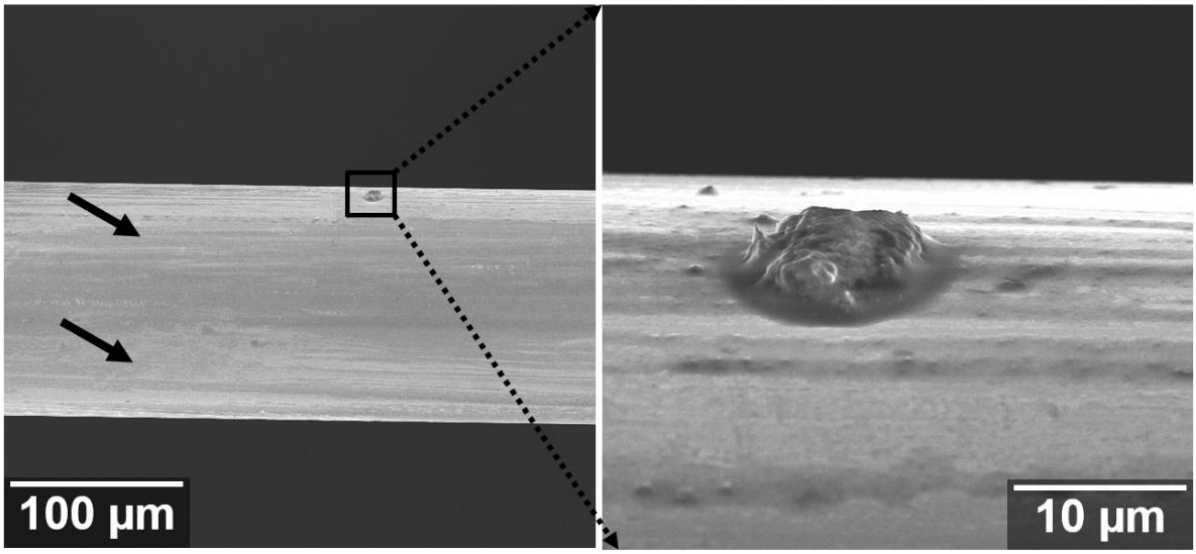

Figure 4.24: *The SEM image of untreated SST wire showing the manufacturing process-oriented defect lines and embedded particles.*

4.4.1 Constant current application

Influence of electrolyte concentration and sculpturing time

Figure 4.25 SEM images show the surface structures on the SST wire, as influenced by electrolyte concentration and sculpturing time variation. There are two distinctive surface morphologies between the low-concentration electrolytes (0.03 M and 0.25 M) and the high-concentration electrolytes (1 M and 1.6 M) at the application of 2 A (4 A/cm^2) constant current. The low-concentration electrolytes irrespective of the sculpturing time shows non-preferential etching on the manufacturing process-oriented defect lines.

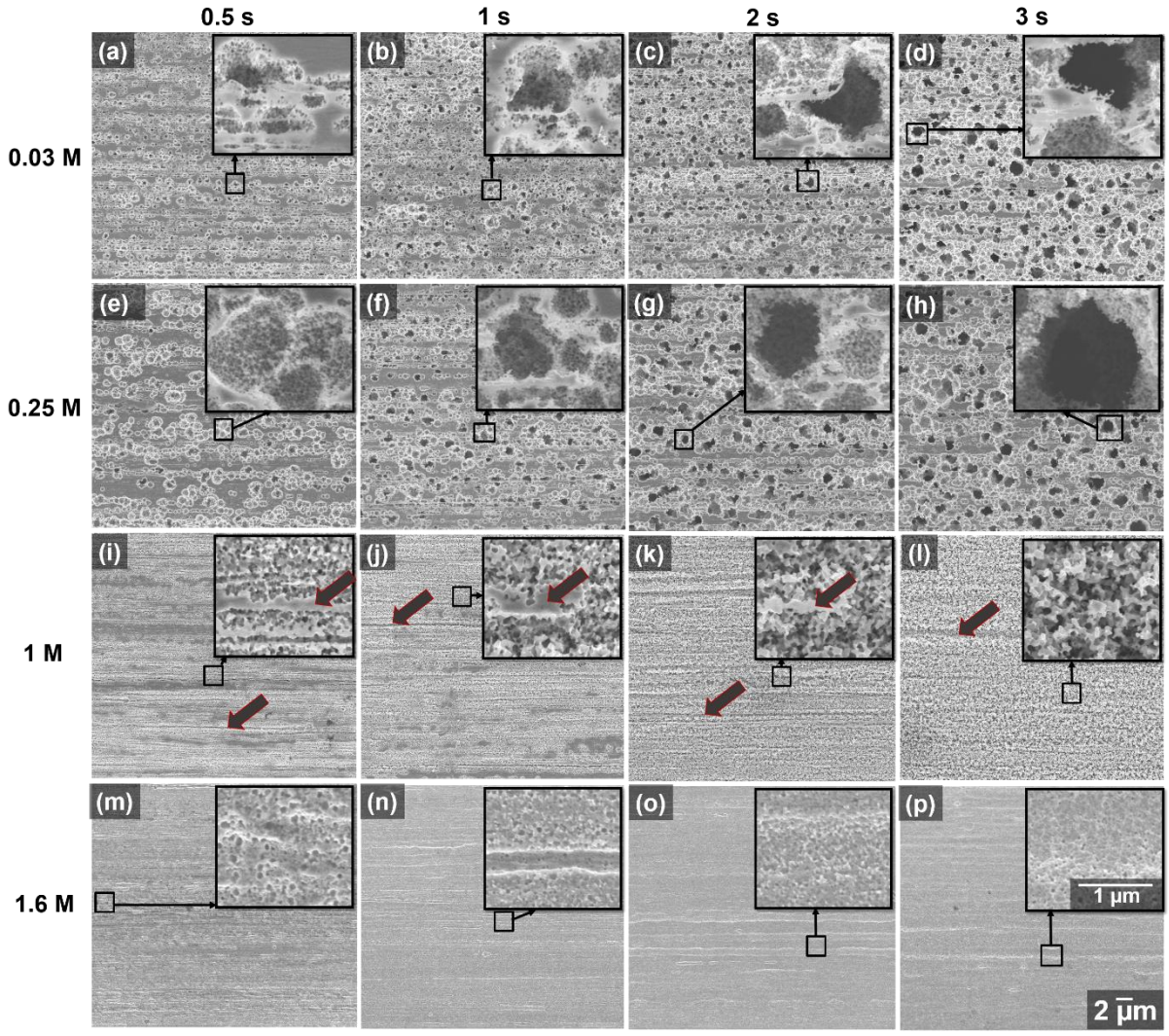

***Figure 4.25*: *SEM images of different structures formed as influenced by electrolyte concentration and sculpturing time*.**

In contrast, the high-concentration electrolytes lead to spongy-pits structures, which increase in density as islands of unsculptured surface diminish with increasing sculpturing time. [see arrows in the insets of Figure 4.25 (i) – (k) of 1 M]. In addition, the spongy-pits structures

show some preferential etching along the manufacturing process-oriented defect lines, as shown with arrows in Figure 4.25 (i) – (l). At 1.6 M electrolyte concentration, an isotropic etching phenomenon (electropolishing) tends to occur. The formed pit structures, which possess rather low depth, diminish in size and density as the sculpturing time increases [see Figure 4.25 (m) – (p) and the insets].

From the above results, further investigation and analysis on the pre-treated SST wire were carried out using the 0.25 M electrolyte concentration at 2 A (4 A/cm^2) current application. This is because the 0.25 M electrolyte led to a high density of shallow and broad bowl-like structures, which increased laterally and in-depth with increasing sculpturing time and bowl-in-bowl structure formation. These characteristics are suitable for the intense pre-treatment of the SST wire (surface cleaning), easy removal of the embedded particles, and enhanced surface adhesion while preserving the intrinsic mechanical property.

As depicted in Figure 4.26, the diameter of the pre-treated SST wires at different sculpturing times of 0.5 s, 1 s, 2 s, and 3 s was measured using a digital micrometer gauge with flat circular contact points of 20 mm^2 surface area. As shown in Figure 4.26 plot, the PS sample with an average wire diameter of 152.4 ± 1.3 µm shows a large overshoot in the error bars. This results from the sporadically distributed embedded die particles on the surface of the wire (see Figure 4.24) during the cold drawing process. Correspondingly, the sculpturing times of 0.5 s, 1 s, 2 s, and 3 s, as depicted in Figure 4.26 plot showed an average pre-treated wire diameter of 150.7 ± 0.5 µm, 150.6 ± 0.5 µm, 150.6 ± 0.5 µm, and 150.4 ± 0.5 µm respectively. This shows a significant statistical difference in the diameter of the pre-treated SST wires compared to the PS wire. However, the seeming change in the pre-treated SST wire diameter (in the range of 1 µm) can be attributed to the etching of the native oxide layer and the removal of the embedded particles as shown in Figure 4.24. This is because the used digital micrometer gauge possibly contacted a large number of islands of unsculptured surfaces. Therefore, the localized bowl-like structure depth has no significant effect on the pre-treated SST wire diameter measurements.

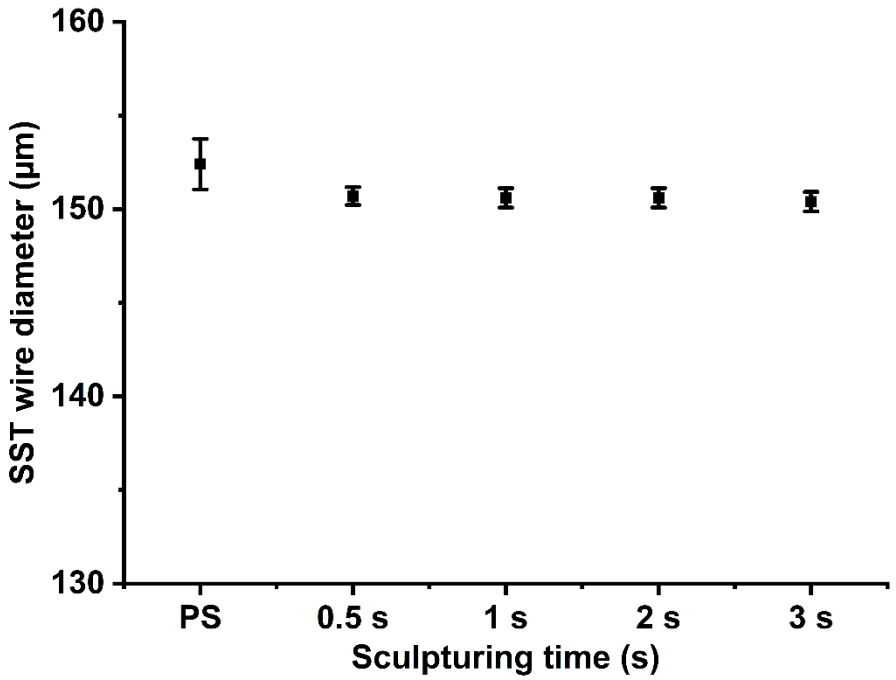

Figure 4.26**:** *The corresponding diameter of the pre-treated SST wire using 0.25 M at constant 2 A (4 A/cm2) and varying sculpturing time. For statistical analysis of the mean values of the diameter, a one-way ANOVA followed by a Tukey test was performed. The PS showed a statistically significant difference ($p < 0.05$) compared to the diameters obtained using the constant current approach at 0.5 s, 1 s, 2 s, and 3 s, respectively.*

The characteristic features of the bowl-like structures, as depicted in Figure 4.27, show variations in the structure's density, diameter, and depth, whereas the aspect ratio is quasi-constant as the sculpturing time increases. In Figure 4.27 (a) plot, one can see a linear decrease of the bowl-like structure density from the 0.5 s to 3 s sculpturing times. The 0.5 s show the highest bowl-like structure density of 3095 bowls / µm^2, whereas the 1 s, 2 s, and 3 s sculpturing times are in decreasing order with bowl-like structure density of 2408 bowls / µm^2, 1845 bowls / µm^2, and 1431 bowls / µm^2 respectively.

The bowl-like structure aspect ratio, as depicted in Figure 4.27 (b) plot, shows relatively similar values irrespective of the sculpturing time. From this plot, one can say that the rate of bowl-like structure broadening per sculpturing time is relatively constant, leading to an average aspect ratio of 1.18 ± 0.1 for the 0.5 s. 1.16 ± 0.2 for the 1 s, 1.16 ± 0.2 for the 2 s, and 1.11 ± 0.1 for the 3 s sculpturing time, respectively.

As depicted in Figure 4.27 (c) and (d) plots, there is a linear increase in bowl-like structure diameter and depth as the sculpturing time increases [also see Figure 4.25 (e) to (h) insets]. Here, the measured average bowl-like structure diameter of the 0.5 s sculpturing time is 1.11 ± 0.1 µm with a corresponding average depth of 2.46 ± 0.5 µm, whereas the 1 s sculpturing time has a bowl-like structure average diameter and depth of 1.26 ± 0.5 µm and

2.95 ± 0.4 µm respectively. In the subsequent sculpturing times, the 2 s shows an average bowl-like structure diameter of 1.71 ± 0.1 µm and an average depth of 3.94 ± 0.4 µm, whereas the 3 s with an average bowl-like structure diameter of 1.95 ± 0.3 µm and an average depth of 5.54 ± 0.5 µm respectively.

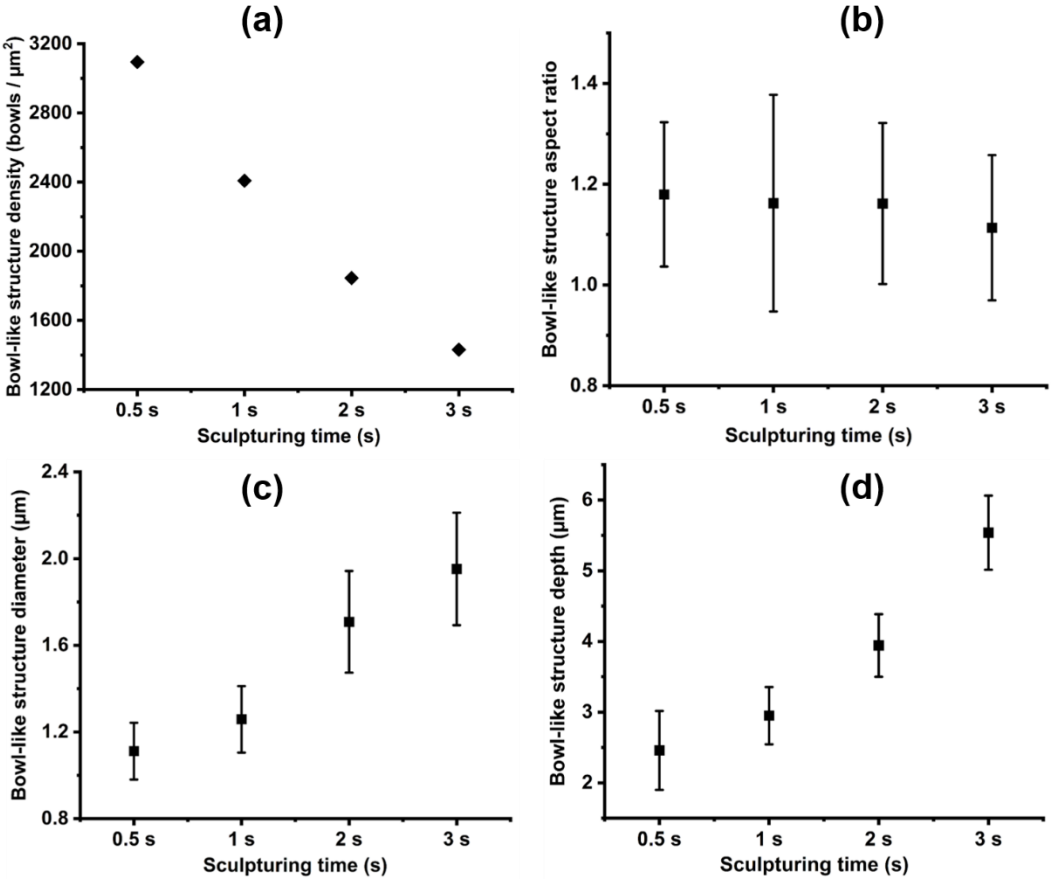

Figure 4.27**:** *The characteristics features of the bowl-like structure obtained using 0.25 M at constant 2 A (4 A/cm2) current application showing:* ***(a)*** *a linear decrease in bowl-like structure density,* ***(b)*** *quasi-constant aspect ratio,* ***(c)*** *linear increase in bowl-like structure diameter, and* ***(d)*** *linear increase in bowl-like structure depth with increasing sculpturing time respectively.*

Influence of applied current density

The variation of applied current density, i.e., varying the applied constant current of 0.5 A, 1 A, 2 A, and 3 A, respectively, for 0.5 s sculpturing time using the 0.25 M electrolyte led to an increase in bowl-like structure density with a corresponding overlapping of bowl-like structures as shown in Figure 4.28 (a) – (d). This can be understood as increased etching species' kinetic energy and mobility.

At 0.5 A, one can see sparingly distributed bowl-like structures, whose average diameter is 0.5 µm and covers less than 30 % of the total sculptured surface area, as shown in Figure 4.28 (a). In addition, the bowl-like structure is interconnected and shows preferential etching

along the manufacturing process-oriented defect line, as shown in Figure 4.28 (a) magnified SEM image.

In Figure 4.28 (b), the applied constant current of 1 A shows an increase in bowl-structures density when compared with the 0.5 A structure density. The bowl-like structures are not preferentially formed along the manufacturing process-oriented defect line but rather randomly distributed, forming more independent bowl-like structures. The total structure surface area coverage is in the range of 50 %, while the bowl-like structure diameter is in the average of 0.7 µm.

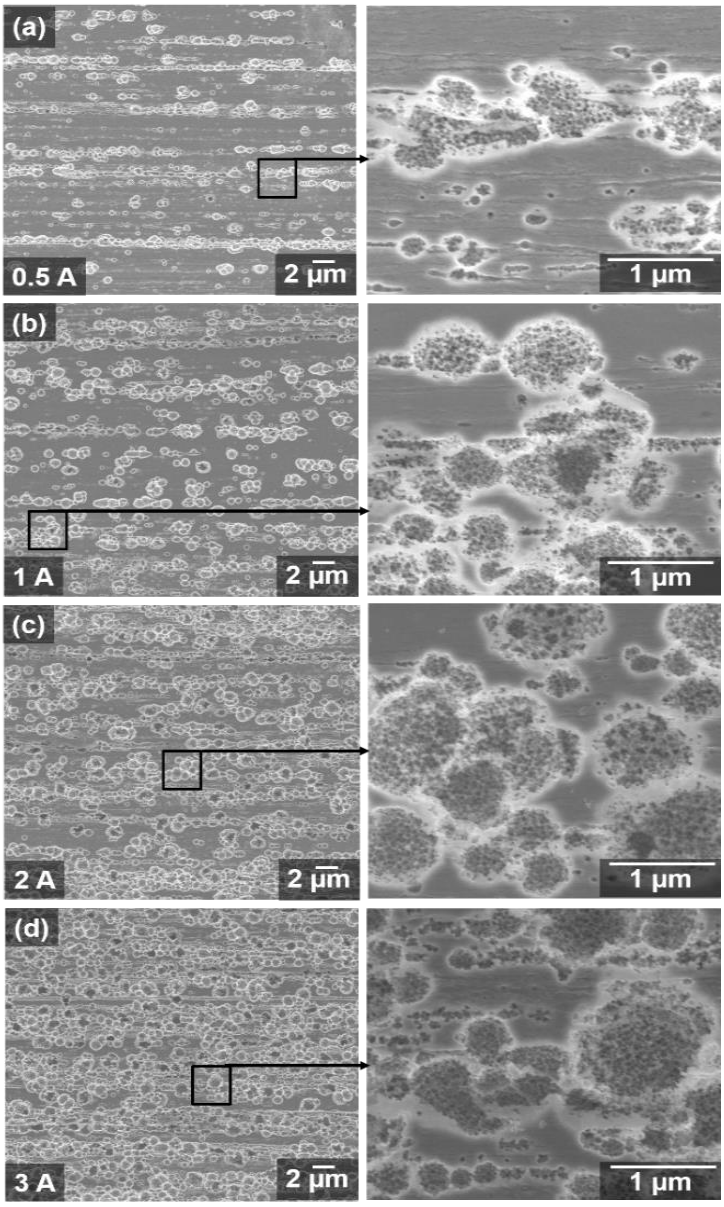

Figure 4.28: *SEM images of different structures formed as influenced by varying current density at 0.5 s sculpturing time using 0.25 M electrolyte concentration.*

As depicted in Figure 4.28 (c) SEM image, further increase in constant current application to 2 A led to a high density of bowl-like structures compared with the structure density of 0.5 A and 1 A. The structures show an average diameter in the range of 1 µm and are randomly distributed with interconnected and overlapping bowl-like structures as shown in Figure 4.28 (c) magnified image. Furthermore, the total sculptured surface area coverage is in the range of 80 %, with deep bowl-like structures that are sparsely distributed [see Figure 4.28 (c) bowl-like structures that appear dark in depth].

Figure 4.28 (d) demonstrates the highest density of bowl-like structures with high total structures surface area coverage in the range of 90 % at a constant current application of 3 A compared with 0.5 A, 1 A, and 2 A. The bowl-like structures are broad with an average diameter of 1.2 µm and are randomly distributed with a high density of sparingly distributed deep bowl-like structures [see Figure 4.28 (d) bowl-like structures that appears dark in dept] when compared with the 2 A. As already seen in the 1 A and 2 A constant current application, the 3 A constant current application bowl-like structure is also non-preferentially etched along the manufacturing process-oriented defect lines.

4.4.2 Current pulsing application

Variation of waiting time at the cathodic regime

In Figure 4.29 (a) – (c) SEM images, the corresponding effects of the increase in waiting time in the cathodic regime at constant two anodic regimes pulsing spikes (TPS) of 0.5 s is as shown. The waiting time in the cathodic regime is increased from 0.5 s, 1 s, and 2 s, respectively, while keeping the sculpturing time at constant 0.5 s in each of the anodic regimes (i.e., total sculpturing time of 1 s) with a current density of 4 A/cm^2 (i.e., 2 A current application). One can see some differences in the bowl-like structure formation as the waiting time in the cathodic regime increases.

At 0.5 s waiting time, as depicted in Figure 4.29 (a) SEM image, the formed bowl-like structures are broad with another formation of bowl-like structure inside already formed bowl-like structures (i.e., bowl-in-bowl-structure formation as shown in Figure 4.29 magnified image red-dotted circled). Therefore, one can say that the in-bowl-structure formation arises from the second anodic regime´s current application. As a result of the bowl-in-bowl-structure formation, deep bowl-like structures are formed [see some dark bowl-like structures in Figure 4.29 (a)], which are uniformly distributed. In addition, the wide bowl-like structure formation

leads to sparingly distributed small islands of unsculptured surfaces (see Figure 4.29 brown dotted circled points in the magnified images).

Increasing the waiting time to 1 s as shown in Figure 4.29 (b) SEM images, the diameter of the formed bowl-like structure became smaller [see Figure 4.29 (b) magnified image] compared to the bowl-like structure diameter at 0.5 s waiting time [see Figure 4.29 (a) magnified image]. On the other hand, bowl-in-bowl structures, which led to uniformly distributed deep bowl-like structures, are formed [see dark bowl-like structures in Figure 4.29 (b)] with small islands of the unsculptured surface.

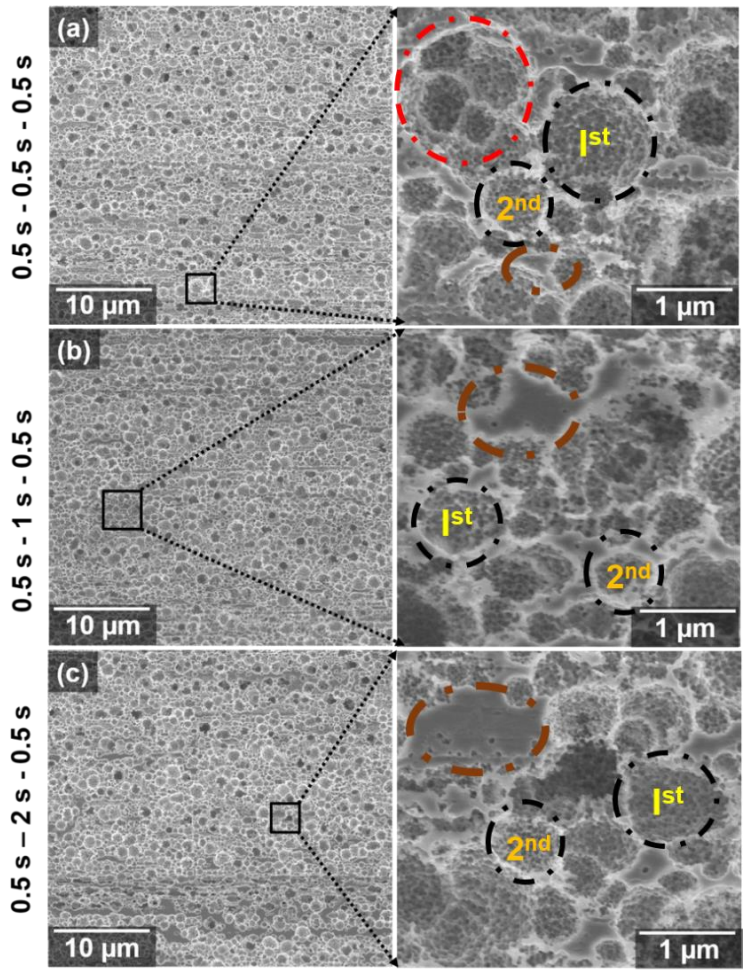

Figure 4.29: *SEM micrograph of nanoscale sculptured SST wire showing the effect of waiting time in the cathodic regime (passivation time), first (1^{st}) and second (2^{nd}) generation bowl-like structure formation (black-dotted circled), bowl-in-bowl structure (red-dotted circled), and the island of unsculptured surface (brown-dotted circled).* ***(a)*** *0.5 s,* ***(b)*** *1 s, and* ***(c)*** *2 s.*

At a 2 s waiting time, as shown in Figure 4.29 (c) SEM images, small bowl-like structures similar in diameter to the 1 s waiting time can be observed. More so, other features of the bowl-like structures formed at the 2 s waiting time are similar to those observed in the 1 s waiting time. These results demonstrate that the formation of broad bowl-like structures is

time-dependent, specifically on the cathodic regime wait time when using the current pulsing approach. This dependency leads to the formation of bowl-in-bowl structures, resulting in deep bowl-like structures. This indicates that the cathodic waiting time is related to the passivation rate of the first-generation bowl-like structures in the first anodic regime current spike before the second-generation bowl-like structure formation in the subsequent anodic regime current spike. Furthermore, the characteristics of these generational structures, including their diameter and depth are also influenced by the number of anodic current spikes, applied anodic current density, and the duration of applied anodic current density.

Figure 4.30 plot depicts the corresponding diameters of the pre-treated SST wire at different cathodic waiting times, measured using a digital micrometer gauge with flat circular contact points of 20 mm^2. As mentioned earlier (see the PS in Figure 4.26 plot), the PS sample has an average diameter of 152.4 ± 1.3 µm resulting from the sporadically distributed embedded die particles during the cold drawing process. However, increasing the waiting time in the cathodic regime (i.e., 0.5 s, 1 s, and 2 s) shows an average wire diameter of 150.8 ± 0.4 µm, 150.5 ± 0.5 µm, and 150.5 ± 0.5 µm respectively with a seeming change in the wire diameter (in the range of 1 µm) when compared with the PS.

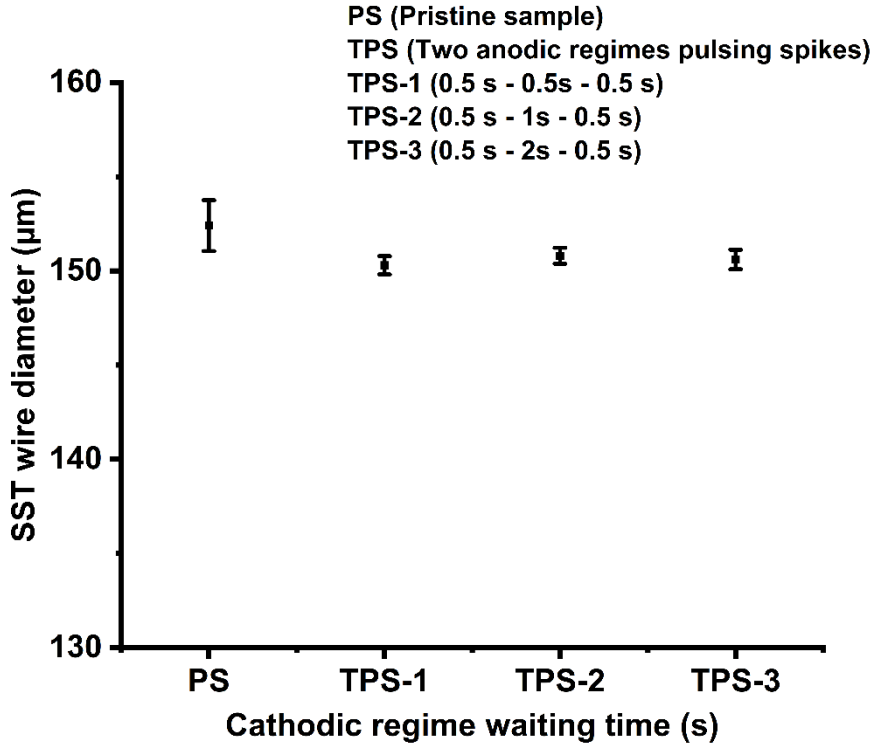

Figure 4.30: *The corresponding diameter of the pre-treated SST wire using the TPS current pulsing approach at increasing cathodic waiting time. For statistical analysis of the mean values of the diameter, a one-way ANOVA followed by a Tukey test was performed. The PS showed a statistically significant difference ($p < 0.05$) compared to the diameters obtained using the TPS approach.*

Increasing the number of anodic current pulsing spikes at constant total sculpturing time

In Figure 4.31 (a) – (c) SEM images, the effect of multiple anodic current pulsing spikes (MPS) at a constant total sculpturing time of 1 s with a current density of 4 A/cm^2 (i.e., 2 A current application) is as depicted. In each of the cathodic regimes, a constant waiting time of 1 s is used, while in the anodic regimes, the number of current spikes and pulsing times is varied however, at a constant total sculpturing time of 1 s irrespective of the total number of the anodic spikes.

As shown in Figure 4.31 (a) SEM images (MPS-1), the formed bowl-like structures with the sculpturing parameter of **A** (0.25 s) – **C** (1 s) – **A** (0.25 s) – **C** (1 s) – **A** (0.5 s), i.e., A is an anodic regime and C is cathodic regime has broad bowl-like structures with an estimated average bowl-like structure diameter of 1 µm [see Figure 4.31 (a) magnified image] with bowl-in-bowl structures and deep bowl-like structures. One can see a high density of broad bowl-like structures [see Figure 4.31 (a) – (c)] compared to MPS-2 and MPS-3 with islands of unsculptured surface areas, which are rather large.

A corresponding effect of the bowl-like structure size is observed at a change in the position of one of the anodic pulsing times [**A** (0.5 s) – **C** (1 s) – **A** (0.25 s) – **C** (1 s) – **A** (0.25 s)] as depicted in Figure 4.31 (b) SEM images (MPS-2). The bowl-like structure has an estimated average diameter of 0.7 µm, less formation of bowl-in-bowl structure, and deep bowl-like structures compared to MPS-1. However, there is a high density of bowl-like structures with small islands of the unsculptured surface compared to MPS-1.

Increasing the number of current pulsing spikes with the same current pulsing time of 0.25 s [**A** (0.25 s) – **C** (1 s) – **A** (0.25 s) – **C** (1 s) – **A** (0.25 s) – **C** (1 s) – **A** (0.25 s)] as depicted in Figure 4.26 (c) SEM images (MPS-3) led to the high density of small bowl-like structures [see Figure 4.31 (c) magnified image], with the islands of unsculptured surface areas similar in size to those observed in MPS-2. This high density of bowl-like structures results from the increased number of current pulsing spikes, whereas the high number of small bowl-like structures arises from the repeated numbers of 0.25 s pulsing time, which led to multiple generations of bowl-like structures.

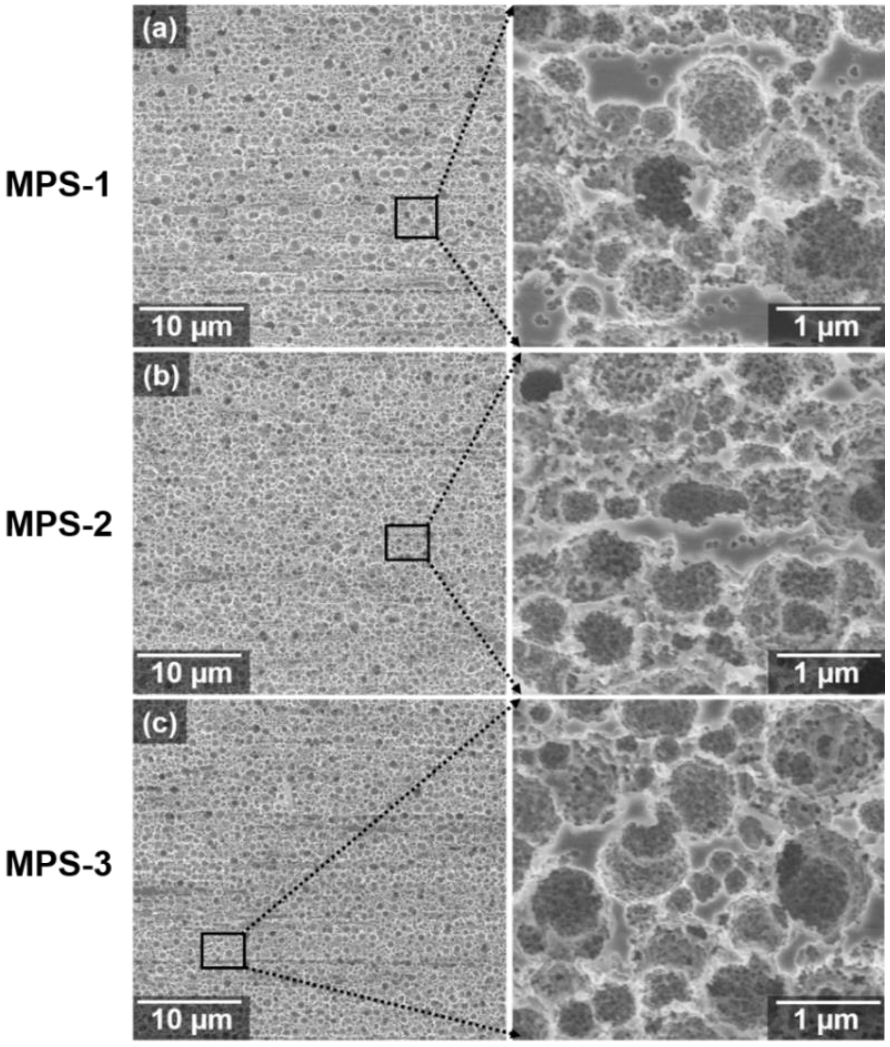

Figure 4.31**:** *SEM micrograph of nanoscale sculptured SST wire showing the increase in structure density and different bowl-like structure diameter resulting from repositioning the 0.5 s anodic current pulsing time and increasing the number of anodic current spikes at a total sculpturing time of 1 s.*

In Figure 4.32, it is observed that the repositioning of the current pulsing time of 0.5 s in MPS-1 and MPS-2 with the same number of anodic regime current pulsing spikes and increasing the number of the anodic current pulsing spikes while maintaining the same current pulsing time of 0.25 s in MPS-3 show some seeming variation in the pre-treated SST wire bowl-like structure diameter. Furthermore, the PS with an average wire diameter of 152.4 ± 1.3 µm showed a statistically significant difference in diameter compared to the pre-treated SST wire with an average wire diameter of 150 ± 0.0 µm for the MSP-1, 150 ± 0.0 µm for the MPS-2 and 149.9 ± 0.3 µm for the MPS-3 respectively.

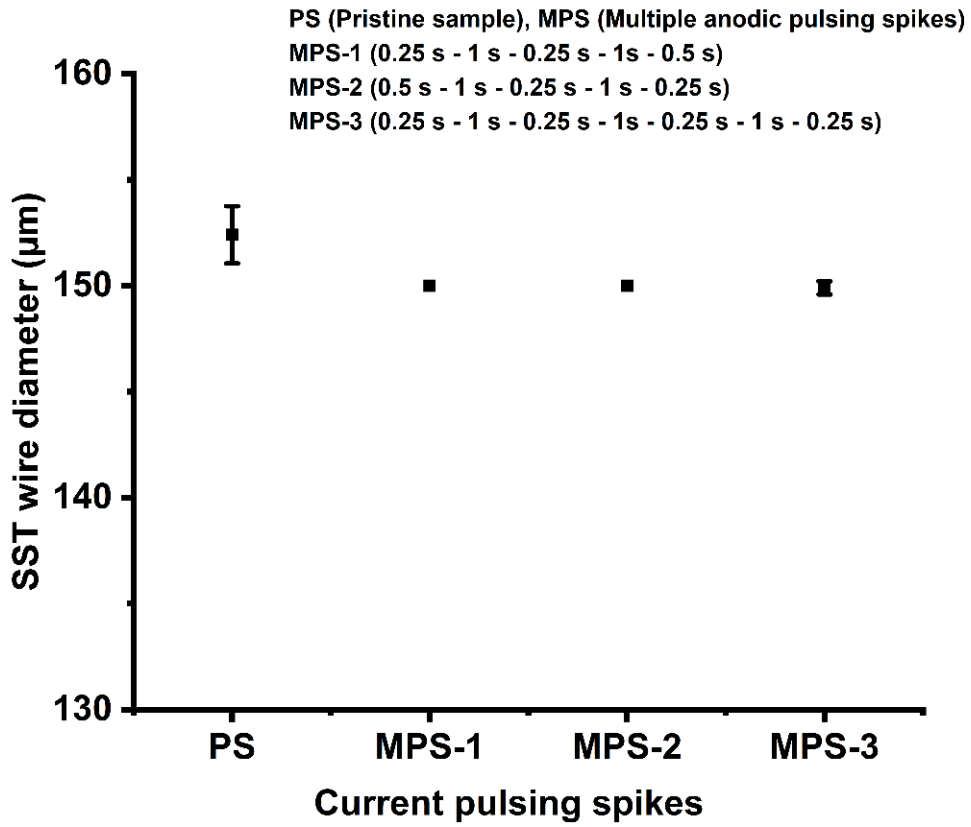

Figure 4.32: *The diameter of pre-treated SST wire with changes in sculpturing parameters such as repositioning the 0.5 s pulsing time in MPS-1 and MPS-2 and increasing the number of anodic current spikes. For statistical analysis of the mean values of the diameter, a one-way ANOVA followed by a Tukey test was performed. The PS showed a statistically significant difference ($p < 0.05$) compared to the diameters obtained using the MPS approach.*

As depicted in Figure 4.33 (a) – (d) SEM images, a corresponding effect of increasing the anodic current pulsing time (IPT), hence increasing the total sculpturing time at constant 1 s cathodic waiting time is demonstrated using TPS sculpturing process approach. One can see an increase in the bowl-like structure diameter with increasing anodic regime pulsing time and total sculpturing time at a current density of 4 A/cm^2. This is similar to the results of Figure 4.25 (e) – (h) using the TPS sculpturing approach. This led to a high density of deep and broad bowl-like structures, the interconnection of individual bowl-like structures, which however collapsed into one another [see Figure 4.33 (c) and (d)]. In addition, there is seemingly no island of unsculptured surface in the 4 s and 6 s total sculpturing time [see Figure 4.33 (c) – (d)] magnified images rather, deep and broad bowl-like structures are observed.

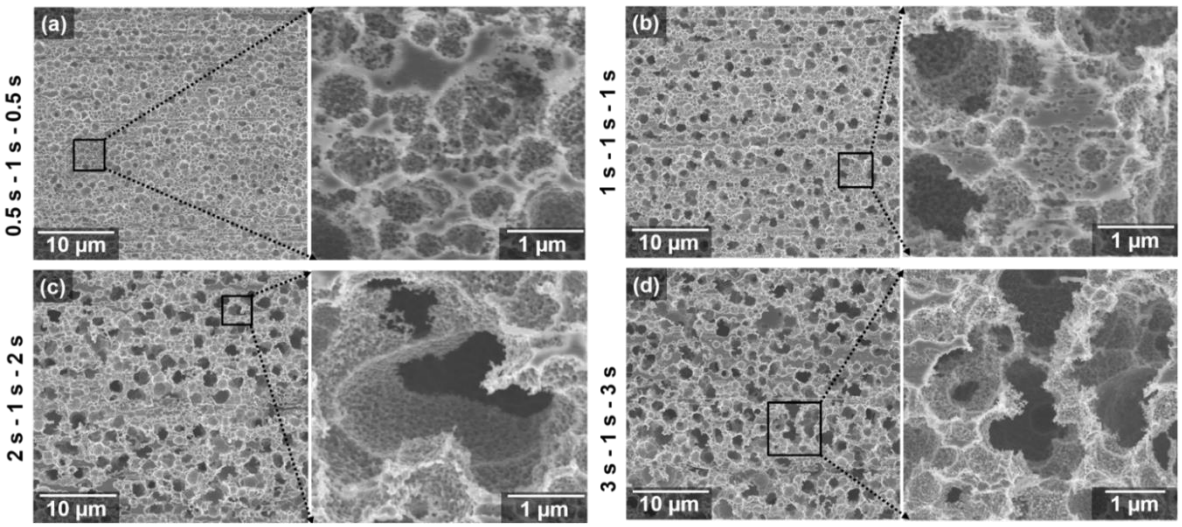

Figure 4.33: *SEM images of nanoscale sculptured SST wire showing the corresponding effect of increased total sculpturing time in the anodic regime at a constant 1 s cathodic waiting time using the TPS sculpturing approach.*

4.4.3 Chemical and mechanical properties of sculptured stainless steel wire

Elemental analysis of sculptured stainless steel wire

The elemental surface composition of the sculptured SST wire has been investigated by EDX analysis. The SEM images of the investigated surface area and the corresponding Fe, Cr, Ni, and O elemental maps are illustrated in Fig. 4.34 both for the unsculptured (PS) and sculptured surfaces.

Similar to what was observed on the SST strip 2 samples, the signal intensity in the maps was found to be uniformly distributed with no dependence on morphology on all the unsculptured surface signal maps. However, for the pre-treated SST wire surface, the signal intensity of Fe seems uniformly distributed, while the signal intensity of Cr and Ni (mostly) showed some dependence on the pre-treated SST wire sculptured surface. Regions with depleted intensity were found to correspond to bowl-like structures on the sculptured surface, while the signal intensity increased at the walls of the bowl-like structure. This confirms the selective de-alloying process during the nanoscale sculpturing of SST samples, which includes the etching of less noble constituents and less stable metal oxides, and in this case with respect to Ni.

The intensity of the O signal on the surfaces of the SST samples was found to be significantly influenced by the morphology of the sculptured structures. Specifically, the intensity of the O signal was observed to increase at the walls of the structures and decrease within the bowl structure. The source of this O signal can be attributed to the passive oxide

layer formed during the sculpturing process and the native oxide layer that forms on the surface upon exposure to air following the sculpturing process. However, the EDX analysis cannot detect the oxide layer (Cr_2O_3).

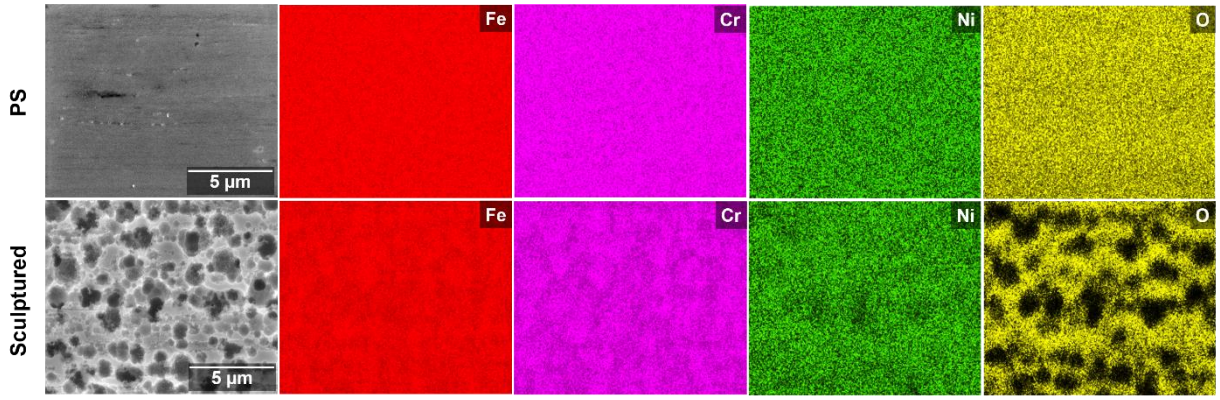

Figure 4.34: *EDX elemental surface composition analysis of stainless steel wire.*

Cross-sectional view of sculptured stainless steel wire

The cross-sectional view of the pre-treated SST wire through electrochemical nanoscale sculpturing using 0.25 M HCl-based electrolyte at the application of 2 A (4 A/cm^2) constant current is depicted in Figure 4.35 SEM images. This was achieved after the 10 cm long sculptured SST wire was embedded into a PTU matrix, cut into 4 equal lengths after curing, polished with different grades of abrasive paper until a mirror-like surface was achieved, and thereafter coated with a 10 nm thick gold layer on the polished surface. One can see an increase in surface morphology as the bowl-like structure depth increases with an increase in sculpturing time [see also Figure 4.25 (e) – (h) and Figure 4.27 (d)]. In addition, the increase in depth of the bowl-like structures with mechanically stable hook-like features is advantageous to improved surface adhesion when coating material such as polymer fills the bowl-like structures, as shown in Figure 4.35. However, one could say that the increase in depth of the bowl-like structures will hinder the sustainability of the mechanical property of the pre-treated SST wire. This is because as the bowl-like structure becomes broader and deeper (see Figure 4.35 3 s images), the pre-treated SST wire thickness is locally reduced (effective thickness), while the deep bowl-like structures could serve as a notch under a tensile load, for example.

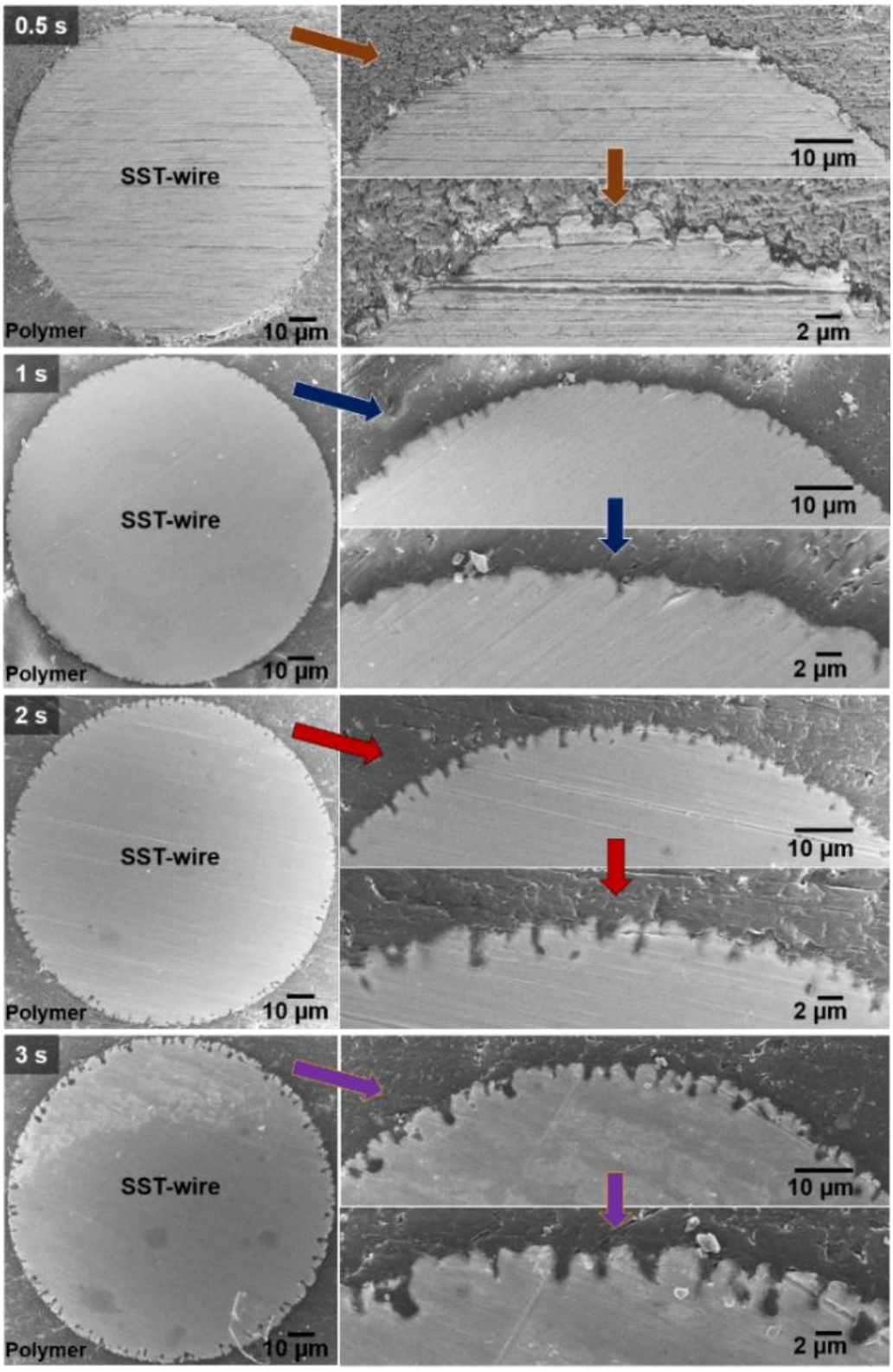

***Figure 4.35*: *The SEM images showing the cross-sectional view of nanoscale sculptured SST-wire at 2 A (4 A/cm^2) constant current application for 0.5 s, 1 s, 2 s, and 3 s, respectively, using 0.25 M HCl-based electrolyte*.**

Tensile testing of stainless steel wire at different sculpturing times

The tensile test of the pre-treated SST wire at a constant current application of 2 A (4 A/cm^2) and increasing sculpturing time is depicted in Figure 4.36 bar chart. The ultimate tensile strength (UTS) showed some variation between the sculpturing times of 0.5 s, 1 s, 2 s, and 3 s compared with the UTS of the PS. For example, the PS with UTS of 2.21 ± 79.01 GPa shows no significant difference statistically to 0.5 s, 1 s, and 2 s sculpturing times with UTS of 2.16 ± 17.60 GPa, 2.15 ± 37.75 GPa and 2.09 ± 28.63 GPa respectively while a significant statistical difference to 3 s sculpturing time with UTS of 2.03 ± 27.67 GPa is observed. This means that there is a measurable difference in the mechanical property of the pre-treated SST wire after 3 s sculpturing time compared to the PS. This can be due to the increased bowl-like structure diameter and, most crucially, the depth after 3 s sculpturing time (see Figure 4.35 SEM images cross-sectional view), which invariably affected the sculptured SST wire mechanical property.

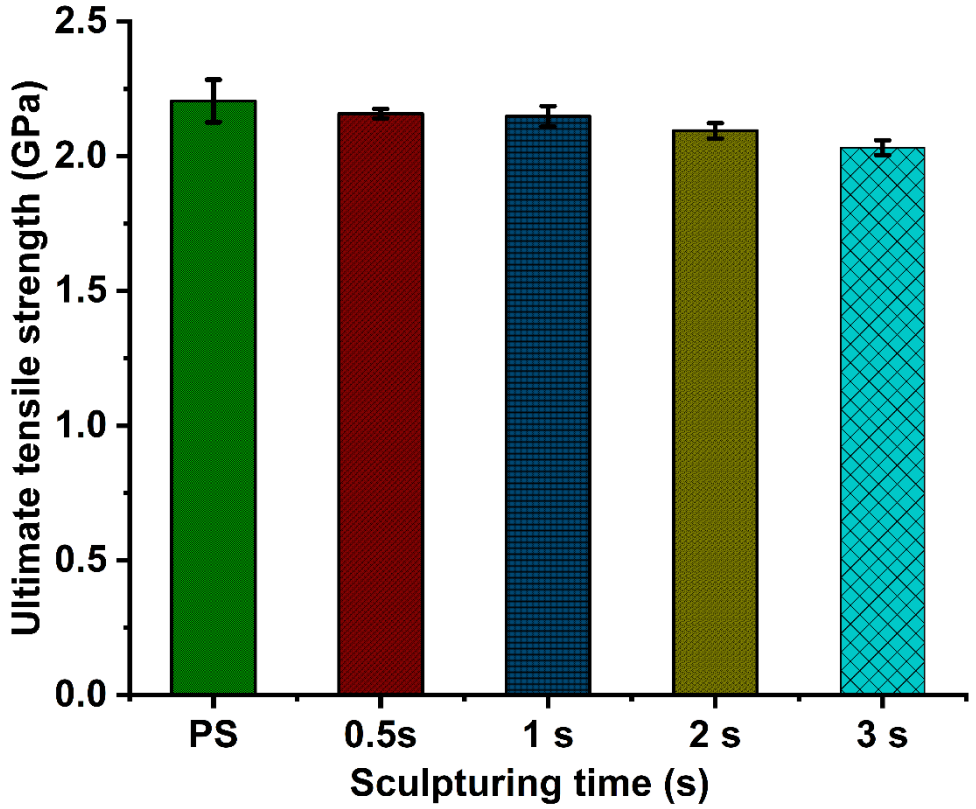

Figure 4.36: *Ultimate tensile strength as a function of sculpturing time influence on the mechanical property of the SST wire at constant 2 A (4 A/cm^2) using 0.25 M electrolyte. Mean values and corresponding standard deviation of tensile strength are shown as a function of sculpturing time. For statistical analysis of the mean values of tensile strength, a one-way ANOVA followed by a Tukey test was performed. The PS, 0.5 s, 1 s, and 2 s sculpturing times showed no significant difference between each other ($p > 0.05$), while the PS, compared to the 3 s sculpturing time, showed a significant difference ($p < 0.05$) statistically.*

On the contrary, the tensile test of the pre-treated SST wire using the TPS sculpturing approach at a constant anodic current pulsing time of 0.5 s, total sculpturing time of 1 s, and increasing cathodic regime waiting time as depicted in Figure 4.37 bar chart shows no measurable change in tensile strength. In the statistical analysis, the PS with UTS of 2.21 ± 79.01 GPa shows no significant difference in the tensile strength of the pre-treated SST wires with 2.14 ± 24.22 GPa for TPS-1, 2.19 ± 120.86 GPa for TPS-2 and 2.19 ± 104.85 GPa for TPS-3 respectively. This means that at a total sculpturing time of 1 s, using the TPS sculpturing approach within the 2 s cathodic regime waiting time will result in no change in the mechanical property of the pre-treated SST wire.

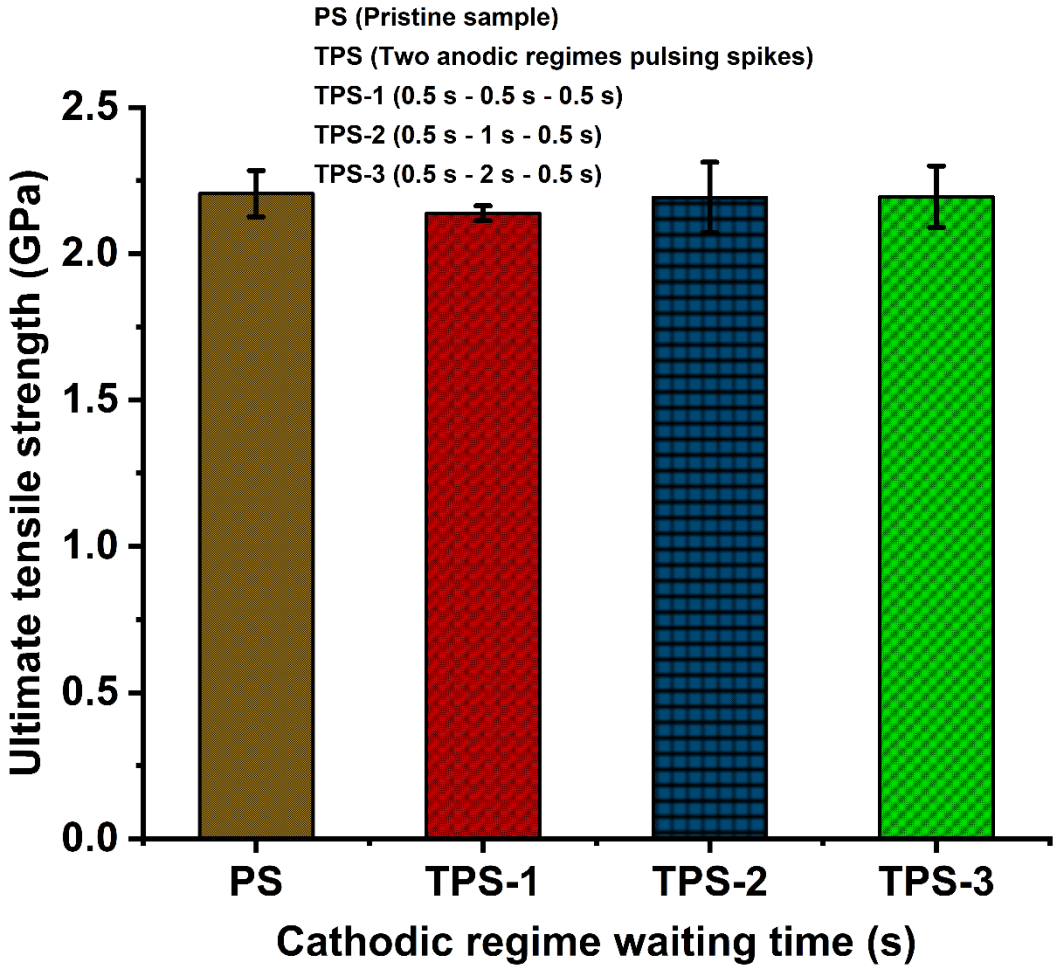

Figure 4.37: *Ultimate tensile strength as a function of increase in passivation waiting time in the cathodic regime at constant 0.5 s two-anodic regime pulsing current of 2 A (4 A/cm^2) using 0.25 M electrolyte. Mean values and corresponding standard deviation of tensile strength are shown as a function of passivation waiting time in the cathodic regime. For statistical analysis of the mean values of tensile strength, a one-way ANOVA followed by a Tukey test was performed. The PS and other samples, irrespective of the passivation waiting time, showed no significant differences between each other ($p > 0.05$).*

Similarly, no measurable change was observed in the tensile strength of pre-treated SST wire using the MPS sculpturing approach within 1 s total sculpturing time, as depicted in Figure 4.38 bar chat. The PS with UTS of 2.21 ± 79.01 GPa shows statistically similar UTS compared to the MPS-1, MPS-2, and MPS-3 with UTS of 2.15 ± 53.42 GPa, 2.15 ± 9.02 GPa, and 2.16 ± 51.69 GPa respectively. This confirms the results of the TPS sculpturing approach, as shown in Figure 4.37 bar chat, and further elaborates the robustness and flexibility of the anodic current pulsing approach.

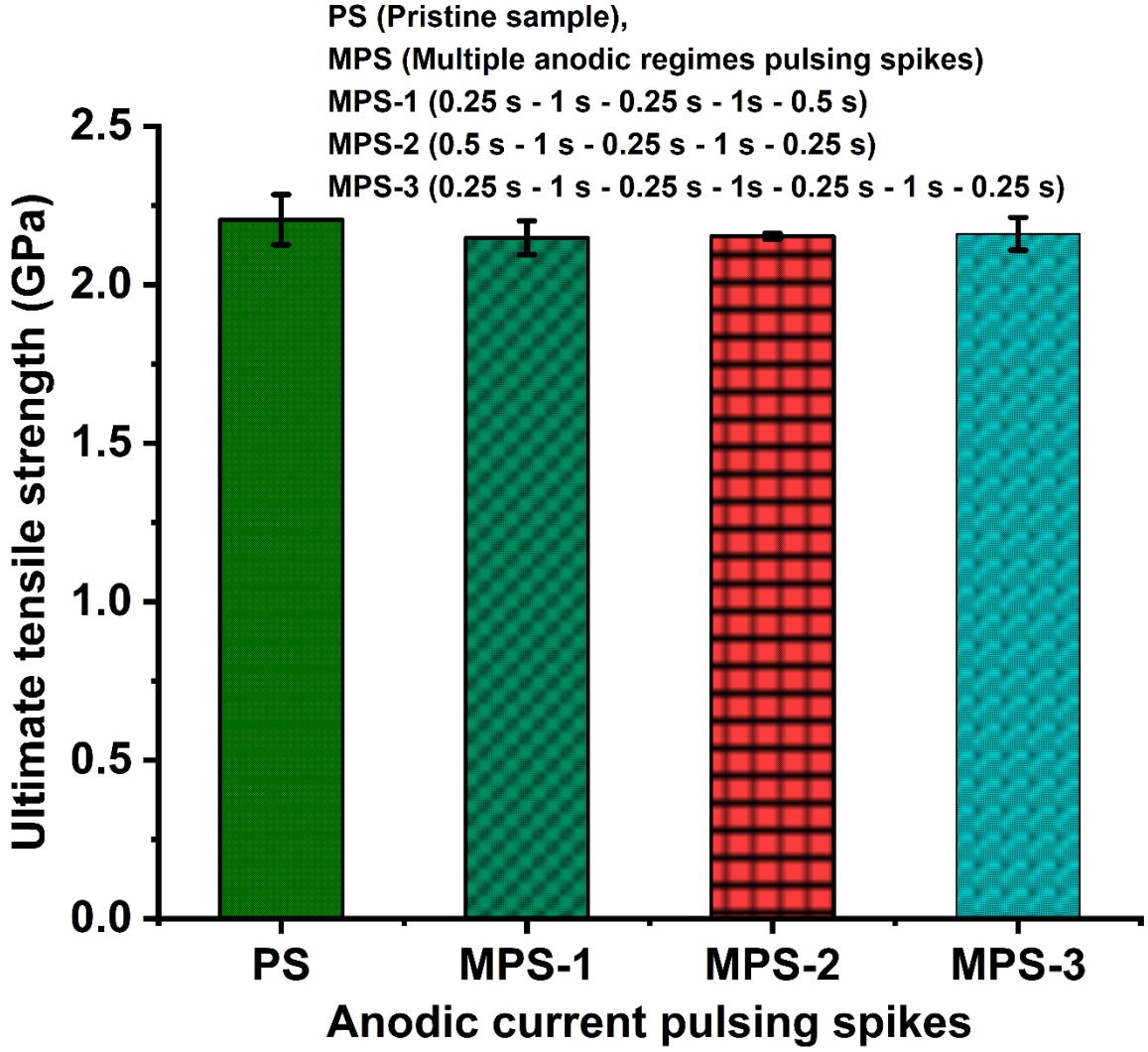

Figure 4.38: *Ultimate tensile strengths as a function of the increasing number of anodic current spikes, repositioning current pulsing time at constant 2 A (4 A/cm^2), total sculpturing time of 1 s, and individual cathodic regime waiting time of 1 s using 0.25 M electrolyte. Mean values and corresponding standard deviation of tensile strength are shown as a function of the increasing number of anodic current spikes and repositioning of current pulsing time. For statistical analysis of the mean values of tensile strength, a one-way ANOVA followed by a Tukey test was performed. The PS and the other samples, irrespective of the number of anodic current spikes and repositioning of current pulsing time, showed no significant difference between each other ($p > 0.05$).*

Furthermore, the bar chart in Figure 4.39 shows the individual tensile strength of the pre-treated SST wires using the TPS sculpturing approach at increasing anodic current pulsing time and total sculpturing time (IPT) as investigated [see also Figure 4.33 SEM images]. The PS with UTS of 2.21 ± 79.01 GPa shows statistically no measurable change in tensile strength when compared with the IPT-1 and IPT-2 UTS of 2.18 ± 120.18 GPa and 2.09 ± 17.96 GPa, respectively. On the contrary, a measurable statistical difference in the tensile strength is observed when the PS UTS is compared with the IPT-3 and IPT-4 UTS of 2.01 ± 26.56 GPa and 1.99 ± 15.13 GPa, respectively. One can see that a sculpturing time of 3 s and above at constant anodic current application and anodic pulsing time of 3 s and above (using the TPS approach) leads to a statistically significant difference in the UTS hence a measurable change in the mechanical property of the sculptured SST wire. This can be related to the high density of deep bowl-like structures [see Figure 4.27 SEM images], which could serve as a notch, leading to stress propagation and weakening of the pre-treated SST wire mechanical property.

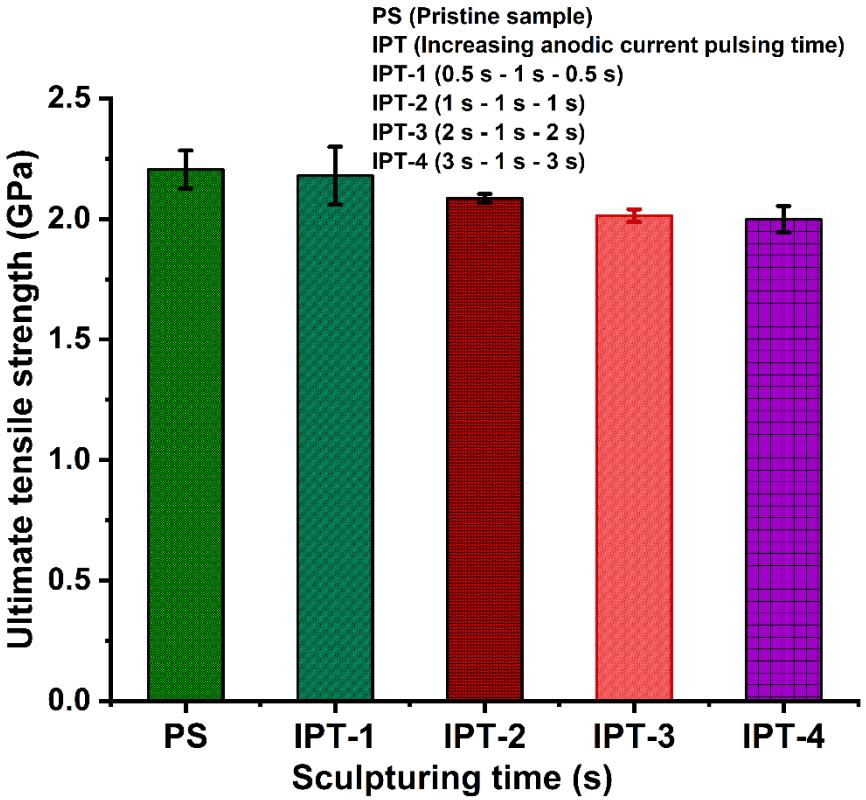

Figure 4.39**:** *Ultimate tensile strengths as a function of increasing total sculpturing time at constant 2 A (4 A/cm^2) and individual passivation time of 1 s using 0.25 M electrolyte. Mean values and corresponding standard deviation of tensile strength are shown as a function of increasing sculpturing time. For statistical analysis of the mean values of tensile strength, a one-way ANOVA followed by a Tukey test was performed. The PS, the IPT-1, and IPT-2 sculpturing time showed no significant differences between each other ($p > 0.05$), while the PS when compared with the IPT-3 and IPT-4 sculpturing time, showed significant differences ($p < 0.05$).*

Chapter 5

5.0 Discussion

5.1 Structures nucleation efficiency as influenced by initial surface morphology of the substrates during mechanically stable interlocking structure evolution and structure formation on AlMg3 and stainless steel

5.1.1 Chemical structure formation of AlMg3 strip

The formation of mechanically stable interlocking structures on aluminium alloy strips, such as AlMg3-W19 (AW5754), through chemical nanoscale sculpturing by using a 7.25 wt. % dilute HCl electrolyte can be explained by the kinetics of oxide formation, which is the primary key phenomenon in the sculpturing process [33]. Compared to other metal alloys, AlMg3 exhibits a higher susceptibility to chemical nanoscale sculpturing in an acidic aqueous electrolyte. This susceptibility of AlMg3 to chemical etching in acidic aqueous media can be attributed to the selective leaching process of the less electronegative (high activity) magnesium (standard reduction potential E^0 = -2.37 V) alloy content compared to aluminium (standard reduction potential E^0 = -1.66 V). Furthermore, the preferential dissolution of magnesium in AlMg3 can be attributed to its inability to exhibit surface passivation [148], which leads to the exposure of the aluminium in the bulk material. This exposure, in turn, triggers the formation of an amorphous oxide layer on the surface of the alloy [76]. As previously discussed in the theoretical part of this thesis, the formation of the oxide layer leads to volume expansion and the subsequent formation of cracks through the adsorption of Cl^- on the aluminium surface, which is driven by the open circuit potential. The adsorbed Cl^- leads to temporal surface passivation (temporal surface protection but not surface inertness), resulting in different degrees of preferential lattice plane passivation. This leads to the formation of cubic structures through the preferential passivation of the {100} plane, which has the second highest packing density after the {111} planes [33,73,75]. This is due to the crystallographic symmetry of the {100} plane and surface energy, which enhances its rapid passivation tendency and is thus considered the stopping plane, whereas the slower passivating lattice planes have a higher probability of dissolution [33]. These cubic structure formation processes, which results from the interplay

between oxide formation, dissolution, and specific crystalline plane passivation, occur millions of times over the entire aluminium surface, leading to surface structures with characteristic quasi-freestanding mechanically stable hook-like interlocking structure [21,33] as schematically depicted in Figure 2.7.

As shown in Figure 4.5 SEM images, the formation rate of the cubic crystallographic structures strongly depends on the sample's initial surface morphology. This significantly impacts the nucleation efficiency of the cubic structures and can be understood through the degree of surface roughness [149,150] and, most importantly, the tip curvatures of the individual topography, as depicted in Figure 4.1. This is indicative of the electric field strength effect [61,62,151] at the tip curvatures of the individual sample´s initial surface morphology, which is influenced by the open circuit potential of the chemical sculpturing process, electrolyte concentration, and tip curvatures. This can be explained using basic physics theories. In principle, electric field strength (E) is a vector quantity characterized by both magnitude and direction, while potential (V) is a scalar quantity with no direction. Therefore, the work done by the force in moving fully solvated anions through the Inner Helmholtz Plane (IHP) onto the positively charged high surface energy metal surface is a function of the charge, surface curvature, and distance of separation [57]. In this case, the electric field points in the direction of the potential and increases as the potential decreases, leading to a high accumulation of the electric field at the sharp tip curvatures compared to a quasi-flat surface [see Figure 5.1 (a) – (e)]. The accumulation of the electric field at the tip curvatures leads to aggregation of positive charges at the sharp tip curvature of the positively charged metal electrode, which enhances large adsorption of the fully solvated anion (Cl^{-}) [151] (see Figure 5.1 schematic). The adsorption process of the fully solvated anion leads to cracks in the temporal passive oxide layer due to volume expansion, resulting in porous structures and etch pits [41,60–62,71,151,152].

This phenomenon leads to different degrees of structure nucleation density and total sculptured surface area on the individual samples after 6 min of sculpturing time (see Figure 4.2). Figure 4.6 indicate that samples with deep and sharp tip curvatures, specifically PGBS, PA-PGBS, and PS in that order, exhibit a higher mass loss than the quasi-flat surface of the PAS as measured. As a result, longer sculpturing time is required to achieve the formation of mechanically stable hook-like interlocking structures from PGBS, PA-GBS, PS, to PAS respectively. This can be attributed to the degree of positive charge accumulation and fully solvated anion adsorption, which vary with respect to the density, depth, and sharpness of the tip curvature. Following the nucleation stage, as illustrated in Figure 4.6, the sculpturing process proceeds in a three-dimensional manner, causing an increase in the total sculptured surface area

as nucleation sites continue to expand and interconnect until the surface is completely sculptured and attends their maximum depth [33]. Subsequently, the initial surface morphology no longer plays a role in the formation of the structure, and the process becomes self-sustaining/amplifying (Figure 4.7). This means a continuous etching of the topmost structures, resulting from the breakdown of passivation of the {100} stopping plane as it is long exposed to fresh electrolyte and the regeneration of new cubic crystallographic structure in depth.

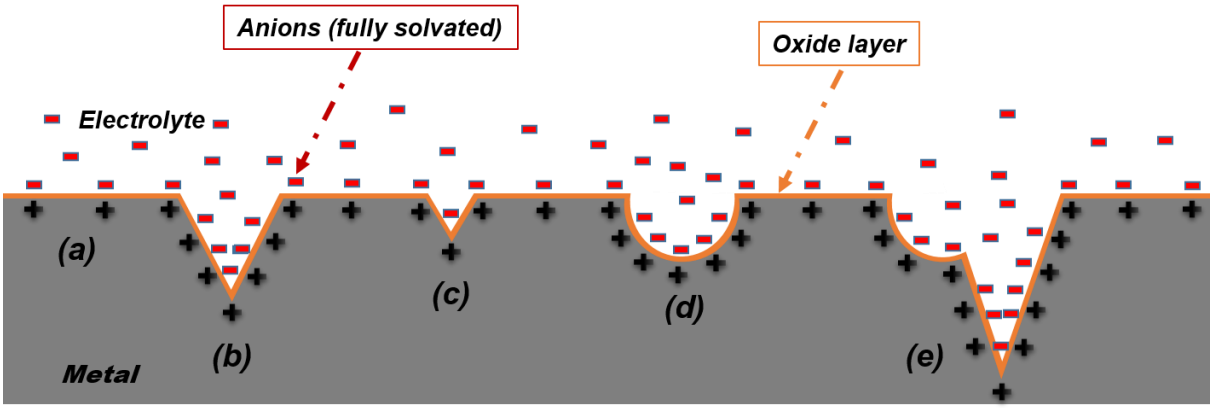

Figure 5.1**:** *Schematic of electric field strength effect on charge distribution as influenced by the surface tip curvature: quasi-flat surface* ***(a)****, deep grove* ***(b)****, shallow grove* ***(c)****, indentation/round tip curvature* ***(d)****, and mixed tip curvatures* ***(e)****.*

5.1.2 Electrochemical structure formation on stainless steel samples

The different structure formations on the SST strip and SST wire demonstrate the nonlinearity of the electrochemical nanoscale sculpturing process in relation to the kinetics of oxide formation, dissolution, and passivation interplay. To further understand these results, primary and more general theories will be used to explain the structure nucleation efficiency, the influence of HNO_3 concentration and sculpturing time on the SST strip, and electrolyte concentration (Cl^- concentration), sculpturing times, current density, constant current and current pulsing effects in structure formation on the SST wire.

Generally, SST is a strong corrosion-resistant metal alloy, primarily due to the presence of a passive oxide layer predominantly made up of Chromium (III) oxide (Cr_2O_3) when exposed to an aqueous acidic electrolyte. The oxide layer forms as a result of the rapid oxidation of Cr (standard reduction potential E^0 = -0.74 V), a less electronegative (high activity), and a major constituent of the SST sample (18 % Cr, 8 % Ni, and Fe). The oxide layer is very stable in a corrosive environment and cannot be chemically dissolved in a low-concentrated electrolyte such as the 0.25 M HCl-based electrolyte used in this work. Moreover, the insulating nature of the Cr_2O_3 layer prevents its etching through an electrochemical equilibrium reaction, as described by the Nernst equation (equation 2.6), due to the incapability of applying a significant

potential to the Helmholtz layers. Instead, the applied potential will drop across the Cr_2O_3 layer, leading to high electric fields that raise the current tunneling effect, avalanche breakdown, and local electrical breakthrough [41,60–62]. This led to local cracking of the Cr_2O_3 passive oxide layer, thereby exposing the Cr atoms and other less noble components of the SST bulk to the attack of the fully solvated Cl^- anion. Unlike the structure formation on the AlMg3 strip, which is preferential passivation of the {100} plane hence cubic crystallographic structures formation, the structure formation on SST samples is instead a result of kinetically influenced dealloying of less noble constituents in the alloy composition, temporal and partial passivation, and rate-dependent dissolution of less stable metal oxide [32].

In the SST strip, as shown schematically in Figure 5.2 (a) – (d), the structures nucleate randomly within a grain after the localized cracking of the passive oxide layer and grow into depth as the sculpturing time increases. The structure reaches its maximum depth (approx. 15 µm) after 60 s of sculpturing and grows self-similar into depth. The self-similar growth feature is the removal of the top layer structures and a simultaneous similar structure formation into the depth. Furthermore, the structure is rather porous, with wavy walls and a shape that exhibits a remote resemblance to pores grown in semiconductors (see Figure 4.14 and Figure 4.16). The intergrows forming interconnected undercut into depth with grain boundaries preservation hence it's characteristic mechanically stable hook-like interlocking feature. This unusual non-preferential etching at the grain boundaries results from a voltage drop at the grain boundaries risen from this simple, unique aqueous electrolyte which clearly shows the peculiarity of this electrochemical etching electrolyte and the chosen etching parameters. Therefore, the structure formation model can be understood by the strong influence of the HNO_3 in the seawater-like HCl-based electrolyte, current density, and the applied DC voltage.

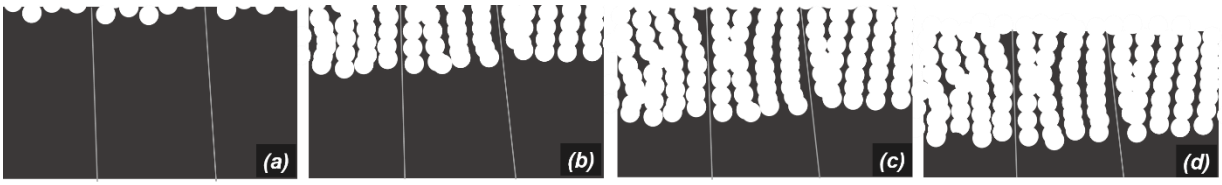

Figure 5.2**:** *Schematic illustration of structure growth on the SST strip surface at different stages without preferential grain boundaries etching,* ***(a)*** *structure nucleation,* ***(b)*** *increasing of structures depth with time,* ***(c)*** *reaching of maximum structuring depth, and* ***(d)*** *continued structure formation into the bulk with constant structuring depth.*

HNO_3, a strong oxidizing agent, increases the rate of oxide layer formation on the SST strip surface. However, the application of a DC voltage ranging from 6 V to 7 V results in the formation of a high-density porous oxide layer due to local electrical breakdown. This is

followed by the spontaneous dissolution of less noble metal oxides, dealloying of less noble constituents such as nickel, and temporal surface passivation through the adsorption of Cl ions.

Figure 4.12 demonstrates that with different initial surface morphology of the SST strip surface, structure nucleation efficiency on individual samples varies with respect to the tip curvatures of the topography. This results in different total sculptured surface areas and individual sample mass loss in the first 6 s of the sculpturing process. In addition, the completely sculptured surface of individual sample surfaces was attained at different sculpturing times ranging from the PAB-GBS, PABS, PGBS, and PS, respectively. This can be understood by the effect of the electric field strength (as shown in Figure 5.1) on the tip curvatures of the sample's initial surface morphology, which plays a significant role in this process, as described in the case of the AlMg3 strip. However, in this case, the applied voltage (during the electrochemical sculpturing process) is responsible for the increased sculpturing rate. In addition, the completely sculptured surface between the grit-blasted samples (PAB-GBS and PGBS) and the non-grit-blasted ones (PABS and PS) looks quite different. The grit-blasted ones show a spongy-like structure, while the non-grit-blasted ones show an oriented wavy porous wall structure with interconnected undercuts, as described earlier. The spongy-like structure can be understood as a resultant effect of the defect-minded grit-blasting process, which leads to the surface near individual grain re-orientation and fragmentation.

Further systematic increase of the sculpturing time, as depicted in Figure 4.16, shows no observable difference in the formed structures but rather a reduction in sample thickness (see Table 4.1). This can be explained by the self-similar growth phenomena similar to that in AlMg3 described earlier. However, different concentration of the HNO_3 constituent in the HCl-based seawater-like electrolyte, as shown in Figure 4.18, illustrates the oxidizing capability of HNO_3. Here, a transition is observed from nanometer-scale porous, spongy-pits structures to micrometer-scale, mechanically stable, free-standing wavy wall porous structures, followed by a quasi-flat surface with randomly distributed etch pits. This can be understood by a transition from anisotropic etching to isotropic etching (electropolishing) as the oxidizing power of HNO_3 increases with its increase in concentration in the HCl-based seawater-like electrolyte, hence the higher etching rate [32,153].

In the SST wire, the structure nucleation process and structure formation mechanism are similar to those observed in the SST strip. However, using an HCl-based electrolyte (without HNO_3) at an applied current density of 4 A/cm^2 results in different structure morphology formations on the SST wire surface. This can be attributed to local cracking of the passivating oxide layer, which is mainly dependent on the applied DC voltage, electrolyte concentration,

sculpturing time, electric field strength, and the pristine SST wire surface irregularities resulting from cold working process-induced defects and surface-embedded impurities (as shown in Figure 4.15).

Different surface structures were formed using different electrolyte concentrations, as depicted in Figure 4.25. At lower HCl electrolyte concentrations (0.03 M and 0.25 M), uniformly distributed bowl-like structures are formed with islands of unsculptured surfaces (see Figure 5.3). These structures grow laterally due to preferential etching on the surface near the edges of the bowl-like structures, leading to the formation of broader and deeper bowl-like structures as well as bowl-in-bowl structures at increasing sculpturing time. In contrast, using highly concentrated electrolytes (1 M) leads to the formation of spongy-pit structures, which increase in density with increasing sculpturing time. In 1.6 M electrolytes, a transition from anisotropic to isotropic etching is observed. These results can be understood as a self-amplifying process in which the etching preferentially occurs at the edges of existing structures and grows laterally over time due to more exposed atoms and delayed passivation. The corresponding increase in depth in the low-concentration electrolyte (0.25 M) is at a slower rate compared to the lateral growth. This can be related to the time-dependent formation of the passivating iron oxide and Cr_2O_3 oxide layer in depth [154,155]. This mechanism explains the broadening of the bowl-like structures and the formation of bowl-in-bowl structures on the low electrolyte concentration, while the high electrolyte concentration leads to spongy-pit structures and a tendency towards isotropic etching at the same applied current density of 4 A/cm^2.

Figure 5.3 schematically illustrates the formation and characteristics of the bowl-like structures at a constant current approach using a 0.25 M HCl-based electrolyte and a current density of 4 A/cm^2. As the sculpturing time increases, the bowl-like structures' density decreases while the structures' diameter and depth increase. This is due to the collapse of the structures into one another, reducing the density of the bowl-like structures. This collapse increases the diameter and depth of the bowl-like structures while the broadening of the structures remains relatively constant in all directions [see Figure 4.27 (b)]. In addition, the diameter of the SST wire exhibits a statistically significant difference after the surface pre-treatment processes, regardless of the sculpturing time (see Figure 4.20). This seeming change in the pre-treated SST wire diameter (approximately 1 µm) is attributed to the etching of the native oxide layer and the removal of the embedded particles, as the used digital micrometer gauge for diameter measurement possibly contacted a large number of islands of unsculptured surfaces. These circular contact points (20 mm^2) effectively contact only the nominal wire thickness on the islands of unsculptured surfaces (as shown in Figure 5.4 with the green arrow).

Therefore, the effective wire thickness has no significant effect on the pre-treated SST wire diameter measurements.

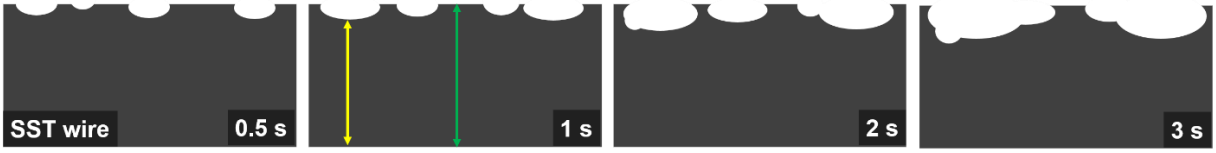

Figure 5.3**:** *Schematic illustration of bowl-like structure formation at the constant current application of 2 A (4 A/cm2) with increasing sculpturing time using 0.25 M HCl-based electrolyte and showing the nominal SST wire thickness (green arrow) and the effective thickness (yellow arrow).*

As the applied current density increases, the density of the bowl-like structure also increases, exhibiting broader structures and sporadically distributed deep bowl-like structures (as shown in Figure 4.28). This can be attributed to the increase in applied DC voltage at each applied current density, which leads to an increase in the number of structure nucleation sites (through high local electrical breakdown) [41] and the rate of bowl-like structure formation.

As schematically illustrated in Figure 5.4, the use of the current pulsing approach results in the formation of a high density of bowl-like structures with smaller structure diameters compared to the constant current approach using 0.25 M HCl-based electrolyte at a current density of 4 A/cm^2 and a total sculpturing time of 1 s [see Figure 4.25 (f) and Figure 4.29]. This can be understood by the time-dependent restrained dissolution process, which enhances passivation of the first-generation bowl-like structures surfaces formed in the first anodic current spike by switching to the cathodic regime. In the cathodic regime, the waiting time has to be chosen in such a way that the difference in the kinetic of the surface passivation formation between the bowl-like structure surface and the islands of unsculptured surfaces is at the maximum. That is, the bowl-like structure surfaces have enough time to passivate, while the degree of surface passivation on the islands of unsculptured surfaces is at the minimum [see Figure 4.29 (a) – (c)] [156]. This mechanism leads to the formation of bowl-like structures on the partially passivated islands of unsculptured surfaces resulting in multiples of generations of bowl-like structures of varying diameters depending on the number of anodic current pulsing spikes, for example, TPS and MPS, as shown in Figure 4.29 and Figure 4.31. However, it is also possible to tune the passivation kinetics to favor the unsculptured surface islands, resulting in the formation of bowl-in-bowl structures.

Figure 5.4**:** *Schematic illustration of bowl-like structure formation at the current pulsing application of 2 A (4 A/cm2) using 0.25 M HCl based electrolyte and 1 s total sculpturing time;* ***(a)*** *One anodic current spike (constant current application),* ***(b)*** *Two anodic regimes current spikes (TPS) and* ***(c)*** *Multiple anodic current spikes (MPS).*

Figure 4.33 (a) - (d) demonstrates that increasing the anodic current pulsing time in individual current spikes using the two anodic regimes pulsing spikes (TPS) approach at a current density of 4 A/cm^2 with a 0.25 M HCl-based electrolyte and a 1 s cathodic regime waiting time results in the broadening of the diameter and increase in depth of the bowl-like structures. In this case, the mechanism of bowl-like structure formation and growth is similar to that observed using a constant current approach with increasing sculpturing time. However, the TPS current pulsing approach as used here leads to a longer total sculpting time, resulting in the formation of a double-fold density of bowl-like structures with smaller diameters than the constant current approach, as shown in Figure 4.25 (e) - (h). This is due to the periodic passivation, hence generational bowl-like structure formation in the TPS approach.

The results of the current pulsing approach, as demonstrated in Figure 4.30 and Figure 4.32, show that there is no statistically significant difference in the wire diameter of the pre-treated SST wire compared to the constant current approach, at a current density of 4 A/cm^2 and a total sculpturing time of 1 s using a 0.25 M HCl-based electrolyte. However, a seeming statistically significant difference in sculptured wire diameter was measured compared to the PS wire diameter, possibly resulting from native oxide etching as previously described.

5.2 Surface wettability measurements

In Figure 4.19, the effect of surface morphology on the water contact angle of the SST strip is presented. The order of decreasing water contact angle is observed as pristine SST strip surface (PS) > grit-blasted SST strip surface > nanoscale sculptured SST strip surface, with the latter exhibiting super-hydrophilicity. This behavior can be explained by the Wenzel model [107], which states that surface roughness, represented by the roughness ratio (r), plays a crucial role in determining the wetting behaviour of a liquid on a surface. According to Wenzel´s model, the roughness ratio (r) is a crucial factor in determining the wetting behaviour of a liquid on a surface (see equation 2.21). The surface roughness can either increase or decrease the

contact angle of the droplet, depending on the surface Young's contact angle *(θ_Y)*. If the θ_Y is above 90°, the surface is hydrophobic, and roughness increases the contact angle of the droplet. Conversely, if the contact angle θ_Y is below 90°, the surface is hydrophilic, and roughness decreases the contact angle of the droplet [102]. This behaviour is due to the fact that the chemical property of the surface determines the wetting behaviour, while surface roughness amplifies the contact angle in the direction of either hydrophobic or hydrophilic [157]. Thus, the super-hydrophilicity observed in the sculptured SST strip surface can be explained by the fact that the contact angle decreases with increasing surface roughness, leading to a roughness ratio ($r > 1$).

5.3 Mechanical testing

5.3.1 Single lap shear tensile test of stainless steel strip composite

Figure 4.21 demonstrate the ultimate shear strength hierarchy of SST – polymer – SST sandwich composite for nanoscale sculptured SST strip 2 surfaces compared to the reference SST strip 2 grit-blasted surface using different types of polymer classes. The nanoscale sculptured SST strip 2 sandwich composite failed cohesively, with a double-fold ultimate shear strength compared to the reference grit-blasted SST strip 2 surfaces, which failed adhesively. The cohesive failure of the sculptured SST strip 2 sandwich composite can be attributed to mechanical interlocking between the wavy-wall porous structure with in-depth undercuts of the SST surface, which, when enclosed with polymer, act as hooks that mechanically interlock the nanoscale sculptured SST strip 2 surface and the polymer (see Figure 4.23). This is schematically depicted in Figure 5.5 (a) and (b), where it can be seen that the porous structure is filled up by the polymer enclosing the undercuts with hook-like features [see Figure. 5.5 (a)]. These undercuts with hook-like features anchor the polymer to the SST surface, preventing delamination under shear load. The failure can occur within the polymer or the SST bulk, depending on the mechanical strength of each component. In the case of the SST – PTU composites, the lower shear and tensile strength of PTU cause the failure to occur within the PTU, as shown in Figure 5.5 (b) schematic. On the other hand, the adhesive failure of the grit-blasted SST sandwich composites is due to the lack of anchoring structures on the grit-blasted surface, which only increases the surface area with poor mechanical hooking features, as shown in Figure 5.5 (c). As a result, the polymer delaminates from the grit-blasted SST surface upon shear testing, as schematically depicted in Figure 5.5 (d).

These results clearly show that the adhesion of the polymers to the mechanical interlocking SST surface structure obtained by nanoscale sculpturing is completely independent of the chemical nature of the investigated polymer classes and always results in a cohesive failure within the polymer. This means that the limiting factor for SST – polymer – SST joints is not the SST surface/polymer interface anymore but the mechanical properties of the polymer itself. This is completely different from the grit-blasted SST surfaces where the limiting factor for the SST – polymer – SST joint is the SST surface/polymer interface which is also similar to [123]. It also demonstrates that surface roughness plays a minor role in achieving high ultimate shear strength in bond structures, but is primarily dependent on interconnected undercuts and mechanical hooking structures [34]. The high values for all the polymers, as well as the relatively small variation in the ultimate shear strengths, indicate that just the (bulk) mechanical properties of the different polymers are leading to the corresponding slight variations as different polymers have different binding energies, rigidity, and surface interactions [158–161]. In addition, the similar failure mechanism (mainly due to slight crack initiation on the sandwich composite sample tips, which further propagates into the polymer) of the sandwich composite in the single-lap shear test is the (only) reason nanoscale sculptured surfaces failed below the polymer's bulk values.

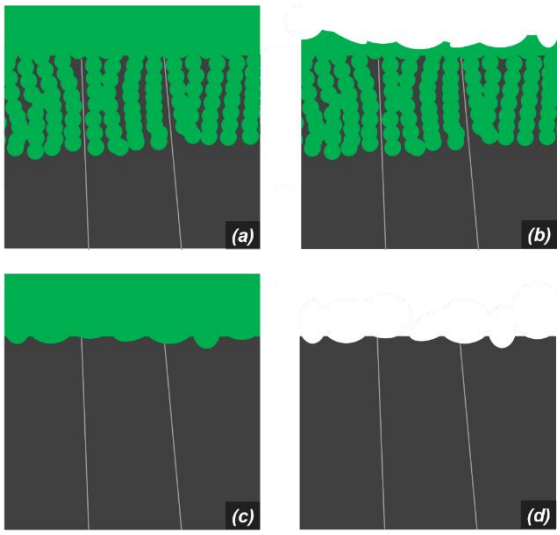

Figure 5.5: *Schematic illustration of polymer-covered SST strip surfaces:* ***(a)*** *before the shear test of the sculptured SST strip,* ***(b)*** *after the failure of the sculptured SST strip, and* ***(c)*** *before the shear test of the grit-blasted SST strip surfaces,* ***(d)*** *after the failure of the grit-blasted SST strip surface.*

5.3.2 Tensile test of surface pretreated stainless steel wire

The bar chart in Figure 4.36 shows the ultimate tensile strength of pristine (PS) SST wire and pre-treated SST wire surfaces obtained through nanoscale sculpturing using a 0.25 M

HCl-based electrolyte at a constant current of 2 A (4 A/cm^2) for 0.5 s, 1 s, 2 s, and 3 s. The chart shows no significant statistical difference in the UTS values of pre-treated SST wire surfaces within the sculpturing times of 0.5 s, 1 s, and 2 s. Therefore, no observable change in the mechanical properties of pre-treated SST wire. In contrast, a significant statistical difference in the UTS value of the 3 s sculpturing times of the pre-treated SST wire is observed. This can be understood from the characteristics of the formed bowl-like structures, which show different degrees of bowl-like structures' density, diameter, and depth [see also Figure 4.27 (a), (c), and (d)] at individual sculpturing times. Here, the depth of the bowl-like structures plays a major role. As schematically illustrated in Figure 5.6 (a) and (b), with the sculpturing times of 0.5 s and 1 s, the bowl-like structure is rather shallow with an effective thickness that leads to localized pre-treated SST wire average thickness reduction of 2.5 % and 4 % respectively. On the other hand, at sculpturing times of 2 s and 3 s, as shown in Figure 5.6 (c) and (d) schematics, the bowl-like structures are deep with an effective thickness that leads to localized pre-treated SST wire average thickness reduction of 5 % and 8 % respectively. This effect statistically leads to no significant difference in UTS between the pristine SST wire and the pre-treated SST wire, retaining the mechanical property at sculpturing times of 0.5 s, 1 s, and 2 s. In contrast, a statistically significant difference in UTS is measured in the 3 s sculpturing, therefore, the change in mechanical property. This change is not due to an overall change in the SST wire microstructure but rather an effect of the localized broadened and deep bowl-like structure acting as a notch under tensile load.

In Figure 4.37, the UTS of a pre-treated SST wire is shown as a function of the cathodic regime waiting time when an anodic current of 2 A (4 A/cm^2) is applied for a total sculpting time of 1 s using a 0.25 M HCl-based electrolyte and a TPS approach. The results indicate that similar to the constant current application for 0.5 s and 1 s, the UTS of the pre-treated SST wire does not differ significantly from that of the pristine SST wire, likely due to the similar sculpturing parameters and the total anodic regime current spike of 1 s. Additionally, the TPS approach leads to a high density of shallow bowl structures with smaller generational bowl-like structures, as shown in Figure 5.3, which helps to preserve the mechanical properties of the pre-treated SST wire by minimizing the average wire effective thickness reduction.

Using similar sculpturing parameters and an MPS approach, as shown in Figure 4.38, there is no statistically significant change in the UTS of the pre-treated SST wire compared to the TPS approach and the pristine SST wire. This result is consistent with the findings obtained using a current pulsing approach and a total sculpting time of 1 s. Additionally, the MPS approach leads to a higher density of small, shallow bowl-like structures compared to the TPS

approach. This high density of small and shallow bowl-like structures enhances the intensity of the surface pre-treatment (cleaning) and as well helps in the preservation of the mechanical properties of the pre-treated SST wire by minimizing the average wire effective thickness reduction.

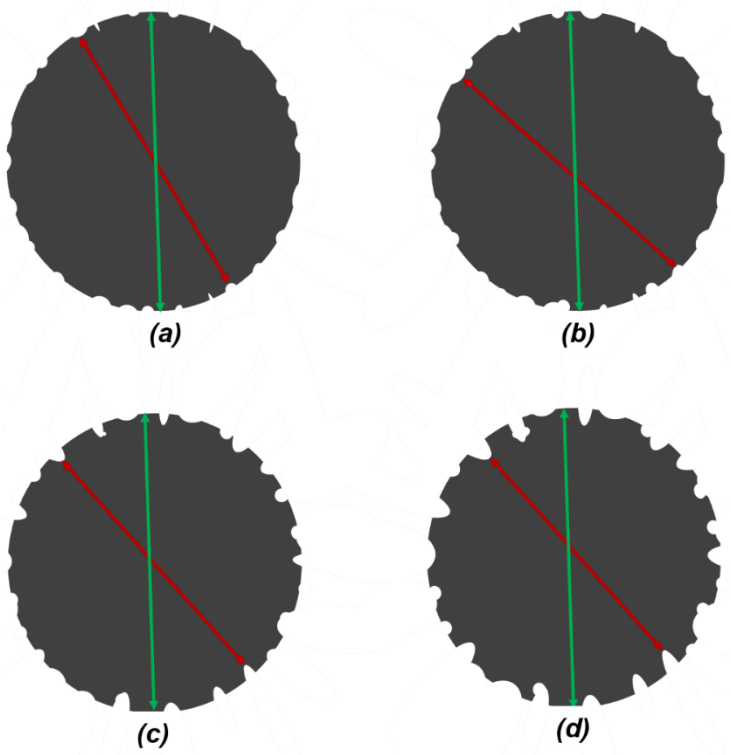

Figure 5.6: *A schematic illustration of the effect of bowl-like structure characteristics on the mechanical property of the SST wire is shown.* ***(a)*** *0.5 s constant current application with 2.5 % effective wire thickness reduction,* ***(b)*** *1 s constant current application with 4 % effective wire thickness reduction,* ***(c)*** *2 s constant current application with 5 % effective wire thickness reduction, and* ***(d)*** *3 s constant current application with 8 % effective wire thickness reduction. The green arrow indicates the nominal SST wire thickness and the red arrow indicates the effective thickness.*

Figure 4.39 shows the UTS of a pre-treated SST wire using an IPT approach. The results indicate that there is no significant change in the UTS of the pre-treated SST wire at anodic current spikes of 0.5 s and 1 s (i.e., total anodic current spikes of 1 s and 2 s, respectively) compared to the PS SST wire thereby preserving the pre-treated SST wire mechanical property. However, there is a statistically significant change in the UTS of the pre-treated SST wire at anodic current spikes of 2 s and 3 s (i.e., total anodic current spikes of 4 s and 6 s respectively), which leads to measurable change in the pre-treated SST wire mechanical property. This can be attributed to the total sculpturing time of 4 s and 6 s, which leads to the formation of deep bowl-like structures, similar to the effect observed using a constant current approach at the sculpturing time of 3 s.

Chapter 6

6.0 Summary & Future research areas

In the framework of this thesis, the pre-treatment of metal surfaces through nanoscale sculpturing is presented. The objective was to investigate the effect of initial surface morphology on the nucleation efficiency of stable mechanical interlocking structures (for the AlMg3 strip and SST strip) and to enhance surface adhesion (for the SST strip). In addition, a novel model has been successfully developed, which improved the surface adhesion property and as well preserved the intrinsic mechanical property of a thin SST wire (< 200 μm) after intense surface pre-treatment through nanoscale sculpturing.

The concept of nanoscale sculpturing aims at modifying the adhesion functionality of metal surfaces, typically through chemical or electrochemical sculpturing processes. This involves crystallographic etching (for AlMg3) or dealloying less noble alloy constituents (for SST) on the surface near grain structures while preserving grain boundaries and intrinsic mechanical properties of the bulk material. By controlling the kinetics of intermediate oxide formation, dissolution, and surface passivation, the process achieves preferential oxidation and dissolution of the slowest oxidizing grains, constituents, and lattice planes. This results in the formation of a sculptured metal surface with stable mechanical interlocking features, improving surface adhesion while maintaining the intrinsic mechanical property of the metal.

In an acidic aqueous electrolyte (7.25 wt. % HCl-based electrolyte), it was discovered that AlMg3 is exceptionally susceptible to the chemical nanoscale sculpturing process resulting from the selective leaching of the ineffective passive magnesium oxide layer, which exposed the bulk aluminium. This resulted in the formation of cubic crystallographic structures due to the preferential passivation of the Al {100} plane. These structures manifested as self-supporting free-standing cubic crystallographic structures, characterized by mechanically stable interlocking surface features. It was found that the efficiency of the nucleation rate of these structures depended on the initial surface morphology of the sample, specifically the degree of surface roughness and the shape of the tip curvatures. The PGBS showed the shortest time to complete structure formation, followed by the PA-GBS and PS, while the PAS had the longest sculpturing time. Additionally, the structure nucleation density and the total sculptured surface area increased with increasing sculpturing time. The structures formed on samples with deep

and sharp tip curvatures (PGBS and PA-GBS) showed higher mass loss compared to those with shallow and quasi-flat surfaces (PS and PAS).

The formation of stable mechanical interlocking structures on SST strips by electrochemical nanoscale sculpturing using seawater-like and dilute HNO_3 resulted from the control of the oxidation and passivation kinetics of the electrolyte composition, which in turn, depended on the electrolyte flow rate and the chosen voltage/current regime. The resulting structures were formed by dealloying less noble components in the alloy and dissolving less stable metal oxides. The efficiency of the nucleation rate of these structures was found to depend on the initial surface morphology of the sample, characterized in particular by the degree of surface roughness and the shape of the tip curvatures. For the non-grit-blasted defect-oriented surfaces (PABS and PS), the structures consisted of a multitude of bowl-like interconnected undercuts of various sizes, which can also intergrow to form larger undercuts with wavy, porous walls, while the grit-blasted surfaces (PGBS and PAB-GBS) consisted of a sponge-like structure. The PABS and PAB-GBS showed the shortest time to complete structure formation, followed by the PGBS, while the PS had the longest sculpturing time. These structures are formed in a self-organized manner. Therefore, the nucleation density, the total sculptured surface area, and the surface texture of the structures vary based on the initial surface morphology and HNO_3 concentration in the electrolyte. Additionally, deep and sharp tip curvature initial surface morphology showed higher mass loss compared to those with shallow and quasi-flat surfaces in the nucleation regime and subsequently grew self-similarly into the depth with increasing sculpturing time.

The sculptured surface of the SST strip achieved through electrochemical nanoscale sculpturing exhibited enhanced wetting behavior and surface adhesion compared to a grit-blasted reference surface *($\theta \approx 70°$)*. The super-hydrophilic nature of the sculptured SST strip surface *($\theta \approx 0°$)* facilitated the complete filling of polymers into the wavy-wall porous structure and interconnected undercuts, resulting in robust mechanical interlocking and improved bonding. This led to a significant increase in the ultimate shear strength (USS) in a single-lap shear test, with at least a two-fold improvement compared to the grit-blasted reference. This significant improvement was observed with various polymers, including acrylates, polyurethanes, and epoxy resins. The analysis of the fracture surfaces revealed that the nanoscale sculptured SST sample experienced cohesive failure within the polymer, while the grit-blasted references exclusively showed adhesive failure at the SST-polymer interface.

The electrochemical nanoscale sculpturing process on SST wire resulted in the formation of distinct structures influenced by factors such as electrolyte concentration, applied

current density, sculpturing time, and surface irregularities. Varying electrolyte concentrations led to the formation of different structures, including uniformly distributed bowl-like structures that grow both laterally and deeper with increasing sculpturing time, spongy-pit structures, and a transition from anisotropic to isotropic etching. The characteristics of these structures were further influenced by the sculpturing time and the use of constant current and current pulsing approaches. The bowl-like structures, particularly when filled with polymers or other materials, demonstrated significant potential for enhancing surface adhesion. This process effectively encloses the hook-like bowl-in-bowl structures, thereby forming a robust joint.

The intrinsic mechanical property of an intensely pre-treated SST wire surface, achieved through electrochemical nanoscale sculpturing using a 0.25 M HCl-based electrolyte at a current density of 4 A/cm^2, remains preserved even after intense surface pre-treatment. Tensile testing revealed that the ultimate tensile strength (UTS) of the pre-treated SST wire, using a constant current approach, did not exhibit a statistically significant difference compared to the pristine SST wire for sculpturing times of 0.5 s, 1 s, and 2 s. However, a statistically significant difference in UTS was observed for a sculpturing time of 3 s compared to the pristine SST wire. Furthermore, using the current pulsing approach for a total sculpturing time of 1 s, irrespective of the number of spikes, the UTS of the pre-treated SST wire exhibited similar results to that of the constant current approach for a total sculpting time of 1 s, as well as the pristine SST wire. However, the UTS was found to be statistically significantly different from the pristine SST wire for sculpturing times exceeding 1 s at individual spikes.

The transfer of the static-laboratory nanoscale sculpturing of SST wire to a dynamic-industrial-large-scale process was successfully achieved using the current pulsing approach. The results showed a high degree of similarity, with no statistically significant difference observed in the thickness of the SST wire between both approaches. Similarly, the UTS of both approaches showed no measurable difference when compared to the pristine wire following the intense surface pre-treatment.

Therefore, the here demonstrated and newly developed model of surface pre-treatment techniques exhibits significant potential for application in various functional coatings, including those with friction-reducing properties, corrosion protection capabilities, and biocompatible characteristics. Furthermore, it is also possible to form high-performance metal/SST coatings, such as Cu/SST, which has already been reported for Al/Cu. The retention of the intrinsic mechanical properties of the SST wire using the current pulsing approach, even in industrial large-scale nanoscale sculpturing, represents a significant improvement and is particularly valuable in the production of a medical guidewire and within the medical industry.

6.1 Future research areas

The addition of copper to aluminum alloy results in enhanced mechanical strength and improved resistance to corrosion. The resulting material possesses a high strength-to-weight ratio, making it a desirable engineering material in fields where weight reduction is a critical consideration, such as aerospace, automotive, and infrastructure. These characteristics render copper-containing aluminum alloys particularly interesting for use in composite materials. Therefore, its surface sculpturing using electrochemical nanoscale sculpturing is recommended. However, its oxidation stability is rather tricky because of its readiness to form a passive protective layer in a corrosive environment [162,163]. Nevertheless, the nanoscale sculpturing current pulsing model in a preliminary experiment leads to successful results.

As shown in Figure 6.1 (a) – (d), one can see cubic crystallographic facets structures with undercuts [see Figure 6.1 (d)] similar to those observed in AlMg3 after a series of multiples of only anodic current regime pulsing spikes (MOPS) application (i.e., without cathodic regime) using 1 wt. % HCl-based electrolyte at 4 A/cm^2 current density.

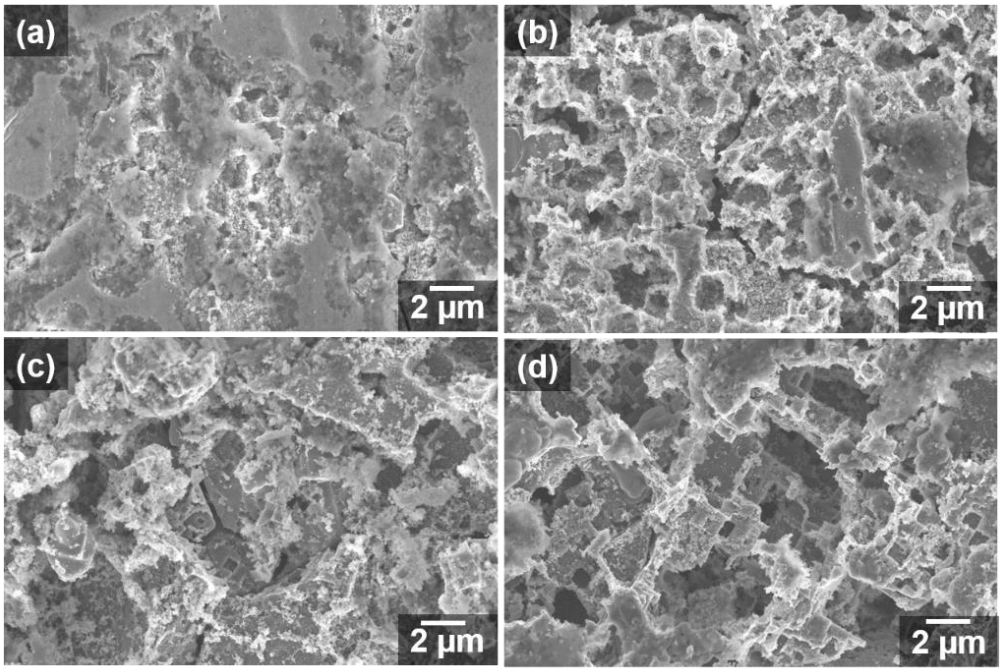

Figure 6.1**:** *SEM images of a copper-rich Al alloy nanoscale sculptured using the MOPS approach with a 1 wt. % HCl-based electrolytes at a current density of 4 A/cm² are presented. These images depict four different conditions:* ***(a)*** *200 ms anodic regime current pulsing spike with two 500 ms waiting times at zero current,* ***(b)*** *600 ms anodic regime current pulsing spike with two 500 ms waiting times at zero current,* ***(c)*** *1200 ms anodic regime current pulsing spike with two 500 ms waiting times at zero current, and* ***(d)*** *1200 ms anodic regime current pulsing spike with five 500 ms waiting times at zero current.*

Structural steel is a construction material with a wide range of applications where high strength and high load-carrying capacity such as tall buildings, bridges, railway tracks, etc., are very crucial. As a result, a wide range of structural steel grades is available, with the most popular being ASTM A572 and ASTM A36. While other structural steel grades (A514) have closely resembling structures, they may likewise have extra compounds or have gone through extra preparation.[164]. The major constituents of structural steel, which are the fundamental factor that characterizes the mechanical properties, are Manganese (1.60 % max), Silicon (0.50 % max), Phosphorus (0.025 % max), Carbon (0.12 max), and Iron (rest). However, the alloy composition is such that the oxidation process (rusting), when exposed or in contact with the oxidizing atmosphere, leads to a complete deterioration of its physical, chemical, and mechanical properties with time [165]. Therefore, enhancing surface functionality through nanoscale sculpturing will improve surface adhesion through stable mechanical interlocking structure formation. This will improve the stability of the surface coating, i.e., after a complete filling of a coating material such as polymer into the mechanical interlocking structure. This could also be tailored for a wide range of applications, such as composite formation and joining with other metals.

Appendix A

Static to dynamic nanoscale sculpturing of stainless steel wire

The findings from static laboratory nanoscale sculpturing of stainless steel (SST) wire were successfully replicated in a dynamic industrial large-scale nanoscale sculpturing. The two anodic regime pulsing spikes (TPS) current pulsing approach was used with an HCl-based electrolyte at a current density of 4 A/cm^2 and a sculpturing time of 0.5 s per anodic current pulsing spike (for a total sculpturing time of 1 s). As shown in Appendix Figure 1 SEM images, the results obtained displayed similar characteristics, including the formation of bowl-like structures, which are quite similar in structure density, diameter, generational bowl-like structure formation, bowl-in-bowl structure formation, and distributed islands of unsculptured surfaces.

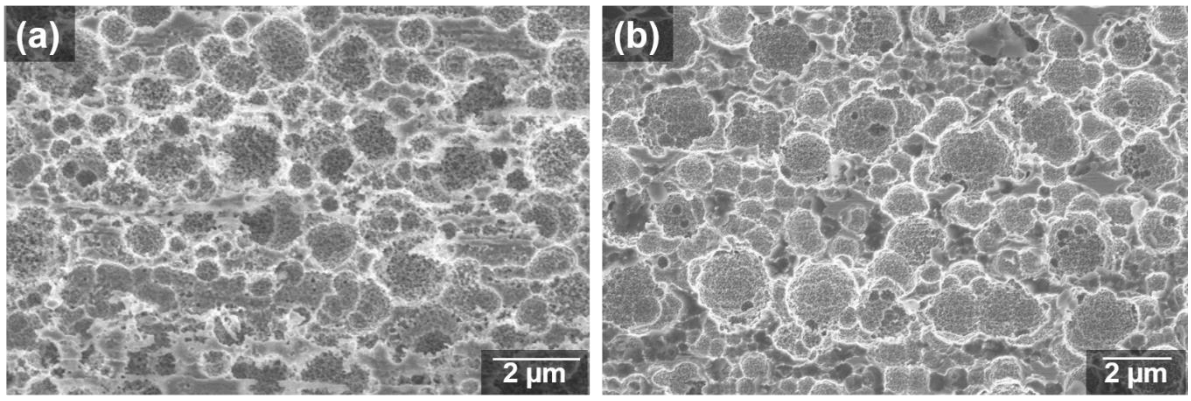

Appendix Figure 1: *SEM images of sculptured SST wire using the TPS current pulsing approach;* ***(a)*** *static nanoscale sculpturing, and* ***(b)*** *dynamic nanoscale sculpturing.*

Similarly, the dynamic nanoscale sculpturing process using the multiple anodic pulsing spikes (MPS) current pulsing approach also resulted in a higher density of bowl-like structures with smaller structure diameters and randomly distributed islands of unsculptured surfaces [see Appendix Figure 2 (b)]. This is due to generational bowl-like structure formation, similar to those observed in the static nanoscale sculpturing [see Appendix Figure 2 (a)]. Additionally, 12 km of SST wire was sculptured in 8 hrs [see Appendix Figure 2 (d) images] using the MPS current pulsing approach with three anodic current regimes and two cathodic waiting times regimes at a total sculpturing time of 0.75 s.

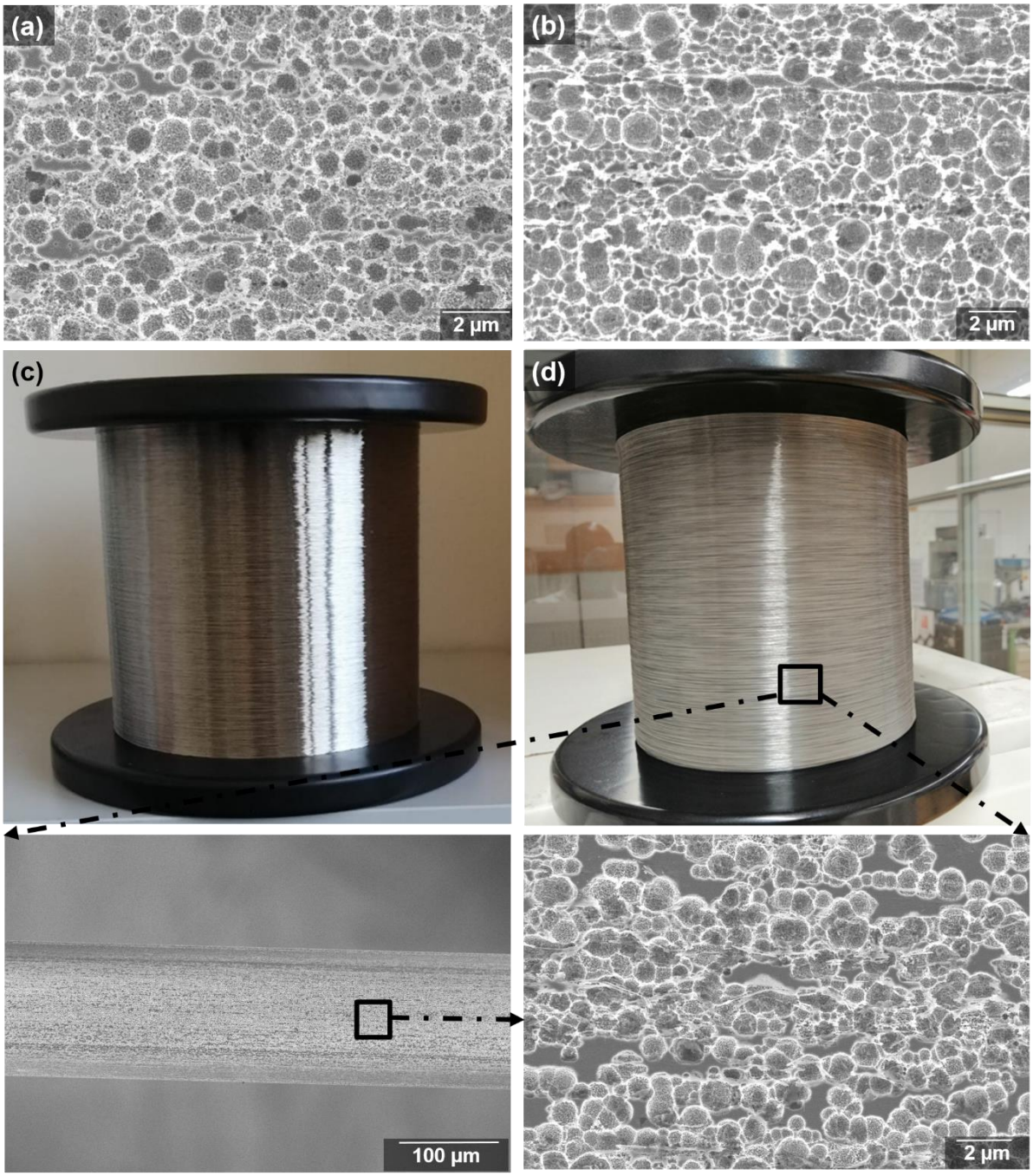

Appendix Figure 2: *SEM images of sculptured SST wire using the MPS current pulsing approach;* ***(a)*** *static nanoscale sculpturing with [2* ***A*** *(0.5 s) –* ***C*** *(1 s) – 2* ***A*** *(0.25 s) –* ***C*** *(1 s) – 2* ***A*** *(0.25 s)],* ***(b)*** *dynamic nanoscale sculpturing with [2* ***A*** *(0.25 s) –* ***C*** *(0.25 s) – 2* ***A*** *(0.25 s) –* ***C*** *(0.25 s) – 2* ***A*** *(0.25 s)],* ***(c)*** *unsculptured SST wire, and* ***(d)*** *sculptured SST wire (12 km) using the MPS current pulsing approach as shown in magnified image with [1* ***A*** *(0.25 s) –* ***C*** *(0.25 s) – 1* ***A*** *(0.25 s) –* ***C*** *(0.25 s) – 1.5* ***A*** *(0.25 s)].*

The dynamic nanoscale sculpturing using the MPS approach showed a large degree of freedom in forming different bowl-like structure morphologies by simply increasing and interchanging the applied DC voltage in the anodic regimes (as depicted in Appendix Figure 3). This result is closely related to the observed effect in the static nanoscale sculpturing, which

was achieved by interchanging the sculpturing time in the first and last anodic regimes, as depicted in Figure 4.25. Through this modification, the rolling speed of the SST wire was increased, resulting in the successful pre-treatment of 28 km of SST wire within 6 hrs.

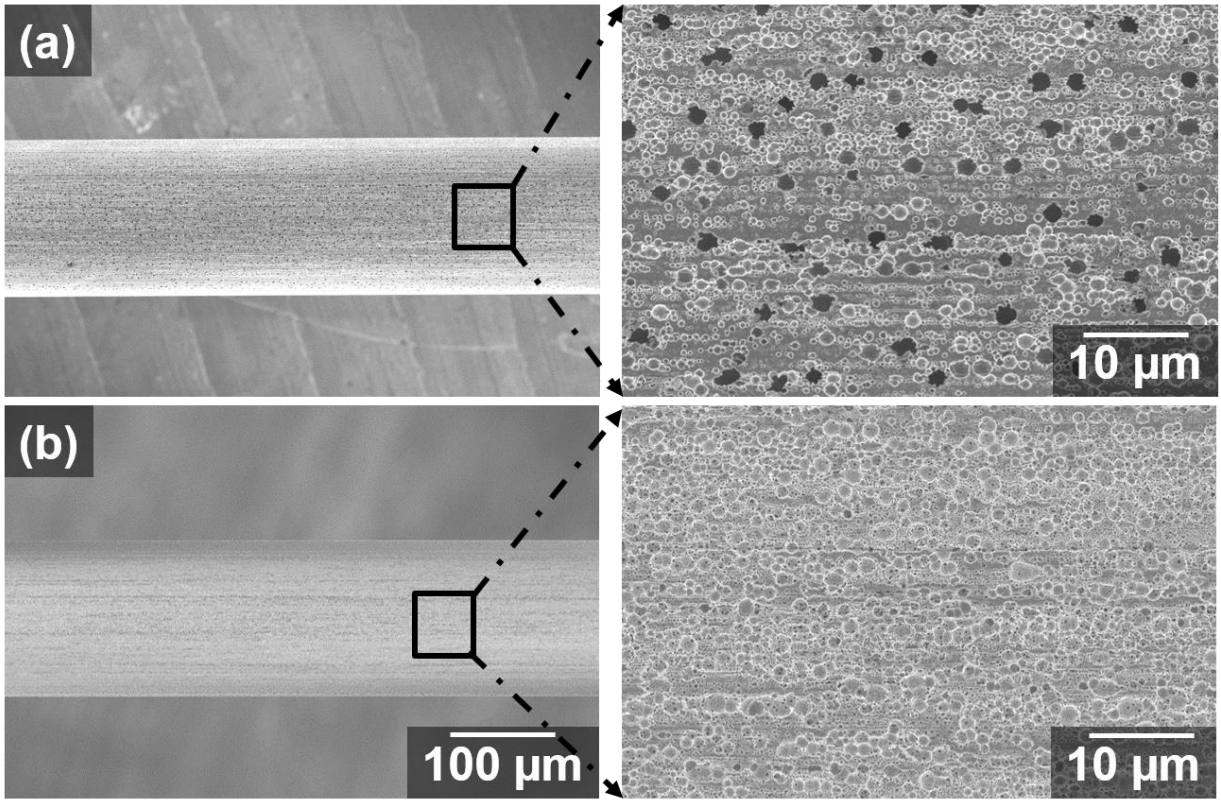

Appendix Figure 3: *SEM images of dynamically pre-treated SST wire by interchanging the applied DC voltage in the first and last anodic regimes at 0.75 s sculpturing time respectively* ***(a)*** *A (2 A) – C – A (2 A) – (C) – A (6 A), and* ***(b)*** *A (6 A) – C – A (2 A) – (C) – A (2 A).*

Furthermore, the mechanical properties of dynamically sculptured SST wire were evaluated using a tensile test. As shown in the bar chart in Appendix Figure 4, irrespective of the sculpturing approach, there was no statistically significant difference in the ultimate tensile strength (UTS) of the SST wire between the static and dynamic sculpturing processes, as compared to the pristine SST wire. In addition, the thickness of the dynamically sculptured SST wire, which may be influenced by the presence of randomly distributed islands of unsculptured surfaces, was found to be within the range of 150.80 ± 0.6 µm and did not show a statistically significant difference compared to the statically sculptured SST wire.

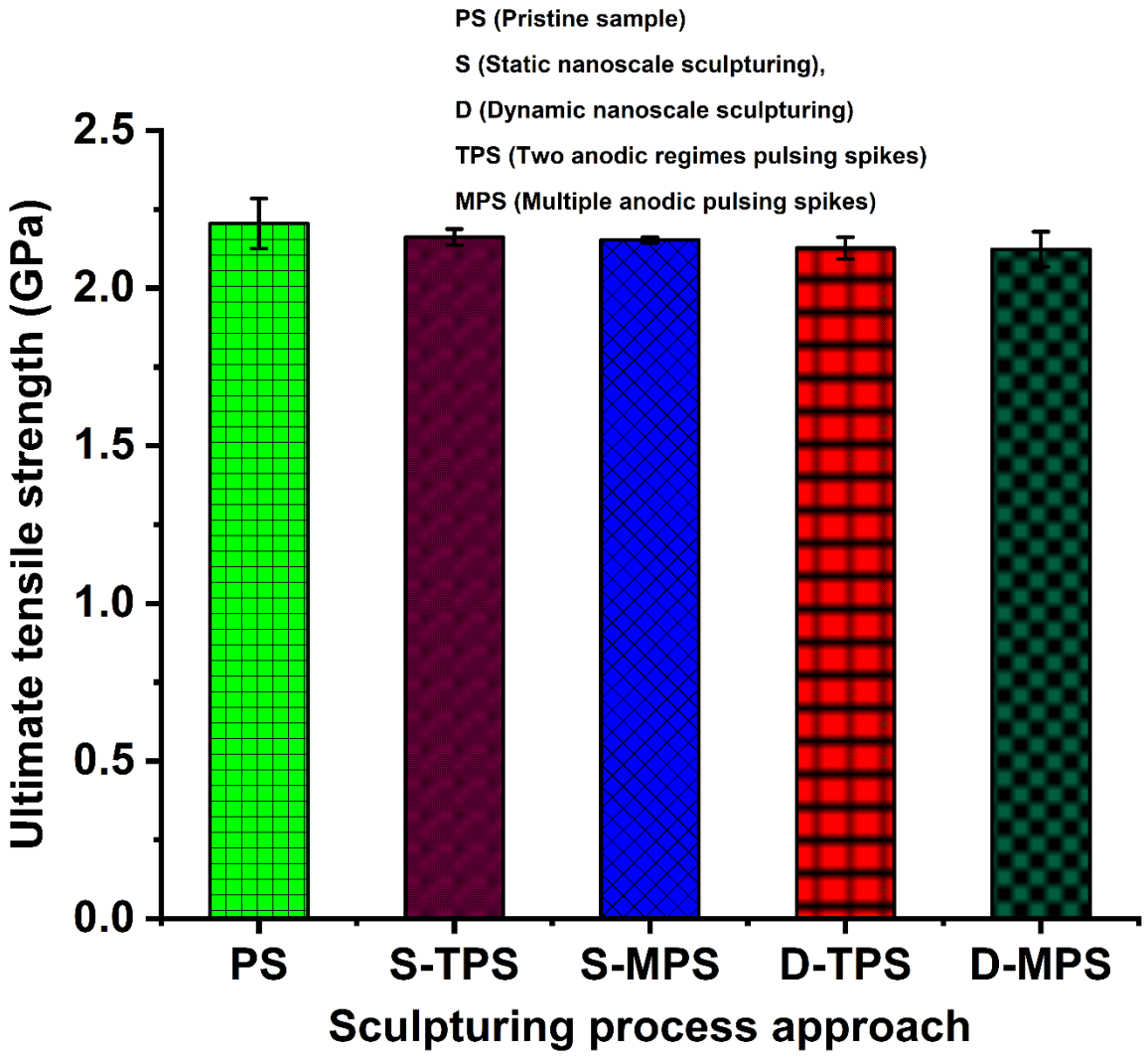

Appendix Figure 4: *Ultimate tensile strength of statistically and dynamically nanoscale sculptured SST wire using the TPS and MPS sculpturing approaches. For statistical analysis of the mean values of tensile strength, a one-way ANOVA followed by a Tukey test was performed. The PS compared to the two sculpturing approaches showed no significant difference between each other ($p > 0.05$).*

Appendix B

Improved surface adhesion of the pre-treated stainless steel wire

Preliminary coating experiments were performed on both pristine and pre-treated SST wires. This was achieved by passing the SST wires through a fully saturated felt material, which was impregnated with a green polyamide-imides base coat in a water-based solvent solution. The coated SST wires were dried for 1 hr in air and an oven at 200 °C for 1 hr. The results were as depicted in Appendix Figure 5 after the coated SST wires underwent a severe bending of approximately 270°. The results showed that the pristine SST wire surface exhibited delamination of the polymer base coat at the edge of the severe bending as a result of poor interface adhesion due to inadequate mechanical interlocking [see Appendix Figure 5 (a) insert]. In contrast, the pre-treated SST wire surface displayed no observable delamination or pilling of the polymer base-coat at the edge of the severe bending [see Appendix Figure 5 (b) insert]. This improvement in adhesion is a result of the presence of the bowl-like structures, which facilitated strong interface adhesion through mechanical interlocking after complete penetration of the polymer base-coat into the bowl-like structures.

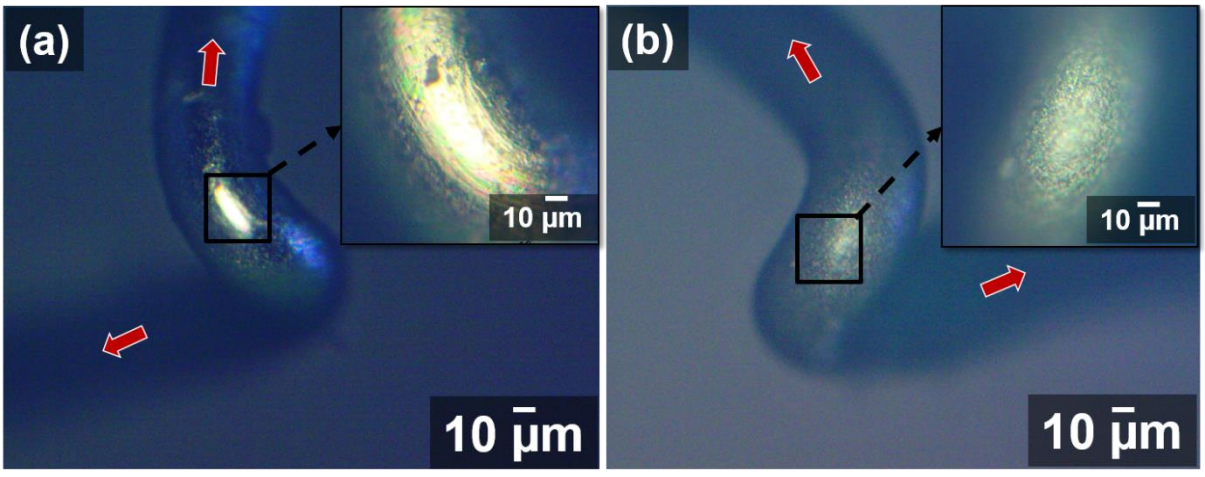

Appendix Figure 5: *Confocal microscope images of coated SST wires showing their surface adhesion properties after a severe bend test;* ***(a)*** *base-coat delamination at the edge of the severe bending of the pristine SST wire surface, and* ***(b)*** *no observable base-coat delamination at the edge of the severe bending of the pre-treated SST wire. The red arrows showed the direction of pulling during bending.*

Similarly, pre-treated SST wires (as depicted in Appendix Figure 3) coated using an industrial large-scale automated SST wire coating process (Meyband & Draht, Bad Arolsen,

Germany) showed no observable delamination of the base coat at the edge of the severe bending and breaking points [see Appendix Figure (a) and (b)]. This demonstrates the large degree of freedom in the morphology of the bowl-like structures using this intense surface pre-treatment process. Additionally, the top layer of the base coat exhibited an average roughness of 0.6 µm and 0.8 µm respectively, which is less than 1 µm average roughness and thus indicative of a quasi-flat surface coating layer.

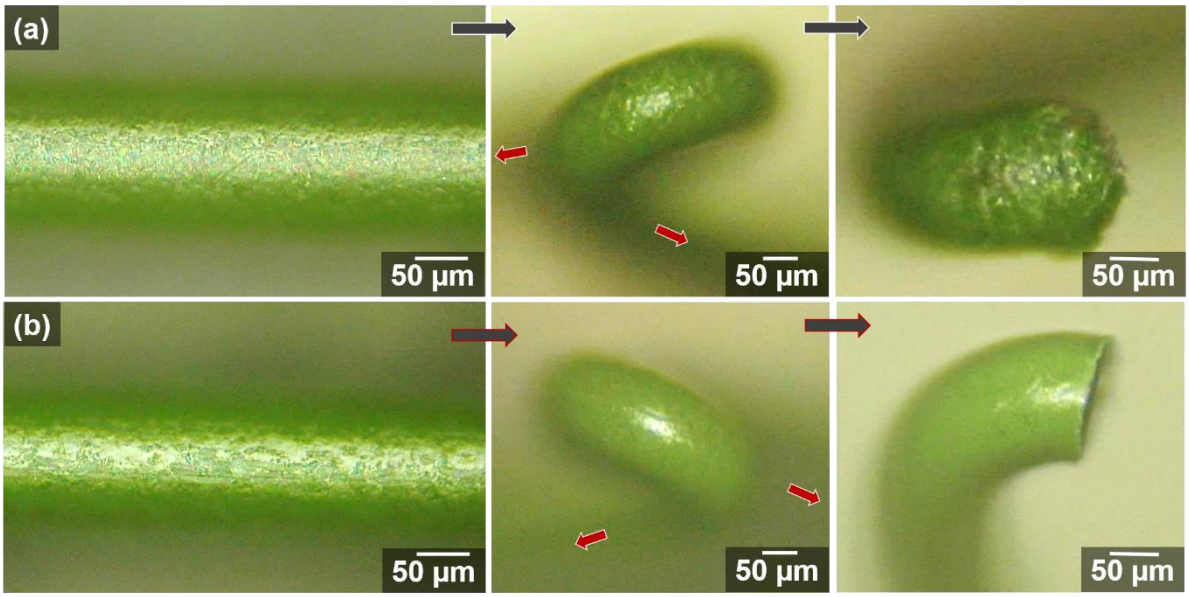

Appendix Figure 6: *Confocal microscope images of coated SST wires showing their surface adhesion properties after a severe bend test to breaking and the red arrows showing the directions of pulling;* ***(a)*** *A (2 A) – C – A (2 A) – (C) – A (6 A), and* ***(b)*** *A (6 A) – C – A (2 A) – (C) – A (2 A). No observable base-coat delamination at the edge of the severe bending and breaking of the pre-treated SST wires.*

As shown in Appendix Figure 7(a) squared area, the cross-sectional view of the coated pre-treated SST wire depicted in Appendix Figure 6 (a) exhibits complete penetration of the base-coat into the bowl-like structures, resulting in strong adhesion through mechanical interlocking, as previously discussed. This finding highlights the potential for the use of different polymers (see Figure 4.34) in coating the pre-treated SST wire surface. Furthermore, an EDX analysis of the cross-section of the coated pre-treated SST wire indicated a quasi-uniform thickness of the base-coat layer, as depicted in Appendix Figure 7 (b). This observation, along with the average surface roughness of the base-coat top layer, suggests that the bowl-like structure topography has no significant effect on the base-coat thickness distribution and top layer flatness. This can be attributed to the presence of unstructured surface islands that compensate for thickness variations by releasing excess base-coat material to neighboring bowl-like structures during the coating process.

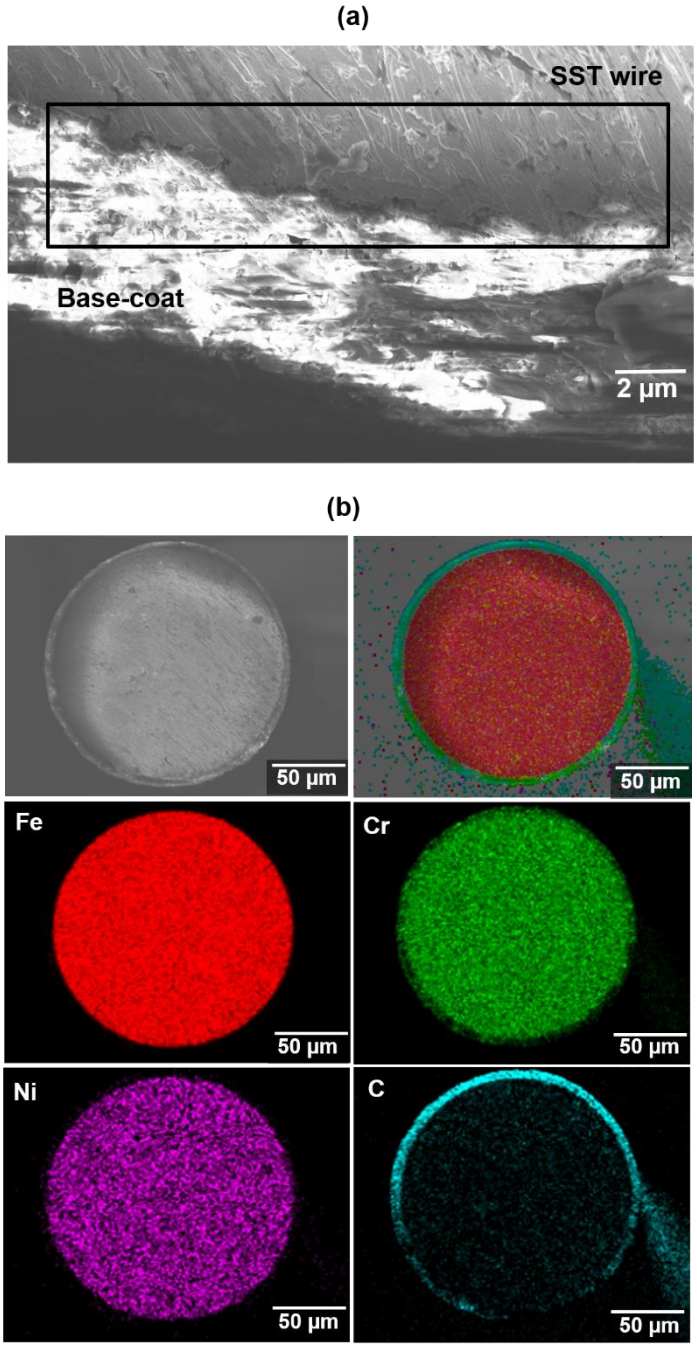

Appendix Figure 7: *EDX analysis of the cross-sectional view of the coated pre-treated SST wire showing: (a) the complete penetration of the base-coat into the bowl-like structures, and (b) the quasi-uniformly distributed base-coat thickness layer.*

A tensile test was performed on pristine SST wire, pre-treated SST wire, and coated pre-treated SST wire. The results, as depicted in Appendix Figure 8, indicate that all three samples exhibit similar UTS of 2.3 GPa. The initial linear regime, indicated by the dotted green arrow, is attributed to the slip-to-grip interaction of the SST wire with the tensile test machine holder. Furthermore, all three samples displayed similar linear increase with similar slopes (see blue dotted arrow in Appendix Figure 7) until breaking points. These results suggest that the intense

pre-treatment process did not alter the microstructure of the SST wire and thus, its mechanical properties such as brittleness remain unchanged [see also Figure 2.23 (a)]. The retention of the intrinsic brittleness of the SST wire is crucial as it is a vital factor in the SST wire spring manufacturing, which is used in the medical guidewire.

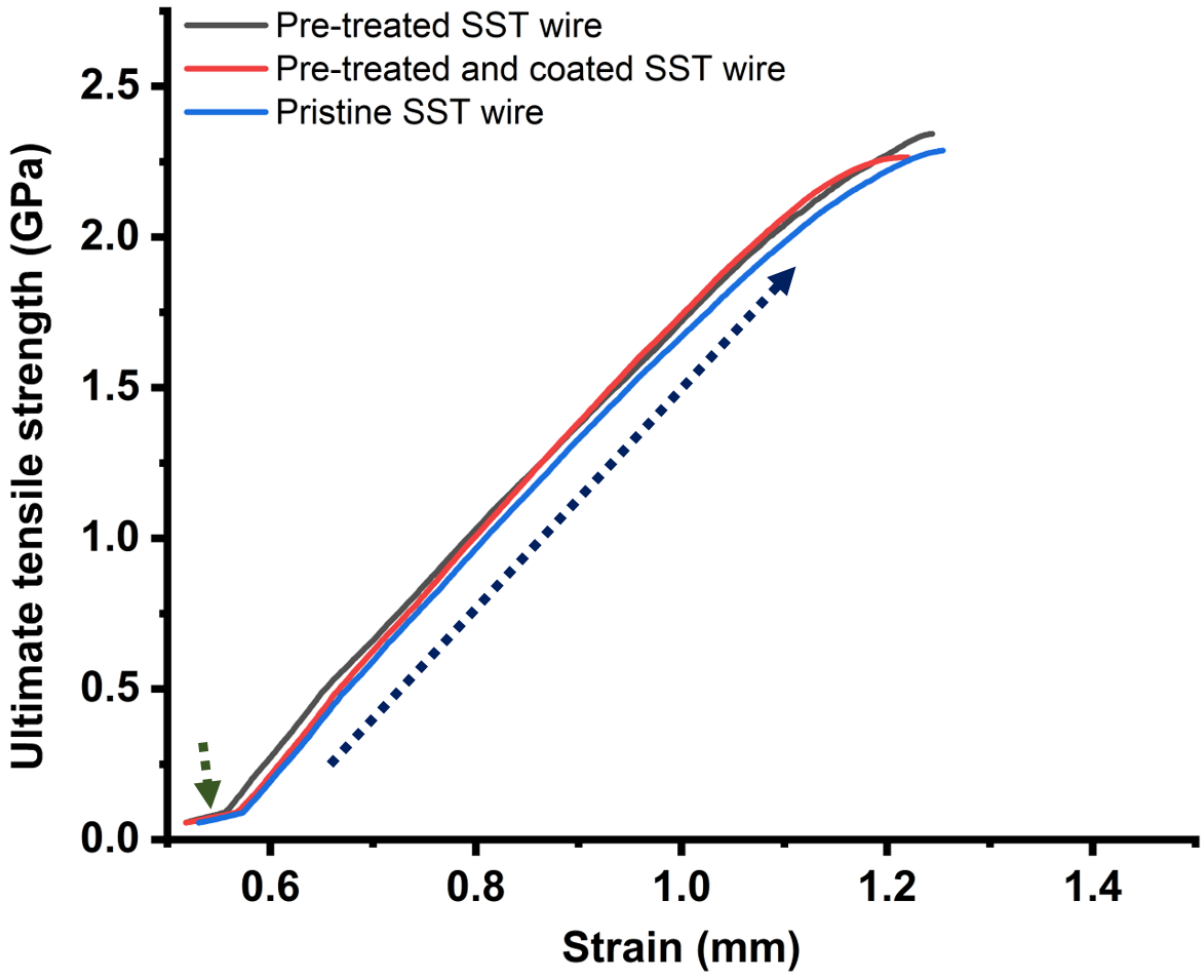

Appendix Figure 8: *The Ultimate tensile strength-strain curves of the tensile test of the pristine, pre-treated, and coated pre-treated SST wires.*

Bibliography

[1] M. Pearce, The 'Copper Age'—A History of the Concept, J. World Prehistory. 32 (2019) 229–250. https://doi.org/10.1007/s10963-019-09134-z.

[2] E.N. Chernykh, Ancient Metallurgy in the USSR. The Early Metal Age, Cambridge university press, 1992.

[3] P.T. Summers, Y. Chen, C.M. Rippe, B. Allen, A.P. Mouritz, S.W. Case, B.Y. Lattimer, Overview of aluminum alloy mechanical properties during and after fires, Fire Sci. Rev. 4 (2015). https://doi.org/10.1186/s40038-015-0007-5.

[4] J. Hirsch, Aluminium alloys for automotive application, Mater. Sci. Forum. 242 (1997) 33–50. https://doi.org/10.4028/www.scientific.net/msf.242.33.

[5] A.T. Kermanidis, Aircraft Aluminum Alloys: Applications and Future Trends BT - Revolutionizing Aircraft Materials and Processes, (2020) 21–55. https://doi.org/10.1007/978-3-030-35346-9_2.

[6] L. Zhu, N. Li, P.R.N. Childs, Light-weighting in aerospace component and system design, Propuls. Power Res. 7 (2018) 103–119. https://doi.org/10.1016/j.jppr.2018.04.001.

[7] P. h. Decléty, Metals Used in the Food Industry, Encycl. Food Sci. Nutr. (2003) 3869–3876. https://doi.org/10.1016/b0-12-227055-x/00772-0.

[8] S. Samavedi, L.K. Poindexter, M. Van Dyke, A.S. Goldstein, Synthetic biomaterials for regenerative medicine applications, Elsevier Inc., 2014. https://doi.org/10.1016/B978-0-12-398523-1.00007-0.

[9] A. Saha Podder, A. Bhanja, Applications of stainless steel in automobile industry, Adv. Mater. Res. 794 (2013) 731–740. https://doi.org/10.4028/www.scientific.net/AMR.794.731.

[10] R.M. Wang, S.R. Zheng, Y.P. Zheng, Polymer matrix composites and technology, 2011. https://doi.org/10.1533/9780857092229.

[11] Y.Y. Kolbovskti, N.P. Shanin, The classification of composite materials, Sov. Powder Metall. Met. Ceram. 17 (1978) 649–650. https://doi.org/10.1007/BF00797347.

[12] V. V. Vasiliev, E. V. Morozov, Advanced Mechanics of Composite Materials and Structures, (2018) 882.

[13] H.M.S. Iqbal, S. Bhowmik, R. Benedictus, Study on the effect of surface morphology on adhesion properties of polybenzimidazole adhesive bonded composite joints, Int. J. Adhes. Adhes. 72 (2017) 43–50. https://doi.org/10.1016/j.ijadhadh.2016.10.002.

[14] R.F. Wegman, Surface Preparation Technique for Adhesive Bonding, Noyes Publ. (1985) 66–77.

[15] J.I. Iribarren-Mateos, I. Buj-Corral, J. Vivancos-Calvet, C. Alemán, J.I. Iribarren, E. Armelin, Silane and epoxy coatings: A bilayer system to protect AA2024 alloy, Prog. Org. Coatings. 81 (2015) 47–57. https://doi.org/10.1016/j.porgcoat.2014.12.014.

[16] B.A. Hariss. A.F, Effects of grit-blasting on surface properties for adhesion, Int. J.

Adhesion & Adhesives. 19 (1999) 445–452.

[17] T. Hisakado, The influence of surface roughness on abrasive wear, Wear. 41 (1977) 179–190. https://doi.org/10.1016/0043-1648(77)90200-9.

[18] J. W. McBain, and D.G.H. On adhesives and adhesives actions, J. Phys. Chem. 2 (1925) 188–204.

[19] A.J. Kinloch, The science of adhesion - Part 1 Surface and interfacial aspects, J. Mater. Sci. 17 (1982) 617–651. https://doi.org/10.1007/BF00540361.

[20] C.W. Jennings, Surface roughness and bond strength of adhesives1, J. Adhes. 4 (1972) 25–38. https://doi.org/10.1080/00218467208072208.

[21] M. Baytekin-Gerngross, M.D. Gerngross, J. Carstensen, R. Adelung, Making metal surfaces strong, resistant, and multifunctional by nanoscale-sculpturing, Nanoscale Horizons. 1 (2016) 467–472. https://doi.org/10.1039/c6nh00140h.

[22] E. Sancaktar, R. Gomatam, A study on the effects of surface roughness on the strength of single lap joints, J. Adhes. Sci. Technol. 15 (2001) 97–117. https://doi.org/10.1163/156856101743346.

[23] M. Baytekin-Gerngross, M.-D. Gerngross, J. Carstensen, R. Adelung, Surface Structuring of Ti-Al-V and Al-Mg Alloys by Chemical Etching for Advanced Polymer Adhesion, ECS Trans. 66 (2015) 19–27. https://doi.org/10.1149/06622.0019ecst.

[24] J.P.B. van Dam, S.T. Abrahami, A. Yilmaz, Y. Gonzalez-Garcia, H. Terryn, J.M.C. Mol, Effect of surface roughness and chemistry on the adhesion and durability of a steel-epoxy adhesive interface, Int. J. Adhes. Adhes. 96 (2020) 102450. https://doi.org/10.1016/j.ijadhadh.2019.102450.

[25] C. Mandolfino, E. Lertora, S. Genna, C. Leone, C. Gambaro, Effect of laser and plasma surface cleaning on mechanical properties of adhesively bonded joints, Procedia CIRP. 33 (2015) 458–463. https://doi.org/10.1016/j.procir.2015.06.054.

[26] J.R.J. Wingfield, Treatment of composite surfaces for adhesive bonding, Int. J. Adhes. Adhes. 13 (1993) 151–156. https://doi.org/10.1016/0143-7496(93)90036-9.

[27] B.G. Yacobi, S. Martin, K. Davis, A. Hudson, M. Hubert, Adhesive bonding in microelectronics and photonics, J. Appl. Phys. 91 (2002) 6227–6262. https://doi.org/10.1063/1.1467950.

[28] L. Surface, B.M.L. Hao, J. Lawrence, Laser Surface Treatment of Bio-Implant Materials Laser Surface Treatment of Bio-Implant Materials, 2005.

[29] U. Beck, R. Lange, H.G. Neumann, Micro-plasma textured Ti-implant surfaces, Biomol. Eng. 24 (2007) 47–51. https://doi.org/10.1016/j.bioeng.2006.05.009.

[30] A.Y. Vorobyev, C. Guo, Multifunctional surfaces produced by femtosecond laser pulses, J. Appl. Phys. 117 (2015). https://doi.org/10.1063/1.4905616.

[31] M. Stöver, M. Renke-Gluszko, T. Schratzenstaller, J. Will, N. Klink, B. Behnisch, A. Kastrati, R. Wessely, J. Hausleiter, A. Schömig, E. Wintermantel, Microstructuring of stainless steel implants by electrochemical etching, J. Mater. Sci. 41 (2006) 5569–5575. https://doi.org/10.1007/s10853-006-0257-7.

[32] C.O. Kalu, M. Hoppe, I. Hölken, M. Baytekin-Gerngross, M.D. Gerngross, J. Carstensen, R. Adelung, Formation of micro-mechanical interlocking sites by nanoscale sculpturing for composites or hybrid materials with stainless steel, J. Mater. Res. 35 (2020) 3145–3156. https://doi.org/10.1557/jmr.2020.284.

[33] M. Baytekin Gerngroß, Nanoscale sculpturing of metals and its applications, CAU Kiel, Germany, 2018. https://macau.uni-kiel.de/receive/diss_mods_00023801.

[34] T. Kleffel, D. Drummer, Investigating the suitability of roughness parameters to assess the bond strength of polymer-metal hybrid structures with mechanical adhesion, Compos. Part B Eng. 117 (2017) 20–25. https://doi.org/10.1016/j.compositesb.2017.02.042.

[35] P. Mahmoudi Hashemi, E. Borhani, M.S. Nourbakhsh, A review on nanostructured stainless steel implants for biomedical application, Nanomedicine J. 3 (2016) 202–216. https://doi.org/10.22038/nmj.2016.7574.

[36] K.R. Hebert, Kinetics of anodic oxidation of aluminum and titanium: Formation of porous alumina and titanium oxide nanotube layers, Elsevier, 2018. https://doi.org/10.1016/B978-0-12-409547-2.13628-5.

[37] B. Tribollet, V. Vivier, M.E. Orazem, EIS technique in passivity studies: Determination of the dielectric properties of passive films, Elsevier, 2018. https://doi.org/10.1016/B978-0-12-409547-2.13817-X.

[38] W. Plieth, Oxides, and Semiconductors, Electrochem. Mater. Sci. (2008) 263–290. https://doi.org/10.1016/b978-044452792-9.50011-7.

[39] J. Knobloch, and B.V. A. Goetzberger, Crystalline Silicon Solar Cells: Technology and Systems Applications, Wiley, 1998.

[40] D. Der Ingenieurwissenschaften, G. Rojas, Mesoporous Germanium Layer Formation by Electrochemical Etching, (2010).

[41] V. Lehmann, Electrochemistry of Silicon: Instrumentation, Science, Materials and Applications., Wiley-VCH Verlag GmbH, 2002.

[42] Krishnan Rajeshwar, Fundamentals of Semiconductor Electrochemistry and Photoelectrochemistry, Encycl. Electrochem. (2002). https://doi.org/10.1002/9783527610426.bard060001.

[43] J.R. Davis, Alloying: Understanding the Basics, ASM Int. (2001) 351–416. https://doi.org/DOI:10.1361/autb2001p351.

[44] R. Kotipalli, R. Delamare, O. Poncelet, X. Tang, L.A. Francis, D. Flandre, Passivation effects of atomic-layer-deposited aluminum oxide, EPJ Photovoltaics. 4 (2013) 1–8. https://doi.org/10.1051/epjpv/2013023.

[45] L. Avala., Concepts in Physical Metallurgy, Morgan and Claypool. (2017).

[46] J.G. Kaufman, Introduction to Aluminum alloys and temper, 2000th ed., ASM International, Columbus, Ohio, 1931. http://www.asminternational.org.

[47] R. Singh, Physical Metallurgy, Appl. Weld. Eng. (2016) 13–26. https://doi.org/10.1016/b978-0-12-804176-5.00003-7.

[48] D.E. Laughlin, Magnetic Transformations and Phase Diagrams, Metall. Mater. Trans. A Phys. Metall. Mater. Sci. 50 (2019) 2555–2569. https://doi.org/10.1007/s11661-019-05214-z.

[49] O. Mathon, F. Baudelet, J.P. Itié, A. Polian, M. D'Astuto, J.C. Chervin, S. Pascarelli, Dynamics of the magnetic and structural α-ε phase transition in iron, Phys. Rev. Lett. 93 (2004) 1–4. https://doi.org/10.1103/PhysRevLett.93.255503.

[50] T. Massalski, P. Submanian, H. Okamoto, Binary Alloy Phase Diagrams 2nd ed. (ASM

International Materials Park, OH), 1998.

[51] J. W.D. Forgeng and W.D. Foreng, "Carbon-Chromium Iron," Metals Handbook, 8th, vol 8 ed., ASM, Metal Park, OH, 1973.

[52] B. Leffler, High-performance stainless steel, http://www.outokumpu.com/, (2017).

[53] S. Paul, C. Mandal, Biocompatible coated 304 stainless steel as superior corrosion-resistant implant material to 316L steel, J. Mater. Eng. Perform. 22 (2013) 3147–3154. https://doi.org/10.1007/s11665-013-0590-3.

[54] M. Nakamura, N. Sato, N. Hoshi, O. Sakata, Outer Helmholtz plane of the electrical double layer formed at the solid electrode-liquid interface, ChemPhysChem. 12 (2011) 1430–1434. https://doi.org/10.1002/cphc.201100011.

[55] X. Wang, K. Liu, J. Wu, Demystifying the Stern layer at a metal-electrolyte interface: Local dielectric constant, specific ion adsorption, and partial charge transfer, J. Chem. Phys. 154 (2021). https://doi.org/10.1063/5.0043963.

[56] D.C. Grahame, The electrical double layer and the theory of electrocapillarity, Chem. Rev. 41 (1947) 441–501. https://doi.org/10.1021/cr60130a002.

[57] T.H.E. Electric, F. Field, Fundamentals of Electric Fields, Electromagn. Explain. (2002) 25–49. https://doi.org/10.1016/b978-075067403-4/50003-3.

[58] Bo Chen, Caiwu Liang, Wentao Yao, Yuanzheng Cui, Shengyu Hu, Peichao Zou, Hua Zhang, Hong Jin Fan, and C.Y. Peng Liu, Tip-Enhanced Electric Field: A New Mechanism Promoting Mass Transfer in Oxygen Evolution Reactions, Adv.Mater.,. 33 (2021). https://doi.org/DOI: 10.1002/adma.202007377.

[59] https://www.physicsclassroom.com/class/estatics/Lesson-4/Electric-Fields-and-Conductors.

[60] G. Moddel, S. Grover, Rectenna solar cells, Rectenna Sol. Cells. 9781461437 (2013) 1–399. https://doi.org/10.1007/978-1-4614-3716-1.

[61] B. Da Costa Fernandes, M. Pfiffer, P. Cormont, J. Neauport, Understanding the effect of wet etching on damage resistance of surface scratches, Sci. Rep. 8 (2018) 1–9. https://doi.org/10.1038/s41598-018-19716-0.

[62] B. Lee, I. Yun, Effect of different etching processes on edge breakdown suppression for planar InP/InGaAs avalanche photodiodes, Microelectronics J. 33 (2002) 645–649. https://doi.org/10.1016/S0026-2692(02)00032-0.

[63] I. Sevim, Effect of Abrasive Particle Size on Abrasive Wear Resistance in Otomotive Steels, Tribol. Eng. (2013). https://doi.org/10.5772/55914.

[64] W.T. Harris, Chemical Machining: The Technology of Cutting Materials by Etching., Clarendon Press, Oxford [England], 1976.

[65] M.C. Sanz, Process of chemically milling structural shapes and resultant article, Patent no.: 2,739,047, USA, 1956.

[66] O. Çakir, Chemical etching of aluminium, J. Mater. Process. Technol. 199 (2008) 337–340. https://doi.org/10.1016/j.jmatprotec.2007.08.012.

[67] M.F. Geer, J. Mazzuca, M.D. Smith, L.S. Shimizu, Short, strong halogen bonding in co-crystals of pyridyl bis-urea macrocycles and iodoperfluorocarbons, CrystEngComm. 15 (2013) 9923–9929. https://doi.org/10.1039/c3ce41413b.

[68] E. Parsons, B.; Jordon, J., Standard Potentials in Aqueous Solutions, in Dekker, New

York, 1985.

[69] S. S. Milazzo, G.; Caroli, V. K., Tables of Standard Electrode Potentials, in Wiley, London, 1978.

[70] E.A. Swift, E. H.; Butler, Quantitative Measurements and Chemical Equilibria, in Freeman, New York, 1972.

[71] V. Jovancicevic, J.O. Bockris, J.L. Carbajal, P. Zelenay, T. Mizuno, Adsorption and Absorption of Chloride Ions on Passive Iron Systems, J. Electrochem. Soc. 133 (1986) 2219–2226. https://doi.org/10.1149/1.2108377.

[72] P.M. Natishan, W.E. O'Grady, Chloride Ion Interactions with Oxide-Covered Aluminum Leading to Pitting Corrosion: A Review, J. Electrochem. Soc. 161 (2014) C421–C432. https://doi.org/10.1149/2.1011409jes.

[73] K.J. Kirkpatrick, The anodic behaviour of aluminium in aqueous solution, (1967).

[74] D.R. Turner, On the Mechanism of Chemically Etching Germanium and Silicon, J. Electrochem. Soc. 107 (1960) 810. https://doi.org/10.1149/1.2427519.

[75] P.N.H. Nakashima, The Crystallography of Aluminum and Its Alloys, 2019. https://doi.org/10.1201/9781351045636-140000245.

[76] W. Vedder, D.A. Vermilyea, Aluminum + water reaction, Trans. Faraday Soc. 65 (1969) 561–584. https://doi.org/10.1039/TF9696500561.

[77] A.T. Tabereaux, R.D. Peterson, Aluminum Production, Elsevier Ltd., 2014. https://doi.org/10.1016/B978-0-08-096988-6.00023-7.

[78] A.M.O. Brett, Christopher M. A. and Brett, Electrochemistry: Principles, methods, and applications, Oxford University Press, New York, 1993.

[79] Stephen K. Lower, Electrochemistry: Chemical reactions at an electrode, galvanic and electrolytic cells, 2004.

[80] I. Olefjord, B.O. Elfstrom, Composition of the Surface During Passivation of Stainless Steels., Corrosion. 38 (1982) 46–52. https://doi.org/10.5006/1.3577318.

[81] I. Epelboin, C. Gabrielli, M. Keddam, H. Takenouti, The Study of the Passivation Process by the Electrode Impedance Analysis, Electrochem. Mater. Sci. (1981) 151–192. https://doi.org/10.1007/978-1-4757-4825-3_3.

[82] Y.S. Hedberg, I. Odnevall Wallinder, Metal release from stainless steel in biological environments: A review, Biointerphases. 11 (2016) 018901. https://doi.org/10.1116/1.4934628.

[83] L. Lazzari, Cathodic protection: Basic principles, Elsevier, 2018. https://doi.org/10.1016/B978-0-12-409547-2.13445-6.

[84] R.T. Loto, O.O. Joseph, O. Akanji, Electrochemical corrosion behaviour of austenitic stainless steel (type 304) in dilute hydrochloric acid solution, J. Mater. Environ. Sci. 6 (2015) 2409–2417.

[85] K. V. Akpanyung, R.T. Loto, Pitting corrosion evaluation: A review, J. Phys. Conf. Ser. 1378 (2019). https://doi.org/10.1088/1742-6596/1378/2/022088.

[86] A.C. Marques, A. Mocanu, N.Z. Tomić, S. Balos, E. Stammen, A. Lundevall, S.T. Abrahami, R. Günther, J.M.M. de Kok, S.T. de Freitas, Review on adhesives and surface treatments for structural applications: Recent developments on sustainability and implementation for metal and composite substrates, Materials (Basel). 13 (2020) 1–43.

https://doi.org/10.3390/ma13245590.

[87] C. Campbell, Kirk-Othmer Encyclopedia of Chemical Technology (Adhesives), 2016. https://doi.org/10.1002/0471238961.0104080516150309.a01.pub4.

[88] H. Ma, N. Hu, C. Wu, Y. Zhu, Y. Cao, Q.Q. Chen, Synthesis, and research of epoxy resin toughening agent, Springerplus. 5 (2016). https://doi.org/10.1186/s40064-016-2356-5.

[89] Fi.J. K., Reactive polymers fundamentals and applications, 2nd ed, William Andrew, New York, 2013.

[90] C.H. Hore, Epoxy resins, J. Prot. Coatings Linings. 11 (1994).

[91] J.F. Lancaster, The use of adhesives for making structural joints, Metall. Weld. (1999) 54–84. https://doi.org/10.1533/9781845694869.54.

[92] F. Gamardella, X. Ramis, S. De la Flor, À. Serra, Preparation of poly(thiourethane) thermosets by controlled thiol-isocyanate click reaction using a latent organocatalyst, React. Funct. Polym. 134 (2019) 174–182. https://doi.org/10.1016/j.reactfunctpolym.2018.11.019.

[93] Y. Yanping, The development of polyurethane, Mater. Sci. Mater. Rev. 1 (2018) 1–8. https://doi.org/10.18063/msmr.v1i1.507.

[94] Y. Inoue, K. Matsumoto, T. Endo, Synthesis and properties of poly(thiourethane)s having soft oligoether segments, J. Polym. Sci. Part A Polym. Chem. 53 (2015) 1076–1081. https://doi.org/10.1002/pola.27535.

[95] J. Shin, H. Matsushima, J.W. Chan, C.E. Hoyle, Segmented polythiourethane elastomers through sequential thiol-ene and thiol-isocyanate reactions, Macromolecules. 42 (2009) 3294–3301. https://doi.org/10.1021/ma8026386.

[96] C. Huh, S.G. Mason, Effects of surface roughness on wetting (theoretical), J. Colloid Interface Sci. 60 (1977) 11–38. https://doi.org/10.1016/0021-9797(77)90251-X.

[97] F. Wegman, Reprint edition, 2006., (2006).

[98] L. Heepe, S.N. Gorb, Biologically inspired mushroom-shaped adhesive microstructures, Annu. Rev. Mater. Res. 44 (2014) 173–203. https://doi.org/10.1146/annurev-matsci-062910-100458.

[99] R.F. Wegman, J. Van Twisk, Introduction, Surf. Prep. Tech. Adhes. Bond. (2013) 1–8. https://doi.org/10.1016/b978-1-4557-3126-8.00001-4.

[100] W.C. Wake, Theories of adhesion and uses of adhesives: a review, Polymer (Guildf). 19 (1978) 291–308. https://doi.org/10.1016/0032-3861(78)90223-9.

[101] E. Dinte, B. Sylvester, Adhesives: Applications and Recent Advances, Appl. Adhes. Bond. Sci. Technol. (2018). https://doi.org/10.5772/intechopen.71854.

[102] S.J. Park, M.K. Seo, Solid-Liquid Interface, 2011. https://doi.org/10.1016/B978-0-12-375049-5.00003-7.

[103] B. Shaoxian, W. Shizhu, Vapor-condensed gas lubrication of face seals, Gas Thermohydrodynamic Lubr. Seals. (2019) 143–165. https://doi.org/10.1016/b978-0-12-816716-8.00007-3.

[104] J. Genzer, K. Efimenko, Recent developments in superhydrophobic surfaces and their relevance to marine fouling: A review, Biofouling. 22 (2006) 339–360. https://doi.org/10.1080/08927010600980223.

[105] S. Wang, L. Jiang, Definition of superhydrophobic states, Adv. Mater. 19 (2007) 3423–3424. https://doi.org/10.1002/adma.200700934.

[106] R.F. Wegman, J. Van Twisk, Steel and Stainless Steel, Surf. Prep. Tech. Adhes. Bond. (2013) 67–82. https://doi.org/10.1016/b978-1-4557-3126-8.00004-x.

[107] R.N. Wenzel, Resistance of solid surfaces to wetting by water, Ind. Eng. Chem. 28 (1936) 988–994. https://doi.org/10.1021/ie50320a024.

[108] A. Marmur, Wetting on hydrophobic rough surfaces: To be heterogeneous or not to be? Langmuir. 19 (2003) 8343–8348. https://doi.org/10.1021/la0344682.

[109] A.B.D. and CASSIE., S. BAXTER, Large Contact Angles of Plant and Animal Surfaces, Nature. 22 (1945) 72.

[110] G.B. Bacskay, J.R. Reimers, S. Nordholm, The mechanism of covalent bonding, J. Chem. Educ. 74 (1997) 1494–1502. https://doi.org/10.1021/ed074p1494.

[111] N. Suzuki, H. Ishida, A review on the structure and characterization techniques of silane/matrix interphases, Macromol. Symp. 108 (1996) 19–53. https://doi.org/10.1002/masy.19961080105.

[112] V. V. Verkholantsev, Adhesion promoters, Elsevier, 1999. https://doi.org/10.1016/b978-1-4377-3514-7.10029-7.

[113] G. Concepts, Adhesion Promoters 12.1, (2014) 301–329. https://doi.org/10.1016/B978-0-323-26435-8.00012-5.

[114] Dow, Limitless Silanes Bonding Organic and Inorganic Materials, (2020).

[115] T. Geminger, S. Jarka, Injection Molding of Multimaterial Systems, Elsevier Inc., 2016. https://doi.org/10.1016/B978-0-323-34100-4.00004-3.

[116] B. Mieke, C. Von Der Leeden, G. Frens, Surface Properties of Plastic Mqteriqls in Relation to their Adhering Performance, 2648 (2002) 280–289. https://doi.org/10.1002/1527-2648(20020503)4.

[117] A. Baldan, Adhesively-bonded joints and repairs in metallic alloys, polymers, and composite materials: Adhesives, adhesion theories and surface pretreatment, J. Mater. Sci. 39 (2004) 1–49. https://doi.org/10.1023/B:JMSC.0000007726.58758.e4.

[118] L. Ryan, J. Monaghan, Failure mechanism of riveted joint in fibre metal laminates, J. Mater. Process. Technol. 103 (2000) 36–43. https://doi.org/10.1016/S0924-0136(00)00416-7.

[119] Y. Liu, M. Li, X. Lu, X. Zhu, Failure mechanism and strength prediction model of t-joint of composite sandwich structure, Metals (Basel). 11 (2021). https://doi.org/10.3390/met11081197.

[120] S. Ebnesajjad, A.H. Landrock, Joint Design, Adhes. Technol. Handb. (2015) 183–205. https://doi.org/10.1016/b978-0-323-35595-7.00007-3.

[121] K. Martinsen, S.J. Hu, B.E. Carlson, Joining of dissimilar materials, CIRP Ann. - Manuf. Technol. 64 (2015) 679–699. https://doi.org/10.1016/j.cirp.2015.05.006.

[122] A. Gursel, Adhesion Mechanism and Failure Modes in Adhesively Bonded Joints, Int. Conf. Mater. Sci. Technol. Kızılcahamam/ANKARA. (2019) 108–114.

[123] M.J. Davis, D.A. Bond, the Importance of Failure Mode Identification in Adhesive Bonded, ICCM-12 Conf. (1999) 5–9.

[124] J. Hart-Smith, Effects of Flaws and Porosity on Strength of Adhesive-Bonded Joints,

Douglas Aircr. Co. Rep. MDC J4699. (n.d.).

[125] Jacob J. Bikerman, Causes of poor adhesion: Weak boundary layers, Ind. Eng. Chem, 9 (1967) 40–44.

[126] D. Fernando, J.G. Teng, T. Yu, X.L. Zhao, Preparation and Characterization of Steel Surfaces for Adhesive Bonding, J. Compos. Constr. 17 (2013) 04013012. https://doi.org/10.1061/(ASCE)cc.1943-5614.0000387.

[127] E. H., Adhesives and adhesive action, Nature. 118 (1926) 320–321. https://doi.org/10.1038/118320b0.

[128] M.J. Davis, A. McGregor, Importance of Failure Mode Indentification.pdf, ISASI Aust. Saf. Semin. Canb Erra. (2010) 1–12.

[129] J. Sanderson, Fundamentals of Microscopy, Curr. Protoc. Mouse Biol. 10 (2020) e76. https://doi.org/10.1002/cpmo.76.

[130] K. Thorn, A quick guide to light microscopy in cell biology, Mol. Biol. Cell. 27 (2016) 219–222. https://doi.org/10.1091/mbc.E15-02-0088.

[131] S.M. Wolniak, Principles of Microscopy, College Park, Maryland, n.d. https://science.umd.edu/cbmg/faculty/wolniak/wolniakmicro.html.

[132] J. Goodhew, John Humphreys, and R.B. Peter Electron microscopy and analysis., Taylor Fr. (2001).

[133] A. Mohammed, A. Abdullah, Scanning Electron Microscopy (Sem): a Review, Proc. 2018 Int. Conf. Hydraul. Pneum. - HERVEX. (2018) 77–85.

[134] J.I. Goldstein, D.E. Newbury, P. Echlin, D.C. Joy, A.D. Romig, C.E. Lyman, C. Fiori, E. Lifshin, Coating and Conductivity Techniques for SEM and Microanalysis, Scanning Electron Microsc. X-Ray Microanal. (1992) 671–740. https://doi.org/10.1007/978-1-4613-0491-3_13.

[135] J.A. Seyforth, Scanning Electron Microscopy (SEM): An Introduction to the Use of SEM for Characterizing the Surface Topology and Composition of Matter with Further Applications, Exp. Tech. Condens. Matter Phys. (2015) 6.

[136] R. Hill, J.A. Notte, L. Scipioni, Scanning helium ion microscopy, Elsevier Inc., 2012. https://doi.org/10.1016/B978-0-12-394396-5.00002-6.

[137] N. Saba, M. Jawaid, M.T.H. Sultan, An overview of mechanical and physical testing of composite materials, Elsevier Ltd, 2018. https://doi.org/10.1016/B978-0-08-102292-4.00001-1.

[138] German Institute for Standardization. Klebsto_e - Bestimmung der Zugscherfestigkeit von Überlappungsklebungen (Adhesives- Determination of tensile lap-shear strength of bonded assemblies)., in Ger. DIN, 2009.

[139] B. Duncan, Developments in testing adhesive joints, Adv. Struct. Adhes. Bond. (2010) 389–436. https://doi.org/10.1533/9781845698058.3.389.

[140] T. Huhtamäki, X. Tian, J.T. Korhonen, R.H.A. Ras, Surface-wetting characterization using contact-angle measurements, Nat. Protoc. 13 (2018) 1521–1538. https://doi.org/10.1038/s41596-018-0003-z.

[141] Attention Biolin Scientific, Static and dynamic contact angles and their measurement techniques, Biolin Sci. c (2018) 1–3.

[142] M. Steinert, J. Acker, S. Oswald, K. Wetzig, Study on the mechanism of silicon etching

in HNO3-rich HF/HNO3 mixtures inf, J. Phys. Chem. C. 111 (2007) 2133–2140. https://doi.org/10.1021/jp066348j.

[143] G.I. for S. Der, Zugscherfestigkeit, Kleb. - Bestimmung. (n.d.).

[144] R.G. Cox, The spreading of a liquid on a rough solid surface, J. Fluid Mech. 131 (1983) 1–26. https://doi.org/10.1017/S0022112083001214.

[145] J. Schindelin, I. Arganda-Carreras, E. Frise, V. Kaynig, M. Longair, T. Pietzsch, S. Preibisch, C. Rueden, S. Saalfeld, B. Schmid, J.Y. Tinevez, D.J. White, V. Hartenstein, K. Eliceiri, P. Tomancak, A. Cardona, Fiji: An open-source platform for biological-image analysis, Nat. Methods. 9 (2012) 676–682. https://doi.org/10.1038/nmeth.2019.

[146] J. Hunt, Supplementary XRD Theory, (n.d.) 4–7.

[147] A.R. West, Solid State Chemistry and its applications, Second ed, John Wiley & Sons, Sheffield, UK., 2022.

[148] M. Santamaria, F. Di Quarto, S. Zanna, P. Marcus, Initial surface film on magnesium metal: A characterization by X-ray photoelectron spectroscopy (XPS) and photocurrent spectroscopy (PCS), Electrochim. Acta. 53 (2007) 1314–1324. https://doi.org/10.1016/j.electacta.2007.03.019.

[149] M. Affatigato, D.H. Osborne, R.F. Haglund, Effect of surface roughness on the acid etching of amorphous silica, J. Am. Ceram. Soc. 79 (1996) 688–694. https://doi.org/10.1111/j.1151-2916.1996.tb07930.x.

[150] R.F. Schaller, A. Mishra, J.M. Rodelas, J.M. Taylor, E.J. Schindelholz, The Role of Microstructure and Surface Finish on the Corrosion of Selective Laser Melted 304L, J. Electrochem. Soc. 165 (2018) C234–C242. https://doi.org/10.1149/2.0431805jes.

[151] P. Liu, B. Chen, C. Liang, W. Yao, Y. Cui, S. Hu, P. Zou, H. Zhang, H.J. Fan, C. Yang, Tip-Enhanced Electric Field: A New Mechanism Promoting Mass Transfer in Oxygen Evolution Reactions, Adv. Mater. 33 (2021) 1–9. https://doi.org/10.1002/adma.202007377.

[152] L. R. F. Allen, and J.B. Electrochemical Methods Fundamentals and Applications, Wiley, New York, 2001.

[153] K.F. Nurhaziqah, C.K. Sheng, K.A.M. Amin, M.I.N. Isa, M.F. Hassan, E.A.G.E. Ali, K.H. Kamarudin, R. Aarif, Effect of HNO3 concentration on etch rate and structure of si wafer etched in the mixture of HF and HNO3 solutions, ASM Sci. J. 11 (2018) 68–74.

[154] T. Ohtsuka, Passivation oxide films and rust layers on iron, Charact. Corros. Prod. Steel Surfaces. 7 (2006) 19–31. https://doi.org/10.1007/978-3-540-35178-8_2.

[155] C. Baker, S.K. Hasanain, S.I. Shah, The magnetic behavior of iron oxide passivated iron nanoparticles, J. Appl. Phys. 96 (2004) 6657–6662. https://doi.org/10.1063/1.1806263.

[156] A. Gapeeva, J. Vogtmann, B. Zeller-Plumhoff, F. Beckmann, M. Gurka, J. Carstensen, R. Adelung, Electrochemical Surface Structuring for Strong SMA Wire-Polymer Interface Adhesion, ACS Appl. Mater. Interfaces. 13 (2021) 21924–21935. https://doi.org/10.1021/acsami.1c00807.

[157] J. Drelich, E. Chibowski, D.D. Meng, K. Terpilowski, Hydrophilic and superhydrophilic surfaces and materials, Soft Matter. 7 (2011) 9804–9828. https://doi.org/10.1039/c1sm05849e.

[158] I. Hölken, M. Hoppe, Y.K. Mishra, S.N. Gorb, R. Adelung, M.J. Baum, Complex shaped ZnO nano- and microstructure based polymer composites: Mechanically stable and

environmentally friendly coatings for potential antifouling applications, Phys. Chem. Chem. Phys. 18 (2016) 7114–7123. https://doi.org/10.1039/c5cp07451g.

[159] A. Gapeeva, I. Hölken, R. Adelung, M. Baum, Characterization of a polydimethylsiloxane-polythiourethane polymer blend with potential as fouling-release coating, Proc. 2017 IEEE 7th Int. Conf. Nanomater. Appl. Prop. N. 2017. 2017-Janua (2017) 1–5. https://doi.org/10.1109/NAP.2017.8190200.

[160] J.J. Licari, D.W. Swanson, Chemistry, Formulation, and Properties of Adhesives, 2011. https://doi.org/10.1016/b978-1-4377-7889-2.10003-8.

[161] A. Pizzi, Phenolic resin adhesives, 2017. https://doi.org/10.1201/9781315120942.

[162] A.S. Román, C.M. Méndez, C.A. Gervasi, R.B. Rebak, A.E. Ares, Corrosion Resistance of Aluminum-Copper Alloys with Different Grain Structures, J. Mater. Eng. Perform. 30 (2021) 131–144. https://doi.org/10.1007/s11665-020-05344-1.

[163] S. Huang, W. Long, B. Huang, S. Zhong, L. Bao, A Review on Corrosion Resistant of Cu-Al Joints, IOP Conf. Ser. Mater. Sci. Eng. 381 (2018). https://doi.org/10.1088/1757-899X/381/1/012174.

[164] R.L. Brockenbrough, F.S. Merritt, Structural steel designer's handbook, 1994. https://doi.org/10.5860/choice.32-1557.

[165] D.D.N. Singh, S. Yadav, J.K. Saha, Role of climatic conditions on corrosion characteristics of structural steels, Corros. Sci. 50 (2008) 93–110. https://doi.org/10.1016/j.corsci.2007.06.026.

List of Figures

List of Tables

List of Abbreviations

EDX	**E**nergy **D**ispersive **X**-ray **S**pectroscopy
IPS	**I**ncreasing anodic current **P**ulsing **T**ime
MOPS	**M**ultiples of **O**nly anodic current **P**ulsing **S**pikes
MPS	**M**ultiples anodic current **P**ulsing **S**pikes
PAB-GBS	**P**ristine **Ab**raded-**G**rit **B**lasted **S**urface
PABS	**P**ristine **Ab**raded **S**urface
PA-GBS	**P**ristine **Ab**raded-**G**rit **B**lasted **S**urface
PAS	**P**ristine **A**braded **S**urface
PS	**P**ristine **S**urface/**S**ample
PTU	**P**oly**t**hio**u**rethane
SEM	**S**canning **E**lectron **M**icroscope
SST	**S**tainless **St**eel
TPS	**T**wo anodic regimes **P**ulsing **S**pikes
UTS	**U**ltimate **T**ensile **S**trength
XRD	**X**-ray **D**iffraction **S**pectroscopy

Acknowledgments

Firstly, I would like to thank the ever-supportive, creative, and inspiring Prof. Dr. Rainer Adelung for providing me with the opportunity to work in his group, for the trust, guidance, and encouragement, and for keeping me informed of the latest scientific development in and outside Material science. It has been a delightful and esteemed experience to work under your guidance and mentorship.

I will ever remain grateful to Prof. Dr. Helmut Föll for giving me the chance to initially work in his group, which lay the foundations of my experimentally based Material science understanding, semiconductor etching, and metal surface structuring, which is highly influenced by the knowledge of the later.

A special thanks with profound sincere gratitude go to Dr. Jürgen Carstensen for being more than a supervisor. Your encouragement and willingness to engage in scientific teaching, analysis, and discussion throughout my work are valuably appreciated and by far the most important and helpful.

My sincerest gratitude also goes to Dipl.-Ing. Jörg Bahr for the personal relationship and the great technical support in the laboratory which was crucial in terms of the success of the large-scale setup designs and the 3D printed parts used in this work. Accordingly, words cannot be enough in appreciation of the personality of Dr.-Ing. Sören Kaps for the encouragement, standing in the gap for me, and your contributions to my research works made everything so fulfilling. Furthermore, my joy has no bound for coming across the person of Emmanuel Ossei-Wusu, you are forever appreciated.

I would like to express my deep gratitude to Nascit GmbH in the persons of Karsten Wenige, Dr. -Ing. Henning Winterfeld, Jakob Offermann, and Ibrahim Kassem for such an atmosphere of cordial seriousness with uttermost professional work ethics. Similarly, my sincere appreciation goes to the Phi-Stone AG in the persons of Dr. Iris Hayes, Dr. Ala Cojocaru, Hartmut Schmidt-Niepenberg, and Mathias Hoppe.

I would like to thank Beate Minten, Vivian Wehr, and Katrin Brandenburg for their administrative support and assistance in documenting important files. The TF workshop team, especially Matthias Burmeister and Berndt Neumann, provided essential support in the machining, cutting, and grit-blasting of metal samples, often on short notice.

ACKNOWLEDGMENTS

A special thanks go to Dr. -Ing. Haoyi Qiu (Teacher Qiu) for being an all-around colleague, your encouragement, positivity, readiness to help, and support have been a life support system to me and my work. Words will not be enough in appreciation to a friend, brother, and colleague in the person of Dr. Josiah Ngenev Shondo

Finally, I would like to thank all my colleagues in Prof. Rainer Adelung's research group. Special thanks to Anna Gapeeva, Catarina Schmidt, Kerstin Meurisch, Barnika Chakraborty, and Dr. Oleg Lupan for sharing the office with a great working atmosphere. I thank Dr. Leonard Siebert, Dr. Fabian Schütt, Armin Reimers, Martha Gerhardt, Margarethe Hauck, Lena Marie Saure, Maik-Ivo Terasa, Peter Sommer, Lukas Zimoch, Monja Gronenberg, Morten Möller, Pia Holtz, Roshani Madurawala, Philipp Schadte, Jan-Ole Stern, Erik Greve, Jannik Rank, Deik Petersen, Erfan Topie Osman and all other colleagues for their kind help, friendship, and support.

Lastly, I extend my heartfelt appreciation to my lovely wife, Oziegbe Isibhakhome, for her continuous encouragement, support, love, and patience. I also wish to recognize my late parents, who supported, guided, and embraced me throughout my life until their passing. Finally, my unending gratitude goes to my big sister, Obobi Ugo Kalu, whose support and encouragement have been instrumental in all my achievements.

Authorship/Co-authorship Contributions

The contributions made to the publications and manuscripts presented in this work can be classified based on several criteria: Conceptualization of the investigation (**C**), Methodology (**M**), Data collection (**D**), Interpretation of the data (**I**), Writing of the manuscript (**W**), and Review/Editing (**RE**). The table below provides the subjective estimation, expressed as a percentage, of own contribution to each publication.

Publication 1:

C.O. Kalu, M. Hoppe, I. Hölken, M. Baytekin-Gerngross, M.D. Gerngross, J. Carstensen, R. Adelung, Formation of micro-mechanical interlocking sites by nanoscale sculpturing for composites or hybrid materials with stainless steel, J. Mater. Res. 35 (2020) 3145–3156. https://doi.org/10.1557/jmr.2020.284.

Contribution (%):

C	M	D	I	W	RE
60	40	70	30	50	50

Publication 2:

C. O. Kalu, Catarina Schmidt, S. Kaps, J. Carstensen, R. Adelung, Impact of the initial surface morphology on nucleation efficiency during evolution of mechanical interlocking structures by chemical nanoscale sculpturing of Aluminium Alloy (AlMg3) (manuscript to be submitted).

Contribution (%):

C	M	D	I	W	RE
70	40	70	40	60	50

Publication 3:

C. O. Kalu, S. Kaps, J. Carstensen, R. Adelung, Influence of initial surface morphology on nucleation efficiency of micro-mechanical interlocking sites on stainless steel via electrochemical nanoscale sculpting (manuscript to be submitted).

Contribution (%):

C	M	D	I	W	RE
70	40	70	40	60	50

Publication 4:

C. O. Kalu, E. Ossei-Wusu, S. Kaps, J. Carstensen, R. Adelung, Preservation of the intrinsic mechanical properties of a thin stainless steel wire after electrochemical nanoscale sculpturing for enhanced surface adhesion (manuscript to be submitted).

Contribution (%):

C	M	D	I	W	RE
30	30	70	30	60	50

Kiel, 30.06.2023.

Kalu Chima Obobi

Prof. Dr. Rainer Adelung

Declaration

I hereby certify that my doctoral dissertation entitled "Nanoscale Sculpturing: Enhancing Adhesion and Preserving Intrinsic Mechanical Properties of Metallic Materials for Multifunctional Applications" has not been submitted in an identical or similar form for any other examination process. This thesis represents the product of my independent research and has been composed solely by me, without illegal assistance from others. All sources and materials used in this work have been duly acknowledged and appropriately referenced.

I received scientific support and guidance from Dr. Jürgen Carstensen, Dipl.-lng. (FH) Jörg Bahr, and Dr.-Ing. Sören Kaps in the analysis and discussion of my experimental findings and the designing of the industrial large-scale nanoscale sculpturing setup.

I did not receive any form of support or guidance from commercial consultants or any other individual in the preparation of this work.

I affirm that this thesis has been prepared in accordance with the Rules of Good Scientific Practice promulgated by the German Research Foundation. Furthermore, I declare that no academic degree has been withdrawn from me in the past. Certain aspects of this work have already undergone peer review and have been published in a scientific journal.

Publications

[1] C.O. Kalu, M. Hoppe, I. Hölken, M. Baytekin-Gerngross, M.D. Gerngross, J. Carstensen, R. Adelung, Formation of micro-mechanical interlocking sites by nanoscale sculpturing for composites or hybrid materials with stainless steel, J. Mater. Res. 35 (2020) 3145–3156. https://doi.org/10.1557/jmr.2020.284.

[2] Impact of the initial surface morphology on nucleation efficiency during evolution of mechanical interlocking structures by chemical nanoscale sculpturing of Aluminium alloy (AlMg3) (To be submitted).

[3] Influence of initial surface morphology on nucleation efficiency of micro-mechanical interlocking sites on stainless steel via electrochemical nanoscale sculpturing (To be submitted).

[4] Preservation of the intrinsic mechanical properties of a thin stainless steel wire after electrochemical nanoscale sculpturing for enhanced surface adhesion (To be submitted).

Kiel, the 30.06.2023 Kalu Chima Obobi